CRANFIELD INSTITUTE OF TECHNOLOGY

COLLEGE OF AERONAUTICS

Ph.D. THESIS

C.M. HELLON

On the Use of the Boundary Layer Integral Equations for the Prediction of Skin Friction and Heat Transfer

Supervisor: D.I.A. Poll

October 1986

ABSTRACT

The usefulness of the energy equation integrated over the thickness of the boundary layer, in predicing heat transfer rates to smooth body surfaces in investigated. It is found that on assuming very simple closure relations, similar to those often used with the momentum equation, highly accurate predictions are made. It is shown further that the usefulness of these predictions extend into areas where the momentum equation-skin friction predictions, which have proved so popular, break down such as regions of reverse flow and shock/boundary layer interactions. The technique is has been tested in laminar, transitional and turbulent flows with both experiment and other more complex theories.

The technique is extended to three-dimensional laminar flows with the inclusion of a crossflow model.

ACKNOWLEDGEMENT

I would like to express my thanks to my supervisor Dr. D.I.A. Poll whose invaluable guidance and expertise in a topic quite new to me, was a great help, and also to Dr. T. Holbeche of RAE Farnborough, whose comments on the most important areas ensured the progression of the research in a useful direction. Finally but by no means least Valerie & Francis who coped with illegible handwriting and numerous reiterations to produce this typescript.

The financial support for this work was provided by the Procurement Executive of the Ministry of Defence under Research Agreement number 2028/0133 XR/AW.

If a little knowledge is dangerous, where is the man who has so much as to be out of danger (1877)

CONTENTS

LIST OF FIGURES

2.3.5b-c	Horstmann heat transfer & skin friction, 15 deg leading edge shock generator
2.3.6	Pressure distribution over Colman's cylinder-flare model used in heat transfer predictions
2.3.7	Heat transfer predictions on hollow cylinder-flare (Colman)
2.4.1	Laminar separation on an infinite cylinder, comparison between theories (skin friction)
2.4.2	Laminar flow on an infinite cylinder, comparison between theories (heat transfer)
2.4.3	Laminar flow on an infinite cylinder, comparison between theories (Reynolds analogy factor)
2.4.4	Turbulent separation flow, comparison between prediction using Buri's criteria and experiment
2.5.1	Curve fit of Cohen & Reshotko similarity equation velocity gradient at the wall
2.5.2	Curve fit of Cohen & Reshotko similarity equation temperature gradient at the wall
2.5.3	Heat transfer rates to spherically blunted cones at zero incidence (Widhopf data ref (32))
2.5.4	Heat transfer rates to spherically blunted cones at zero incidence (Miller data ref(33))
2.5.5	Heat transfer rates to spherically blunted cones at zero incidence (Bushnell data ref(34))
2.5.6	Entropy swallowing on a blunt body flow
2.6.1	Transitional flow over a blunted cone
2.6.2	Affect of variation of transition onset location on heat transfer over a blunted cone
2.6.3	Variation of total heat transfer to a blunt cone s/Rn < 5 with onset of transition location
3.1.1	Shape of 3-dimensional boundary layer velocity profiles
3.2.1	Orthogonal curvilinear coordinate system
3.3.1	Kang crossflow profiles
3.4.1	Skin friction/heat transfer on attachment line of a sharp cone
3.5.1	Computational coordinate system notation
3.6.1	Blunted cone at incidence (Widhopf)
3.6.2	Blunted cone at incidence (Bushnell)

3.6.3	Blunted cone at incidence (Davies)
4.0.1	Hemispherically blunted cone at incidence
4.1.1	Pressure distribution predictions over sphere-cones Widhopf ref(32)
4.1.2	Modified Newtonian pressure prediction on 10 deg sharp cone at zero incidence
4.2.1	Pressure distribution prediction on a sphere-cone at incidence
4.2.2	Circumferential pressure variation on a 10 deg sharp cone in a Mach 5 freestream
5.1	Prediction of incompressible laminar similarity boundary layer by the method of integral relations
D1	Generation of Blottner & Ellis coordinate system
D2	Coordinate direction
D3	Mesh notation

MAIN NOTATION

a - speed of sound

C_p - pressure coefficient

c_p - specific heat at constant pressure

C_{fe} - skin friction coefficient

f - streamwise velocity function in similarity equations

F - velocity function in symmetry plane similarity equation

h - enthalpy

H - shape factor

k - thermal conductivity or variable wall temperature parameter eqn.(2.2.2)

m - streamwise velocity gradient parameter in similarity eqns.

M - Mach number

p - pressure

P_i - constants in 3-d integral thickness relations

Pr - Prandtl number

q - heat transfer rate

r - axisymmetric radius or recovery factor

Re_l - Reynolds number based upon length scale l

R_n - blunt body nose radius

S - temperature similarity variable in similarity eqns.

St_e - Stanton number

T - temperature

u - streamwise velocity component

U - transformed streamwise velocity component

v - velocity component normal to wall

u_i - velocity in xi direction (3-d boundary layers)

x - coordinate in streamwise direction

X - compressible transformation in streamwise direction eqn(2.1.2)

x_i - coordinate direction (3-d boundary layers)

y - normal to wall coordinate

Y - compressible transformation in y-direction eqn(2.1.1)

GREEK LETTERS

α - power index for laminar/turbulent closure relations or angle of incidence (3-dimensions)

γ - ratio of specific heats

Γ - enthalpy thickness

δ^* - displacement thickness

η - Howarth-Dorodnitsyn transformed normal to wall coordinate

ϑ - momentum thickness

μ - viscosity

ν - kinematic viscosity

ρ - density

σ - Reynolds analogy factor

τ - shear stress

ψ - temperature function in similarity eqn (2.2.2)

SUFFICEES

e - boundary layer edge value

i - incompressible value

O - total conditions

$*$ - evaluated at Eckert reference enthalpy eqn(1.2.8)

W - wall value

∞ - free-stream value

r - evaluated at recovery or equilibrium temperature

Introduction

An ability to predict heat transfer accurately is a feature of paramount importance in the field of high speed aerodynamics. Over the years many methods with varying degrees of complexity have been developed ranging from the simple 'engineering method' type calculations for early design stages where 10-20% accuracy is adequate, to the full Navier-Stokes equation solution, when hopefully rather better accuracy is achieved. Analytic solutions to the Navier-Stokes equations are very scarce and for practical flow situations numerical calculation is required. Until several orders of magnitude improvement in the speed of computers is achieved these calculations will be too costly for all but the final stages in the aerodynamic design of a vehicle. Also there is still a lot of analysis to be done in the complex flow situations such as shock boundary layer interactions where often the results from these codes are not a significant improvement over the very simple techniques.

The application of Prandtl's 1st order boundary layer theory, which is valid in high Reynolds number flows, allows a great time saving in computational effort when compared with the full Navier-Stokes solution. An inviscid flow calculation around the body is performed and the resulting body surface pressure distribution used in the prediction of the boundary layer surrounding the body. Analytic solutions to the boundary layer equations are available for certain special cases of surface pressure and wall temperature distributions for laminar flow, but again for practical situations numerical calculations are required. Although full field solution of the boundary layer equations are an order of magnitude quicker to compute than the Navier-Stokes equations they are still costly to use. Alternatively the boundary layer equations can be integrated over the thickness of the boundary layer to generate the boundary layer integral equations which require suitable closure relations for the velocity and temperature profiles before they can be solved. Since one of the dimensions is integrated out, the solution process is potentially very much reduced, and indeed the approach has been adopted quite successfully for the prediction of skin friction, using the momentum integral equation, which historically has been more important than heat transfer, due to the relatively low speed involved. For the case of heat transfer, several methods have been proposed, some of these are based upon the energy integral equation which yields heat transfer rates directly whilst others use the well established momentum integral equation with an assumed relationship between skin friction and heat transfer rates, namely the Reynolds analogy factor.

$$\sigma = \frac{2\,St_e}{C_{fe}}$$

This latter technique, which is popular through the success of the momentum integral equation approach, relies upon the accurate determination of σ which is known to vary with pressure and wall temperature distributions in laminar flow, i.e. Stewartson ref (47). For turbulent flow it is not at all clear whether the analogy is satisfactory or not due to the lack of reliable experimental data. However we find most of them adopt a flat plate value for σ similar to that determined by Colburn ref. (1), which may result in poor heat transfer predictions.

$$\sigma_{FP} = Pr^{-2/3}$$

Potentially the energy equation can predict heat transfer rates at least as accurately as the momentum equation can skin friction. This will be investigated by choosing a simple flat plate closure model and carrying out comparisons with other theories, both approximate and exact, and with experiment, which include transition, shock/boundary layer interactions, compression corners and separation regions in axisymmetric and 2-D flows - areas where the supposedly more accurate full field methods discussed earlier may well break down.

A more sophisticated closure technique for laminar flow will also be considered. Improved two parameter closure relations based on the boundary layer thickness and local pressure gradient, are derived using the similarity solutions of Cohen & Reshotko Ref. (10).

The calculation of fully 3-dimensional high speed flows using 3-dimensional boundary layer theory has recently become a substantial research area, where for instance application of a slight yaw to an otherwise axisymmetric flow, can dramatically alter the heating distributions. Unfortunately very little good experimental data is available, with which to assess the various prediction methods produced. Such methods are complex not just because of the added dimension, but also the velocity profiles are not necessarily planar, and non-zero components can be found in the normal to the inviscid surface streamline direction. This causes modelling difficulties for the velocity profile when using the integral equations, since the 'crossflow' component can be of a variety of shapes, thus the model used must be sufficiently flexible. Often for 'simple' 3-dimensional boundary layer predictions the crossflow component is neglected and the equations reduce to an 'axisymmetric analogue' form attributed to Cooke ref. (49), in which axisymmetric/2-D closure

relations are used for the remaining streamwise velocity and temperature profiles. The resulting integral equations being integrable along any given inviscid surface streamline. Here we adopt a compressible form of an incompressible crossflow profile model proposed by Timman ref (55) and consider its influence onthe heat transfer rates tothe windward plane of symmetry of a sharp cone, for which exact solutions are available, and to the windward surface of a blunted cone. For the sharp cone case the existence of an exact solution will be utilised fully to produce a detailed analysis of the influence of wall temperature and boundary layer edge Mach number on the size of the crossflow. For the blunt cone case the 3-dimensional code described in chapter 3 (KHOMP3D) is used for comparison with experimental data.

Finally the quality of any heat transfer predictions depends upon the accuracy of the external pressure distributions used, and a chapter is devoted to pressure predictions. In particular the modified Newtonian method is closely examined, this particular technique is attractive because it is very quick and easy to use.

Chapter 1

1.1 Derivation of boundary layer integral equations

The boundary layer equations in 2-dimensional or axisymmetric flow are given below (see fig.(1.1.1) and Cebeci and Bradshaw, ref. (2)).

$$\frac{\partial(r^{\varepsilon}\rho u)}{\partial x} + \frac{\partial(r^{\varepsilon}\overline{\rho v})}{\partial y} = 0 \qquad (1.1.1)$$

$$\rho u \frac{\partial u}{\partial x} + \overline{\rho v} \frac{\partial u}{\partial y} = -\frac{dP}{dx} + \frac{1}{r^{\varepsilon}} \frac{\partial(r^{\varepsilon}\tau)}{\partial y} \qquad (1.1.2)$$

$$P(x,y) = P(x) \qquad (1.1.3)$$

$$\rho u \frac{\partial T}{\partial y} + \overline{\rho v} \frac{\partial T}{\partial y} = \frac{\mu}{c_p}\left(\frac{\partial u}{\partial y}\right)^2 - \frac{1}{c_p}\frac{\partial}{\partial y}(r^{\varepsilon} q) + \frac{u}{c_p}\frac{dP}{dx} \qquad (1.1.4)$$

with $\varepsilon = 1$, for axisymmetric flow, $\varepsilon = 2$ for 2-dimensional flow.

$$\tau = \mu\frac{\partial u}{\partial y} - \rho\overline{u'v'} - \overline{\rho' u' v'}$$

$$q = -k\frac{\partial T}{\partial y} + \rho c_p \overline{T'v'} + c_p \overline{\rho' T' v'}$$

where the terms in the equations are the mean flow values and

$$\overline{\rho v} = \rho v + \overline{\rho' v'}$$

For the turbulent flow empirical formulae relating the turbulence structure to the mean flow have to be employed (such as the well known eddy viscosity technique). Hence exact solutions of the above only exist in laminar flows and even then for the general case the full field integration of the coupled partial differential equations requires large computation times. Simplification can be achieved by reducing equations (1.1.1) to (1.1.4) to a system of

first order ordinary differential equations, obtained by integration across the thickness of the boundary layer thus eliminating the derivatives.

At the boundary layer edge (1.1.2) becomes

$$\rho_e u_e \frac{du_e}{dx} = -\frac{dP}{dx}$$

which on substitution back into (1.1.2) using (1.1.3) and rearranging we obtain

$$\rho u \frac{\partial}{\partial x}(u - u_e) - (\rho_e u_e - \rho u)\frac{\partial u_e}{\partial x} + \rho v \frac{\partial u}{\partial y}$$

$$= \frac{1}{r^\varepsilon}\frac{\partial}{\partial y}\left\{ r^\varepsilon\left(\mu\frac{\partial u}{\partial y} - \rho\overline{u'v'} - \overline{\rho' u' v'}\right)\right\} \qquad (1.1.5)$$

multiplying (1.1.5) by r^ε and (1.1.1) by $(u - u_e)$ and adding results in

$$\frac{\partial}{\partial x}\left\{\rho_e u_e^2 r_o^\varepsilon\left[\frac{\rho u}{\rho_e u_e}\left(1 - \frac{u}{u_e}\right)\left(\frac{r}{r_o}\right)^\varepsilon\right]\right\} + \rho_e u_e 2 r_o^\varepsilon\left[\left(1 - \frac{\rho u}{\rho u_e}\right)\left(\frac{r}{r_o}\right)^\varepsilon\right]\frac{1}{u_e}\frac{du_e}{dx}$$

$$+ \frac{\partial}{\partial y}\left\{\overline{\rho v}(u - u_e) r^\varepsilon\right\} = \frac{\partial}{\partial y}\left\{ r^\varepsilon\left(\mu\frac{\partial u}{\partial y} - \rho\overline{u'v'} - \overline{\rho' u' v'}\right)\right\}$$

thus upon integrating with respect to y and letting

$$\vartheta = \int_0^\delta \frac{\rho u}{\rho_e u_e}\left(1 - \frac{u}{u_e}\right)\left(\frac{r}{r_o}\right)^\varepsilon dy = \text{momentum thickness}$$

$$\delta^* = \int_0^\delta \left(1 - \frac{\rho u}{\rho_e u_e}\right)\left(\frac{r}{r_o}\right)^\varepsilon dy \qquad \text{displacement thickness}$$

we obtain

$$\frac{d}{dx}\left(\rho_e u_e^2 r_o^\varepsilon \vartheta\right) + r_o^\varepsilon \rho_e u_e \delta^* \frac{du_e}{dx} = r_o^\varepsilon \mu_w \left.\frac{\partial u}{\partial y}\right|_w$$

or

$$\frac{d\vartheta}{dx} + \frac{\vartheta(H+2)}{u_e}\frac{du_e}{dx} + \frac{\vartheta}{\rho_e}\frac{d\rho_e}{dx} + \frac{\varepsilon\vartheta}{r_o}\frac{dr_o}{dx} = \frac{\mu_w}{\rho_e u_e^2}\left.\frac{\partial u}{\partial y}\right|_w \qquad (1.1.6)$$

where H = shape factor = δ^*/ϑ

Multiplying (1.1.2) by u and (1.1.4) by c_p and adding gives

$$\rho u\frac{\partial}{\partial x}(h+\frac{u^2}{2}) + \overline{\rho v}\frac{\partial}{\partial y}(h+\frac{u^2}{2}) = \mu(\frac{\partial u}{\partial y})^2 + \frac{u}{r^\varepsilon}\frac{\partial}{\partial y}\left(r^\varepsilon(\mu\frac{\partial u}{\partial y} - \rho\overline{u'v'} - \overline{\rho'u'v'})\right) + \frac{1}{r^\varepsilon}\frac{\partial}{\partial u}\left(r^\varepsilon(\frac{k}{c_p}\frac{\partial h}{\partial y} - \rho\overline{T'v'} - \overline{\rho'T'v'})\right)$$

but $\mu(\frac{\partial u}{\partial y})^2 + \frac{u}{r^\varepsilon}\frac{\partial}{\partial y}(r^\varepsilon\mu\frac{\partial u}{\partial y}) = \frac{1}{r^\varepsilon}\frac{\partial}{\partial y}(r^\varepsilon\mu\frac{\partial}{\partial y}(\frac{u^2}{2}))$

thus the above becomes

$$r^\varepsilon\rho u\frac{\partial h_o}{\partial x} + r^\varepsilon\overline{\rho v}\frac{\partial h_o}{\partial y} = \frac{1}{Pr}\frac{\partial}{\partial y}\left(r^\varepsilon\mu\frac{\partial}{\partial y}(h+Pr\frac{u^2}{2})\right) - \frac{\partial}{\partial y}\left(r^\varepsilon(\rho\overline{u'v'} + \overline{\rho'u'v'} + \rho\overline{T'v'} + \overline{\rho'T'v'})\right)$$

since $Pr = \frac{\mu c_p}{k}$ and h_o = total enthalpy = $h + \frac{u^2}{2}$

On multiplying (1.1.1) by h_o and adding to the above we obtain

$$\frac{\partial}{\partial x}(r^\varepsilon\rho u h_o) + \frac{\partial}{\partial y}(r^\varepsilon\overline{\rho v}h_o) = \frac{1}{Pr}\frac{\partial}{\partial y}\left(r^\varepsilon\mu\frac{\partial}{\partial y}(h+Pr\frac{u^2}{2})\right) - \frac{\partial}{\partial y}\left(r^\varepsilon(\rho\overline{u'v'} + \overline{\rho'u'v'} + \rho\overline{T'v'} + \overline{\rho'T'v'})\right)$$

which upon integration yields

$$\int_0^{\delta} \frac{\partial}{\partial x}(r^{\varepsilon}\rho u h_o)dy + (r^{\varepsilon}\overline{\rho v}\, h_o)\Big|_{\delta} = \frac{1}{Pr}\left(r^{\varepsilon}\mu \frac{\partial}{\partial y}(h + Pr\frac{u^2}{2})\right)_0^{\delta} \qquad (1.1.7)$$

Now consider (1.1.1) integrated over the boundary layer

$$r^{\varepsilon}\overline{\rho v}\Big|_{\delta} = -\int_0^{\delta} \frac{\partial}{\partial x}(r^{\varepsilon}\rho u)dy$$

which substituted into (1.1.7) and the assumption of homoenergic outer flow we obtain

$$\int_0^{\delta} \frac{\partial}{\partial x}(r^{\varepsilon}\rho u(h_o - h_{oe}))dy = -\frac{1}{Pr} r_o^{\varepsilon}\mu_w \frac{\partial h}{\partial y}\Big|_w$$

thus letting

$$\Gamma = \int_0^{\delta} \frac{\rho u}{\rho_e u_e}\left(1 - \frac{h_o}{h_{oe}}\right)\left(\frac{r}{r_o}\right)^{\varepsilon} dy \qquad \text{we have}$$

$$\frac{d\Gamma}{dx} + \frac{\Gamma}{\rho_e}\frac{d\rho_e}{dx} + \frac{\Gamma}{u_e}\frac{du_e}{dx} + \frac{\varepsilon\Gamma}{r_o}\frac{dr_o}{dx} = \frac{k}{h_{oe}\rho_e u_e}\frac{\partial T}{\partial y}\Big|_w \qquad (1.1.8)$$

define T_r as the recovery or equilibrium temperature

$$T_r = T_e\left(1 + r\frac{(\gamma-1)}{2}M_e^2\right)$$

with r, the recovery factor usually approximated by

$$r = Pr^{1/2} \qquad \text{for laminar flow}$$

and

$$r = Pr^{1/3} \qquad \text{for turbulent flow.}$$

$$Ste = \text{Stanton number} = \frac{k}{\rho_e u_e c_p(T_r - T_w)}\frac{\partial T}{\partial y}\Big|_w$$

Thus for unit Prandtl number flows $r = 1$ and $T_r = T_{oe}$

Equations (1.1.6) and (1.1.8) are the momentum and energy integral equations respectively, a third, the continuity integral, or entrainment equation, can also be derived (Head ref (3)). We note from these derivations that the energy integral equation does not use the zero normal-to-wall pressure gradient condition required by the momentum integral equation, the consequences of this are discussed later when shock/boundary layer interactions and compression corners are considered.

Before integration we notice equations (1.1.1) to (1.1.4) are a system of 4 equations for 5 unknowns $\rho, u, v, T, \& p$ in the laminar flow case, and a set of at least 7 unknowns $p\rho, u, v, T, \rho\overline{u'v'}$ & $\rho\overline{T'v'}$ in the turbulent case. More than 2 equations may be introduced with the turbulence modelling, and strictly there is an equation of state tying up the density. Now we have a set of two equations with 5 unknowns $\vartheta, \Gamma, H, Cfe$ & Ste, thus 3 additional, or closure, relations are required to mathematically determine the system. These relations should be obtained from boundary layer solutions or experimental data.

1.2 Use of flat plate closure

The simplest model is that of flat plate closure, which has been found to be quite adequate for the prediction of skin friction eg. ref (4). Considering first incompressible flow, the relationship between skin friction coefficient and momentum thickness is obtained from the Blasius similarity solution, ref. (2), for laminar flow, and semi-empirical formulae for turbulent flow (Hopkins, ref. (5), summarises the more well known turbulent $Cf_e - \vartheta$ relations). We shall use here the 1/7th power law boundary layer velocity profile, see Schlichting, ref. (6), i.e. $u/ue = (y/\delta)^{1/7}$. In a zero pressure gradient the momentum integral equation (1.1.6) reduces to

$$\frac{d\vartheta}{dx} = \frac{Cfe}{2} = 0.332\,Re_x^{-1/2} \quad \text{Laminar}$$
$$= 0.0296\,Re_x^{-1/5} \quad \text{Turbulent} \qquad (1.2.1)$$

and

Upon integration we obtain

$$\frac{Cfe}{2} = 0.221 Re_{\vartheta}^{-1} \quad \text{laminar}$$
$$\text{and} \quad = 0.013 Re_{\vartheta}^{-1/4} \quad \text{turbulent} \qquad (1.2.2)$$

Using the velocity profiles described above we obtain values of 2.6 and 1.3 for the shape factor H_i in laminar and turbulent flows, respectively.

It has been suggested (e.g. ref (7)) that the natural extension of flat plate closure to the prediction of heat transfer is to assume the flat plate Reynolds analogy factor is valid, i.e.

$$\frac{Ste}{Cfe/2} = \sigma_{FP} \qquad (1.2.3)$$

where the Colburn (ref. (1)) value of $\sigma_{FP} = Pr^{-2/3}$ is often adopted. Clearly in doing this no guarantee is made for conservation of energy within the boundary layer. However using (1.2.3) with the energy integral equation (1.1.8) for a zero pressure gradient we obtain

$$\frac{d\Gamma}{dx} = (1 - \frac{Tw}{Te})Ste = (1 - \frac{Tw}{Te})\sigma_{FP}\, 0.332\, Re_x^{-1/2} \quad \text{laminar}$$
$$\text{and} \quad = (1 - \frac{Tw}{Te})\, \sigma_{FP}\, 0.0296\, Re_x^{-1/5} \quad \text{turbulent}$$

Upon integration yields

$$Ste = (1 - \frac{Tw}{Te})\sigma_{FP}^2\, 0.221 Re_{\Gamma}^{-1} \quad \text{laminar}$$
$$(1 - \frac{Tw}{Te})^{1/4}\, \sigma_{FP}^{5/4}\, 0.013 Re_{\Gamma}^{-1/4} \quad \text{turbulent} \qquad (1.2.4)$$

Thus Stanton number is assumed to be a function of enthalpy thickness, and this approach at least allows the energy conservation equation to influence the heat transfer predictions. The importance

of using this latter option can be demonstrated by considering the flow over a flat plate with an unheated initial portion, Cebeci and Bradshaw, ref. (2).

Let the unheated length $X < X_o$ have the wall temperature T_e, and for $X \geqslant X_o$ a step change to T_w which is not equal to T_e. An analysis has been carried out by Cebeci and Bradshaw using Pohlhausen's technique which approximates the velocity and temperature profiles with polynomial expressions used to satisfy the integral momentum and energy equations. The momentum boundary layer growth is independent of temperature and is thus a simple flat plate flow, however the thermal boundary layer only starts at the wall temperature jump when $X = X_o$ and hence initially develops well inside the thicker momentum layer. The solution for this thermal layer could therefore be thought of as growing in an accelerating flow until its thickness becomes comparable with the momentum layer.

In Cebeci and Bradshaw's analysis this concept is included, resulting in the following expression for heating rate

$$St_e = \frac{0.332\sigma_{FP}Re_{x_o}^{-1/2}}{\left(\frac{x}{x_o}\right)^{1/2}\left[1-\left(\frac{x_o}{x}\right)^{3/4}\right]^{1/3}} \qquad (1.2.5)$$

As mentioned earlier the momentum boundary layer growth is unaffected by the unheated initial length, hence the momentum integral equation/ flat plate Reynolds analogy factor approach for heating rate is simply

$$St_e = 0.332\sigma_{FP}Re_{x_o}^{-1/2}\left(\frac{x_o}{x}\right)^{1/2} \qquad (1.2.6)$$

Finally the energy integral equation with flat plate closure results in

$$St_e = \frac{0.332\sigma_{FP}Re_{x_o}^{-1/2}}{\left(\frac{x}{x_o}-1\right)^{1/2}} \qquad (1.2.7)$$

These 3 results (1.2.5), (1.2.6) and (1.2.7) are compared in fig. (1.2). Assuming (1.2.5) to be accurate, we see the momentum

integral equation/flat-plate-Reynolds-analogy factor technique is clearly inadequate. Also the difference in the predictions of (1.2.5) and (1.2.6) show the importance of the unequal momentum and thermal layers, which is negligible for $X/X_o > 3$.

The flat plate closure relations can be generalised to compressible flows with heat transfer by adopting the intermediate enthalpy concept. That is the closure for the boundary layer shear stress and heat transfer at the wall can be approximated by incompressible expressions with the temperature dependent terms evaluated at a certain 'reference' temperature, we use here the reference temperature proposed by Eckert, ref. (8).

$$\frac{T_*}{T_e} = 1 + A\left(\frac{T_w}{T_e} - 1\right) + B\left(\frac{T_r}{T_e} - 1\right) \qquad (1.2.8)$$

where $A = 0{\cdot}50$, $B = 0{\cdot}22$. This has the advantage of being valid for both laminar and turbulent flows.

Thus the expressions for skin friction become

$$\tau_w = \rho_e u_e^2 \frac{C_{fe}}{2} = 0{\cdot}332 \rho_* u_e^2 \left[\frac{\mu_*}{\rho_e u_e x}\right]^{1/2} \quad \text{laminar}$$

and

$$0{\cdot}0296 \rho_* u_e^2 \left[\frac{\mu_*}{\rho_e u_e x}\right]^{1/5} \quad \text{turbulent}$$

Following the earlier analysis yields the following expressions for skin friction and Stanton number

$$\frac{C_{fe}}{2} = A\left(\frac{\rho_*}{\rho_e}\right)\left(\frac{\mu_*}{\mu_e}\right)^{1/\alpha} Re_\vartheta^{-1/\alpha}$$

$$St_e = A\sigma_{FP}^{\frac{\alpha+1}{\alpha}} \left(\frac{\rho_*}{\rho_e}\right)\left(\frac{\mu_*}{\mu_e}\right)^{1/\alpha} \left(\frac{T_r - T_w}{T_{oe}}\right)^{1/\alpha} Re_\Gamma^{-1/\alpha} \qquad (1.2.9)$$

where $A = 0{\cdot}221$ $\alpha = 1$ for laminar flow

$A = 0{\cdot}013$ $\alpha = 4$ for turbulent flow.

To determine the shape factor H in compressible flow a relation between the velocity and temperature in the boundary layer is required. Crocco derived the following linear relationship for unit Prandtl number, laminar, zero pressure gradient flows (see Rotta, ref. (9))

$$\left[\frac{To - Tw}{Toe - Tw}\right] = \left(\frac{u}{ue}\right) \qquad (1.2.10)$$

The usefulness of this approximation can be assessed by comparison with solutions of the boundary layer similarity equations due to Cohen and Reshotko, ref. (10). Details of these equations are given in section (3.3). We show in fig. 2.3 the two extremes of the pressure gradient parameter $m=-0.09$ corresponding to near separation flow, and $m \rightarrow \infty$, infinite acceleration. We see (1.2.10) is a satisfactory approximation even for those extreme cases particularly for the cooler wall conditions.

Van Driest, refs. (11) and (12) extended (1.2.10) to include non unit Prandtl number, laminar and turbulent flows, resulting in

$$\frac{To - Tw}{Toe - Tw} = \left[\frac{Tr - Tw}{Toe - Tw}\right]\left(\frac{u}{ue}\right) + \left[\frac{Toe - Tr}{Toe - Tw}\right]\left(\frac{u}{ue}\right)^2 \qquad (1.2.11)$$

Extensive comparisons of (1.2.11) with experimental data for zero pressure gradient turbulent flows has been conducted by Fernholtz and Finley, ref. (13), where excellent agreement is found, most of the data falling well within 10%, see fig. (1.3a). They also consider pressure gradient flows, for both adiabatic and isothermal wall cases, fig. (1.3b). For the adiabatic wall case (1.2.11) becomes

$$\frac{To - Tw}{Toe - Tw} = \left(\frac{u}{ue}\right)^2 \qquad (1.2.12)$$

However there is only a limited amount of data available for the isothermal wall, pressure gradient flows, which is inadequate for a true comparison, but since the adoption of (1.2.11) would be

consistent with the flat plate closure used so far, we shall assume it valid.

From the definitions of momentum thickness ϑ and displacement thickness δ^*, we obtain, using (1.2.11) (see Spence, ref. (4))

$$H = \frac{\delta^*}{\vartheta} = H_i \frac{T_w}{T_e} + r\left(\frac{\gamma-1}{2}\right)M_e^2 \qquad (1.2.13)$$

which is valid for both laminar and turbulent flows. Thus (1.2.9) and (1.2.13) constitute the flat plate closure relation for compressible flow.

Chapter 2

2.0 Appraisal of flat plate closure in pressure gradient and variable wall temperature flows

A number of exact solutions to the laminar boundary layer equations in pressure gradient flows have been obtained, and these can be used to assess the accuracy with which flat plate closure predicts skin friction and heat transfer. Solutions exist for special kinds of velocity distribution in both compressible and incompressible flow, and, in the incompressible flow case, variable wall temperature solutions also exist. Under these special conditions the boundary layer equations have similarity solutions, i.e. the partial differential equations can be reduced to a set of ordinary differential equations by suitable choice of parameters, and solutions are produced by suitable numerical techniques.

It is found in these flows the boundary layer integral equations with flat plate closure have very simple analytic solutions. We shall derive these for the cases of incompressible laminar and turbulent pressure gradient flow with variable wall temperature and for compressible laminar pressure gradient flow with isothermal wall and unit Prandtl number.

2.1 Derivation of integral equation prediction using flat plate closure for flows with a special class of velocity distribution

Similarity solutions of the laminar boundary layer equations under the influence of certain types of velocity distributions exist. The general solution of the integral equations with flat plate closure, will be derived for an isothermal wall compressible flow with an allowance for non-isothermal wall flows in the incompressible limit, of the type

$$\frac{Te - Tw}{Te} \quad \alpha \quad x^k$$

Consider the Illingworth-Stewartson and Howarth-Dorodritsyn compressibility transformations equations (2.1.1) and (2.1.2)

$$Y = \int_0^y \left(\frac{\rho}{\rho_{o\infty}}\right)\left(\frac{a}{a_{o\infty}}\right)^{c_1} dy \qquad (2.1.1)$$

$$X = \int^{x} \xi \left(\frac{\rho_e}{\rho_{o_\infty}}\right)\left(\frac{a_e}{a_{o_\infty}}\right)^{c_3} dx \qquad (2.1.2)$$

Applying these to the integral equations (1.1.6) and (1.1.8) for 2-dimensional flow we obtain

$$\frac{d\bar{\vartheta}}{dx} + (2+H)\bar{\vartheta}\left(\frac{1}{U_e}\frac{dU_e}{dX} + \frac{c_2}{a_e}\frac{da_e}{dX}\right) - \frac{c_1\bar{\vartheta}}{a_e}\frac{da_e}{dx} = \left[\frac{a_{o_\infty}}{a_e}\right]^{c_3-2c_1+c_2} \left.\frac{\nu_{o_\infty}}{U_e}\frac{\partial u/u_e}{\partial Y}\right|_w \qquad (2.1.3)$$

$$\frac{d\bar{\Gamma}}{dx} + \frac{\bar{\Gamma}}{U_e}\frac{dU_e}{dX} + \frac{\bar{\Gamma}(c_2 - c_1)}{a_e}\frac{da_e}{dX} = \left[\frac{a_{o_\infty}}{a_e}\right]^{c_3-2c_1+c_2} \frac{\nu_{o_\infty}}{U_e Pr}\left.\frac{\partial T/T_{o_\infty}}{\partial Y}\right|_w \qquad (2.1.4)$$

where c_1, c_2, c_3 are constants, $\xi = \left(\frac{T_{o_\infty}\mu_w}{T_w \mu_{o_\infty}}\right)$

$$U = u\left(\frac{a_{o_\infty}}{a_e}\right)^{c_2}$$

$$\bar{\vartheta} = \int_0^{\Delta} \frac{u}{u_e}\left(1 - \frac{u}{u_e}\right) dY = \frac{\rho_e}{\rho_{o_\infty}}\left(\frac{a_e}{a_{o_\infty}}\right)^{c_1}\vartheta$$

$$\bar{\Gamma} = \frac{u}{u_e}\left(1 - \frac{T_o}{T_{o_e}}\right) dY = \frac{\rho_e}{\rho_{o_\infty}}\left(\frac{a_e}{a_{o_\infty}}\right)^{c_1}\Gamma$$

rearranging (2.1.3) we obtain

$$\frac{d\bar{\vartheta}}{dX} + \left[\frac{(2+H)T_e + c_1(T_{o_e} - T_e)}{T_e + c_2(T_{o_e} - T_e)}\right]\frac{\bar{\vartheta}}{U_e}\frac{dU_e}{dX} = \left[\frac{a_{o_\infty}}{a_e}\right]^{c_3-2c_1+c_2} \frac{\nu_{o_\infty}}{U_e}\left.\frac{\partial u/u_e}{\partial Y}\right|_w \qquad (2.1.5)$$

thus using Spence's relation for shape factor (1.2.13),(2.1.5) becomes

$$\frac{d\bar{\vartheta}}{dX} + \left[\frac{(2-c_1-r)T_e + HiT_w + (r+c_1)T_{o_e}}{c_2 T_{o_e} + (1-c_2)T_e}\right]\frac{\bar{\vartheta}}{U_e}\frac{dU_e}{dX} = \left[\frac{a_{o_\infty}}{a_e}\right]^{c_3-2c_1+c_2} \frac{\nu_{o_\infty}}{U_e}\left.\frac{\partial u/u_e}{\partial Y}\right|_w \qquad (2.1.6)$$

We see that on assuming $c_1 = 2-r,\ c_2 = 1$ the bracketed term reduces to a constant value $(H_i T_w/T_{oe} + 2)$, and the further assumption $c_3 = 2c_1 - c_2$ completely eliminates the compressibility from the equation to allow easy integration. Further, by choosing $c_1 = c_2 = c_3 = 1$ the compressibility is removed from the energy equation (2.1.4) which can also be integrated. For direct comparison of the results from these two equations, however, it is necessary to have the set of constants c_1 & c_2 & c_3 similar for both equations, which is only possible in unit Prandtl number flows, i.e. $r = 1$. Since the exact solutions are only available for unit Prandtl number flows we shall continue the analysis with this restriction, thus (2.1.6) and (2.1.4) become

$$\frac{d\bar{\vartheta}}{dX} + (H_i \frac{T_w}{T_{oe}} + 2)\frac{\bar{\vartheta}}{U_e}\frac{dU_e}{dX} = \frac{\nu_{o\infty}}{U_e}\frac{\partial u/u_e}{\partial Y}\bigg|_w \qquad (2.1.7)$$

$$\frac{d\bar{\Gamma}}{dX} + \frac{\bar{\Gamma}}{U_e}\frac{dU_e}{dX} = \frac{\nu_{o\infty}}{U_e}\frac{\partial T/T_{oe}}{\partial Y}\bigg|_w \qquad (2.1.8)$$

Using the flat plate closure relations equations (1.2.9) the above become

$$\frac{d\bar{\vartheta}}{dX} + (H_i\frac{T_w}{T_{oe}} + 2)\frac{\bar{\vartheta}}{U_e}\frac{dU_e}{dX} = A(\frac{T_*}{T_e})^{\frac{1-\alpha}{\alpha}} \lambda^{1/\alpha} (\frac{\nu_{o\infty}}{U_e \bar{\vartheta}})^{1/\alpha} \qquad (2.1.9)$$

$$\frac{d\bar{\Gamma}}{dX} + \frac{\bar{\Gamma}}{U_e}\frac{dU_e}{dX} = A\left[\frac{T_{oe} - T_w}{T_{oe}}\right]^{\frac{\alpha+1}{\alpha}} \sigma_{FP} (\frac{T_*}{T_e})^{\frac{1-\alpha}{\alpha}} \lambda^{1/\alpha} (\frac{\nu_{o\infty}}{U_e \bar{\Gamma}})^{1/\alpha} \qquad (2.1.10)$$

where $\lambda = \left[\frac{\rho_* \mu_*}{\rho_e \mu_e}\right]^{1/\alpha}$

with a linear viscosity-temperature law assumption (λ = const) equations (2.1.9) and (2.1.10) can be integrated for a given edge velocity and wall temperature distribution. Consider the following distributions,

$$U_e \ \alpha \ X^m$$

$$\frac{To_e - Tw}{To_e} \quad \alpha \quad X^k$$

where K = 0 for compressible flow but may take any constant value in the limit of incompressible flow.

Then assuming the flow type restrictions discussed earlier we obtain

$$\bar{\vartheta} = \left[\frac{\frac{\alpha+1}{\alpha} A\lambda^{1/\alpha} \left(\frac{\nu_{o\infty}}{U_e}\right)^{1/\alpha} X}{\frac{m}{\alpha}\left[(\alpha+1)(H_i \frac{T_w}{To_e} + 2) - 1\right] + 1}\right]^{\alpha+1}$$

$$\Gamma = \sigma_{FP}\left(\frac{To_e - Tw}{To_e}\right)\left[\frac{\frac{\alpha+1}{\alpha} A\lambda^{1/\alpha} \left(\frac{\nu_{o\infty}}{U_e}\right)^{1/\alpha} X}{(k+m)\left(\frac{\alpha+1}{\alpha}\right) + 1 - \frac{m}{\alpha}}\right]^{\frac{\alpha}{\alpha+1}}$$

giving the following expressions for skin friction, heat transfer and Reynolds analogy factor

$$\frac{C_{fe}}{2} = \left(\frac{T_e}{To_\infty}\right)^{1/\alpha}\left[\frac{\alpha A\lambda}{\alpha+1}\left(\frac{\nu_{o\infty}}{U_e X}\right)\left[\frac{m}{\alpha}(\alpha+1)\left(Hi \frac{T_w}{To_e} + 2\right) - 1\right) + 1\right]\right]^{\frac{1}{\alpha+1}} \qquad (2.1.11)$$

$$St_e = \left(\frac{T_e}{To_\infty}\right)^{1/\alpha} \sigma_{FP}\left[\frac{\alpha A\lambda}{\alpha+1}\left(\frac{\nu_{o\infty}}{U_e X}\right)\left[(k+m)\left(\frac{\alpha+1}{\alpha}\right) + 1 - \frac{m}{\alpha}\right]\right]^{\frac{1}{\alpha+1}} \qquad (2.1.12)$$

$$\sigma = \sigma_{FP}\left[\frac{(k+m)(\alpha+1) + \alpha - m}{(Hi \frac{T_w}{To_e} + 2)(\alpha+1)m + \alpha - m}\right]^{\frac{1}{\alpha+1}} \qquad (2.1.13)$$

The incompressible results are obtained by replacing To_e with T_e and $Hi \frac{T_w}{To_e}$ with Hi .

2.2 Comparison of flat plate closure predictions and similarity solutions

Equations (2.1.11), (2.1.12) and (2.1.13) can be compared directly with several similarity equation solutions that are available, for the types of flow discussed in the previous section. Firstly we shall consider incompressible laminar flow, Falkner and Skan, ref. (14) and Fage and Falkner, ref. (15) derived the following similarity forms of the momentum and energy equations respectively

$$f'''(\eta) + \left(\frac{m+1}{2}\right) f(\eta) f''(\eta) + m(1 - f'(\eta)^2) = 0 \qquad (2.2.1)$$

$$\psi''(\eta) + Pr\left[\left(\frac{m+1}{2}\right) f(\eta)\, \psi'(\eta) - k f'(\eta)(\psi(\eta) - 1)\right] = 0 \qquad (2.2.2)$$

where $f'(\eta) = u/u_e$, $\psi(\eta) = \frac{T - T_w}{T_e - T_w}$, $\eta = y\left(\frac{u_e}{\nu x}\right)^{1/2}$

and the usual boundary conditions apply. Thus the skin friction, heat transfer and Reynolds analogy factor can be expressed

$$\frac{Cfe}{2} = f''(0) Re_x^{-1/2} \qquad (2.2.3)$$

$$Ste = \psi'(0) Re_x^{-1/2} \qquad (2.2.4)$$

$$\sigma = \frac{\psi'(0)}{Pr\, f'(0)} \qquad (2.2.5)$$

For such flows the flat plate closure predictions equations (2.1.11), (2.1.12) and (2.1.13) reduce to

$$\frac{Cfe}{2} = \frac{0.332}{\sqrt{Re_x}} \sqrt{1 + m(3 + 2Hi)} \qquad (2.2.6)$$

$$Ste = \frac{0.332}{\sqrt{Re_x}} \sqrt{1 + m + 2k}\; \sigma_{FP} \qquad (2.2.7)$$

$$\sigma = \sigma_{FP} \sqrt{\frac{1 + m + 2k}{1 + m(3 + 2Hi)}} \qquad (2.2.8)$$

These are compared in figs. (2.2.1) to (2.2.3) for the case of an isothermal wall ($k = 0$), and Prandtl numbers of 0.7 and 1.0. Also shown in figs. (2.2.4) and (2.2.5) are the Stanton number and Reynolds analogy factor predictions for the variable wall temperature case. In the favourable pressure gradient region considered we see a maximum error of 18% in both skin friction and heat transfer predictions when the momentum and energy integral equations are used respectively. However, when the skin friction prediction/flat plate Reynolds analogy factor technique is used for heat transfer prediction, the error increases to 82%. In the adverse region, the separation velocity gradient parameter of $m = -.12$ predicted using flat plate closure is an underprediction of the exact value $m = -.09$. We notice a trend in these figures that the skin friction and heat transfer rates are underpredicted in favourable pressure gradient regions and over-predicted in adverse regions, this is repeated throughout most of the comparisons made. Also from fig. (2.2.2) we see the Colburn, ref. (1), Stanton number dependence on Prandtl number $St_e \propto Pr^{-2/3}$, is an excellent approximation over this pressure gradient range for Prandtl numbers of 0.7 its use causing a maximum error of 3%.

The effects of variable wall temperature on the heat transfer rates and Reynolds analogy factor are shown in figs. (2.2.4), (2.2.5) and (2.2.6) for a unit Prandtl number. We notice the accuracy of the flat plate closure prediction is unchanged with varying wall temperature, and a flow which develops along a surface with an increasing wall to edge temperature difference $k > 0$ has a higher Stanton number than the equivalent isothermal wall, this being a consequence of the fuller temperature profile observed and also the thermal boundary layer grows more slowly, see fig. (2.2.7a). The converse is true for decreasing wall to edge temperature differences $k < 0$, see fig. (2.2.7b). Two interesting features are demonstrated in fig. (2.2.6), for a value of $k = -\frac{(1+Hi)}{(3+2Hi)} = -0.44$

the flat plate closure prediction equation (2.2.8) implies the Reynolds analogy factor is independent of pressure gradient. The exact solution shows this is in fact not true but the pressure gradient

dependence is very weak. Also we see that for a given velocity gradient we can obtain a value for k that results in zero heat transfer. In fact this result can be obtained directly from (2.2.2), rearranging we obtain

$$\psi''(\eta) + Pr\left[\frac{(m+1)}{2}\frac{d}{d\eta}(f(\eta)\psi(\eta)) - (\frac{m+1}{2} + k)\psi(\eta)f'(\eta) + kf'(\eta)\right] = 0$$

or upon integration

$$\psi'(\eta) + Pr\left[\frac{(m+1)}{2}f(\eta)\psi(\eta) + kf(\eta)\right] = Pr(\frac{m+1}{2} + k)\int\psi(\eta)f'(\eta)d\eta + C$$

where C is a constant, thus considering the case $\frac{m+1}{2} + k = 0$,

in the limit $\eta \longrightarrow \infty$ we see $C = 0$ and hence

$$\psi'(\eta) + Pr(\frac{m+1}{2})f(\eta)(\psi(\eta) - 1) = 0$$

thus $\psi'(0) = 0$ when $k = -\frac{m+1}{2}$.

However whereas the flat plate closure predictions break down for values of k less than this zero heat transfer rate value, the exact solution does not, it continues into the situation where the Stanton number becomes negative. It is not surprising though that the flat plate closure technique cannot predict such situations as this, since the closure for the Stanton number is based on isothermal wall temperature profiles. It is only through obtaining an infinite enthalpy thickness that the prediction technique can predict the zero heat transfer rate condition.

Turbulent flows under the same velocity gradients have been investigated by Tetervin, ref. (16) and Nakayama et al, ref. (17). Both authors derive expressions for Reynolds analogy factor in isothermal wall conditions. Tetervin assumes a power law boundary layer velocity profile $u/u_e = (y/\delta)^n$ defined via the shape factor $H = 1 + 2n$, and a cubic expression for the boundary layer normal temperature gradient of the form.

$$\frac{\partial T}{\partial y}\Big/\frac{\partial T}{\partial y}\Big|_{y=0} = (1 - \frac{y}{\delta})^2(1 + 2y/\delta)$$

These profiles are used in the boundary layer equations to obtain an expression for Reynolds analogy factor in a unit Prandtl number flow which is subsequently generalised to non unit Prandtl number via the Colburn factor $P_r^{-2/3}$.

The more detailed analysis of Nakayama also relies on the power law velocity profile but uses the temperature profile obtained from a temperature 'law-of-the-wall' assumed to be applicable in mild pressure gradients. These two predictions, and the flat plate closure technique prediction, obtained from (2.1.13)

$$\sigma = \left[\frac{4(m+1)}{(5H+9)m+4}\right]^{1/5} \qquad (2.2.9)$$

are shown in fig. (2.2.8) for a unit Prandtl number flow. Comparison with fig. (2.2.3) shows that the turbulent Reynolds analogy factor varies less with pressure gradient than the laminar value, particularly in favourable pressure gradient regions. This being a consequence of the fuller turbulent boundary layer mean profiles distorting less under the influence of pressure gradient.

In compressible unit Prandtl number, linear viscosity-temperature law laminar flows, Cohen and Reshotko, ref. (10) derived a set of similarity equations by applying the transformations equations (2.1.1) and (2.1.2) to the boundary layer equations resulting in

$$f'''(\eta) + f(\eta)f''(\eta) = \frac{2m}{m+1}(f'(\eta)^2 - 1 - S(\eta)) \qquad (2.2.10)$$

$$S''(\eta) + f(\eta)S'(\eta) = 0 \qquad (2.2.11)$$

with $f'(\eta) = u/u_e$, $S(\eta) = To/Toe$

Thus the skin friction coefficient and Stanton number are

$$\left(\frac{Toe}{Te}\right)\frac{Cfe}{2} = \frac{\overline{Cfe}}{2} = f''(0)Re_x^{-1/2} \qquad (2.2.12)$$

$$\frac{Toe}{Te}Ste = \overline{Ste} = \frac{S'(0)}{1-S(0)}Re_X^{-1/2} \qquad (2.2.13)$$

and hence

$$\sigma = \frac{S'(0)}{f''(0)(1-S(0))} \qquad (2.2.14)$$

The flat plate closure solutions equations (2.1.11), (2.1.12) and (2.1.13) become

$$\frac{\overline{Cfe}}{2} = 0.332\sqrt{1 + m(3 + 2Hi\frac{Tw}{Toe})}\,Re_X^{-1/2} \qquad (2.2.15)$$

$$\overline{Ste} = 0.332\sqrt{1+m}\,Re_X^{-1/2} \qquad (2.2.16)$$

$$\sigma = \sqrt{\frac{1+m}{1 + m(3 + 2Hi\frac{Tw}{Toe})}} \qquad (2.2.17)$$

The above equations are compared in figures (2.2.9) to (2.2.12). The adverse pressure gradient regions in figs. (2.2.9) and (2.2.10) being expanded in fig. (2.2.11) for clarity. In the case of Stanton number the maximum error in the favourable region is 10% when the wall temperature equals the total temperature (adiabatic wall case). Hence as the wall temperature decreases relative to the total temperature, and the heating becomes more important, the accuracy of the energy integral equation prediction increases. This is also the case for the momentum integral equation prediction of Stanton number, but there is an order of magnitude difference in the errors (100% max with the momentum equation). Considering fig. (2.2.11), we see the prediction of both Stanton number and skin friction are not so accurate in the adverse region, where the maximum error of 25% in predicted heating rates occurs at separation. The separation velocity gradient parameter is slightly under-predicted, but this is not surprising since the velocity profiles near separation are vastly different from the zero pressure gradient

profile shapes used in the closure. The question of flat plate closure predicting separation at all is answered by the fact that it does so by allowing the boundary layer thickness to become infinite. The phenomena of separation is discussed further in sections (2.3) and (2.4). The Reynolds analogy factor comparison Fig. (2.2.12) is excellent in the favourable pressure gradient region, as was the case with incompressible flow, but the poor skin friction predictions in the adverse region corrupt the Reynolds analogy factor.

2.3 Turbulent flow comparisons

In order to carry out a true analysis of the accuracy of the flat plate closure approximations in general compressible turbulent flows it is necessary to perform comparisons with experimental data. A substantial amount of work has been done in this area for flows with and without heat transfer. A detailed compilation of such experiments in compressible flow has been prepared by Fernholtz & Finley ref. (18), we select here several supersonic flow examples from this report and others, for comparison with predictions obtained using the KHOMP2D axisymmetric/2D boundary layer code, Appendix E. The cases are chosen to test the closure in both adverse and favourable pressure gradients, including shock/boundary layer interactions and compression corners.

In all the cases the boundary layers are initially laminar with either a natural or forced transition at some location well upstream of the test zone. For comparison purposes we determine a turbulent boundary layer virtual origin, by matching the measured and predicted boundary layer over the initial part of the test flow. This approach is valid since the flows are in a zero pressure gradient in this region and hence the flat plate closure is locally an 'exact' solution. The experimentally measured wall pressure distributions are also used in the prediction with the assumption of isentropic outer flow. The exception to this being in the shock/boundary layer comparisons, where pressures meaured at the edge of the layer are used. On some of the figures we also show the predictions from the method due to Stollery ref. (19), which essentially assumes the skin friction and Stanton number expressions eqns (1.2.1) and (1.2.3) are valid in pressure gradient flows, with a suitably defined virtual origin.

Thomann, ref. (20) carried out some 2-dimensional tests at Mach 2.5 and a wall to total temperature ratio $T_w/To_e = 0.73$. The test surface consisted of a flat plate connected to a variety of curved plates designed to produce adverse or favourable pressure gradients. Wall pressure and heat transfer measurements were made at several streamwise locations.

Figs. (2.3.1) and (2.3.2) show the pressure distributions, and comparisons of heat transfer results between the theory and experiment for the favourable and adverse pressure distribution flows respectively. We notice that the overall predictions are in excellent agreement, a reassuring point since the pressure distributions are quite mild, dropping to a 1/4 of the free stream value in the favourable pressure distribution case, and rising to 3½ times the free stream in the adverse. Consequently Stollery's method also agrees quite well. It is also worth noting that the trend found in laminar flow of the flat plate closure underpredicting heat transfer and skin friction in favourable pressure distribution flows and overpredicting in adverse flows appears to extend to turbulent flows.

Hoydysh and Zakkay, ref. (21) carried out some experiments at a Mach number of 5.75 and $T_w/To_e = 0.63$. Their axisymmetric, hollow model, 15 cms long, had increased in radius from 6 cms at the upstream end to 10 cms thus allowing the effects of concave curvature to be considered. Wall and boundary layer edge pressure measurements were made along with heat transfer rates at several streamwise locations. The effect of a normal pressure gradient within the boundary layer is an important issue, we have already seen the strong dependence of the momentum integral equation derivation upon the assumption of a zero normal to the wall pressure gradient. The energy integral equation however is not so dependent upon this assumption, the only effect being through the difficulty with which the true boundary layer edge pressure can be measured. We shall leave further discussion of this topic until a later comparison (Horstmans test case) is considered, where both skin friction and heat transfer measurements are available. The graph in fig. (2.3.3) shows the predictions obtained using both wall and edge pressures, and we can see that use of wall pressures results in

over prediction of the heat transfer rates. The Stollery comparison is perhaps a little unfair since no account of the change in radius is made. The effect of a positive radius gradient in the integral equations serves to reduce the magnitude of the adverse pressure gradient term, and inclusion of this would increase the underpredicted values.

Kassoy and Horstman, ref. (22) carried out a detailed experimental survey in an axisymmetric shock/turbulent boundary layer region with a Mach 7.2 freestream and $T_w/T_{o_e} = 0.4$. As well as measuring the velocity and temperature profiles both skin friction and heat transfer rates were also recorded. The test model consisted of a circular cylinder with a streamlined nose, around which collar shock generators of 7.5° and 15° leading edge chamfers were positioned.

The ability of the simple method described here to accurately predict such a boundary layer growth would be suspect since not only is there no allowance made for the drastic effect the shock has on the velocity and temperature profiles in this highly non-equilibrium boundary layer, but also there is the problem discussed earlier of a normal pressure gradient. However a comparison has been made and figs. (2.3.4a) and (2.3.5a) show the measured pressure distribution for the two flows at the wall and the edge of the boundary layer, the boundary layer thickness being chosen as the Pitot tube position at which the Pitot pressure was maximum in the interaction region, and downstream, where the Pitot pressure continuously increased. Figs. (2.3.4, 2.3.5 b and c) compare the predicted heat transfer and skin friction using the wall and edge pressures, with the experimental data. Consider first the 7.5° case, where the heat transfer predictions are satisfactory, the peak heating rate being predicted to within 7%. Also shown is the prediction obtained when the wall pressures are used giving an increase of 17% in the predicted peak heating. The skin friction predictions at first sight seem satisfactory, the peak value being 13% out. Although this is an overprediction whereas the heat transfer was an underprediction. Since the momentum integral equation used to obtain the skin friction is invalid in the interaction region for the reasons discussed earlier, it seems likely that the good agreement is rather fortuitous.

The 15° case comparisons, fig. (2.3.5b and c) are shown for completeness, again we have fortuitous good agreement for skin friction, but the true accuracy of the closure is displayed in the heat transfer results where the peak heating is underpredicted by . 40%. Reasons for the breakdown of the prediction being a combination of the separation bubble and the much stronger shock both of which dramatically distort the boundary layer profiles.

Coleman, ref. (23) performed some experiments in axisymmetric compression corners at Mach 9 freestream, and $T_w/T_{oe} = 0.27$. The cylindrical portion before the corner was hollow thus giving an initial zero pressure gradient boundary layer growth. Several skirt angles were used to generate a number of adverse pressure gradients, the 15°, 30°, 35° and 40° cases will be considered here. Both surface pressures and heat transfer rates were measured, and these pressure distributions, fig. (2.3.6), were used in the prediction. The experimentor detected separation ahead of the corner for the 35° and 40° cases. The predicted heating rates, fig..(2.3.7) agree well with the experiment for all four cases. The peak heating rates being underpredicted by -8%, 15%, 19% and 6% for the four cases respectively. For the larger flare angle cases the unmeasured boundary layer edge pressures may vary significantly from the wall values, which suggest a steeper adverse pressure gradient than is actually present. This would explain the improved agreement between theory and experiment for the peak heating in the largest flare angle case.

2.4 Prediction of Separation

An area of great interest in boundary layer flows is that of separated, or reverse flow, conditions. Such phenomena can significantly affect the aerodynamic characteristics of a body, and can also have large effects on the heat transfer rates. For instance, shock-induced separation regions ahead of a compression corner have been known to have high heating rates within it, Coleman, ref. (23). The reasons for this are not well understood.

The correct way in which boundary layer prediction techniques determine separation in two-dimensions is through the attainment of a local zero in the skin friction distribution. Existence of

negative skin friction downstream of this point implying a reverse flow region close to the wall. However, integral methods which rely upon local flat plate expressions for the skin friction closure, do not have sufficient flexibility to allow this condition. Those integral methods that solve the continuity integral or entrainment equation such as Head, ref. (3), and predit the incompressible shape factor growth, can specify a critical value for this parameter, above which separation is assumed to have taken place. Green et al, ref. (24), who extended the analysis of Head to compressible flows developed an empirical skin friction relation which is based upon momentum thickness Reynolds number and shape factor. This improved relation allows zero skin friction to be achieved giving the physically correct separation criteria. Although the zero skin friction is the physically correct criteria for separation in 2-d, and the second technique relies upon empirical determination of the critical value for H_i, this second technique is often used in cases where detailed profile calculations are made. In this region the viscous/inviscid interactions become important, since small changes in the boundary layer edge pressure dramatically alter the predicted boundary layer growth and skin friction, which in turn influences the boundary layer edge pressure. Also the boundary layer equations become elliptic in nature thus upstream influence also plays a part. Thus large changes in the separation location can be experienced with changes in computational step size etc, see Raven, ref. (25).

From a computational point of view, the shape factor approach, which has a much more stable behaviour, is a more attractive option.

With the flat plate closure method described in Chapter 1, neither of the above criteria can be applied.

However, considering the incompressible 2 parameter integral method of Thwaites (see Cebeci and Bradshaw, ref. (2)) an alternative separation criteria based on boundary layer thickness and local pressure gradient is derived, and according to this approximate method based on the Falkner and Stan similarity equation solutions, separation will occur if

$$\lambda_{crit} = \frac{\vartheta^2}{\nu}\frac{du}{dx}e = -0.09 \qquad (2.4.1)$$

This criteria has been tried using the momentum integral equation with flat plate closure for a sinusoidal velocity distribution

$$u_e = 2u_\infty \sin\varphi \quad , \quad \varphi = x/Ro \qquad (2.4.2)$$

This particular distribution corresponds to the inviscid flow over a circular cylinder. For such a flow the momentum integral equation, equation (1.1.6), reduces to

$$\frac{d\bar{\vartheta}}{dx} + \frac{(H+2)\bar{\vartheta}}{\tan\varphi} = \frac{0.221}{2\overline{Re}\sin\varphi\,\bar{\vartheta}}$$

where $\bar{\vartheta} = \vartheta/Ro$, $\overline{Re} = (u_\infty Ro)/\nu$

thus giving the solution

$$\bar{\vartheta}^2 = \frac{0.442}{2\overline{Re}}\int_0^\varphi \frac{(\sin\varphi)^{2H+3}\,d\varphi}{(\sin\varphi)^{2H+4}}$$

hence

$$\frac{Cfe}{2}\overline{Re}^{1/2} = \frac{0.332(\sin\varphi)^{H+1}}{\left[2\int_0^\varphi (\sin\varphi)^{2H+3}\,d\varphi\right]^{1/2}} \qquad (2.4.3)$$

and from (2.4.1)

$$\lambda_{crit} = \frac{0.442\cos\varphi}{(\sin\varphi)^{2H+4}}\int_0^\varphi (\sin\varphi)^{2H+3}\,d\varphi$$

(2.4.3) and (2.4.4) have been integrated and the results are plotted in figs. (2.4.1a and b). Also shown is the solution obtained using Thwaites method, and using a full field solution, Beasley, ref. (26). We see that the skin friction prediction is satisfactory over the

favourable pressure gradient region but overpredicts in the adverse region. However the Thwaites criteria applied to the solution predicts the separation location within 2% of those of Thwaites and Beasley, albeit rather unphysical since the skin friction is not predicted as zero at this point. Heat transfer predictions in such flows have been carried out using Smith and Spalding's integral method, see ref. (2), and the energy integral equation with flat plate closure results in the following expression

$$St_\infty = \frac{\sqrt{2}\,\sigma_{FP}\,0.332\sin\varphi\,Re^{-1/2}}{(1-\cos\varphi)^{1/2}} \qquad (2.4.5)$$

The two results are compared in figure (2.4.2) for Prandtl numbers of 1 and 0.7. As can be seen the two methods produce similar results right up to separation, with a max difference of 14% occurring at the stagnation point. The Smith and Spalding method adopts a similar technique to that of Thwaites, only based on solutions of the Fage and Falkner similarity energy equation, ref. (15), and hence should be as accurate in its prediction of Stanton number, as we have seen the Thwaites method is at predicting skin friction. We also show the Reynolds analogy factor predictions in (2.4.3).

This technique for producing a separation criterion can be generalised to compressible flows by firstly applying the compressibility transformations in section (3.1) and using the Cohen and Reshotko similarity solutions which will produce the required λ_{crit} for a given wall temperature (see section 2.5 where the use of pressure gradient closure prediction of separation is discussed).

A similar criteria has been developed for turbulent flow by Buri, ref. (27), though based on experimental data, his non dimensional critical pressure gradient parameter takes the form

$$\Gamma_{BURI} = \frac{\vartheta}{u_e}\frac{du_e}{dx}\left(\frac{u_e\vartheta}{\nu}\right)^{1/4} = -0.06 \qquad (2.4.6)$$

Subsequent work by Allan, ref. (28) concerning continuously critical adverse pressure gradients, (that is, a pressure gradient that keeps the turbulent boundary layer on the verge of separation) uses Buri's pressure gradient parameter to derive theoretically such pressure distribution and comparisons with experiment show excellent agreement when the value is dropped to $\Gamma_{BURI} = -0.04$. Although this is a large difference, in practical cases near separation ϑ grows quickly and hence $d\Gamma_{BURI}/dx$ is large. Therefore only minor changes in separation location would be observed if Γ_{BURI} were allowed to vary from $-0.04 \rightarrow -0.06$.

The criteria has been used in conjunction with the momentum integral equation with flat plate closure, to predict separation on a flat plate experiencing a favourable-then-adverse pressure gradient. The experimental results of Simpson, ref. (29) give a useful indication of its accuracy in non-equilibrium flows. Figure (2.4.4) shows the skin friction predictions which as we approach separation become a severe overprediction - as expected. In this region the existence of a separation flattens out the adverse pressure gradient and we see a sharp fall in Γ_{BURI} , which does not quite reach -0.06. However if the pressure gradient is smoothed out to remove this effect we see Γ_{BURI} passes through the critical value very close to the separation position.

2.5 Laminar flow comparisons with experiment over blunted cones

The stagnation region on a blunted body is perhaps the most important area insofar as laminar convective heating is concerned. Several stagnation point heating methods have been produced e.g. Fay & Riddel Ref. (39) and Vaglio-Laurin Ref. (31). In this region, the boundary layer edge velocity grows linearly with surface distance from the stagnation point which can be expressed in the form required for the similarity equation solutions of Cohen & Reshotko Ref. (10). Firstly however the integral equations must be transformed from axisymmetric to 2-dimensional form using the Mangler transformations see Stewartson Ref. (47).

$$\bar{x} = \int r^2 dx \qquad \bar{y} = ry \tag{2.5.1}$$

defining $\vartheta_r = r\vartheta$, $\Gamma_r = r\Gamma$ the boundary layer integral equations (1.1.6) and (1.1.8) become

$$\frac{d\vartheta_r}{d\bar{x}} + \vartheta_r \frac{(H+2-M_e^2)}{u_e} \frac{du_e}{d\bar{x}} + \frac{\vartheta_r}{\rho_e} \frac{d\rho_e}{d\bar{x}} = \frac{\mu_e}{\rho_e u_e^2} \left.\frac{\partial u}{\partial \bar{y}}\right|_{y=0} \tag{2.5.2}$$

$$\frac{d\Gamma_r}{d\bar{x}} + \frac{\Gamma_r}{u_e} \frac{du_e}{d\bar{x}} + \frac{\Gamma_r}{\rho_e} \frac{d\rho_e}{dx} = \frac{\mu_e}{Pr \rho_e u_e} \left.\frac{\partial T/T_{oe}}{\partial \bar{y}}\right|_{y=0} \tag{2.5.3}$$

Near the stagnation point $r \alpha X$ and hence $u_e \alpha \bar{x}^{1/3}$ i.e. the pressure gradient parameter in the similarity equation $m = 1/3$ Fay and Riddell use this solution in their analysis, which is generalised to non-unit Prandtl number using corrections similar to that obtained by Colburn Ref. (1). This concept of locally similar flow was first used in incompressible flow by Thwaites, see Ref. (2), who based his closure on the Falkner-Skan similarity solutions Ref. (14). We shall derive here a similar method, based on the Cohen & Reshotko similarity solutions for a general compressible laminar flow.

Applying the compressibility transformations of section (2.1) to equations (2.5.2) and (2.5.3) we obtain

$$\frac{d\bar{\vartheta}_r}{d\bar{X}} + \bar{\vartheta}_r \left(H_i \frac{T_w}{T_{oe}} + 2\right) \frac{1}{U_e} \frac{dU_e}{d\bar{X}} = \frac{v_{o_\infty}}{U_e} \left.\frac{\partial u/u_e}{\partial \bar{Y}}\right|_w \tag{2.5.4}$$

$$\frac{d\overline{\Gamma}r}{d\overline{X}} + \frac{\overline{\Gamma}r}{Ue}\frac{dUe}{d\overline{X}} = \frac{\nu o_\infty}{Pr\,Ue}\left.\frac{\partial T/Toe}{\partial \overline{Y}}\right|_w \qquad (2.5.5)$$

where $$\overline{Y} = \frac{a_e}{a_{o\infty}}\int \rho/\rho_e\, d\overline{y} \quad , \quad \overline{X} = \int \frac{a_e P_e}{a_{o\infty} P_{o\infty}}\, d\overline{x} \quad , \quad \overline{\vartheta}_r = r\overline{\vartheta}$$

Considering a velocity distribution of the form $Ue \;\alpha\; \overline{X}^m$ then the right hand sides of equations (2.5.4) and (2.5.5) can be expressed in terms of the Cohen & Reshotko similarity solution velocity and temperature profile gradients at the wall $f''(\eta=0)$, $S'(\eta=0)$

i.e.

$$\frac{\nu_{o\infty}}{Ue}\left.\frac{\partial u/ue}{\partial \overline{Y}}\right|_w = \frac{\nu_{o\infty}}{Ue} f''(\eta=0)\left(\frac{Ue}{\nu_{o\infty}\overline{X}}\right)^{1/2}$$

$$\frac{\nu_{o\infty}}{Pr\,Ue}\frac{\partial T/Toe}{\partial \overline{Y}} = \frac{\nu_{o\infty}}{UePr} S'(\eta=0)\left(\frac{Ue}{\nu_{o\infty}\overline{X}}\right)^{1/2}$$

where $$\eta = \overline{Y}\left(\frac{Ue}{\nu_{o\infty}\overline{X}}\right)^{1/2}$$

Thus equations (2.5.4) and (2.5.5) become

$$\frac{d\vartheta r}{d\overline{X}} + \vartheta_r \frac{m}{\overline{X}}\left(Hi\frac{Tw}{Toe} + 2\right) = f''(0)\left(\frac{\nu_{o\infty}}{Ue\overline{X}}\right)^{1/2}$$

$$\frac{d\overline{\Gamma}r}{d\overline{X}} + \frac{\overline{\Gamma}r\, m}{\overline{X}} = \frac{S'(0)}{Pr}\left(\frac{\nu_{o\infty}}{Ue\overline{X}}\right)^{1/2}$$

and hence upon integration we find

$$Re_{\overline{\vartheta}r} = \frac{2f''(0)}{1 + m\left(2Hi\frac{Tw}{Toe} + 3\right)} Re_{\overline{X}}^{1/2} \qquad (2.5.6)$$

$$Re_{\overline{\Gamma}r} = \frac{2S'(0)}{(1+m)Pr} Re_{\overline{X}}^{1/2} \qquad (2.5.7)$$

and thus

$$\frac{Cfe}{2} = \frac{2f''(0)^2}{1 + m\left(2Hi\frac{Tw}{Toe} + 3\right)}\left(\frac{\rho_w\mu_w}{\rho_e\mu_e}\right) Re_{\vartheta}^{-1} \qquad (2.5.8)$$

$$Ste = \left(\frac{Toe}{Tr - Tw}\right)\frac{2S'(0)^2}{(1+m)Pr^2}\left(\frac{\rho_w\mu_w}{\rho_e\mu_e}\right) Re_{\Gamma}^{-1} \qquad (2.5.9)$$

The idea behind the new technique 'pressure gradient closure' is to assume the 2 parameter relations $Cfe(Re_\vartheta, m), Ste(Re_\Gamma, m)$ (2.5.8) and (2.5.9) are valid when the pressure gradient parameter m is allowed to vary, i.e. $m = m(\bar{X})$. By definition

$$m = \frac{\bar{X}}{Ue}\frac{dUe}{d\bar{X}}$$

which by using equation (2.5.7) and transformation back to physical variables becomes

$$m = \left(\frac{Toe}{Te}\right)\Gamma^2\left(\frac{1+m}{2S'(0)}\right)^2\frac{Pr^2}{Ve}\frac{du_e}{dx}\left(\frac{\mu_e\rho_e}{\mu_w\rho_w}\right) \qquad (2.5.10)$$

Thus the parameter m can be obtained from the above as a function of the local velocity gradient and enthalpy thickness. A similar expression to equation (2.5.10) can be derived, using equation (2.5.6) resulting in m being a function of momentum rather than enthalpy thickness and strictly each should be used in the integral equation from which it was derived. However, since in the present context we are primarily interested in heat transfer we shall consider equation (2.5.10) only.

In order to apply the new closure the numerical values of $f''(0)$ and $S'(0)$ have to be curve fitted. The following result is suggested as a suitable fit, particularly for the temperature gradient $S'(0)$

$$f''(0) = 0.3321\left(1 + m\left(3 + 13\frac{Tw}{Toe}\right)\right)^{1/2} \qquad (2.5.11)$$

$$S'(0) = 0.3321Pr^{1/3}\left(\frac{Tr-Tw}{Toe}\right)\left(1+m\left(1.36+0.563\frac{Tw}{Toe}\right)\right)^{1/2} \qquad (2.5.12)$$

The temperature gradient at the wall has been generalised to non-unit Prandtl number using the Colburn criteria Ref. (1), and the velocity gradient at the wall has been assumed to be independent of Prandtl number. This latter result is shown to be a reasonable approximation in Ref. (47). Equation (2.5.11) and (2.5.12) are compared with the exact values, for a unit Prandtl number in Figs. (2.5.1) and (2.5.2). We see from equation (2.5.11) that separation will be predicted if

$$m = -\frac{1}{3 + 13\frac{Tw}{Toe}} \qquad (2.5.13)$$

although the adverse pressure gradient region of Fig. (2.5.1) shows this criteria to be rather inaccurate when compared with exact solution. By deriving a more accurate curve fit for $f''(0)$ however, a better laminar, compressible separation condition would be obtained.

The resulting pressure gradient closure (PGC) method has been applied, using the KHOMP2D code of Appendix E, to several blunted cone flows, for which experimental heat transfer and pressure measurements are available see Figs. (2.5.3) - (2.5.5). The rather sparse pressure measurements in the stagnation region were augmented by fitting a modified Newtonian type pressure variation in the range $0 < s/Rn < 0.5$ where this type of distribution is known to be reasonably accurate. In order to start the boundary layer computation the stagnation point boundary layer thicknesses have to be determined, and the singular nature of the equations in this region uniquely defines them, see Appendix A.

In the figures the expected increase in predicted stagnation heating rate using pressure gradient closure over flat plate closure is a predominate feature, although the experimentally measured rate is still underpredicted. Further downstream the two methods agree well with the experimental data.

The enhanced stagnation heating observed in experiments has been a cause of concern for many years and several possible mechanisms for the phenomena have been proposed. Prime suspects are surface roughness, transition, radiated noise and particle/shock layer interaction. Wind tunnel tests have shown that high levels ofnoise can promote early transition, but an extensive study carried out by Holden Ref. (35) revealed the great reluctance of a boundary layer to undergo transition near the stagnation point and when forced, relaminarisation occurred. He also demonstrated that when forced transition at a position before the sonic point took place no upstream influence occurred and the stagnation heating remained unchanged. Surface roughness tests proved to have little effect, and he finally concluded that dust particles present within the air flow were the cause of the enhanced heating. In fact he demonstrated ten fold increases in stagnation heating when particularly dusty air was used.

Another important flow feature which is often considered is that of entropy swallowing (Ref. (36) for example). This occurs at higher free-stream Mach numbers, where the bow shock over the blunt body is highly curved, and streamlines experience differing entropy increases depending upon the local shock inclination to the freestream. Thus as streamlines are entrained into the boundary layer the total pressure at the edge increases. This can be estimated if a suitable shock shape model can be found, i.e. the shock angle $\psi = \psi(r_s)$ where r_s is the radius of a freestream tube, see Fig. (2.5.6). Assuming the flow to be isentropic along a streamline, from behind the shock until entrainment into the boundary layer, then by equating the mass flux within the layer to that in a freestream tube an expression for r_s, and hence $\psi(r_s)$ is obtained.

$$\pi \rho_\infty u_\infty r_s^2 = 2\pi r \int_0^\delta \rho u \, dy$$

or

$$r_s^2 = \frac{2\rho_e u_e r(\delta - \delta^*)}{\rho_\infty u_\infty} \qquad (2.5.15)$$

For the case of a spherically blunted cone, Billing Ref. (37) suggests a hyperbola as an approximation to the shock shape, which he defines from an empirically determined radius of curvature R_c at the apex, and the limiting angle ψ_s equal to that of the sharp cone shock angle.

$$\left(\frac{R_c}{r_s}\right)^2 = \tan^2\psi - \tan^2\psi_s \qquad (2.5.16)$$

and

$$R_c = 1.143 \exp\left\{0.54/(M_\infty - 1)^{1.2}\right\} \qquad (2.5.17)$$

The sharp cone shock angle can be estimated from the approximate similarity equation derived by Linnell & Bailey Ref. (38).

$$\sin\psi_s = \frac{1}{M_\infty}\left\{1 - \cos\vartheta_c + \sqrt{1 + \frac{\gamma+1}{2}(\beta\sin\vartheta_c)^2}\right\} \qquad (2.5.18)$$

where β is the Mach angle $\sqrt{M_\infty^2 - 1}$ and ϑ_c the cone half angle. For moderate Mach numbers the streamtube radius r_s will not become large enough for the limiting shock angle to affect the entropy change at the boundary layer edge, and thus this particular shock shape could be applied to any hemispherically blunted body for entropy swallowing affects to be

considered.

The above shock model has been applied to several blunted cone flows, but the effect of entropy swallowing on nose heating was found to be negligible. For instance the case of a Mach 20 freestream in an altitude range 0-80 km the total pressure increased by a maximum of only 2% at a distance of 5 nose radii from the stagnation point of a 9° blunted cone, resulting in a 0.05% increase in the heating rate. At much greater distances along the body, however, the order of 30 nose radii, the effect can be important. Varner Ref.(39) showed a 25% increase in predicted local heating rate at such distances, when entropy swallowing was included, but these heating rates so far downstream are small compared with the stagnation region.

2.6 Transition in the 2-Dimensional/Axisymmetric Boundary Layer

A feature which strongly affects both the skin friction drag and heat transfer rates on a body surface is the transition of the boundary layer from the laminar to the turbulent state. The physics of this phenomena is very complex and our understanding is limited, at present realistic modelling is only possible in the case of smooth walls. The problem can be broken down into two parts. Firstly the conditions under which transition begins have to be predicted, and secondly, the subsequent downstream development towards fully turbulent flow needs to be described.

It is the first of these which has so far proved almost impossible to predict, although some attempts have been made e.g. Refs. (40) and (41). Rather more success has been achieved in predicting the development of turbulent flow once the location is known. Insofar as heat transfer is concerned the latterprocess is extremely important since local hot spots are produced near the end of the transition region, which may cause thermal stress problems.

Emmons Ref. (42) proposed that the transition region of a boundary layer is composed of a field of isolated turbulent spots generated according to some rate density function and each growing as they travel downstream. This theory has been developed for flat plates by Narashima and is supported by the experimental results of Dhawan and Narashima Ref. (43) and Elder Ref. (44). These theories lead to an

intermittency distribution γ_{int}, which is the probability of the flow being turbulent at some point downstream of the onset location. Thus γ_{int} varies from zero at the onset location($s_t = 0$) to unity when fully developed turbulent flow exists at some point downstream of s_t From this, time averaged heat transfer rates in the transition region can be calculated using the expression

$$q_w = \gamma_{int} q_{w_{turb}} + (1-\gamma_{int}) q_{w_{lam}}$$

where $q_{w_{turb}}$ and $q_{w_{lam}}$ are the heating rates in the turbulent and laminar boundary layers respectively. Thus in order to obtain in the transitional region the laminar boundarylayer prediction must be continued right through to the fully developed turbulent region. Similarly the turbulent boundary layer prediction must begin at a virtual origin which is coincident with the transition onset location.

Extension to flows over axisymmetric shapes has been proposed by Chen & Thyson Ref. (45) who give results for the intermittency function distribution γ_{int} for cylindrical, conical and hemispherical flow-fields.

$$\text{flat plate:} \quad \gamma_{int} = 1 - \exp\{-G(s-s_t)^2/u_e\}$$

$$\text{cone:} \quad \gamma_{int} = 1 - \exp\{-G s_t \ln(s/s_t)(s-s_t)/u_e\} \qquad (2.6.1)$$

$$\text{hemiphere:} \quad \gamma_{int} = 1 - \exp\left\{-G\sin(s_t/R_n)\ln\left[\frac{\tan(s/2R_n)}{\tan(s_t/2R_n)}\right]\frac{\ln(s/s_t)}{R_n \frac{du_e}{ds}}\right\}$$

where G is defined as the spot formation rate parameter, and is determined experimentally. Consider (2.6.1) for a flat plate, then defining $\Delta s = s_{\gamma_{int}=0.95} - s_t$ i.e. the 95% transition length.

We obtain, after rearranging

$$G = \frac{3.0 Re_{\Delta s}^{-2} U_e^3}{\nu^2}, \quad Re_{\Delta s} = \frac{u_e \Delta s}{\nu}$$

Empirical data fits in Ref. (45) indicate that this 95% transition length Reynolds number $Re_{\Delta s}$ is related to the onset of transition Reynolds number $Re_{s_t} = \frac{u_e s_t}{\nu}$ via the relation

$$Re_{\Delta s} = 60.0 Re_{s_t}^{0.67} \qquad (2.6.2)$$

This was extended to compressible, adiabatic wall flow by Chen & Thyson using empirical fits to available experimental data, giving

$$Re_{\Delta s} = (60.0 + 4.68Me^{1.92})Re_{s_t}^{0.67} \qquad (2.6.3)$$

Poll Ref. (46), used Eckerts Ref. (8) reference enthalpy concept to produce the following generalised extension to compressible flow conditions

$$Re_{\Delta s} = 60.0\left(\frac{T*}{Te}\right)^{0.33(1+\omega)} Re_{s_t}^{0.67} \qquad (2.6.4)$$

where suffix $*$ denotes evaluated at the reference temperature and ω is the power in the approximation to Sutherlands viscosity-temperature law Ref. (6)

$$\left(\frac{\mu_*}{\mu_e}\right) = \left(\frac{T*}{Te}\right)^{\omega}$$

He also demonstrated, for the adiabatic wall case equation (2.6.4) reduces to

$$Re_{\Delta s} = \left[60.0 + \begin{Bmatrix} 4.53 \\ 5.15 \end{Bmatrix} Me^2\right] Re_{s_t}^{0.67} \quad \text{with } \omega = \begin{Bmatrix} 0.76 \\ 1.0 \end{Bmatrix}$$

which is in close agreement with Chen & Thysons' result equation (2.6.3).

The method has been tested with experiment for the case of a 9° blunted cone $(R_n = 0.0635m)$ in a Mach 5 airflow, Widhopf Ref. (32). The experimentally measured pressure distribution was used in the predictions, with the sparse nose region values augmented using a Modified Newtonian distribution. Figure (2.6.1) shows the comparisons between the theory and themeasured heating rates. Figure (2.6.2) shows a series of predictions having onset locations varying from $s_t/R_n = 0$ up to 3.0, well into the conical portion of the model, and Figure (2.6.3) shows the integrated heat transfer rate Q_w for each of these predictions up to $s/R_n = 5$ where the fully turbulent boundary layers for each case are of similar thickness.

$$Q_w = 2\pi \int_0^{s_o} r q_w \, ds \qquad (2.6.5)$$

Fromthese figures we see that the onset location significantly effects themagnitude and, location of the peak heating rate, but the overall heat input Q_W has a much reduced variation. Obviously the decrease in peak heating rate as the onset moves away from the stagnation point is cancelled by the increased area over which it acts. Hence in conclusion we can see that an accurate prediction of the onset location on the nose of a blunted body isnot necessary unless problems with thermal stressing are anticipated such as in the case of a thin ceramic radome.

Chapter 3

3-Dimensional Laminar Boundary Layers

3.1 Introduction

When we consider 3-dimensional boundary layers the problem is augmented, not only in scale by the extra dimension, but also the velocity profiles within the boundary layer need not stay in the plane of the inviscid streamline. These twisted boundary layer profiles can be conveniently resolved into two components, parallel and normal to the local inviscid streamline, giving the streamwise and crossflow shapes respectively. The streamwise profile assumes shapes similar to the axisymmetric/2D boundary layers but the cross-flow profile can take several forms depending upon the nature of the surface pressure distribution. Typically these can take a 'c' or an 's' shape, see fig. (3.1.1) and thus the chosen relation modelling such a profile for use with the integral equation has to be flexible enough to allow these variations.

3.2 Derivation of the laminar boundary layer integral equations

Starting with the Navier Stokes equations in tensor (or invariant) form the laminar boundary layer equations are derived for a body fitting orthogonal curvilinear coordinate system (x_1, x_2, x_3) with x_1 and x_2 lying on the surface and x_3 normal to the surface (see Fig. (3.2.1)

The coordinate line tangent vectors are given by

$$\begin{aligned} \underline{e_1} &= \underline{e_1}(x_1, x_2) \\ \underline{e_2} &= \underline{e_2}(x_1, x_2) \\ \underline{e_3} &= \underline{e_3}(x_1, x_2) \end{aligned} \qquad (3.2.1)$$

and hence the scale factors

$$h_1 = h_1(x_1, x_2, x_3)$$
$$h_2 = h_2(x_1, x_2 x_3) \qquad (3.2.2)$$
$$h_3 = 1$$

An assumption that the x_3 dependence of h_1 and h_2 is negligible within the boundary layer (i.e. the surface curvature is large compared with the boundary layer thickness) will allow the momentum and energy integral equations to be derived.

$$h_1 = h_1(x_1, x_2)$$
$$h_2 = h_2(x_1, x_2) \qquad (3.2.3)$$
$$h_3 = 1$$

The Navier-Stokes equations for a viscous compressible gas can be written in the following tensor form (Ref. 46)

continuity $$\frac{D\rho}{Dt} + \rho \nabla . \underset{\sim}{u} = 0 \qquad (3.2.4)$$

momentum $$\rho \frac{D\underset{\sim}{u}}{Dt} = -\nabla p - \frac{2}{3}\nabla(\mu \nabla . \underset{\sim}{u}) + \nabla . (\mu D) \qquad (3.2.5)$$

energy $$\rho \frac{DH}{Dt} = \frac{Dp}{Dt} + \frac{\mu}{2} D . D - \frac{2}{3}\mu(\nabla . \underset{\sim}{u})^2 + \nabla . (k \nabla T) \qquad (3.2.6)$$

where $\underset{\sim}{u}$ = fluid velocity,

$\frac{D}{Dt}$ represents the convective time derivative $\frac{D}{Dt} = (\frac{\partial}{\partial t} + \underset{\sim}{u} . \nabla)$, H is the static enthalpy, μ is the coefficient of viscosity, k is the coefficient of thermal diffusivity and D is the rate of strain tensor, $D = \nabla \underset{\sim}{u} + \nabla \underset{\sim}{u}^T$ (see Appendix B for the derivation of D in orthogonal curvilinear coordinates). The

product $D.D = D_{ij}\underline{e}_i\underline{e}_j \cdot D_{kl}\underline{e}_k\underline{e}_l = D_{ij}D_{jl}$

thus in Cartesian coordinates

$$D.D = \left(\frac{\partial u_i}{\partial x_j} + \frac{\partial u_j}{\partial x_i}\right) \qquad \text{summed over } i \text{ \& } j$$

Following the first order boundary layer approximations for large Reynolds numbers i.e. assuming

$$u_3/u_1 \,,\ \frac{\partial}{\partial x_1}\Big/\frac{\partial}{\partial x_3} \,,\ \frac{\partial}{\partial x_2}\Big/\frac{\partial}{\partial x_3} = O(Re^{-1/2}) \qquad \text{then}$$

equations (3.2.4) and (3.2.5) become

$$\frac{D'\varrho}{D't} + \varrho\left[\frac{1}{h_1h_2}\frac{\partial(u_1h_2)}{\partial x_1} + \frac{1}{h_1h_2}\frac{\partial(u_2h_1)}{\partial x_2} + \frac{1}{h_1h_2}\frac{\partial(u_3h_1h_2)}{\partial x_3}\right] = 0 \qquad (3.2.7)$$

where

$$\frac{D'}{D't} = \left[\frac{\partial}{\partial t} + \frac{u_1}{h_1}\frac{\partial}{\partial x_1} + \frac{u_2}{h_2}\frac{\partial}{\partial x_2} + \frac{u_3}{h_3}\frac{\partial}{\partial x_3}\right]$$

$$\varrho\frac{Du}{Dt} = -\nabla p + \frac{1}{h_1h_2}\frac{\partial}{\partial x_3}\left[h_1h_2\mu\frac{\partial u_1}{\partial x_3}\underline{e}_1 + h_1h_2\mu\frac{\partial u_2}{\partial x_3}\underline{e}_2\right]$$

and since $\underline{e}_1$ and $\underline{e}_2$ are independent of x_3

$$\varrho\frac{D\underline{u}}{Dt} = -\nabla p + \frac{1}{h_1h_2}\left[\frac{\partial}{\partial x_3}\left(h_1h_2\mu\frac{\partial u_1}{\partial x_3}\right)\underline{e}_1 + \frac{\partial}{\partial x_3}\left(h_1h_2\mu\frac{\partial u_2}{\partial x_3}\right)\underline{e}_2\right] \qquad (3.2.8)$$

The acceleration term introduces curvature effects since we have the gradient of a vector, i.e.

$$\frac{D\underline{u}}{Dt} = \frac{\partial\underline{u}}{\partial t} + (\underline{u}.\nabla)\underline{u} \qquad (3.2.9)$$

where

$$(\underline{u}.\nabla)\underline{u} = \frac{u_i}{h_i}\frac{\partial(u_j\underline{e}_j)}{\partial x_i} = \frac{u_i}{h_i}\frac{\partial u_j}{\partial x_i}\underline{e}_j + \frac{u_i u_j}{h_i}\frac{\partial \underline{e}_j}{\partial x_i}$$

so we can write (3.2.9)

$$\frac{D\underline{u}}{Dt} = \frac{\partial u_1}{\partial t}\underline{e}_1 + \frac{\partial u_2}{\partial t}\underline{e}_2 + \frac{\partial u_3}{\partial t}\underline{e}_3 + \frac{u_1}{h_1}\frac{\partial u_j}{\partial x_1}\underline{e}_j$$

$$+ \frac{u_2}{h_2}\frac{\partial u_j}{\partial x_2}\underline{e}_j + u_3\underline{e}_j\frac{\partial u_j}{\partial x_3} + \frac{u_1 u_j}{h_1}\frac{\partial \underline{e}_j}{\partial x_1} + \frac{u_2 u_j}{h_2}\frac{\partial \underline{e}_j}{\partial x_2}$$

and by using the expressions for $\partial\underline{e}_j/\partial x_i$ derived in Appendix C we have

$$\frac{D\underline{u}}{Dt} = \left[\frac{D'u_1}{D't} + \frac{u_1 u_2}{h_1 h_2}\frac{\partial h_1}{\partial x_2} - \frac{u_2^2}{h_1 h_2}\frac{\partial h_2}{\partial x_1}\right]\underline{e}_1$$

$$+ \left[\frac{D'u_2}{D't} - \frac{u_1^2}{h_1 h_2}\frac{\partial h_1}{\partial x_2} + \frac{u_1 u_2}{h_1 h_2}\frac{\partial h_2}{\partial x_1}\right]\underline{e}_2 - \left[\frac{u_1^2}{h_1}\frac{\partial h_1}{\partial x_3} - \frac{u_2^2}{h_2}\frac{\partial h_2}{\partial x_3}\right]\underline{e}_3 \quad (3.2.10)$$

combining equations (3.2.8) and (3.2.10) we have the following boundary layer momentum equations

$$\rho\left[\frac{D'u_1}{D't} - u_1 u_2 K_2 + u_2^2 K_1\right] = -\frac{1}{h_1}\frac{\partial p}{\partial x_1} + \frac{\partial}{\partial x_3}\left(\mu\frac{\partial u_1}{\partial x_3}\right) - K_3\mu\frac{\partial u_1}{\partial x_3} \quad (3.2.11)$$

$$\rho\left[\frac{D'u_2}{D't} + u_1^2 K_2 - u_1 u_2 K_1\right] = -\frac{1}{h_2}\frac{\partial p}{\partial x_2} + \frac{\partial}{\partial x_3}\left(\mu\frac{\partial u_2}{\partial x_3}\right) - K_3\mu\frac{\partial u_2}{\partial x_3} \quad (3.2.12)$$

$$\rho\left[\frac{u_1^2}{h_1}\frac{\partial h_1}{\partial x_3} + \frac{u_2^2}{h_2}\frac{\partial h_2}{\partial x_3}\right] = \frac{\partial p}{\partial x_3} \quad (3.2.13)$$

where

$$K_1 = -\frac{1}{h_1 h_2}\frac{\partial h_2}{\partial x_1}, \quad K_2 = -\frac{1}{h_1 h_2}\frac{\partial h_1}{\partial x_2}, \quad K_3 = -\frac{1}{h_1 h_2}\frac{\partial(h_1 h_2)}{\partial x_3}$$

The energy equation becomes

$$\rho \frac{D'H}{D't} = \frac{D'p}{D't} + \mu\left[\left(\frac{\partial u_1}{\partial x_3}\right)^2 + \left(\frac{\partial u_2}{\partial x_3}\right)^2\right] + \frac{\partial}{\partial x_3}\left(K\frac{\partial T}{\partial x_3}\right) \qquad (3.2.14)$$

Equation (3.2.13) shows that a direct result of curvature is that the normal pressure gradient is non zero. In order to continue and derive the integral equations the assumption discussed earlier equations (3.2.3) will be employed leaving K_1, K_2 & p independent of x_3 and reducing K_3 to zero. The equations become

$$\rho\left[\frac{D'u_1}{D't} - u_1u_2K_2 + u_2^2K_1\right] = -\frac{1}{h_1}\frac{\partial p}{\partial x_1} + \frac{\partial}{\partial x_3}\left(\mu\frac{\partial u_1}{\partial x_3}\right) \qquad (3.2.15)$$

$$\rho\left[\frac{D'u_2}{D't} + u_1^2K_2 - u_1u_2K_1\right] = -\frac{1}{h_2}\frac{\partial p}{\partial x_2} + \frac{\partial}{\partial x_3}\left(\mu\frac{\partial u_2}{\partial x_3}\right) \qquad (3.2.16)$$

$$p = p(x_1, x_2) \qquad (3.2.17)$$

the energy equation remains unchanged.

We shall derive the steady laminar flow momentum integral equation in the x_1-direction, and by similarity the equation in the x_2-direction will follow. At the edge of the boundary layer equation (3.2.11) will become using equations (3.2.3) and the condition that the pressure gradient normal to the surface is zero equation (3.2.17):

$$\rho_e\frac{D'u_{1e}}{D't} - u_{1e}u_{2e}K_2 + u_{2e}^2K_1 = -\frac{1}{h_1}\frac{\partial p}{\partial x_1}$$

Where the suffix e denotes values at the edge of the layer. Using this equation to eliminate the pressure gradient from equation (3.2.11) we have:

$$-\frac{1}{h_1}(\rho_e u_{1e} u_{1,1e} - \rho u_1 u_{1,1}) - \frac{1}{h_2}(\rho_e u_{2e} u_{1,2e} - \rho u_2 u_{1,2})$$

$$-(\rho_e u_{3e} u_{1,3e} - \rho u_3 u_{1,3}) + K_2(\rho_e u_{1e} u_{2e} - \rho u_1 u_2)$$

$$-K_1(\rho_e u_{2e}^2 - \rho u_2^2) = \frac{\partial}{\partial x_3}(\mu u_{1,3})$$

where $u_{i,j}$ denote $\frac{\partial u_i}{\partial x_j}$ etc.

re-arranging and noting that $u_{1,3} \approx 0$ we get

$$\frac{1}{h_1} u_{1,1e}(\rho_e u_{1e} - \rho u_1) + \frac{1}{h_1} \rho u_1 (u_{1,1e} - u_{1,1})$$

$$+\frac{1}{h_2} u_{1,2e}(\rho_e u_{2e} - \rho u_2) + \frac{1}{h_2} \rho u_2 (u_{1,2e} - u_{1,2}) + \rho u_3 (u_{1,3e} - u_{1,3})$$

$$-K_2(\rho_e u_{1e} u_{2e} - u_1 u_2) + K_1(\rho_e u_{2e}^2 - \rho u_2^2) = -\frac{\partial}{\partial x_3}(\mu u_{1,3}) \qquad (3.2.18)$$

Now consider the continuity equation (3.2.7) multiplied by $(u_{1e} - u_1)$

$$\frac{(u_{1e} - u_1)}{h_1}\frac{\partial}{\partial x_1}(\rho u_1) + \frac{(u_{1e} - u_1)}{h_2}\frac{\partial}{\partial x_2}(\rho u_2) + (u_{1e} - u_1)\frac{\partial}{\partial x_3}(\rho u_3) - (u_{1e} - u_1)\rho u_1 K_1$$

$$-(u_{1e} - u_1)\rho u_2 K_2 = 0$$

if we add this to equation (3.2.18) we get

$$\frac{1}{h_1} u_{1,1e}(\rho_e u_{1e} - \rho u_1) + \frac{1}{h_2} u_{1,2e}(\rho_e u_{2e} - \rho u_2)$$

$$+\frac{1}{h_1}\left[\rho u_1 (u_{1,1e} - u_{1,1}) + (u_{1e} - u_1)\frac{\partial}{\partial x_1}(\rho u_1)\right]$$

$$+\frac{1}{h_2}\left[\rho u_2(u_{1,2e}-u_{1,2}) + (u_{1e}-u_1)\frac{\partial}{\partial x_2}(\rho u_2)\right]$$

$$+\left[\rho u_3(u_{1,3e}-u_{1,3}) + (u_{1e}-u_1)\frac{\partial}{\partial x_3}(\rho u_3)\right]$$

$$-K_2(\rho_e u_{1e} u_{2e} - \rho u_1 u_2 + \rho u_2(u_{1e}-u_1))$$

$$+K_1(\rho_e u_{2e}^2 - \rho u_2^2 - \rho u_1(u_{1e}-u_1)) + \frac{\partial}{\partial x_3}(\mu u_{1,3}) = 0$$

Integrating over the boundary layer $(x_3=0\rightarrow\delta)$:

$$\frac{\rho_e v_e u_{1,1e}}{h_1}\delta_1 + \frac{\rho_e v_e u_{1,2e}}{h_2}\delta_2 + \frac{1}{h_1}\frac{\partial}{\partial x_1}(\rho_e v_e^2 \vartheta_{11})$$

$$+\frac{1}{h_2}\frac{\partial}{\partial x_2}(\rho_e v_e^2 \vartheta_{12}) + \rho u_3(u_{1e}-u_1)\Big|_w +$$

$$K_1(-\rho_e v_e^2 \vartheta_{11} + \rho_e v_e^2 \vartheta_{22} + \rho_e v_e u_{2e}\delta_2) +$$

$$K_2(-\rho_e v_e^2 \vartheta_{12} - \rho_e v_e^2 \vartheta_{21} - \rho_e v_e u_{2e}\delta_1) = \mu u_{1,3}\Big|_w$$

where

$$v_e = \sqrt{u_{1e}^2 + u_{2e}^2} \qquad \delta_1 = \int_0^\delta \frac{\rho_e u_{1e} - \rho u_1}{\rho_e v_e} dx_3 \qquad \delta_2 = \int_0^\delta \frac{\rho_e u_{2e} - \rho u_2}{\rho_e v_e} dx_3$$

$$\vartheta_{11} = \int_0^\delta \frac{(u_{1e}-u_1)\rho u_1}{\rho_e v_e^2} dx_3 \qquad \vartheta_{12} = \int_0^\delta \frac{(u_{1e}-u_1)\rho u_2}{\rho_e v_e^2} dx_3$$

$$\vartheta_{21} = \int_0^\delta \frac{(u_{2e}-u_2)\rho u_1}{\rho_e v_e^2} dx_3 \qquad \vartheta_{22} = \int_0^\delta \frac{(u_{2e}-u_2)\rho u_2}{\rho_e v_e^2} dx_3$$

dividing by $\rho_e v_e^2$ we obtain

$$\frac{u_{1,1e}\,\delta_1}{v_e h_1} + \frac{u_{1,2e}\,\delta_2}{v_e h_2}$$

$$+ \frac{1}{\varrho_e v_e^2}\left[\frac{1}{h_1}\frac{\partial}{\partial x_1}(\varrho_e v_e^2 \vartheta_{11}) + \frac{1}{h_2}\frac{\partial}{\partial x_2}(\varrho_e v_e^2 \vartheta_{12})\right]$$

$$- \frac{\varrho_w u_{3w} u_{1e}}{\varrho_e v_e^2} - K_1(\vartheta_{11} - \vartheta_{22} - \frac{u_{2e}}{v_e}\delta_2)$$

$$- K_2(\vartheta_{12} + \vartheta_{21} + \frac{u_{2e}}{v_e}\delta_1) = \frac{\tau_{w1}}{\varrho_e v_e^2} \qquad (3.2.19)$$

Where $\tau_{w1} = \mu \frac{\partial u_1}{\partial x_3}\Big|_w$ similarly we get from equation (3.2.12)

$$\frac{u_{2,1e}\,\delta_1}{v_e h_1} + \frac{u_{2,2e}\,\delta_2}{v_e h_2}$$

$$+ \frac{1}{\varrho_e v_e^2}\left[\frac{1}{h_1}\frac{\partial}{\partial x_1}(\varrho_e v_e^2 \vartheta_{21}) + \frac{1}{h_2}\frac{\partial}{\partial x_2}(\varrho_e v_e^2 \vartheta_{22})\right]$$

$$- \frac{\varrho_w u_{3w} u_{2e}}{\varrho_e v_e^2} - K_1(\vartheta_{21} + \vartheta_{12} + \frac{u_{1e}}{v_e}\delta_2)$$

$$- K_2(\vartheta_{22} - \vartheta_{11} - \frac{u_{1e}}{v_e}\delta_1) = \frac{\tau_{w2}}{\varrho_e v_e^2} \qquad (3.2.20)$$

where $\tau_{w2} = \mu \frac{\partial u_2}{\partial x_3}\Big|_w$

Multiplying the two momentum equations (3.2.11) and (3.2.12) by u_1, and u_2 respectively and adding the results to the energy equation (3.2.14) we obtain the following equation:

$$e\frac{D'H}{Dt} + e\left[u_1 \frac{D'u_1}{D't} - K_2 u_1^2 u_2 + K_1 u_2^2 u_1\right] - u_1 \frac{\partial}{\partial x_3}\left(\mu \frac{\partial u_1}{\partial x_3}\right)$$

$$+\ \rho\left[u_2\frac{D'u_2}{D't} - K_1 u_1 u_2^2 + K_2 u_1^2 u_2\right]$$

$$-u_2\frac{\partial}{\partial x_3}\left(\mu\frac{\partial u_2}{\partial x_3}\right) = \mu\left(\frac{\partial u_1}{\partial x_3}\right)^2 + \mu\left(\frac{\partial u_2}{\partial x_3}\right)^2 + \frac{1}{Pr}\frac{\partial}{\partial x_3}\left(\mu\frac{\partial H}{\partial x_3}\right)$$

rearranging gives

$$\rho\frac{D'}{D't}\left[H + \frac{u_1^2 + u_2^2}{2}\right] = u_1\frac{\partial}{\partial x_3}\left(\mu\frac{\partial u_1}{\partial x_3}\right) + \mu\left(\frac{\partial u_1}{\partial x_3}\right)^2 + u_2\frac{\partial}{\partial x_3}\left(\mu\frac{\partial u_2}{\partial x_3}\right)$$
$$+\mu\left(\frac{\partial u_2}{\partial x_3}\right)^2 + \frac{1}{Pr}\frac{\partial}{\partial x_3}\left(\mu\frac{\partial H}{\partial x_3}\right)$$

$$\text{or}\quad \rho\frac{D'H_T}{D't} = \frac{1}{Pr}\frac{\partial}{\partial x_3}\left[\mu\frac{\partial}{\partial x_3}\left(H + \frac{(u_1^2 + u_2^2)}{2}Pr\right)\right] \qquad (3.2.21)$$

where H_T is defined as the total enthalpy $H_T = H + (u_1 + u_2)/2$
If we multiply the continuity equation (3.2.7) by H_T and add to the above we have

$$\frac{1}{h_1}\frac{\partial}{\partial x_1}(\rho u_1 H_T) + \frac{1}{h_2}\frac{\partial}{\partial x_2}(\rho u_2 H_T) + \frac{\partial}{\partial x_3}(\rho u_3 H_T)$$
$$+\rho\frac{u_1 H_T}{h_1 h_2}\frac{\partial h_2}{\partial x_1} + \rho\frac{u_2 H_T}{h_1 h_2}\frac{\partial h_1}{\partial x_2} = \frac{1}{Pr}\frac{\partial}{\partial x_3}\left[\mu\frac{\partial}{\partial x_3}\left(H + \frac{(u_1^2 + u_2^2)Pr}{2}\right)\right]$$

Hence on integrating over the boundary layer

$$\frac{1}{h_1}\int_0^\delta\frac{\partial}{\partial x_1}(\rho u_1 H_T)dx_3 + \frac{1}{h_2}\int_0^\delta\frac{\partial}{\partial x_2}(\rho u_2 H_T)dx_3 + \left[\rho u_3 H_T\right]_0^\delta$$
$$-K_1\int_0^\delta\rho u_1 H_T\,dx_3 \quad -K_2\int_0^\delta\rho u_2 H_T dx_3 = -\frac{\mu}{Pr}C_p\frac{\partial T}{\partial x_3}\bigg|_w \qquad (3.2.22)$$

Consider the continuity equation (3.2.7) integrated over the boundary layer

$$[\rho u_3]_0^\delta = -\frac{1}{h_1}\int_0^\delta \frac{\partial}{\partial x_1}(\rho u_1)dx_3 - \frac{1}{h_2}\int_0^\delta \frac{\partial}{\partial x_2}(\rho u_2)$$

$$+ K_1\int_0^\delta \rho u_1 dx_3 + K_2\int_0^\delta \rho u_2 dx_3$$

and since H_{Te}= const. on multiplying the above by H_{Te} we have

$$H_{Te}(\rho_e u_{3e} - \rho_w u_{3w}) = -\frac{1}{h_1}\int_0^\delta \frac{\partial}{\partial x_1}(H_{Te}\rho u_1)dx_3 - \frac{1}{h_2}\int_0^\delta \frac{\partial}{\partial x_2}(H_{Te}\rho u_2)dx_3$$

$$+ K_1\int_0^\delta \rho u_1 H_{Te}\, dx_3 + K_2\int_0^\delta \rho u_2 H_{Te} dx_3$$

and on eliminating $\rho_e u_{3e} H_{Te}$ from equation (3.2.22) we obtain

$$\frac{1}{h_1}\frac{\partial}{\partial x_1}(\rho_e v_e H_{Te}\Gamma_1) + \frac{1}{h_2}\frac{\partial}{\partial x_2}(\rho_e v_e H_{Te}\Gamma_2)$$

$$-K_1\rho_e v_e H_{Te}\Gamma_1 - K_2\rho_e v_e H_{Te}\Gamma_2 + (H_{Te}-H_{Tw})\rho_w u_{3w}$$

$$= -K\frac{\partial T}{\partial x_3}\Big|_w$$

where

$$\Gamma_1 = \int_0^\delta \frac{\rho u_1}{\rho_e v_e}\left(\frac{H_T}{H_{Te}} - 1\right)dx_3 \qquad \Gamma_2 = \int_0^\delta \frac{\rho u_2}{\rho_e v_e}\left(\frac{H_T}{H_{Te}} - 1\right)dx_3$$

or

$$\frac{1}{\rho_e v_e h_1}\frac{\partial}{\partial x_1}(\rho_e v_e \Gamma_1) + \frac{1}{\rho_e v_e h_2}\frac{\partial}{\partial x_2}(\rho_e v_e \Gamma_2)$$

$$-K_1\Gamma_1 - K_2\Gamma_2 + \left(1 - \frac{H_{Tw}}{H_{Te}}\right)\frac{\rho_w u_{3w}}{\rho_e v_e} = Ste\left(\frac{Tr-Tw}{Toe}\right) \quad (3.2.23)$$

where

$$Ste = -\frac{K\frac{\partial T}{\partial x_3}\Big|_w}{\rho_e v_e C_p(Tr-Tw)}$$

In a steady flow with no wall transpiration the integral equations become

1st Mom

$$\frac{u_{1,1e}\delta_1}{v_e h_1} + \frac{u_{1,2e}\delta_2}{v_e h_2} + \frac{1}{\rho_e v_e^2}\left[\frac{1}{h_1}\frac{\partial}{\partial x_1}(\rho_e v_e^2 \vartheta_{11}) + \frac{1}{h_2}\frac{\partial(\rho_e v_e^2 \vartheta_{12})}{\partial x_2}\right]$$

$$-K_1(\vartheta_{11} - \vartheta_{22} - \frac{u_{2e}}{v_e}\delta_2) - K_2(\vartheta_{12} + \vartheta_{21} + \frac{u_{2e}}{v_e}\delta_1) = \frac{Cfe_1}{2} \qquad (3.2.24)$$

2nd Mom

$$\frac{u_{2,1e}\delta_1}{v_e h_1} + \frac{u_{2,2e}\delta_2}{v_e h_2} + \frac{1}{\rho_e v_e^2}\left[\frac{1}{h_1}\frac{\partial(\rho_e v_e^2 \vartheta_{21})}{\partial x_1} + \frac{1}{h_2}\frac{\partial(\rho_e v_e^2 \vartheta_{22})}{\partial x_2}\right]$$

$$-K_1(\vartheta_{21} + \vartheta_{12} + \frac{u_{1e}}{v_e}\delta_2) - K_2(\vartheta_{22} - \vartheta_{11} - \frac{u_{1e}}{v_e}\delta_1) = \frac{Cfe_2}{2} \qquad (3.2.25)$$

Energy Equation

$$\frac{1}{\rho_e v_e h_1}\frac{\partial}{\partial x_1}(\rho_e v_e \Gamma_1) + \frac{1}{\rho_e v_e h_2}\frac{\partial(\rho_e v_e \Gamma_2)}{\partial x_2}$$

$$-K_1\Gamma_1 - K_2\Gamma_2 = Ste\left(\frac{T_r - T_w}{T_{oe}}\right) \qquad (3.2.26)$$

Thus we have 3 equations with 11 unknowns consisting of 8 integral thicknesses and Cfe_1, Cfe_2 & Ste . This can be immediately reduced to 10 since by definition

$$\vartheta_{12} = \vartheta_{21} - \delta_2\cos\psi + \delta_1\sin\psi$$

where $\psi = \tan^{-1}\left(\frac{u_{2e}}{u_{1e}}\right)$ i.e. the angle between the inviscid streamline and the x_1 coordinate. In order to obtain closure relations for these variables, an obvious move is to relate them to the local streamwise and crossflow coordinate system variables via the equations overleaf

$$\begin{bmatrix} \vartheta_{11} \\ \vartheta_{12} \\ \vartheta_{21} \\ \vartheta_{22} \end{bmatrix} = \begin{bmatrix} \cos^2\psi & -\sin\psi\cos\psi & -\sin\psi\cos\psi & \sin^2\psi \\ \sin\psi\cos\psi & \cos^2\psi & -\sin^2\psi & -\sin\psi\cos\psi \\ \sin\psi\cos\psi & -\sin^2\psi & \cos^2\psi & -\sin\psi\cos\psi \\ \sin^2\psi & \sin\psi\cos\psi & \sin\psi\cos\psi & \cos^2\psi \end{bmatrix} \begin{bmatrix} \vartheta_{ss} \\ \vartheta_{sn} \\ \vartheta_{ns} \\ \vartheta_{nn} \end{bmatrix} \quad (3.2.27)$$

$$\begin{bmatrix} \delta_1 \\ \delta_2 \end{bmatrix} = \begin{bmatrix} \cos\psi & \sin\psi \\ -\sin\psi & \cos\psi \end{bmatrix} \begin{bmatrix} \delta_s \\ \delta_n \end{bmatrix} \quad (3.2.28)$$

$$\begin{bmatrix} \Gamma_1 \\ \Gamma_2 \end{bmatrix} \quad \begin{bmatrix} \cos\psi & \sin\psi \\ -\sin\psi & \cos\psi \end{bmatrix} \begin{bmatrix} \delta_s \\ \delta_n \end{bmatrix} \quad (3.2.29)$$

where

$$\delta_s = \int_0^\delta \left(1 - \frac{\rho u_s}{\rho_e v_e}\right) dy \qquad \delta_n = \int_0^\delta - \frac{\rho u_n}{\rho_e v_e} dy$$

$$\vartheta_{ss} = \int_0^\delta \frac{\rho u_s}{\rho v_e}\left(1 - \frac{u_s}{v_e}\right) \qquad \vartheta_{sn} = \int_0^\delta \frac{\rho u_n}{\rho_e v_e}\left(1 - \frac{u_s}{v_e}\right)$$

$$\vartheta_{ns} = \int_0^\delta - \frac{\rho}{\rho_e} \frac{u_n u_s}{v_e^2} \qquad \vartheta_{nn} = \int_0^\delta - \frac{\rho}{\rho}\left(\frac{u_n}{v_e}\right)^2 dy$$

$$\Gamma_s = \int_0^\delta \frac{\rho u_s}{\rho_e v_e}\left(1 - \frac{T_o}{T_{oe}}\right) dy \qquad \Gamma_n = \int_0^\delta \frac{\rho u_n}{\rho_e v_e}\left(1 - \frac{T_o}{T_{oe}}\right) dy$$

3.3 Discussion of Closure relations

Closing the integral equations (3.2.24),(3.2.25) and (3.2.26) requires more relations than for 2-dimensional flows. The simplest approach is to assume that the crossflow profile has negligible effect. Hayes, ref. (48) has shown this to be a good approximation if the streamline curvature is small, or, as demonstrated by Vaglio-Laurin, ref. (31), the wall is cold. Under these conditions $\vartheta_{sn}, \vartheta_{ns}, \vartheta_{nn}, \delta_n$ & Cfe_n are zero and the second momentum equation is a simple multiple of the first, and thus useless. The remaining equations constitute the axisymmetric analogue technique attributed to Cooke, ref. (49), with the effects of wall curvature and streamline divergence still being taken into account. A great reduction in computer time is achieved with this method, particularly if streamline coordinates are used since the equations reduce to a pair of ordinary differential equations. However this requires the determination of the streamline pattern over the surface of the body. In hypersonic flows this can be approximated using simple methods such as steepest descent or simplified streamlines, see ref. (50), but in the lower speed ranges is not so easy to compute.

The remaining variables $\vartheta_{ss}, \Gamma_s, \delta_s, Cfe_s$ & Ste can be related using the axisymmetric closure derived in Chapter 1, equations (1.2.9) and (1.2.13).

In general, the zero crossflow approach is unjustifiable. Therefore when highly 3-dimensional flows with warmer wall temperatures are considered, the crossflow profile has to be included. Extensive research into incompressible 3-dimensional boundary layers with crossflow has been conducted. Cooke, ref. (51) extended the laminar flow similarity equation analysis of Falkner and Skan, ref. (14), to flows over infinite swept cylinders. This can exhibit a similarity crossflow profile. In turbulent flows at least two correlations with experimental data by Mager, ref. (52) and Johnston, ref. (53) have been developed. It is possible to generalise these to compressible flow using the Howarth-Dorodnitsyn transformaiton equation (2.1.1), indeed Smith, ref. (54) does this with the turbulent profiles and obtains reasonable agreement with experiment for skin friction in

adiabatic wall flows.

However his comparisons, and indeed all the above closure models are restricted to pressure gradients with a monotonic variation, keeping the crossflow profiles 'c' shaped. Therefore, these exercises are of limited value, and an allowance for the 's' shape should be included in the model. Timman, ref. (55) produced a 2 parameter profile, based upon error functions, which allows both 'c' and 's' shapes. This has been generalised to compressible flows by Kang, ref. (56) giving

$$\frac{u_n}{v_e} = G\bar{k}(\eta) + Q_1\bar{g}(\eta) \qquad (3.3.1)$$

where η = Howarth compressibility transformation $= \dfrac{\int_0^{x_3} \frac{\rho}{\rho_e} dx_3}{\eta_\delta}$

and $\eta_\delta = \int_0^{\delta} \frac{\rho}{\rho_e} dx_3$

$$\bar{k}(\eta) = \frac{3\sqrt{\pi}}{2}\eta \exp\left(-\frac{9\pi}{4}\eta^2\right)$$

$$\bar{g}(\eta) = \frac{1}{2}\left[\operatorname{erfc}\left(\frac{3\sqrt{\pi}}{2}\eta\right) + (\eta - 1)\exp\left(-\frac{9\pi}{4}\eta^2\right)\right]$$

An expression for Q_1, can be found by considering equation (3.2.25) when (x_1, x_2) are taken as streamline coordinates (s, n). At the wall we obtain

$$\left[\frac{\partial}{\partial x_3}\left(\mu \frac{\partial u_n}{\partial x_3}\right)\right]_w = \frac{1}{h_n}\frac{\partial p}{\partial n}$$

but the same equation applied at the boundary layer edge gives

$$\frac{1}{h_n}\frac{\partial p}{\partial n} = -\rho_e K_n v_e^2 \qquad \text{where} \quad K_n = -\frac{1}{h_s h_n}\frac{\partial h_s}{\partial n}$$

thus combining gives

$$\left[\frac{\partial}{\partial x_3}\left(\mu \frac{\partial u_n}{\partial x_3}\right)\right]_w = -\rho_e K_n v_e^2$$

or on assuming $\mu \alpha T$

$$\frac{1}{\eta_\delta^2}\left(\frac{\rho_w}{\rho_e}\right)^2 \mu_w \frac{\partial^2}{\partial \eta^2}(u_n/v_e)\Big|_w = -\rho_e K_n v_e$$

thus

$$\frac{\partial^2}{\partial \eta^2}(u_n/v_e)\Big|_w = -\left(\frac{\rho_e}{\rho_w}\right)^2 \frac{\eta_\delta^2}{\mu_w} \rho_e K_n v_e$$

which on substitution into (3.3.1) gives

$$Q_1 = -\frac{4}{9\pi}\left(\frac{\rho_e}{\rho_w}\right)^2 \frac{\eta_\delta^2}{\mu_w} \rho_e K_n v_e \qquad (3.3.2)$$

and the crossflow skin friction becomes

$$Cfen = \frac{\mu_w \frac{\partial u_n}{\partial y}\Big|_w}{1/2 \rho_e v_e^2} = C\mu_e\left(\frac{T_w}{T_e}\right)\left(\frac{\rho_w}{\rho_e}\right)\frac{1}{1/2 \rho_e v_e \eta_\delta}\frac{\partial (u_n/v_e)}{\partial \eta}\Big|_w$$

$$Cfen = \frac{\mu_e C p_o}{1/2 \rho_e v_e \vartheta_{ss}}\left(\frac{3\sqrt{\pi}}{2} G - Q_1\right) \qquad (3.3.3)$$

where $C = \dfrac{\mu_w T_e}{\mu_e T_w}$

As mentioned earlier the above profile has the ability of assuming both 'c' and 's' shaped profiles, depending on the value Q_1/G see fig. (3.3.1). We will couple this with the axisymmetric/2D equivalent streamwise profiles assumed in the zero crossflow model to give an improved closure. Use of axisymmetric/2D profiles in a fully three dimensional flow, being justified by the similarity in shape between these and the streamwise profile.
i.e. from equations (1.2.9) and (1.2.13)

$$\frac{Cfes}{2} = 0.221\left(\frac{\rho_* \mu_*}{\rho_e \mu_e}\right) Re_\vartheta^{-1} \qquad (3.3.4)$$

$$Ste = 0.221 \sigma_{FP}^2 \left(\frac{T_r - T_w}{T_{oe}}\right)\left(\frac{\rho_* \mu_*}{\rho_e \mu_e}\right) Re_\Gamma^{-1} \qquad (3.3.5)$$

The above equations are derived from local flat plate closure, or more specifically the Blasius similarity profile. This will also be used in the derivation of the relations between the integral thicknesses, and taking the edge of the profile as

$$u_s/v_e = f'(\bar{\eta}) = 0.995$$

then from the results in Schlichting, ref. (6) we have $\bar{\eta}_\delta = 5$ thus for the correct scaling we choose $\bar{\eta} = 5\eta$. For the temperature field, by considering the Cohen and Reshotko unit Prandtl number, similarity energy equation (2.2.11), in a zero pressure gradient and letting

$$\varphi(\bar{\eta}) = \frac{T_o - T_w}{T_{oe} - T_w} = S(\bar{\eta}) \frac{T_{oe}}{T_{oe} - T_w} - \frac{T_w}{T_{oe} - T_w}$$

then we see

$$\varphi(\bar{\eta}) = f'(\bar{\eta}), \quad Pr = 1$$

However in non-unit Prandtl number, the Crocco relation (1.2.11) becomes

$$\varphi(\eta) = \left[\frac{T_r - T_w}{T_{oe} - T_w}\right] f'(\bar{\eta}) + \left[\frac{T_{oe} - T_r}{T_{oe} - T_w}\right] f'(\bar{\eta})^2 \qquad (3.3.6)$$

It will be assumed, for the purposes of calculating the integral thickness relations, that the unit Prandtl number values will hold in non-unit Prandtl number flows.

Thus the integral thicknesses become

$$\frac{\delta_s}{\Delta} = \frac{H\vartheta_{ss}}{\Delta} = \left[2.6 \frac{T_w}{T_e} + \left(\frac{T_{oe}}{T_e} - 1\right) r\right] \frac{\vartheta_{ss}}{\Delta}$$

$$\frac{\delta_n}{\Delta} = \int_0^1 -\frac{u_n}{v_e} d\eta = -G\int_0^1 \bar{k}(\eta) d\eta - Q_1 \int_0^1 \bar{g}(\eta) d\eta$$

$$\frac{\vartheta_{ss}}{\Delta} = \int_0^1 \frac{u_s}{v_e}\left(1 - \frac{u_s}{v_e}\right) d\eta = \int_0^1 f'(5\eta)(1 - f'(5\eta)) d\eta$$

$$\frac{\vartheta_{sn}}{\Delta} = \int_0^1 \frac{u_n}{v_e}\left(1 - \frac{u_s}{v_e}\right) d\eta = G\int_0^1 \bar{k}(\eta)(1 - f'(5\eta)) d\eta + Q_1 \int_0^1 \bar{g}(\eta)(1 - f'(5\eta)) d\eta$$

$$\frac{\vartheta_{ns}}{\Delta} = \int_0^1 -\frac{u_n u_s}{v_e^2} d\eta = -G\int_0^1 \bar{k}(\eta)\, f'(5\eta)\, d\eta \; - Q_1 \int_0^1 \bar{g}(\eta)\, f'(5\eta)\, d\eta$$

$$\frac{\vartheta_{nn}}{\Delta} = \int_0^1 -\frac{u_n^2}{v_e^2} d\eta = -G^2\int_0^1 \bar{k}^2(\eta) d\eta \; - 2GQ_1\int_0^1 \bar{k}(\eta)\bar{g}(\eta) d\eta - Q_1^2\int_0^1 \bar{g}(\eta)^2 d\eta$$

$$\frac{\Gamma_s}{\Delta} = \int_0^1 \frac{u_s}{v_e}\left(1 - \frac{T_o}{T_{oe}}\right) d\eta = \frac{T_{oe} - T_w}{T_{oe}} \int_0^1 f'(5\eta)(1 \; - \; f'(5\eta)) d\eta$$

$$\frac{\Gamma_n}{\Delta} = \int_0^1 \frac{u_n}{v_e}\left(1 - \frac{T_o}{T_{oe}}\right) d\eta = \frac{T_{oe} - T_w}{T_{oe}} \left[G\int_0^1 \bar{k}(\eta)(1 \; - \; f'(5\eta)) d\eta \right.$$

$$\left. + Q_1 \int_0^1 \bar{g}(\eta)(1 \; - \; f'(5\eta)) d\eta \right]$$

The above integrals have been evaluated and are given in table (3.3.1), thus we have

$$\left.\begin{aligned}
\vartheta_{ss} &= P_o \Delta \\
\bar{\delta}_s &= \frac{\delta_s}{\vartheta_{ss}} = 2.6\frac{T_w}{T_e} + \left(\frac{T_{oe}}{T_e} - 1\right) r \\
\bar{\delta}_n &= \frac{\delta_n}{\vartheta_{ss}} = P_{12} G + P_{13} Q_1 \\
\bar{\vartheta}_{sn} &= \frac{\vartheta_{sn}}{\vartheta_{ss}} = P_1 G + P_2 Q_1 \\
\bar{\vartheta}_{ns} &= \frac{\vartheta_{ns}}{\vartheta_{ss}} = P_3 G + P_4 Q_1 \\
\bar{\vartheta}_{nn} &= \frac{\vartheta_{nn}}{\vartheta_{ss}} = P_5 G^2 + P_6 G Q_1 + P_7 Q_1^2
\end{aligned}\right\} \quad (3.3.7)$$

$$\overline{\Gamma_n} = \frac{\Gamma_n}{\Gamma_s} = \frac{(P_8 + P_9)G + (P_{10} + P_{11})Q_1}{P_{14} + P_{15}}$$

Hence the 3 governing integral equations (3.2.24), (3.2.25) and (3.2.26) become 3 equations for 3 variables ϑ_{ss}, Γ_s, & G by substitution of (3.2.27), (3.2.28), (3.2.29), (3.3.2), (3.3.3), (3.3.4), (3.3.5) and (3.3.7), with the following form.

$$F_{11}\frac{\partial \vartheta_{ss}}{\partial x_1} + F_{12}\frac{\partial G}{\partial x_1} + F_{13}\frac{\partial \vartheta_{ss}}{\partial x_2} + F_{14}\frac{\partial G}{\partial x_2} = Res_1 \qquad (3.3.8)$$

$$F_{21}\frac{\partial \vartheta_{ss}}{\partial x_1} + F_{22}\frac{\partial G}{\partial x_1} + F_{23}\frac{\partial \vartheta_{ss}}{\partial x_2} + F_{24}\frac{\partial G}{\partial x_2} = Res_2 \qquad (3.3.9)$$

$$F_{31}\frac{\partial \Gamma_s}{\partial x_1} + F_{32}\frac{\partial G}{\partial x_1} + F_{33}\frac{\partial \Gamma_s}{\partial x_2} + F_{34}\frac{\partial G}{\partial x_2} = Res_3 \qquad (3.3.10)$$

where the coefficients F_{ij} are listed in Appendix F.

$$P_o = 1/5 \int_0^5 f'(\bar{\eta})(1 - f'(\bar{\eta}))d\bar{\eta} = 0.1328$$

$$P_1 = 1/5 \int_0^5 \bar{k}(\bar{\eta}/5)(1 - f'(\bar{\eta}))d\bar{\eta}/P_o = 0.6925$$

$$P_2 = 1/5 \int_0^5 \bar{g}(\bar{\eta}/5)(1 - f'(\bar{\eta}))d\bar{\eta}/P_o = -0.1175$$

$$P_3 = -1/5 \int_0^5 \bar{k}(\bar{\eta}/5)\, f'(\bar{\eta})d\bar{\eta}/P_o = -0.7197$$

$$P_4 = -1/5 \int_0^5 \bar{g}(\bar{\eta}/5)\, f'(\bar{\eta})d\bar{\eta}/P_o = 0.0713$$

$$P_5 = -1/5 \int_0^5 \bar{k}(\bar{\eta}/5)^2 d\bar{\eta}/P_o = -0.4438$$

$$P_6 = -2/5 \int_0^5 \bar{k}(\bar{\eta}/5)\, \bar{g}(\bar{\eta}/5)d\bar{\eta}/P_o = 0.1264$$

$$P_7 = -1/5 \int_0^5 \bar{g}(\bar{\eta}/5)^2 d\bar{\eta}/P_o = -0.0108$$

$$P_8 = 1/5 \int_0^5 \bar{k}(\bar{\eta}/5)d\bar{\eta} = 0.1875$$

$$P_9 = -1/5 \int_0^5 \bar{k}(\bar{\eta}/5)f'(\bar{\eta})d\eta = -0.0956$$

$$P_{10} = 1/5 \int_0^5 \bar{g}(\bar{\eta}/5)d\bar{\eta} = -0.0251$$

$$P_{11} = -1/5 \int_0^5 \bar{g}(\bar{\eta}/5)\, f'(\bar{\eta})\, d\bar{\eta} = 0.0095$$

$$P_{12} = -1/5 \int_0^5 \bar{k}(\bar{\eta}/5)d\bar{\eta}/P_o = -1.4119$$

$$P_{13} = -1/5 \int_0^5 g(\bar{\eta}/5)d\bar{\eta}/P_o = 0.1888$$

$$P_{14} = 1/5\, f(5) = 0.6567$$

$$P_{15} = -1/5 \int_0^5 f'(\bar{\eta})^2 d\bar{\eta} = -0.5239$$

Table 3.3.1

3.4 Calculation on the windward plane of symmetry of a yawed body

We shall consider first a comparison with an exact solution, that of the boundary layer growth along the windward plane of symmetry of a sharp cone. Reshotko, ref.(57) derives similarity equations for a unit Prandtl number, linear viscosity temperature law flow, from the boundary layer equations (3.2.11), (3.2.12) & (3.2.14), with x_1 the distance along the generator and x_2 the azimuth. Since equation (3.2.14) is identically zero on the plane of symmetry it is differentiated with respect to x_2, to allow solution for $F(\lambda)$ and $\Phi(\lambda)$.

$$\frac{Cfe}{2} = F''(\lambda)\left(\frac{3}{Re_x}\right)^{1/2}$$

$$Ste = \Phi'(\lambda)\left(\frac{3}{Re_x}\right)^{1/2}$$

where

$$\lambda = \sqrt{\frac{3}{x}}\int_0^1 \frac{\rho}{\rho_e} dy/\Delta \quad , \quad F'(\lambda) = \frac{u}{v_e} \quad , \quad \Phi(\lambda) = \frac{To - Tw}{Toe - Tw}$$

Applying the integral equations (3.3.8), (3.3.9) & (3.3.10) to this problem, it is also necessary to differentiate the x_2 -momentum equation (3.3.9) with respect to x_2 . Recalling (3.3.9)

$$F_{21}\frac{\partial \vartheta_{ss}}{\partial x_1} + F_{22}\frac{\partial G}{\partial x_1} + F_{23}\frac{\partial \vartheta_{ss}}{\partial x_2} + F_{24}\frac{\partial G}{\partial x_2} = Res_2$$

on the plane of symmetry , by definition

$$\left.\frac{\partial u_{1e}}{\partial x_2}\right|_{x_2=0} , \left.\frac{\partial \rho_e}{\partial x_2}\right|_{x_2=0} , \left.\frac{\partial \vartheta_{ss}}{\partial x_2}\right|_{x_2=0} , \left.\frac{\partial Q_1}{\partial x_2}\right|_{x_2=0} = 0$$

and also the inviscid streamline inclination to the x_1 coordinate $\psi = 0$, then differentiation with respect to x_2 yields

$$\frac{(\psi' + P_3 G')}{h_1}\left[\frac{\partial \vartheta_{ss}}{\partial x_1} + \frac{\vartheta_{ss}}{\rho_e}\frac{\partial \rho_e}{\partial x_1} + \frac{2\vartheta_{ss}}{v_e}\frac{\partial v_e}{\partial x_2}\right] + \frac{\vartheta_{ss}}{h_1} P_3 \frac{\partial G'}{\partial x_1} + \frac{\vartheta_{ss}}{h_1}\frac{\partial \psi'}{\partial x_1}$$

$$+\vartheta_{ss}\left\{\frac{2}{h_2}\left(\psi'^2+\psi'(P_1+P_3)G'+P_5G'^2\right)+\frac{1}{h_1}\left[\bar{\delta}_1\frac{\partial\psi'}{\partial x_1}+\frac{\bar{\delta}_1\psi'}{v_e}\frac{\partial v_e}{\partial x_1}\right]\right.$$

$$+\frac{\psi'}{h_2}(P_{12}G'+\psi'\bar{\delta}_1)\quad-K_1(P_{12}G'+\psi'\delta_1)$$

$$\left.-K_1(2\psi'+(P_1+P_3)G')\right\}=\frac{\mu_e}{\rho_e v_e}\left[\frac{0.221\psi'}{\vartheta_{ss}}+\frac{3\sqrt{\pi}P_0G'}{2\vartheta_{ss}}\right]\qquad(3.4.1)$$

where $G',\psi'=\left.\frac{\partial G}{\partial x_2}\right|_{x_2=0}\cdot\left.\frac{\partial\psi}{\partial x_2}\right|_{x_2=0}$

On a sharp cone plane of symmetry the above becomes

$$(\psi'+P_3G')\frac{\partial\vartheta_{ss}}{\partial x_1}+\vartheta_{ss}P_3\frac{\partial G'}{\partial x_1}+\frac{\vartheta_{ss}}{x_1}\left\{\frac{2}{\sin\vartheta_c}(\psi'^2+(P_1+P_3)\psi'G'+P_5G'^2)\right.$$

$$\left.+\left(\frac{\psi'}{\sin\vartheta_c}+1\right)(\bar{\delta}_s\psi'+P_{12}G')+2\psi'+(P_1+P_3)G'\right\}$$

$$=\frac{\mu_e}{\rho_e v_e\vartheta_{ss}}\left(0.221\psi'+\frac{P_0\,3\sqrt{\pi}}{2}G'\right)\qquad(3.4.2)$$

Where ϑ_c is the cone half angle, and ψ' the gradient of the inclination of the streamlines to the cone generators in the azimuthal x_2 -direction at the plane of symmetry is constant. Its value must be determined from cone flow pressure distributions. As an approximation, in high Mach number flows we may use the method of steepest descent ref.(50), described in the latter part of appendix d to arrive at

$$\psi'=\left.\frac{\partial\psi}{\partial x_2}\right|_{x_2=0}=\frac{\sin\alpha}{\cos(\alpha+\vartheta_c)}$$

where α is the angle of incidence of the cone. The x_1 -momentum and enthalpy equations (3.3.8) & (3.3.10) become

$$\frac{\partial\vartheta_{ss}}{\partial x_1}+\frac{\vartheta_{ss}}{x_1\sin\vartheta_c}\frac{\partial\bar{\vartheta}_{12}}{\partial x_2}+\frac{\vartheta_{ss}}{x_1}=\frac{0.221\mu_e}{\rho_e v_e\vartheta_{ss}}$$

$$\frac{\partial\Gamma_s}{\partial x_1}+\frac{\Gamma_s}{x_1\sin\vartheta_c}\frac{\partial\bar{\Gamma}_2}{\partial x_2}+\frac{\Gamma_s}{x_1}=0.221\left(\frac{T_{oe}-T_w}{T_{oe}}\right)^2\sigma_{FP}^2\frac{\mu_e}{\rho_e v_e\Gamma_s}$$

which on using $\left.\frac{\partial \bar{\vartheta}_{12}}{\partial x_2}\right|_{x_2=0} = \psi' + P_1 G' \,,\; \left.\frac{\partial \bar{\Gamma}_2}{\partial x_2}\right|_{x_2=0} = \psi' + (P_8 + P_9) G'$

become

$$\frac{\partial \vartheta_{ss}}{\partial x_1} + \frac{\vartheta_{ss}}{x_1}\left[1 + \left(\frac{\psi' + P_1 G'}{\sin \vartheta_c}\right)\right] = \frac{0.221 \mu_e}{\rho_e v_e \vartheta_{ss}} \qquad (3.4.3)$$

$$\frac{\partial \Gamma_s}{\partial x_1} + \frac{\Gamma_s}{x_1}\left[1 + \left(\psi' + \left[\frac{P_8 + P_9}{P_{14} + P_{15}}\right] G'\right) \Big/ \sin \vartheta_c\right] = \frac{0.221 \mu_e \sigma_{fp}^2}{\rho_e v_e \Gamma_s}\left[\frac{T_{oe} - T_w}{T_{oe}}\right]^2 \qquad (3.4.4)$$

Also in a cone flow, G' is a constant, thus eqn (3.4.3) & (3.4.4) can be integrated analytically to give

$$\vartheta_{ss} = \left(\frac{0.221 \mu_e}{\rho_e v_e}\right)\left(\frac{x}{3/2 + \bar{\psi}' + P_1 \bar{G}'}\right)^{1/2}$$

$$\Gamma_s = \left(\frac{0.221 \mu_e}{\rho_e v_e}\right)^{1/2} \frac{x^{1/2} \sigma_{fp}\left(\frac{T_r - T_w}{T_{oe}}\right)}{\left[3/2 + \bar{\psi}' + \left[\frac{P_8 + P_9}{P_{14} + P_{15}}\right] \bar{G}'\right]^{1/2}}$$

where

$$\bar{G}' = \frac{G'}{\sin \vartheta_c} \,,\; \bar{\psi}' = \frac{\psi'}{\sin \vartheta_c}$$

Substituting for $\frac{\partial \vartheta_{ss}}{\partial x_1}$ in eqn (3.4.2) we obtain

$$1/2(\bar{\psi}' + P_3 \bar{G}') + 2(\bar{\psi}'^2 + (P_1 + P_3)\bar{\psi}' \bar{G}' + P_5 G'^2)$$
$$+ (\bar{\psi}' + 1)(\bar{\delta}_s \bar{\psi}' + P_{12} \bar{G}') + 2\bar{\psi}' + (P_1 + P_3)\bar{G}'$$
$$= (3/2 + \bar{\psi}' + P_1 \bar{G}')(\bar{\psi}' + \frac{P_o 3\sqrt{\pi}\, \bar{G}'}{0.442})$$

Rearranging the above results in

$$2.0 \bar{G}'^2 + (4.1954 + 3.756 \bar{\psi}')\bar{G}' - (1 + \bar{\delta}_s)(\bar{\psi}' + \bar{\psi}'^2) = 0$$

which can be solved to give

$$\frac{C_{fe}}{2} = 0.3321 \left(3/2 + \bar{\psi}' + P_1 \bar{G}'\right)^{1/2} Re_x^{-1/2} \qquad (3.4.5)$$

$$Ste = 0.3321\sigma_{FP}\left[3/2+\bar{\Psi}'+\left(\frac{P_8+P_9}{P_{14}+P_{15}}\right)\bar{G}'\right]^{1/2} Re_x^{-1/2} \qquad (3.4.6)$$

The above are compared with the unit Prandtl number exact solutions of Reshotko in figures (3.4.1) for boundary layer edge Mach numbers 0,3.5 and 5 with wall temperatures = 0, 0.5 and 1.0. Also shown is the zero crossflow solution. The abscissa $k=\frac{2}{3}\bar{\Psi}'$ is a measure of the three dimensionality of the flow, ie. using the approximation for ψ'earlier

$$k = \frac{2\sin\alpha}{3\cos(\alpha+\vartheta_c)\sin\vartheta_c}$$

We see that the crossflow profile assumed in the closure of the integral equations allows excellent agreement with the exact similarity solution over the whole range considered with a maximum error of 4%. The figures also show the assumption of zero crossflow to be valid for cold wall temperatures $T_W/T_{oe}=0$ and at very low Mach numbers, but deteriorates with increases in both to a maximum of 60% in the ranges considered. For the higher values of $k>6$, Reshotko shows very good agreement between his solutions and the infinite swept cylinder solutions he obtained earlier ref.(58).

3.5 Numerical Procedure

Equations (3.3.8), (3.3.9) and (3.3.10) are hyperbolic in nature, that is at a general point in the solution characteristic lines exist that define a zone of influence and zone of dependence. The zone of influence being the region that contains all the points which can affect the solution at this given point, and the zone of dependence contains all points that can be affected by the solution at this general point. Myring, ref. (72), showed the characteristic lines bounding this region are for a turbulent flow, contained between the inviscid streamline and limiting flow direction at the body surface. Hence if the numerical scheme adopted is to model this behaviour, the integration of the equations must proceed in a direction similar to the characteristic direction.

Ideally the governing equations would be integrated in streamline coordinates, that is a surface coordinate system aligned with and perpendicular to the inviscid streamline direction. Such a system though is an unnecessary luxury and since these are difficult to compute, they will not be used here. A method of calculating a suitable mesh quickly, with its origin at the stagnation point of the blunt body, and in a roughly streamlined direction has been developed by Blottner and Ellis, ref. (59) and is described in Appendix C. This mesh system has been adopted for flows over bodies with an attachment line lying on a plane of symmetry.

The numerical procedure adopted is similar to that used by Smith, ref. (60). The method progresses downstream in the x_1 or (i) direction with successive sweeps in the x_2 or (j) direction round the body from $j = 1$ (the windward plane of symmetry) up to $jmax$ (the leeward plane of symmetry).

Finite difference representation of the derivatives is assumed, see Fig. (3.5.1)

$$\left.\frac{\partial \Phi}{\partial x_1}\right|_{i+1/2\ j} = \frac{\Phi_{i+1\ j} - \Phi_{ij}}{\Delta x_{1i}}$$

$$\left.\frac{\partial \Phi}{\partial x_2}\right|_{i+1/2\ j} = \frac{\Phi_{i+1/2\ j} - \Phi_{i+1/2\ j-1}}{\Delta x_{2\ j-1}} \qquad (3.5.1)$$

where $\Phi = \vartheta_{ss}, G$ & Γ_s . Implicit in the above is the assumption that the streamlines make a positive (or zero) angle with the coordinate direction, which is the case for all the flows considered herein. Although this restriction can be relaxed by allowing the derivative to take the form

$$\left.\frac{\partial \Phi}{\partial x_2}\right|_{i+1/2\ j} = \frac{\Phi_{i+1/2\ j+1} - \Phi_{i+1/2\ j}}{\Delta x_{2j}}$$

when the streamlines make a negative angle with the x_1 -coordinate. An obvious example of such a flow is the windward surface of a delta wing at incidence, where the attachment lines lie off the symmetry line. However such a system would require an implicit scheme to solve a set of jmax simultaneous equations for each j -sweep iteration and hence significantly increase the run time of the algorithm, and so will not be considered here.

Equation (3.5.1) is applied to the integral equations (3.3.8), (3.3.9) and (3.3.10) to give the iterative algorithm below for

$j = 2, jmax$

$$F_{m1}\Big|^{(n)}_{i+1/2\ j}\left(\frac{\Phi^{(n+1)}_{i+1\ j} - \Phi_{ij}}{\Delta x_{1i}}\right) + F_{m2}\Big|^{(n)}_{i+1/2\ j}\left(\frac{G^{(n+1)}_{i+1\ j} - G_{ij}}{\Delta x_{1i}}\right)$$

$$+F_{m3}\Big|^{(n)}_{i+1/2\ j}\left(\frac{\Phi^{(n)}_{i+1/2\ j} - \Phi_{i+1/2\ j-1}}{\Delta x_{2\,j-1}}\right) + F_{m4}\Big|^{(n)}_{i+1/2\ j}\left(\frac{G^{(n)}_{i+1/2\ j} - G_{i+1/2\ j-1}}{\Delta x_{2\,j-1}}\right)$$

$$= Res_m\Big|^{(n)}_{i+1/2\ j} \qquad (3.5.2)$$

where $\Phi = \vartheta_{ss}$ for $m = 1,2$, and $\Phi = \Gamma_s$ for $m = 3$ and denotes the value at the n^{th} iteration. $\Phi_{i+1/2\ j}$ is evaluated by linear interpolation

$$\Phi_{i+1/2\ j} = \frac{(\Phi_{i+1\ j} + \Phi_{ij})}{2}$$

When $j = 1$, i.e. the windward plane of symmetry, the differentiated x_2 -momentum equation (3.4.1) is used, together with the symmetry conditions

$$\left.\frac{\partial \vartheta_{ss}}{\partial x_2}\right|_{x_2 = 0} = 0 , \qquad \left.\frac{\partial \Gamma_s}{\partial x_2}\right|_{x_2 = 0} = 0$$

allows easy integration.

3.6 Heat transfer distributions over blunted cones at incidence

In order to test the accuracy of the closure relations derived, a series of comparisons have been made using the KHOMP3D code with the experimental heat transfer data of Widhopt, ref. (32), Bushnell, ref. (34) and Davies, ref. (61) for flows over blunted cones at incidence. The numerical predictions were carried out in the coordinate system generated using the method described in Appendix D. For convenience the pressure distribution used in the calculations was a modified Newtonian type, which for the larger incidences, i.e. where the angle of attack (α) exceeded the cone half angle (ϑ_c), meant restriction of the calculation to the windward surface only (see Chapter 4).

It is assumed that the flow begins at an axisymmetric stagnation point, and the analysis of appendix A is used, also to avoid stability errors, the initial growth of the boundary layer from the stagnation point for a distance 0.5 R_n is assumed to have zero crossflow.

The heat transfer predictions and experimental results normalised with respect to the stagnation heating are shown in figures (3.6.1), (3.6.2) and (3.6.3) for the Widhopf, Bushnell and Davies cases with Mach 5, 8 and 10 free stream flows respectively. Considering first the Widhopf data with a cone angle of 9^o, measurements were taken at 5, 15 and 26^o of incidence. Full solutions were obtained for the two lower incidences but only windward heat transfer results for the large incidence. The experimental data appears to be transitional at the downstream end resulting in bad agreement in the predictions both with and without crossflow. As expected the crossflow effect increases downstream, with the crossflow profile growing from zero at the sphere-

cone junction, since upstream of this point the flow is axisymmetric. We also see the existence if crossflow increases the heating rate in the region $0^o < \varphi < 90^o$ and lowers it in the region $90^o < \varphi < 180^o$, this being due to the crossflow transporting more of the entrained fluid away from the attachment line, thus thinning the boundary layer in the region $0^o < \varphi < 90^o$ and thickening it elsewhere.

These trends are repeated in the results shown in Figs. (3.6.2) and (3.6.3), we also see that the attachment line predictions have improved agreement as the incidence increases, Fig. (3.6.2c). This rather surprising result is a feature of the increased accuracy of the modified Newtonian pressure field rather than the boundary layer solution. Conversely the less accurate prediction on the leeward plane of symmetry $\varphi = 180^o$ where computed, can be partly blamed on the particularly bad modified Newtonian pressure field in this region.

Chapter 4

Approximate methods for inviscid pressure distribution prediction

As shown by the examples presented, the boundary layer thickness and, hence, skin friction and heat transfer rates depends primarily upon the pressure distribution. Consequently, the accuracy of any boundary layer prediction is determined by the accuracy of the pressure distribution used. If we are to retain the advantages of a quick boundary layer method, then a similarly fast body surface pressure distribution method has to be employed. One of the more commonly used simple methods for blunted bodies is the modified Newtonian approach, see ref. (50). The method is derived in the hypersonic limit $M_\infty \to \infty$, and results in an expression relating the pressure at the surface to the angle the surface normal vector $\underset{\sim}{n}$ makes with the free-stream direction $\underset{\sim}{V}_\infty / V_\infty$

$$p = p_\infty + (p_0 - p_\infty)\left(\frac{\underset{\sim}{V}_\infty}{V_\infty} \cdot \underset{\sim}{n}\right)^2 \qquad (4.0.1)$$

where p_0 is the stagnation pressure, p_∞ the free-stream static pressure. Applying the above to a hemispherically blunted cone, half angle ϑ_c , and incidence α , see fig. (4.0.1), we obtain for the hemisphere portion

$$\left(\frac{\underset{\sim}{V}_\infty}{V_\infty} \cdot \underset{\sim}{n}\right) = \cos\left(\frac{s}{R_n}\right)\cos\alpha + \sin\left(\frac{s}{R_n}\right)\sin\alpha\cos\varphi \qquad (4.0.2)$$

and for the conical portion

$$\left(\frac{\underset{\sim}{V}_\infty}{V_\infty} \cdot \underset{\sim}{n}\right) = \sin\vartheta_c\cos\alpha + \cos\vartheta_c\sin\alpha\cos\varphi \qquad (4.0.3)$$

where s is the surface distance from the axisymmetric apex of the body. For the case of incident flows it is possible when $\alpha > \vartheta_c$ for $\frac{\underset{\sim}{V}_\infty}{V_\infty} \cdot \underset{\sim}{n}$ to be negative, i.e. when the surface slopes away from the free-stream. In such situations the modified Newtonian approx-

imation breaks down, and it is usual to let the surface pressure assume the free-stream static value P_∞ .

4.1 2-dimensional flow

For the special case when the body is at zero incidence equations (4,0.2) and (4.0.3) substituted into equation (4.0.1) become

$$\text{hemisphere:} \quad \frac{p}{p_o} = \frac{p_\infty}{p_o} + (1 - \frac{p_\infty}{p_o})\cos^2(\frac{s}{R_n}) \qquad (4.1.1)$$

$$\text{cone:} \quad \frac{p}{p_o} = \frac{p_\infty}{p_o} + (1 - \frac{p_\infty}{p_o})\sin^2\vartheta_c \qquad (4.1.2)$$

The above is known to be accurate in the stagnation region, but a poor estimation elsewhere. Poll, ref. (62) developed an improved method for blunted cylinders, which consists of 3 matched predictions. A modified Newtonian distribution in the stagnation region up to the sonic point ($s/R_n \approx 1$) followed by a Prandtl Meyer expansion to the shoulder and finally an exponential relaxation to the free stream pressure, where the relaxation coefficient (Ω) has been taken from empirical fits. Poll found that in the region $1 < s/R_n < \pi/2$ the function F , where

$$F(\psi/2, M_\infty) = \frac{Cp_\psi - Cp_{\pi/2}}{Cp_1 - Cp_{\pi/2}} \qquad (4.1.3)$$

and $Cp_\psi = Cp$ at $s/R_n = \psi$, is to a good approximation independent of Mach number, hence $F \approx F(\psi/2)$, and by a simple curve fit

$$F(\psi/2) = 12.389 - 44.395\psi/2 + 55.139(\psi/2)^2 - 23.808(\psi/2)^3 \qquad (4.1.4)$$

The shoulder pressure coefficient may be obtained from another curve fit

$$Cp_{\pi/2} = 0.08 - 4384.0\exp\{-8.3179M_\infty^{0.2}\} \qquad (4.1.5)$$

and the third region is calculated from the expression

$$Cp = Cp_{\infty} + (Cp_{\pi/2} - Cp_{\infty}) \exp\left(\frac{-\Omega(s - s\pi/2)}{Rn}\right) \qquad (4.1.6)$$

This approach has been generalised to predict the pressure distributions over hemispherically blunted cones, by limiting the Prandtl Meyer expansion to the sphere-cone junction S_{SC} and then relaxing the pressure coefficient to the sharp cone value Cp_{cone} hence equation (4.1.6) becomes

$$Cp = Cp_{cone} + (Cp_{sc} - Cp_{cone}) \exp\left(\frac{-\Omega(s - s_{sc})}{Rn}\right) \qquad (4.1.7)$$

which is valid for $s/Rn > s_{sc}/R_n = \frac{\pi}{2} - \vartheta_c$, and $Cp_{sc} = Cp_{s=s_{sc}}$

For ease of computation Cp_{sc} can be obtained from the empirical function derived by Linnel and Bailey, ref. (38)

$$(f^2 + 1/4) Cp_{sc} = \left[2.5 + \frac{4\beta}{\sqrt{f^2 + 1/4}}\right] \Big/ \left[1 + \frac{8\beta}{\sqrt{f^2 + 1/4}}\right] \qquad (4.1.8)$$

where β = Mach angle $= \sqrt{M^2 - 1}$, $f = 1/(2 \tan \vartheta_c)$

This method has been applied to several sphere-cones and the results are shown in figures (4.1.1) along with the modified Newtonian prediction equations (4.1.1) and (4.1.2) for a Mach number range 4 to 7. The relaxation parameter has been taken to give a 25% relaxation over a surface distance of 6 R_n, as suggested by Poll, giving $\Omega = 0.23/Rn$. As expected the modified Newtonian approach underpredicts the pressure on the conical afterbody, an appreciation of how bad this underprediction can be, is found by consulting figure (4.1.2) which compares exact sharp cone pressures tabulated in ref. (64), with modified Newtonian for a 10^0 half angled cone in a range of Mach numbers, from 2 to 10. We see for this set of conditions the modified Newtonian prediction is at best 15% in error. The graphs in figures (4.1.1) do not really justify the improved method since full relaxation of the experimental pressure data back to the

sharp cone value has not occurred.

4.2 3-dimensional flow

The modified Newtonian method is of more value in the predictions of 3-dimensional surface pressure distributions, where its ease of application is unchanged by the extra dimension, a factor that cannot be attributed to most other surface pressure prediction techniques. To perform an assessment of its accuracy, the flow over blunted cones at incidence will be considered. For such flows the modified Newtonian equations have already been shown, equations (4.0.1), (4.0.2) and (4.0.3). These are compared in figs. (4.2.1) with a full field prediction technique, ref. (65), and experimental results of Widhopf ref. (32), for a Mach 5 flow at incidences up to 15^{o}. Two points stand out from these figures, firstly the stagnation region is predicted accurately as expected, but secondly, the modified Newtonian prediction of the conical portion of the windward plane of symmetry, improves with incidence. This can be explained as follows, considering equation (4.0.3) we see that the windward generator pressure is assumed to be that of a cone with half angle $\vartheta_c + \alpha$ in a zero incidence flow. Such an assumption would overpredict the pressure due to the larger radius of curvature involved. Hence this factor cancels out the inherent underprediction already shown to exist with the modified Newtonian method in conical flows (see fig. (4.1.2)), resulting in the fortuitous good prediction.

Also for the conical portion, the azimuthal variation is predicted as follows

$$\frac{p}{p_{\varphi=0}} = \frac{\frac{p_\infty}{p_o} + (1 - \frac{p_\infty}{p_o})(\sin\vartheta_c \cos\alpha + \cos\vartheta_c \sin\alpha \cos\varphi)^2}{\frac{p_\infty}{p_o} + (1 - \frac{p_\infty}{p_o}) \sin^2(\vartheta_c + \alpha)} \qquad (4.2.1)$$

This is compared in fig. (4.2.2) with the exact solutions of ref. (64) for a 10^{o} sharp cone in a Mach 5 freestream at 5^{o}, 10^{o} and 13^{o} incidence. Agreement is excellent up to the $\varphi = 90^{o}$ position, but deteriorates rapidly beyond this. Thus for the windward surface at least it would seem that if an accurate windward generator pressure method were available then equation (4.2.1) would extend this to a

reasonable windward surface pressure description. One such technique, applicable to blunt cones would be the axisymmetric method of Poll just discussed. Over the hemispherical portion the pressure field would be assumed axisymmetric, followed by a relaxation to the sharp cone pressure, determined from equation (4.2.1). In order to do this, the sharp cone pressure $P_{\varphi=0}$ has to be determined. McBrayer, ref. (66), developed a correlation of "equivalent axisymmetric cone angle" $\vartheta_{c_{eq}}$, which is used in place of $(\vartheta_c + \alpha)$, in the determination of $P_{\varphi=0}$, where $\vartheta_{c_{eq}}$ is defined as the cone angle that at zero incidence flow gives a surface pressure coefficient equal to that on the windward generator of a cone at incidence. He found that K_1 where

$$K_1 = \frac{\vartheta_{c_{eq}}}{\vartheta_c + \alpha} \qquad (4.2.2)$$

is to a good approximation independent of Mach number, and a similarity parameter $\psi=(\vartheta_c+\alpha)/\vartheta_c$ combined the two remaining variables. We have fitted a straight line through his data, valid in the region $0 \leqslant \alpha \leqslant 3\vartheta_c$ giving

$$K_1 = 1 - 0.04(\psi - 1) \qquad (4.2.3)$$

This technique is suggested but has not been tried, the 3-dimensional heat transfer predictions of Chapter 3 have all been calculated using modified Newtonian pressure distributions which have been shown here to be sufficiently accurate to carry out a satisfactory appraisal of the boundary layer code KHOMP3D.

Chapter 5

Alternative techniques and suggestions for further work

The results presented in this thesis show the flat plate closure method to be a useful simple technique for skin friction and heat transfer calculations. However, there is still room for improvement, particularly in the severe flow conditions that cause large distortions of the boundary layer profiles from the flat plate shapes. One feature that became apparent from the results of Chapter 2 was the high accuracy with which the Reynolds analogy factor is predicted, and this suggests the possible use of the flat plate closure method as a Reynolds analogy factor predictor, to be used in conjunction with a more sophisticated skin friction code, e.g. Green, ref. (24). Also from an experimental viewpoint, the technique could be employed to transform heat transfer measurements into skin friction data. These applications would, of course, breakdown in or near separation regions or in very rapidly changing wall temperature flows.

We have already demonstrated the use of pressure gradient similarity for laminar flow in section 2.6,, where improved two parameter relations were obtained for skin friction and Stanton number using the similarity solutions of Cohen and Reshotko. For turbulent boundary layers, two parameter empirical relations are available for skin friction e.g. Ludwieg-Tillmann, ref. (6), which use momentum thickness Reynolds number and incompressible shape factor H_i. Hence their application is coupled with an extra integral equation, the entrainment equation of Head, Ref. (3) to allow variations in H_i to be predicted. To obtain improved heat transfer predictions, a similar two parameter model for Stanton number must be found. Incompressible shape factor, may again be appropriate, or a fourth integral differential equation, the kinetic energy deficit equation, derived by Spalding, ref. (68) may prove useful in predicting the growth of an additional integral thickness

$$\delta_3 = \int_0^{\delta} \frac{\rho u}{\rho_e u_e}\left(1-\left(\frac{u}{u_e}\right)^2\right) dy$$

Another technique is available, which involves the generation of any number of boundary layer integral equations (n, say). This method of "integral relations" allows profiles with n variables to be used in their solution resulting in a system of non linear first order differential equations for the n profile variables. Dorodnitsyn, ref. (69) has used this technique to calculate the incompressible laminar boundary layer growth in two-dimensions, where the system of differential equations becomes ordinary. Holt and Modarress, ref. (70) have generalised this technique to three-dimensional flows with, and without, separation. The results obtained by the authors appear very promising, and in view of the ability to cope with reverse flows the method is potentially very powerful.

To assess the accuracy of the heat transfer predictions, we shall extend the incompressible method of Dorodnitsyn to include temperature profile predictions, and compare the results with the exact solutions for the similarity boundary layer solutions derived by Falkner and Skan, ref. (14) and Fage and Falkner, ref. (15).

Consider the boundary layer equation for incompressible 2-D laminar flow

$$uu_x + vu_y = u_e u_{ex} + \nu u_{yy} \qquad (5.1)$$

$$u_x + v_y = 0 \qquad (5.2)$$

$$uT_x + vT_y = k\,T_{yy} \qquad (5.3)$$

where suffix denotes differentiation with respect to that variable.

let $\bar{u} = u/u_e$, $\bar{v} = \dfrac{v}{u_e\sqrt{\nu}}$, $\bar{T} = \dfrac{T - T_w}{T_e - T_w}$

and $\zeta = \int_0^x u_e\,dx$, $\eta = \dfrac{u_e\, y}{\sqrt{\nu}}$

equations (5.1) and (5.2) reduce to

$$\bar{u}\frac{\partial \bar{u}}{\partial \zeta} + \bar{w}\frac{\partial \bar{u}}{\partial \eta} = \frac{u_e}{u_e}x(1-\bar{u}^2) + \frac{\partial^2 \bar{u}}{\partial \eta^2} \qquad (5.4)$$

$$\frac{\partial \bar{u}}{\partial \zeta} + \frac{\partial \bar{w}}{\partial \eta} = 0 \qquad (5.5)$$

where $\bar{w} = \bar{v} + \frac{\eta \bar{u}}{u_e}\frac{\partial u_e}{\partial x}$

and using equations (5.1) and (5.2), equation (5.3) becomes

$$(uT)_x + (vT)_y = kT_{yy}$$

thus

$$(\bar{u}u_e\bar{T})_x + (\bar{v}u_e\sqrt{\nu}\,\bar{T})_y = \frac{kT_{\eta\eta}u_e^2}{\nu}$$

hence after some manipulation

$$(\bar{u}\bar{T})_\zeta + (\bar{w}\bar{T})_\eta = \frac{1}{Pr}\bar{T}_{\eta\eta} \qquad (5.6)$$

Multiplying (5.4) by $f'(\bar{u})$ and (5.5) by $f(u)$ and adding, where $f(u)$ is an arbitrary function with the condition $f(1) = 0$ we obtain

$$(\bar{u}f)_\zeta + (\bar{w}f)_\eta = \frac{u_e}{u_e}x\,f'(\bar{u})(1-\bar{u}^2) + f'(\bar{u})\frac{\partial^2 \bar{u}}{\partial \eta^2}$$

and upon integration with respect to $\eta = 0 \rightarrow \infty$ we obtain

$$\frac{d}{d\zeta}\int_0^\infty \bar{u}f(\bar{u})d\eta = \frac{u_e}{u_e}x\int_0^\infty f'(\bar{u})(1-\bar{u}^2)d\eta - f'(0)\left.\frac{\partial \bar{u}}{\partial \eta}\right|_0 - \int_0^\infty f''(\bar{u})\left(\frac{\partial \bar{u}}{\partial \eta}\right)^2 d\eta \qquad (5.7)$$

We notice if $f(\bar{u}) = (1-\bar{u})$ the momentum integral equation is obtained. Dorodnitsyn represents the reciprocal velocity shear rate by

$$\left.\begin{aligned} \Phi &= \frac{1}{\frac{\partial \bar{u}}{\partial \eta}} = \frac{1}{1-\bar{u}}\sum_{i=0}^{k-1} a_i \bar{u}^i \\ \text{and} \quad \frac{1}{\Phi} &= (1-\bar{u})\sum_{i=0}^{k-1} b_i \bar{u}^i \end{aligned}\right\} \qquad (5.8)$$

Substitution of (5.8) into (5.7) with $f_i(u) = (1-u)^i$, $i = 1, n-1$ results in a set of n ordinary differential equations which can be solved to give a_i

$$\frac{d}{d\zeta}\int_0^1 \phi\bar{u}(1-\bar{u})^i d\bar{u} = -i\frac{u_e x}{u_e}\int_0^1 \phi(1-\bar{u})^{i-1}(1-\bar{u}^2)\,d\bar{u} + \frac{i(1-\bar{u})^{i-1}}{\phi(0)} - i(i-1)\int_0^1 \frac{(1-\bar{u})^{i-2}}{\phi}\,d\bar{u} \qquad (5.9)$$

Similarly multiplying (5.6) by the arbitrary function $g(u)$ and (5.4) by $g'(\bar{u})\bar{T}$ and adding, we obtain

$$(g\bar{u}\bar{T})_\zeta + (g\bar{u}\bar{T})_\eta = \frac{u_e}{u_e}\zeta(1-\bar{u}^2)Tg'(\bar{u}) + Tg'(\bar{u})\frac{\partial^2\bar{u}}{\partial\eta^2} + \frac{1}{Pr}g(\bar{u})T_{\eta\eta}$$

with the restriction $g(1) = 0$ as for f, and integrating from $\eta = 0 \rightarrow \infty$ we obtain

$$\frac{d}{d\zeta}\int_0^1 g\bar{u}\bar{T}\phi\,d\bar{u} = \frac{u_e}{u_e}\zeta\int_0^1 (1-\bar{u}^2)\,g'\bar{T}\phi\,d\bar{u} - (1+1/Pr)\int_0^1 \frac{g'\bar{T}'}{\phi}\,d\bar{u} - \frac{1}{Pr}\frac{g(0)T'(0)}{\phi(0)} \qquad (5.10)$$

a power series is also chosen for $\bar{T}$ i.e.

$$\bar{T} = \sum_{i=0}^{l-1} t_i\bar{u}^i \quad \text{and letting} \quad g_i(\bar{u}) = (1-\bar{u})^i$$

with $i = o \rightarrow l$ produces l ordinary differential equations which can be solved to give t_i

We shall consider now the flow under a velocity gradient $u_e \alpha x^m$, and under such conditions and unit Prandtl number, equations (5.9) and (5.10) can be reduced to a set of nonlinear algebraic equations for the variables a_i & t_i. The algebra involved is very lengthy and will not be included here but the results obtained for Stanton number and skin friction are shown in fig. 5.1 for various order solutions (n, l), the abscissa is the parameter

$$\beta = \frac{2m}{m+1}$$

We see the skin friction predictions are highly accurate for $n \geqslant 2$ in the favourable region and for $n \geqslant 4$ in the adverse. The Stanton number predictions do not give sufficiently improved accuracy over flat plate closure until at least a (5,5) order model is chosen.

However the heat transfer results are still promising and further study of this technique, particularly in the turbulent flow regime, where similar equations can be derived for the momentum equation, if the Von Karman mixing length hypothesis (Schlichting, ref. (6)) is used.

In three dimensions, the effect of cross flow on the turbulent boundary layer heat transfer rates should be considered. Initially empirical profiles of Mager, ref. (52) or Johnston, ref. (53) could be used, to assess the validity of the zero crossflow assumption. Also in such flows the transition onset location will have to be described. For the case of transition caused by attachment line contamination, then once the attachment line transition onset location is specified the analysis of Poll, ref. (71) could be used to trace the onset over the remainder of the windward surface, on bodies with near conical inviscid surface pressure fields. Axisymmetric intermittency distributions γ_{int}, derived by Chen and Thyson, ref. (45) would have to be assumed since no 3-dimensional analyses have been attempted.

Conclusions

We have more than demonstrated the ability of the energy integral equation to predict heat transfer rates as accurately as the momentum integral equation can skin friction. Further, the use of flat plate closures proves satisfactory for engineering design purposes in severe pressure and wall temperature distribution flows. We have also shown the alternative heat transfer prediction technique of assuming a simple Reynolds analogy factor coupled with the momentum integral equation is completely unsatisfactory except for very mild pressure distributions over very cold isothermal walls. In particular we derived analytic solutions for skin friction and heat transfer rates for particular types of pressure and wall temperature distribution incompressible flows. These approximate solutions are compared with exact boundary layer solutions to reveal overall trends in the accuracy of the flat plate closure approach, these being under predictions in favourable pressure gradient flows and over predictions in adverse pressure gradient flows. In compressible flows the momentum integral equation can only be integrated analytically for isothermal or adiabatic wall conditions, a requirement not necessary for the energy equation. The analysis showed the method best predicts accelerating flows in cold wall conditions which are underpredictions, but in decelerating flows where over predicts result, hot wall conditions produce the best agreement. The results also demonstrate the improved accuracy the flat plate closure technique obtains in turbulent boundary layers where profile shapes are less sensitive to pressure gradients. Even in the case of shock boundary layer interactions meaningful results were obtained, particularly for heat transfer data, where the energy integral equation is unaffected by the normal pressure gradient unlike the momentum integral equation which requires the additional assumption of a zero normal to the wall pressure gradient in its derivation. The other main disadvantage of the momentum equation over the energy equation being its singular nature at separation.

We have also demonstrated the ability of the flat plate closure technique to flag separation conditions using simple criteria based on boundary layer thickness and local boundary layer edge velocity gradient in both laminar and turbulent flows.

The use of pressure gradient closure has been investigated for laminar flows and improved heat transfer predictions were obtained in blunt body flows. Also we demonstrated the application of intermittency distributions for the prediction of time averaged heat transfer rates inthe transitional regime of a boundary layer. On the blunt cone flows the total heat transfer rate to the body is fairly insensitive to transition location, but the local peak heating rates obtained towards the rear of the transition region decreases rapidly as transition onset moves away from the stagnation point.

In three dimensional flows, the sharp cone plane of symmetry comparison shows the influence of the crossflow in the boundary layer on the heat transfer and skin friction coefficients. These increase with both wall to total temperature ratio and with boundary layer edge Mach number. The blunt cone comparison agree well with experiment, and again the crossflow is shown to have an important influence on the heating rates quite close to the sphere cone junction at moderate incidences (>10 deg).

Appendix A

Laminar stagnation point boundary layer thicknesses

In blunt body flows the problem of determining the stagnation point momentum and enthalpy thicknesses has first to be overcome before their growth can be predicted.

Consider a spherically blunted nose, radius Rn , assuming a linear growth of boundary layer edge velocity with surface distance in the stagnation point region, i.e.

$$\frac{ue}{u_\infty} = \frac{\bar{u}x}{R_n} \quad \& \quad r/R_n = \sin(x/Rn)$$

then in the limit as $x \longrightarrow 0$ equations (1.1.6) and (1.1.8) become using (2.5.3) and (2.5.4)

$$\left.\frac{d\vartheta}{dx}\right|_{x\to 0} + \frac{(Hi\frac{Tw}{Toe}+3)\vartheta}{x} + \frac{\vartheta}{\varrho_e}\frac{d\varrho_e}{dx} = \frac{2f''^2(o)}{1+m(2Hi\frac{Tw}{Toe}+3)}\frac{\varrho_w\mu_w}{\varrho_{oe}\mu_{oe}}\frac{\mu_{oe}Rn}{\varrho_{oe}\bar{u}x\Gamma}$$

$$\left.\frac{d\Gamma}{dx}\right|_{x\to 0-} + \frac{2\Gamma}{x} + \frac{\Gamma}{\varrho_e}\left.\frac{d\varrho_e}{dx}\right|_{x\to 0} = \frac{2s'^2(o)}{(1+m)Pr^2}\frac{\varrho_w\mu_w}{\varrho_{oe}\mu_{oe}}\frac{\mu_{oe}Rn}{\varrho_{oe}\bar{u}x\Gamma}$$

thus from this we obtain

$$\left.\frac{d(x\vartheta^2)}{dx}\right|_{x\to 0} = \frac{2f''^2(o)\frac{\varrho_w\mu_w}{\varrho_{oe}\mu_{oe}}\frac{\mu_{oe}Rn}{\varrho_{oe}\bar{u}}}{\left[1+m(2Hi\frac{Tw}{Toe}+3)\right](Hi\frac{Tw}{Toe}+3)} = \vartheta^2_{x=0} \qquad (A1)$$

$$\left.\frac{d(x\Gamma^2)}{dx}\right|_{x\to 0} = \frac{s'^2(o)}{(1+m)Pr^2}\frac{\varrho_w\mu_w}{\varrho_{oe}\mu_{oe}}\frac{\mu_{oe}Rn}{\varrho_{oe}\bar{u}} = \Gamma^2_{x=0} \qquad (A2)$$

with $m = 1/3$ at the stagnation point.

Appendix B

Derivation of the rate of strain tensor in orthogonal curvilinear coordinates

In Cartesian coordinates the gradient of a vector tensor can be expressed

$$\nabla \underset{\sim}{u} = \frac{\partial}{\partial x_i}(u_j \underset{\sim}{e}_j)\underset{\sim}{e}_i = \frac{\partial u_j}{\partial x_i}\underset{\sim}{e}_i\underset{\sim}{e}_j$$

Thus the symmetric rate of strain tensor follows:

$$D = \nabla \underset{\sim}{u} + \nabla \underset{\sim}{u}^T = \left(\frac{\partial u_j}{\partial x_i} + \frac{\partial u_i}{\partial x_j}\right)\underset{\sim}{e}_i\underset{\sim}{e}_j$$

In curvilinear coordinate this is not so straight forward since

$$\nabla \underset{\sim}{u} = \frac{1}{h_i}\frac{\partial}{\partial x_i}(u_j \underset{\sim}{e}_j)\underset{\sim}{e}_i = \frac{1}{h_i}\frac{\partial u_j}{\partial x_i}\underset{\sim}{e}_i\underset{\sim}{e}_j + \frac{u_j}{h_i}\frac{\partial \underset{\sim}{e}_j}{\partial x_i}\underset{\sim}{e}_i$$

Using the results of Appendix C for $\underset{\sim}{e}_{j,i}$ we arrive at

$$\nabla \underset{\sim}{u} = \begin{bmatrix} \frac{u_{1,1}}{h_1} + \frac{h_{1,2}u_2}{h_1h_2} + \frac{h_{1,3}u_3}{h_1} & \frac{u_{1,2}}{h_2} - \frac{h_{2,1}u_2}{h_1h_2} & u_{3,3} \\ \frac{u_{2,1}}{h_1} - \frac{h_{1,2}u_1}{h_1h_2} & \frac{u_{2,2}}{h_2} + \frac{h_{2,1}u_1}{h_1h_2} + \frac{h_{2,3}u_3}{h_2} & u_{3,3} \\ \frac{u_{3,1}}{h_1} - \frac{h_{1,3}u_1}{h_1} & \frac{u_{3,2}}{h_2} - \frac{h_{2,3}}{h_2}u_2 & u_{3,3} \end{bmatrix}$$

and thus

$$D = \nabla \underset{\sim}{u} + \nabla \underset{\sim}{u}^T$$

Appendix C

Derivation of coordinate line tangent vector derivatives

The acceleration term in the momentum equation (3.2.8) gave rise to terms involving the derivatives of the coordinate line tangent vectors i.e. $\underset{\sim}{e}_{j,j}$ for $i \& j = 1,2,3$. We see from equation (3.2.1) that $\underset{\sim}{e}_{i,3}$ which leaves six further terms.

Consider $\underset{\sim}{e}_{1,1}$ which we can express as a linear combination of the base vectors i.e.

$$\underset{\sim}{e}_{1,1} = A\underset{\sim}{e}_1 + B\underset{\sim}{e}_2 + C\underset{\sim}{e}_3$$

taking the scalar product with $\underset{\sim}{e}_1$ we get $\underset{\sim}{e}_1 . \frac{\partial \underset{\sim}{e}_1}{\partial x_1} = A$

or $\frac{1}{2}\frac{\partial}{\partial x_1}(\underset{\sim}{e}_1 . \underset{\sim}{e}_1) = A \quad \Longrightarrow \quad A = 0$

hence we can say $\underset{\sim}{e}_{1,1} = B\underset{\sim}{e}_2 + C\underset{\sim}{e}_3$

where $B = \underset{\sim}{e}_2 . \underset{\sim}{e}_{1,1}$, $C = \underset{\sim}{e}_3 . \underset{\sim}{e}_{1,1}$

but since $\frac{\partial}{\partial x_1}(\underset{\sim}{e}_1 . \underset{\sim}{e}_2) = 0$ then $\underset{\sim}{e}_2 . \underset{\sim}{e}_{1,1} = - \underset{\sim}{e}_1 . \underset{\sim}{e}_{2,1}$

and similarly $\underset{\sim}{e}_3 . \underset{\sim}{e}_{1,1} = - \underset{\sim}{e}_1 . \underset{\sim}{e}_{3,1}$

therefore $e_{1,1} = -(e_1 . e_{2,1})\underset{\sim}{e}_2 - (e_1 . e_{3,1})\underset{\sim}{e}_3$ (C1)

since $\underset{\sim}{r}_{,i} = h_i \underset{\sim}{e}_i$

then $\underset{\sim}{r}_{,12} = h_1 \underset{\sim}{e}_{1,2} + h_{1,2}\underset{\sim}{e}_1 = \underset{\sim}{r}_{,21} = h_2 \underset{\sim}{e}_{2,1} + h_{2,1}\underset{\sim}{e}_2$ (C2)

taking the scalar product with $\underline{e}_1$ we get $h_1\underline{e}_1\underline{e}_{1,2} + h_{1,2} = h_2\underline{e}_1\cdot\underline{e}_{2,1}$

but $\underline{e}_1\,\underline{e}_{1,2} = 0$ so $\underline{e}_1\cdot\underline{e}_{2,1} = \frac{1}{h_2}h_{1,2}$ (C3)

and similarly

$$\underline{e}_1\cdot\underline{e}_{3,1} = \frac{1}{h_3}h_{1,3}$$

substituting these into equation (C1) gives

$$e_{1,1} = -\frac{1}{h_2}h_{1,2}\,\underline{e}_2 - \frac{1}{h_3}h_{1,3}\,\underline{e}_3$$

Now consider $\underline{e}_{1,2}$ which by using a similar method as for the previous case we find

$$\underline{e}_{1,2} = (\underline{e}_2\cdot\underline{e}_{1,2})\underline{e}_2 + (\underline{e}_3\cdot\underline{e}_{1,2})\underline{e}_3 \qquad (C4)$$

taking the scalar product of equation (C2) with $\underline{e}_2$ we get

$$h_1\underline{e}_2\cdot\underline{e}_{1,2} = h_2\,\underline{e}_2\,\underline{e}_{2,1} + h_{2,1}$$

hence since $\underline{e}_2\cdot\underline{e}_{2,1} = 0$ $\underline{e}_2\cdot\underline{e}_{1,2} = \frac{1}{h_1}h_{2,1}$ (C5)

Now take the scalar product of equation (C2) with $\underline{e}_3$

$$h_1\underline{e}_3\cdot\underline{e}_{1,2} = h_2\underline{e}_3\cdot\underline{e}_{2,1} +$$

$\therefore$ either $\underline{e}_3$ is perpendicular to $\underline{e}_{1,2}$ or

$$\underline{e}_{1,2} = \frac{h_2}{h_1}\underline{e}_{2,1} \quad \text{thus} \quad \underline{e}_1\cdot\underline{e}_{1,2} = \frac{h_2}{h_1}\underline{e}_1\cdot\underline{e}_{2,1} \Longrightarrow$$

$\underline{e}_1\cdot\underline{e}_{2,1} = 0$ which contradicts equation (C3) so we must assume $\underline{e}_3$ perpendicular to $\underline{e}_{1,2}$ and equation (C4) becomes using equation (C5)

$$e_{1,2} = \frac{1}{h_1}h_{2,1}$$

The remaining 4 terms follow by symmetry, summarising we have

$$\underline{e}_{1,1} = -\frac{1}{h_2}h_{1,2}\,\underline{e}_2 - \frac{1}{h_3}h_{1,3}\underline{e}_3 \qquad e_{1,2} = \frac{1}{h_1}h_{2,1}\underline{e}_2$$

$$\underline{e}_{2,1} = \frac{1}{h_2} h_{1,2} \underline{e}_1 \qquad \underline{e}_{2,2} = -\frac{1}{h_1} h_{2,1} \underline{e}_1 - \frac{1}{h_3} h_{2,3} \underline{e}_3$$

$$\underline{e}_{3,1} = \frac{1}{h_3} h_{1,3} \underline{e}_1 \qquad \underline{e}_{3,2} = \frac{1}{h_3} h_{2,3} \underline{e}_2$$

Appendix D

Calculation of a surface mesh over a blunt body for boundary layer computations

The method described here is that of Blottner and Ellis, ref. (59). Consider figure D1 where a line BB' is drawn parallel to the main axis AA' of the body but passing through the stagnation point (S). Planes are then generated that contain this line and make an angle with the vertical. The intersection of these planes with the surface is the coordinate direction x_1 , and x_2 is defined so as to make the system orthogonal. The position vector on the surface $\underset{\sim}{r}$ is given by

$$\underset{\sim}{r} = x\,\underset{\sim}{i} + r\sin\bar{\varphi}\,\underset{\sim}{j} + r\cos\bar{\varphi}\,\underset{\sim}{k}$$

Hence the x_1 & x_2 coordinate tangent vectors $\underset{\sim}{e}_1$ & $\underset{\sim}{e}_2$ given by

$\left.\frac{\partial r}{\partial x_1}\right|_{x_2}$ & $\left.\frac{\partial r}{\partial x_2}\right|_{x_1}$ respectively are

$$\underset{\sim}{e}_1 = \frac{\partial x}{\partial x_1}\underset{\sim}{i} + (\sin\bar{\varphi}\,\underset{\sim}{j} + \cos\bar{\varphi}\,\underset{\sim}{k})\frac{\partial r}{\partial x_1}$$

$$\underset{\sim}{e}_2 = \frac{\partial x}{\partial x_2}\underset{\sim}{i} + (\frac{\partial r}{\partial x_2}\sin\bar{\varphi} + r\cos\bar{\varphi}\frac{\partial\bar{\varphi}}{\partial x_2})\underset{\sim}{j}$$

$$+ (\frac{\partial r}{\partial x_2}\cos\bar{\varphi} - r\sin\bar{\varphi}\frac{\partial\bar{\varphi}}{\partial x_2})\underset{\sim}{k}$$

for convenience we assume $x_2 = \bar{\varphi}$

the condition of orthogonality $\underset{\sim}{e}.\underset{\sim}{i} = 0$ then yeilds

$$\frac{\partial x}{\partial x_1}\frac{\partial x}{\partial x_2} + \frac{\partial r}{\partial x_1}\frac{\partial r}{\partial x_2} = 0 \qquad \text{(D1)}$$

but since

$$\frac{\partial x}{\partial x_1} = \left.\frac{\partial x}{\partial r}\right|_{x_2}\left.\frac{\partial r}{\partial x_1}\right|_{x_2} \qquad \text{(D2)}$$

and $$\left.\frac{\partial x}{\partial x_2}\right|_{x_1} = \left.\frac{\partial x}{\partial x_2}\right|_{r} + \left.\frac{\partial x}{\partial r}\right|_{x_2}\left.\frac{\partial r}{\partial x_2}\right|_{x_1}$$

we obtain

$$\left.\frac{\partial r}{\partial x_2}\right|_{x_1} = \frac{-\left.\frac{\partial x}{\partial r}\right|_{x_2}\left.\frac{\partial x}{\partial x_2}\right|_{r}}{1+\left(\left.\frac{\partial x}{\partial r}\right|_{x_2}\right)^2} \qquad \text{(D3)}$$

$\left.\frac{\partial x}{\partial r}\right|_{x_2}$ & $\left.\frac{\partial x}{\partial x_2}\right|_{r}$ can be calculated for a given (x,r) location from the surface geometry inputted either numerically or analytically. Using a finite difference representation the mesh is then generated in an x_1-direction with successive x_2 sweeps. Firstly the plane of symmetry $x_2 = 0$ (or $j=1$) coordinate, see fig. D2, is calculated from

$$\delta x_1^2 = \delta r^2 + \delta x^2$$

or

$$\left(\frac{\delta x_1}{\delta r}\right)^2 = 1 + \left(\frac{\partial x}{\partial r}\right)^2_{x_2=0}$$

thus using finite difference representation

$$r_{i+1\,1} - r_{i1} = \delta x_{1_i} / \sqrt{1+\left(\left.\frac{\partial x}{\partial r}\right|_{i+1/2\;1}\right)^2} \qquad \text{(D4)}$$

and consequently

$$(x_{i+1\,1} - x_{i1}) = (r_{i+1\,1} - r_{i1})\left.\frac{\partial x}{\partial r}\right|_{i+1/2\,1} \qquad \text{(D5)}$$

where $\left.\frac{\partial x}{\partial r}\right|_{i+1/2\,1}$ is evaluated at $x = \frac{(x_{i+1\,1} + x_{i1})}{2}$, $\bar{\varphi} = 0$

equations (D4) and (D5) are used iteratively until satisfactory convergence of $x_{i+1\,1}$ is acheived.

Moving off the plane of symmetry in the x_2-direction equation (D3) is employed to obtain $\left.\frac{\partial r}{\partial x_2}\right|_{i+1/2\;j+1/2}$ where

$$\left.\frac{\partial r}{\partial x_2}\right|_{i+1\ j+1/2} = \frac{r_{i+1\ j+1} - r_{i+1\ j}}{\delta x_{2j}}$$

Combining equations (D1) and (D2) we obtain

$$\left.\frac{\partial x}{\partial x_2}\right|_{i+1\ j+1/2} = -\left(\frac{\partial r}{\partial x_2} \Big/ \frac{\partial x}{\partial r}\right)\Bigg|_{i+1\ j+1/2} \qquad \text{(D6)}$$

thus giving

$$(x_{i+1\ j+1} - x_{i+1\ j}) = \delta x_{2j} \left.\frac{\partial x}{\partial x_2}\right|_{i+1\ j+1/2}$$

Thus in a similar way equations (D3) and (D6) are iterated until convergence of $x_{i+1\ j+1}$ & $r_{i+1\ j+1}$ is achieved.

For the case of an axisymmetric body, see fig. D3, the surface is defined by $R = f(z)$ where R is the axisymmetric radius and the axial distance from the apex. Thus from the trigonometric cosine rule we have

$$R^2 = \beta^2 + r^2 + 2\beta r \cos\bar{\varphi}$$

where β is the distance of the stagnation point from the axis of symmetry and thus

$$\left.\frac{\partial R}{\partial r}\right|_{x_2} = \frac{r + \beta\cos\bar{\varphi}}{R}$$

$$\left.\frac{\partial R}{\partial x_2}\right|_{r} = \frac{-\beta r \sin\bar{\varphi}}{R}$$

hence

$$\left.\frac{\partial x}{\partial r}\right|_{x_2} = \frac{r + \beta\cos\bar{\varphi}}{R}\frac{dz}{dR} \qquad \text{(D7)}$$

$$\left.\frac{\partial x}{\partial x_2}\right|_{r} = -\frac{\beta r \sin\bar{\varphi}}{R}\frac{dz}{dR} \qquad \text{(D8)}$$

Hence we see that a mesh can be generated over a general axisymmetric shape, once the geometry $R = f(z)$ is defined. The computer coding for this mesh generation is written in such a way that the above gradients equations (D7) and (D8) are calculated in a subroutine. Two such subroutines have been developed, one for blunted cones, where equations (D7) and (D8) are calculated analytically, the second for a general axisymmetric shape, where equations (D7) and (D8) are calculated from cubic spline segments fitted between the inputted data points.

i.e. in the region $z_{i-1} \rightarrow z_i$

$$y = A + B\bar{z} + C\bar{z}^2 + D\bar{z}^3$$

where

$$\bar{z} = \frac{z - z_{i-1}}{z_i - z_{i-1}}$$

$$A = y_{i-1}$$

$$B = \left.\frac{dy}{dz}\right|_{i-1}$$

$$C = 3(y_i - y_{i-1}) - 2\left.\frac{dy}{dz}\right|_{i-1} - \left.\frac{dy}{dz}\right|_i$$

$$D = \left.\frac{dy}{dz}\right|_i + \left.\frac{dy}{dz}\right|_{i-1} + 2(y_{i-1} - y_i)$$

The gradients $\left.\frac{dy}{dz}\right|_i$ are calculated from the second order finite difference equation

$$\left.\frac{dy}{dz}\right|_i = \frac{((z_i - z_{i-1})^2 y_{i+1} - ((z_i - z_{i-1})^2 - (z_{i+1} - z_i)^2) y_i - (z_{i+1} - z_i)^2 y_{i-1})}{(z_i - z_{i-1})(z_{i+1} - z_i)(z_{i+1} - z_{i-1})}$$

However the cubic spline representation has to be modified in the axisymmetric origin region since $\left.\frac{dy}{dz}\right|_{z\to 0} \longrightarrow \infty$

We use $$y^2 = 2Az + Bz^2$$

where $$\begin{pmatrix} 1 & z_2 \\ 2z_2 & z_2^2 \end{pmatrix} \begin{pmatrix} A \\ B \end{pmatrix} = \begin{pmatrix} y_2 \left.\frac{dy}{dz}\right|_i \\ y_2^2 \end{pmatrix}$$

To calculate the metric coefficients for the coordinate system consider the incremental distance travelled along the surface.

$$\delta s^2 = \delta x^2 + \delta r^2 + r^2 \delta \bar{\varphi}^2$$

Thus using a finite difference representation we obtain expressions for the x_1 & x_2 metrics h_1 & h_2 respectively

$$h1_{ij}^2 (x1_{i+1} - x1_i)^2 = (x_{i+1\,j} - x_{ij})^2 + (r_{i+1\,j} - r_{ij})^2 \qquad \text{(D9)}$$

and

$$h2_{ij}^2 (x2_{j+1} - x2_j)^2 = (x_{ij+1} - x_{ij})^2 + (r_{ij+1} - r_{ij})^2 + \frac{(r_{ij+1}+r_{ij})^2}{4}(x2_{j+1} - x2_j)^2 \qquad \text{(D10)}$$

Finally by making $\delta x_1 = \delta s$ on the plane of symmetry we have $h1_{i1} = 1$.

It is anticipated that the 3-D boundary layer code will be used with a simple pressure prediction method such as Modified Newtonian. Thus it is necessary to calculate the local streamwise direction from this pressure distribution. We have chosen here to use the method of steepest descent, ref. (50) which gives an equation for the surface streamline direction $\underset{\sim}{\lambda}$ thus

$$\underset{\sim}{\lambda} \cdot (\underset{\sim}{\Omega} \wedge \underset{\sim}{V}_\infty) = 0 \qquad \text{(D11)}$$

where $\underset{\sim}{n}$ is the surface normal, $\underset{\sim}{V}_\infty$ the free stream direction. We shall use the notation $\underset{\sim}{e}_1$, $\underset{\sim}{e}_2$ for the coordinate tangent vectors $\frac{\underset{\sim}{s}}{|\underset{\sim}{s}|}$ & $\frac{\underset{\sim}{t}}{|\underset{\sim}{t}|}$ respectively and let $\underset{\sim}{e}_3 = \underset{\sim}{n}$, thus $\underset{\sim}{e}_3 = \underset{\sim}{e}_1 \wedge \underset{\sim}{e}_2$ i.e.

$$\underset{\sim}{e}_1 = \left(\frac{\partial x}{\partial x_1}\underset{\sim}{i} + \sin\bar{\varphi}\frac{\partial r}{\partial x_1}\underset{\sim}{j} + \cos\bar{\varphi}\frac{\partial r}{\partial x_1}\underset{\sim}{k}\right) \Big/ |\underset{\sim}{s}|$$

$$\underset{\sim}{e}_2 = \left(\frac{\partial x}{\partial x_2}\underset{\sim}{i} + \left(\frac{\partial r}{\partial x_2}\sin\bar{\varphi} + r\cos\bar{\varphi}\right)\underset{\sim}{j} + \left(\frac{\partial r}{\partial x_2}\cos\bar{\varphi} - r\sin\bar{\varphi}\right)\underset{\sim}{k}\right)/|\underset{\sim}{t}|$$

$$\underset{\sim}{e}_3 = \underset{\sim}{e}_1 \wedge \underset{\sim}{e}_2$$

or for short hand $\underset{\sim}{e}_i = (e_{i1}, e_{i2}, e_{i3}) \qquad i = 1,2,3$

The freestream flow direction is

$$\frac{\underset{\sim}{V}_\infty}{|\underset{\sim}{V}_\infty|} = \cos\alpha\,\underset{\sim}{i} - \sin\alpha\,\underset{\sim}{k}$$

or

$$\frac{\underset{\sim}{V}_\infty}{|\underset{\sim}{V}_\infty|} = \sum_{i=1}^{3}(\cos\alpha\, e_{i1} - \sin\alpha\, e_{i3})\underset{\sim}{e}_i$$

which we write

$$\frac{\underset{\sim}{V}_\infty}{|\underset{\sim}{V}_\infty|} = v_1\underset{\sim}{e}_1 + v_2\underset{\sim}{e}_2 + v_3\underset{\sim}{e}_3$$

thus we see

$$\underset{\sim}{e}_3 \wedge \frac{\underset{\sim}{V}_\infty}{|\underset{\sim}{V}_\infty|} = -v_2\underset{\sim}{e}_1 + v_1\underset{\sim}{e}_2$$

and using equation (D11)

$$(\lambda_1\underset{\sim}{e}_1 + \lambda_2\underset{\sim}{e}_2).\ \underset{\sim}{N} \wedge \frac{\underset{\sim}{V}_\infty}{|\underset{\sim}{V}_\infty|} = 0$$

$$\Rightarrow \qquad \tan\psi = \frac{\lambda_2}{\lambda_1} = \frac{v_2}{v_1} \tag{D12}$$

where ψ is the angle between the streamline and the x_1-coordinate direction.

Appendix E

Details of the KHOMP2D axisymmetric/2-D boundary layer code

The KHOMP2D code used in the comparisons of the flat plate and pressure gradient closure method with experiment, solves the integral momentum and energy equations (1.2.6) and (1.2.8) using an Euler predictor-trapezoidal corrector method, with a step length halving convergence check. Inviscid pressure data is inputted at known locations, between which linear interpolations are employed. The start up procedure for the program is in three modes.

1) The integral thicknesses are inputted at the start position, for use when comparing with experimental data, where the virtual origin is not known.

2) A pointed nose start

3) A blunted nose laminar start.

In the second and third case the equations are solved in the form

$$\frac{d}{dx}(r\vartheta^{(\alpha+1)/\alpha}) = f(\vartheta, u_e, \rho_e, r)$$

$$\frac{d(r\Gamma^{(\alpha+1)/\alpha})}{dx} = g(\Gamma, u_e, \rho_e, r)$$

with $\alpha=1$ for laminar flow and $\alpha=4$ for turbulent flow. This avoids the singular behaviour and stability problems that arise in this region.

Appendix F

Coefficients for the 3-dimensional integral equations

The terms in the integral equations (3.3.8), (3.3.9) and (3.3.10) are listed below.

$$F_{11} = (b_{11} + \bar{\vartheta}_{sn} b_{12} + \bar{\vartheta}_{ns} b_{13} + \bar{\vartheta}_{nn} b_{14} + 2Fq_{11} Q_1/\bar{\vartheta}_{ss})/h_1$$

$$F_{12} = (b_{12} P_1 + b_{13} P_3 + b_{14}(2P_5 G + P_6 Q_1))\bar{\vartheta}_{ss}/h_1$$

$$F_{13} = (b_{21} + \bar{\vartheta}_{sn} b_{22} + \bar{\vartheta}_{ns} b_{23} + \bar{\vartheta}_{nn} b_{24} + 2Fq_{13} Q_1/\bar{\vartheta}_{ss})h_2$$

$$F_{14} = (b_{22} P_1 + b_{23} P_3 + b_{24}(2P_5 G + P_6 Q_1))\bar{\vartheta}_{ss}/h_2$$

$$F_{21} = (b_{31} + \bar{\vartheta}_{sn} b_{32} + \bar{\vartheta}_{ns} b_{33} + \bar{\vartheta}_{nn} b_{34} + 2Fq_{21} Q_1/\bar{\vartheta}_{ss})/h_1$$

$$F_{22} = (b_{32} P_1 + b_{33} P_3 + b_{34}(2P_5 G + P_6 Q_1))\bar{\vartheta}_{ss}/h_1$$

$$F_{23} = (b_{41} + \bar{\vartheta}_{sn} b_{42} + \bar{\vartheta}_{ns} b_{43} + \bar{\vartheta}_{nn} b_{44} + 2Fq_{23} Q_1/\bar{\vartheta}_{ss})/h_2$$

$$F_{24} = (b_{42} P_1 + b_{43} P_3 + b_{44}(2P_5 G + P_6 Q_1))\bar{\vartheta}_{ss}/h_2$$

$$F_{31} = (\cos\psi - \bar{\Gamma}_n \sin\psi)/h_1$$

$$F_{32} = -\Gamma_s \sin\psi (P_8 + Pr^{1/3} P_9)/h_1$$

$$F_{33} = (\sin\psi + \Gamma_n \cos\psi)/h_2$$

$$F_{34} = \Gamma_s \cos\psi (P_8 + Pr^{1/3} P_9)/h_2$$

$$Fq_{11} = (b_{12} P_2 + b_{13} P_4 + b_{14}(2P_7 Q_1 + G P_6))$$

$$Fq_{13} = (b_{22} P_2 + b_{23} P_4 + b_{24}(2P_7 Q_1 + G P_6))$$

$$Fq_{21} = (b_{32} P_2 + b_{33} P_4 + b_{34}(2P_7 Q_1 + G P_6))$$

$$Fq_{23} = (b_{42} P_2 + b_{43} P_4 + b_{44}(2P_7 Q_1 + G P_6))$$

$$Fq_{31} = -\Gamma_s (\sin\psi (P_{10} + Pr^{1/3} P_{11}))/h_1$$

$$Fq_{32} = \Gamma_s (\cos\psi (P_{10} + Pr^{1/3} P_{11}))/h_2$$

$$Res_1 = \frac{Cfe_1}{2} - \vartheta_{ss}\Bigg[\frac{\bar{\vartheta}_{11}}{h_1}\left(\frac{1}{\varrho_e}\frac{\partial \varrho_e}{\partial x_1} + \frac{2}{v_e}\frac{\partial v_e}{\partial x_1}\right) + \bar{\delta}_1\left(\frac{1}{h_1 v_e}\frac{\partial u_{1e}}{\partial x_1} - K_2\frac{u_{2e}}{v_e}\right)$$

$$+ \frac{\bar{\vartheta}_{12}}{h_2}\left(\frac{1}{\varrho_e}\frac{\partial \varrho_e}{\partial x_2} + \frac{2}{v_e}\frac{\partial v_e}{\partial x_2}\right) + \bar{\delta}_2\left(\frac{1}{h_2 v_e}\frac{\partial u_{1e}}{\partial x_2} + K_1\frac{u_{2e}}{v_e}\right)$$

$$- K_1(\bar{\vartheta}_{11} - \bar{\vartheta}_{22}) \quad - K_2(\bar{\vartheta}_{12} + \bar{\vartheta}_{21})$$

$$- \frac{1}{h_1}\frac{\partial \psi}{\partial x_1}(a_{11} + a_{12}\bar{\vartheta}_{sn} + a_{13}\bar{\vartheta}_{ns} + a_{14}\bar{\vartheta}_{nn})$$

$$- \frac{1}{h_2}\frac{\partial \psi}{\partial x_2}(a_{21} + a_{22}\bar{\vartheta}_{sn} + a_{23}\bar{\vartheta}_{ns} + a_{24}\bar{\vartheta}_{nn})\Bigg]$$

$$- \vartheta_{ss}^2\left(\frac{\partial}{\partial x_1}(Q_1/\vartheta_{ss}^2)Fq_{11} + \frac{\partial}{\partial x_2}(Q_1/\vartheta_{ss}^2)Fq_{13}\right)$$

$$Res_2 = \frac{Cfe_2}{2} - \vartheta_{ss}\Bigg[\frac{\bar{\vartheta}_{21}}{h_1}\left(\frac{1}{\varrho_e}\frac{\partial \varrho_e}{\partial x_1} + \frac{2}{v_e}\frac{\partial v_e}{\partial x_1}\right) + \bar{\delta}_1\left(\frac{1}{v_e h_1}\frac{\partial u_{2e}}{\partial x_1} + K_2\frac{u_{1e}}{v_e}\right)$$

$$+ \frac{\bar{\vartheta}_{22}}{h_2}\left(\frac{1}{\varrho_e}\frac{\partial \varrho_e}{\partial x_2} + \frac{2}{v_e}\frac{\partial v_e}{\partial x_2}\right) + \bar{\delta}_2\left(\frac{1}{v_e h_2}\frac{\partial u_{2e}}{\partial x_2} - K_1\frac{u_{1e}}{v_e}\right)$$

$$- K_1(\bar{\vartheta}_{21} + \bar{\vartheta}_{12}) \quad - K_2(\bar{\vartheta}_{22} - \bar{\vartheta}_{11})$$

$$- \frac{1}{h_1}\frac{\partial \psi}{\partial x_1}(a_{31} + a_{32}\bar{\vartheta}_{sn} + a_{33}\bar{\vartheta}_{ns} + a_{34}\bar{\vartheta}_{nn})$$

$$- \frac{1}{h_2}\frac{\partial \psi}{\partial x_2}(a_{41} + a_{42}\bar{\vartheta}_{sn} + a_{43}\bar{\vartheta}_{ns} + a_{44}\bar{\vartheta}_{nn})\Bigg]$$

$$- \vartheta_{ss}^2\left(\frac{\partial}{\partial x_1}(Q_1/\vartheta_{ss}^2)Fq_{21} + \frac{\partial}{\partial x_2}(Q_1/\vartheta_{ss}^2)Fq_{23}\right)$$

References

1. Colburn A.P. — A method of correlating forces convection heat transfer data and a comparison with fluid friction. Transactions of the American Inst. of Chemical Engineers Vol 29 (1933) pp 174-210

2. Cebeci T., Bradshaw P. — Physical and computational aspects of convective heat transfer Springer - Verlag New York (1984)

3. Head M.R. — Entrainment in the turbulent boundary layer ARC R & M 3152 (1958)

4. Englert G.W. — Estimation of compressible boundary layer growth over insulated surfaces with pressure gradient NACA TN 4022 (1957)

5. Hopkins E.J., Inouye M. — An evaluation of theories for predicting turbulent skin friction and heat transfer on flat plates at supersonic and hypersonic mach numbers AIAA J 9 (1971) pp 993-1003

6. Schlichting H. — Boundary Layer theory McGraw-Hill

7. Stollery J.L., Bates L. — Turbulent boundary layer growth at hypersonic speeds JFM 63 part 1 (1974) pp 145-156

8. Eckert E.R.G. — Engineering relations for friction and heat transfer to surfaces in high velocity flows. J Aero. Sci. Vol. 22 p 585

9. Rotta J.C. — A review of experimental temperature distributions in supersonic and hypersonic boundary layers with heat transfer AVA 64 A 10 Gottingen

10. Cohen C.B., Reshotko E. Similar solutions for the compressible laminar boundary layer with heat transfer and pressure gradient.
NACA R1294 (1956)

11. Van Driest E.R. The laminar boundary layer with variable fluid properties.
1954 Meeting of the Heat Transfer and Fluid Mechanics Institute Berkeley

12. Van Driest E.R. The turbulent boundary layer with variable Prandtl no.
50 Jahre Grenzschichtforschung
Ed. H. Gortler, Vieweg Verlag Braunschweig

13. Fernholtz H.H., Finley M.A. A critical commentary on mean flow data for two-dimensional compressible turbulent boundary layers
AGARDograph No. 253 (1980)

14. Falkner V.M, Skan S.W. Some approximate solutions of the boundary layer equations
Phil. Mag. 12 (1931) pp 865-895
or/ ARC R & M 1314 (1930)

15. Fage A., Falkner, V.M. Relations between heat transfer and surface friction for laminar flow
ARC R & M 1408 (1931)

16. Tetervin N. Approximate calculation of Reynolds analogy for turbulent boundary layers with pressure gradient.
AIAA J Vol 7 No 6 (1969) pp 1079-1085

17. Nakayama A., Koyama H., Ohsawa S. Momentum/heat transfer analogy for turbulent boundary layers in mild pressure gradients
AIAA J Vol 22 No 6 (1984) pp 841-846

18. Fernholtz H.H., Finley M.A. A critical compilation of compressible turbulent boundary layer data
AGARDograph 223 (1977)

19. Stollery J.L. — Turbulent boundary layer growth at hypersonic speeds. IC Aero Rep. 73-04 (1973)

20. Thomann H. — Effect of streamwise wall curvature on heat transfer in a turbulent boundary layer. JFM 33 (1968) pp 283-292

21. Hoydysh W.G., Zakkay V. — An experimental investigation of hypersonic turbulent boundary layers in an adverse pressure gradient. AIAA J (1969) pp 105-116

22. Kussoy M.I., Horstman C.C. — An experimental documentation of a hypersonic shock-wave turbulent boundary layer interaction flow - with and without separation. NASA TM X-62, 412

23. Coleman G.T. — Hypersonic turbulent boundary layer studies. IC Aero Ph.D thesis (1973)

24. Green J.E., Weeks D.J., Broman J.W.F., — Prediction of turbulent boundary layers and wakes in compressible flow by a lag-entrainment method. RAE TR72231 (1973)

25. Raven H.C. — Separation criteria for three-dimensional boundary layer calculations. AIAA J Vol 22 No. 4 (1984) pp 554-556

26. Beasley J.A. — Calculation of laminar boundary layers and prediction of transition on a sheared wing. ARC R & M 3787 (1973)

27. Buri A. — A method of calculation for turbulent boundary layers with accelerated and retarded basic flow. MAP RTP Trans 2073

28. Allan W.K. — The continuously critical boundary layer
JFM Vol 15 (1963) pp 251-261

29. Simpson R.L. — Characteristics of a separating incompressible turbulent boundary layer
Flow Separation AGARD-CP-168 (1975)

30. Fay J.A., Riddell F.R. — Theory of stagnation point heat transfer in dissociated air
Jnl Aero Sci Vol 25 (1958) pp 73-85

31. Vaglio-Laurin R. — Laminar heat transfer on three dimensional bluntnosed bodies in hypersonic flow.
ARS J (1959) pp 123-129

32. Widhopf G.F. — Laminar, Transitional and turbulent heat transfer measurements on a yawed blunt conical nosetip
San Bernardino Operations
Aerospace Rep no. TR-0073 (S3450-60)-1

33. Miller III G.M. — Experimental and predicted heating distributions for biconics at incidence in air at mach 10
NASA-TP-2334 (1984)

34. Bushnell D.M., Jones R.A., Huffman J.K. — Heat-transfer and pressure distributions on spherically blunted 25 (deg) half-angle cone at mach 8 and angles of attack up to 90 (deg)
NASA TN D-4792

35. Holden M.S. — Studies of potential fluid mechanical mechanisms for enhanced stagnation-region heating
AIAA 20th Thermophysics conf.
Williamsburg, VA June 1985
paper AIAA-85-1002

36. Wilson R.E.
Laminar boundary layer growth on slightly blunted cones at hypersonic speeds
J. Spacecraft Vol. 2 No. 4 (1965) pp 490-496

37. Billig F.S.
Shockwave shapes around spherical and cylindrical-nosed bodies.
J. Spacecraft Vol. 4 No. 6 (1967) pp 822-823

38. Linnell R.D., Bailey J.Z.
Similarity-rule estimation methods for cones and parabolic noses
J. Aero. Sci. (1956) pp 796-797

39. Verner, M.D., Adams J.C.
Specific thermal analyzer program for high-temperature resistant transparencies for high speed aircraft (STAPAT) Vol. 1, Methodology
AFWAL TR-84-3086 (1984)

40. Whitfield J.D., Dougherty N.S.
A survey of transition research at AEDC
AGARD CP-224 Laminar-Turbulent Transition Tech. Univ. of Denmark May (1977)

41. Morkovin M.V.
Critical evaluation of transition from laminar to turbulent shear layers with emphasis on hypersonically travelling bodies.
AFFDL-TR-68-149 March (1969)

42. Emmons H.W.
The laminar turbulent transition in a boundary layer - part 1
J. Aero. Sci. Vol. 18 No. 7 (1951) pp 490-498

43. Dhawan S., Narashima R.
Some properties of boundary layer flow during the transition from laminar to turbulent motion.
JFM Vol. 3 (1958) pp 418-436

44 Elder J.
An experimental investigation of turbulent spots and breakdown to turbulence
JFM Vol. 9 (1960) pp 235-246

45. Chen K.K., Thyson N.A. Extension of Emmons' spot theory to flows on blunt bodies
AIAA J Vol. 9 No. 5 (1971) pp 821-825

46. Poll D.I.A. Private communication

47. Stewartson K. The theory of laminar boundary layers in compressible fluids
Oxford Clarendon Press

48. Hayes W.D. The three-dimensional boundary layer
NAVORD Rep. 1313 (Nots 384)
U.S. Naval Ord. Test Station
Inyoken China Lake, California (1951)

49. Cooke, J.C. An axially symmetric analogue for general three-dimensional boundary layers
ARC R & M 3200 (1961)

50. Leigh D.C., Ross B.B. Surface geometry of three-dimensional inviscid hypersonic flows
AIAA J Vol. 7 No. 1 (1969)

51. Cooke J.C. The boundary layer of a class of infinite yawed cylinders
Proc. Camb. Phil. Soc. 46 pp 645-648

52. Mager A. Generalisation of boundary layer momentum integral equations to three-dimensional flows including those of rotating systems
NACA Rep 1067 (1952)

53. Johnston J.P. Three-dimensional turbulent boundary layers
MIT Gas Turbine Lab Rep 39 (1957)

54. Smith P.D. An integral method for three-dimensional compressible boundary layers
ARC R & M 3739

55. Timman R.
The theory of three-dimensional boundary layers
Symp. on Boundary Layer Effects in Aerodynamics NPL March/April 1955

56. Kang S.W., Rae W.J. Dunn M.G.
Studies of 3-dimensional compressible boundary layers on blunt lifting entry bodies
AGARD CP 30

57. Reshotko E.
Laminar boundary layer with heat transfer on a cone at angle of attack in a supersonic stream
NACA TN 4152 (1957)

58. Reshotko E.
Compressible laminar boundary layer over a yawed infinite cylinder with heat transfer and arbitrary Prandtl number
NACA TN 3986 (1957)

59. Blottner F.G., Ellis M.A.
Finite-difference solutions of the incompressible three-dimensional boundary layer equations for a blunt body
Comp. & Fluids Vol 1 (1973) pp 133-158

60. Smith P.D.
An integral method for three dimensional compressible turbulent boundary layers
ARC R & M 3739

61. Davies, Cash, Catley
Measurement of boundary layer transition on an axisymmetric body at hypersonic speeds
RAE TM Aero 1373

62. Poll D.I.A.
Heat transfer, skin friction, pressure and recovery temperature distributions for a hemisphere - cylinder radome travelling at supersonic speeds.
Cranfield Col. of Aero. NFP85/9

63. King J.N.
Details of tests on conical and power law bodies in the ARA M4T and M7T at Mach numbers of 4.25 and 7.0.
ARA model test note M154/1

64. Jones D.J.
Tables of inviscid supersonic flow about circular cones at incidence (GAMMA = 1.4)
AGARDograph - 137

65. Solomen J.M.
A program for computing steady inviscid Three-dimensional supersonic flow on re-entry vehicles
Vol. 1 Analysis and programming
NSWC/WOL/TR77-28 (1977)

66. McBrayer J.D.
Pressure distributions about yawed cones and ogives
J. Spacecraft Vol. 3 No. 6 pp 940-941

67. Ludweig H., Tillmann W.
(Trans) NACA TN 1285 (1950)

68. Spalding D.R.
The kinetic-energy deficit equation of the turbulent boundary layer
Recent development in boundary layer research AGARDograph-97 (1965)

69. Dorodnitsyn A.A.
General method of integral relations and its application to boundary layer theory
Advances in Aero Sci. pp 207-219
New York Macmillan

70. Holt, Modarress
Application of the method of integral relations to laminar boundary layers in three dimensions
Proc. R Soc Lond A 353 pp 319-347 (1977)

71. Poll D.I.A.
Private communication

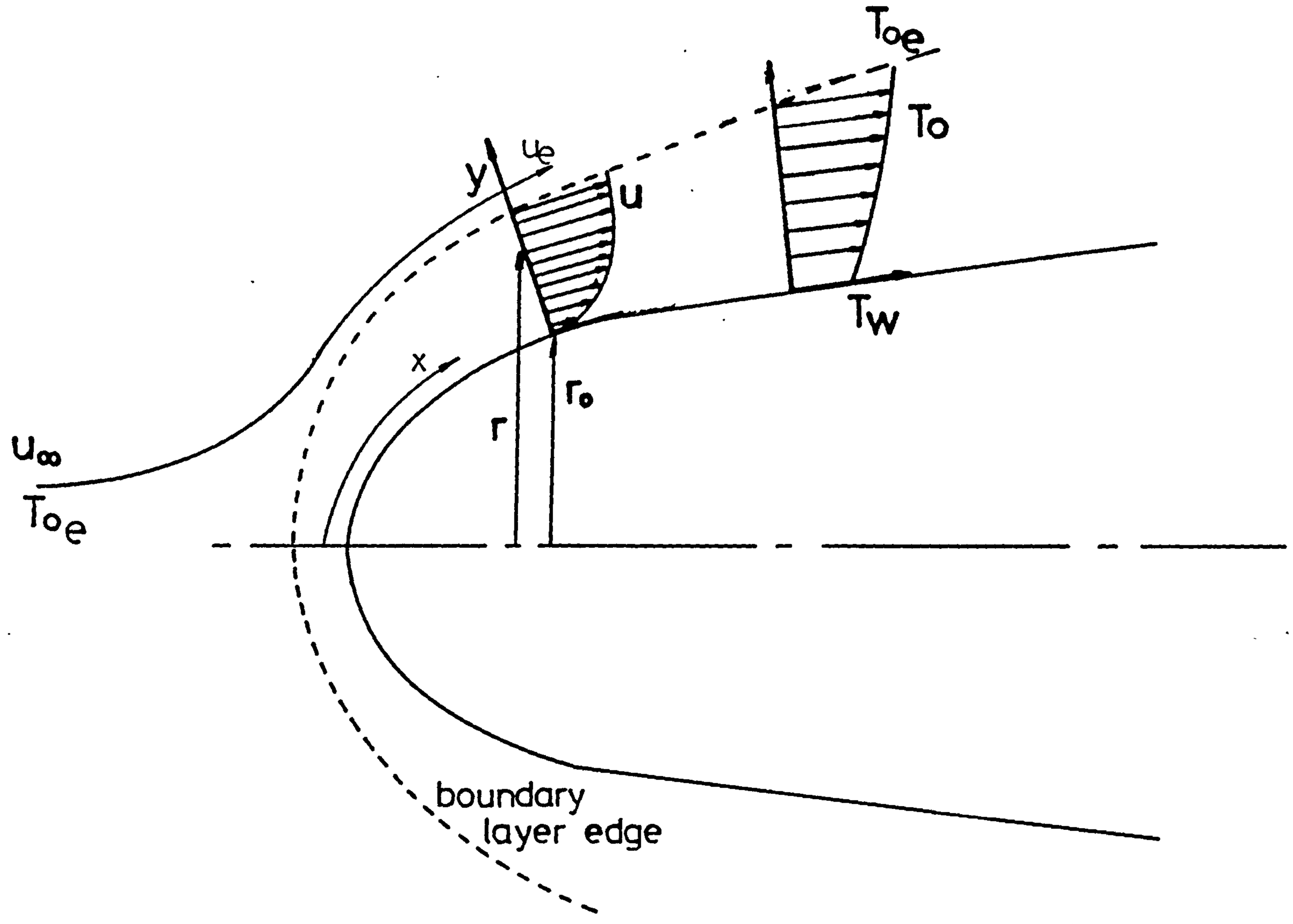

Fig. 1.1.1 Axisymmetric/2D boundary layer notation

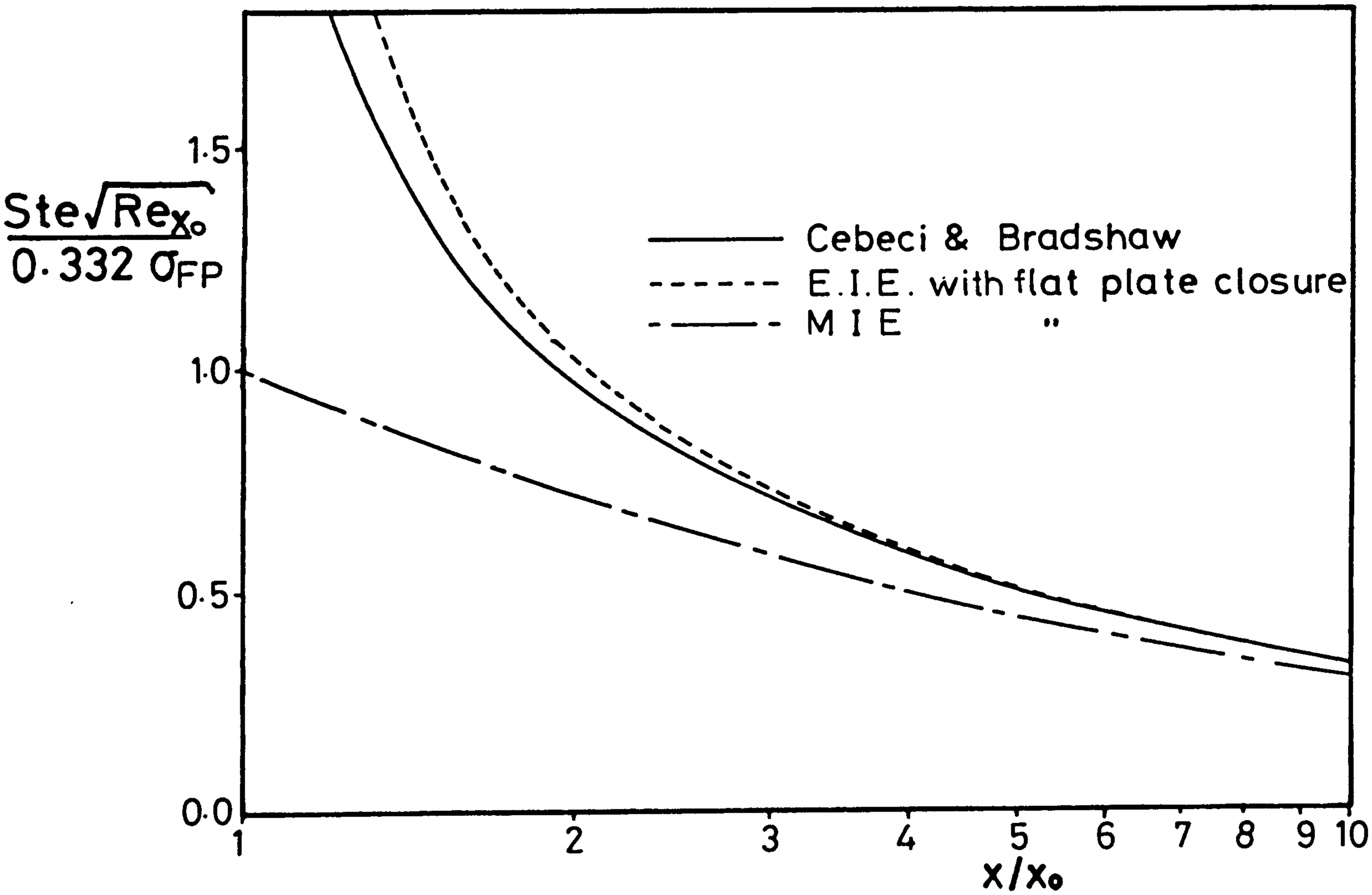

Fig. 1.2.1 Heat transfer to a flat plate with an unheated starting length

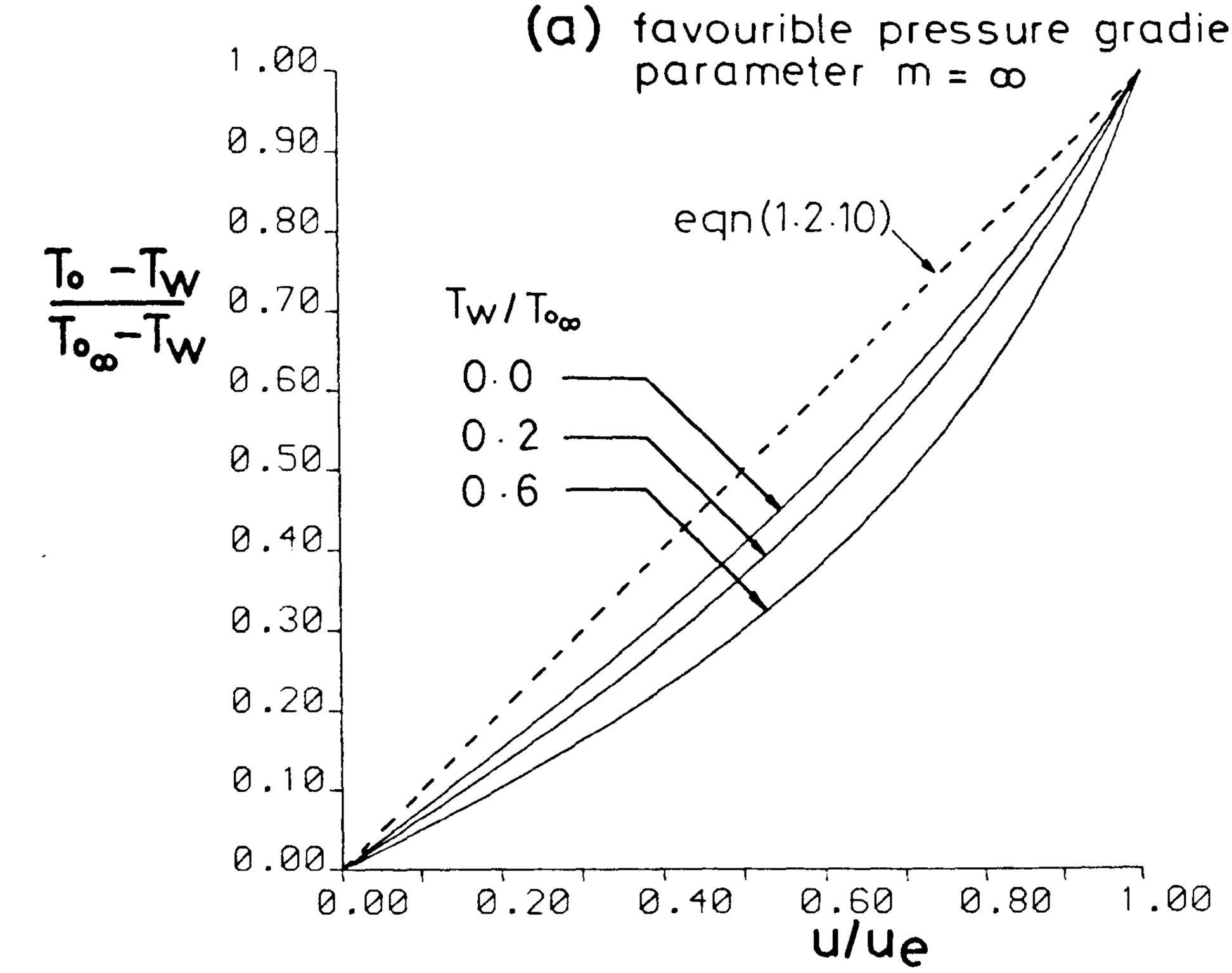

(b) adverse pressure gradient
parameter m = -0·09

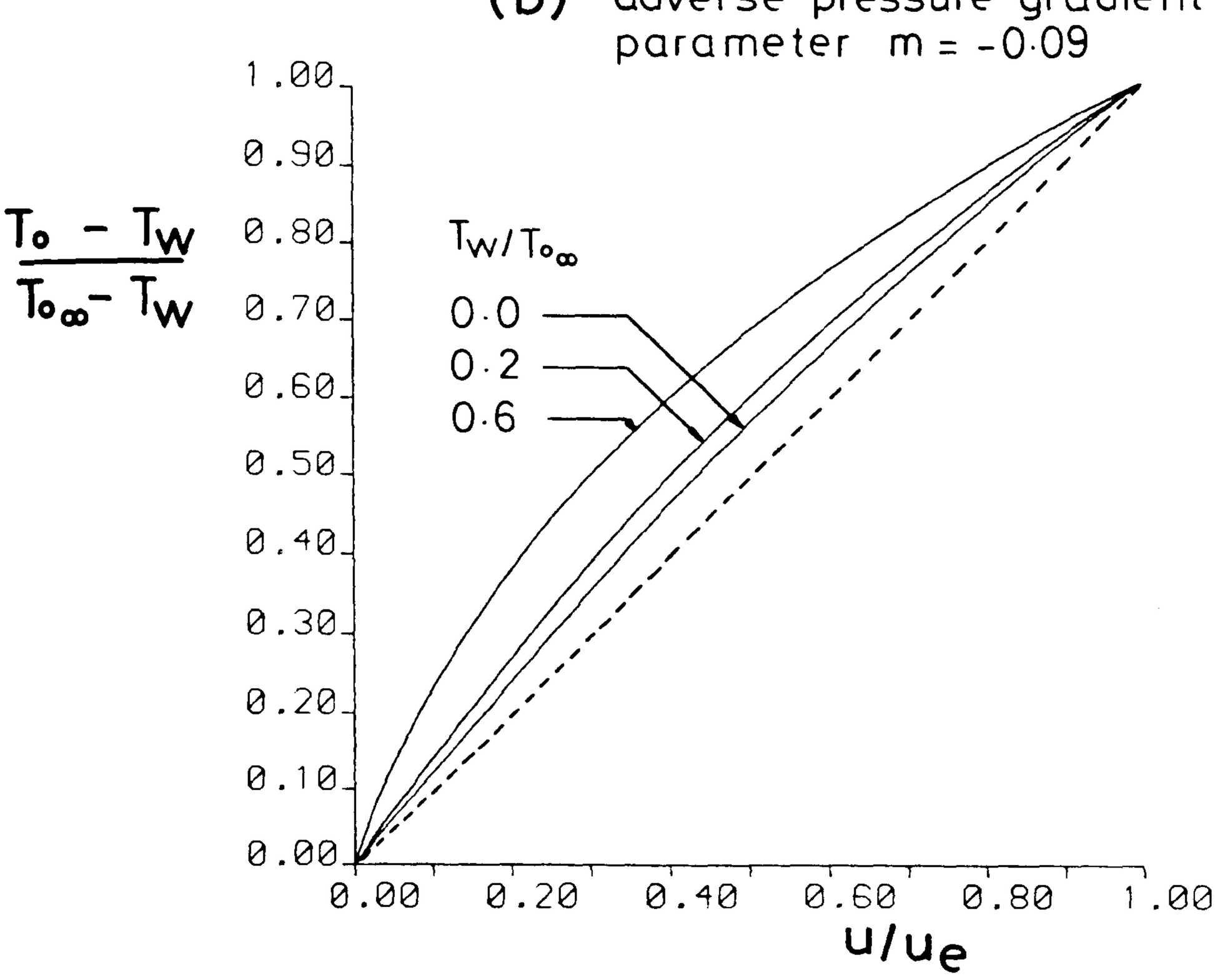

Fig. 1.2.2 Temperature - velocity relation in a compressible similar boundary layer flow (Cohen & Reshotko ref.10)

(a) zero pressure gradient

Profile	M_δ	T_w/T_r	Re_{δ_2}	$(yu_\tau/\nu_w)_{max}$
—●— 7702S0103	3 0	10	1634	26.6
- - -□- - - 7702S0203	2 99	0767	2086	4 1
— — ● — — 7702S0303	2 98	0578	2826	6 2
theoretical				

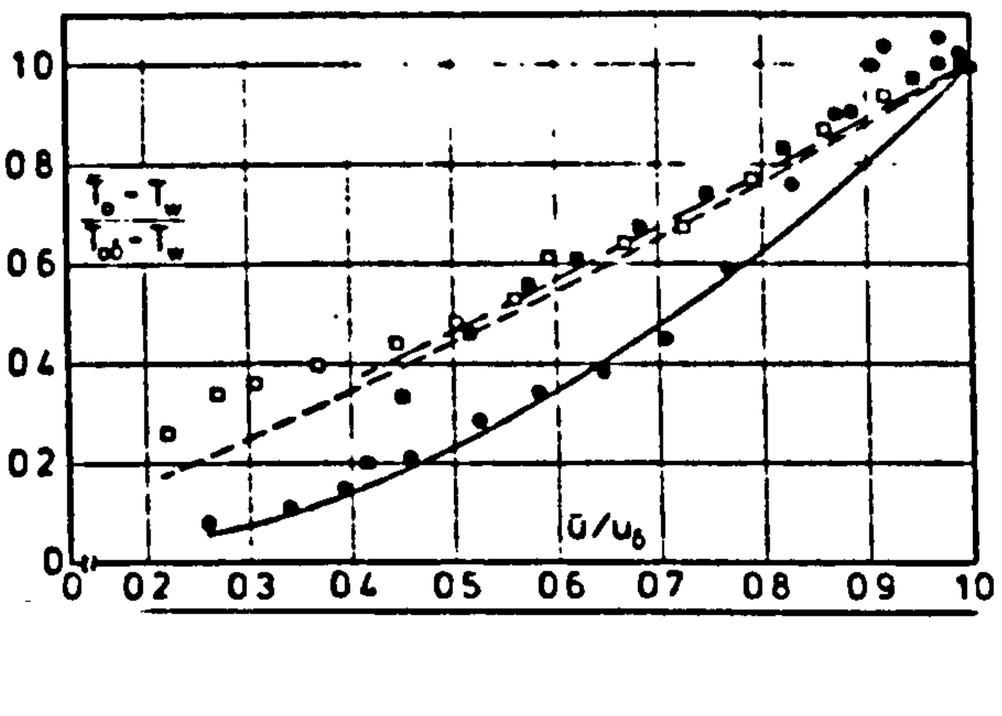

CAT	M_δ	T_w/T_r	Re_{δ_2}	Re_Θ	$(yu_\tau/\nu_w)_{max}$
—o— 67020104	6 49	0525	824	3288	–
—●— 67020201	6 68	0487	774	3054	–
□ 72050102	7 20	0498	2101	9261	26
● 72050103	7 20	0476	3042	12950	24
theoretical					

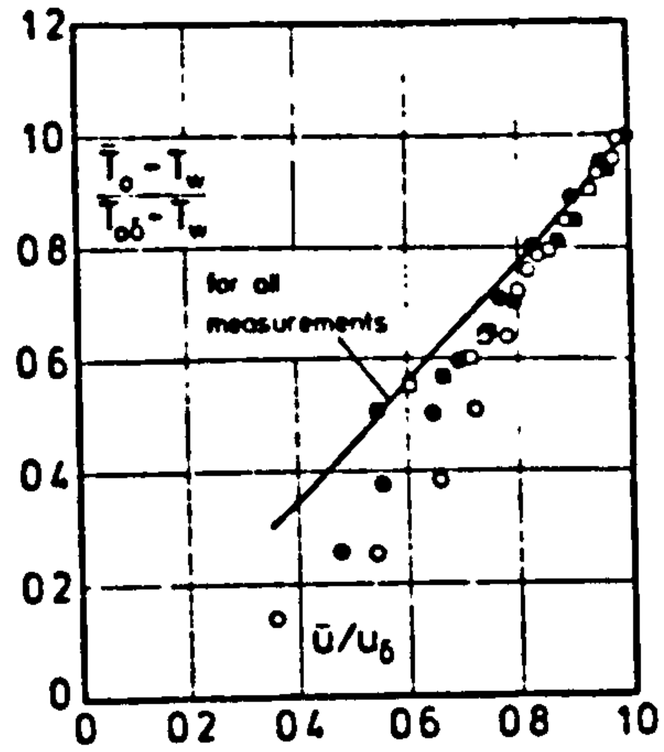

Profile	M_δ	T_w/T_r	Re_{δ_2}	Re_Θ
□ 67020601	6.31	0936	275	1603
■ 67020701	6 43	0928	532	3187
theoretical				

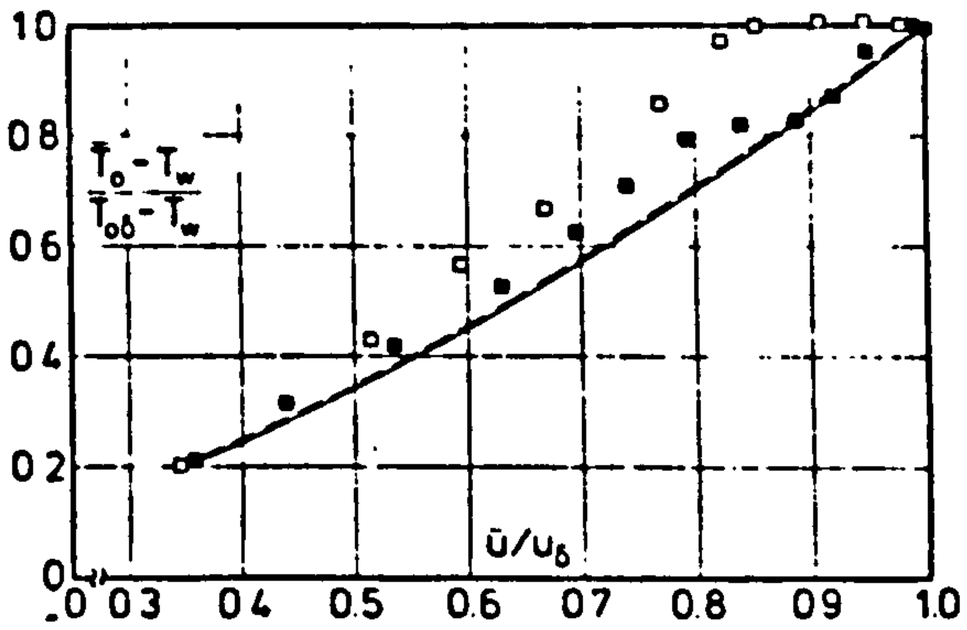

Profile	M_δ	Re_{δ_2}	T_w/T_r
o 67020301	6 41	049	1218	4498
□ 67021001	6.34	052	1669	6395
theoretical				

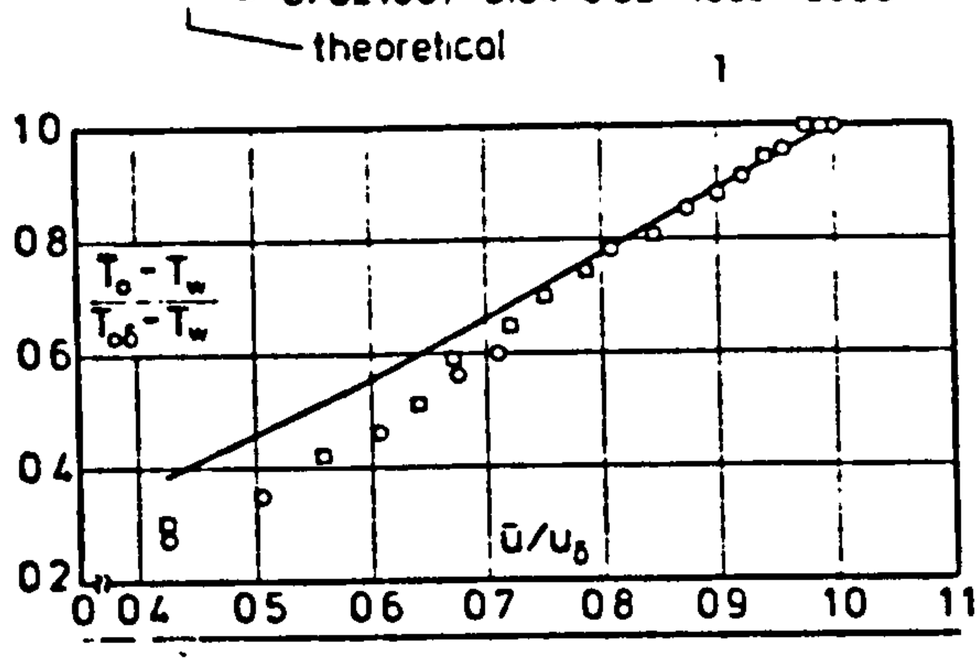

(b) favourible pressure gradient

Profile	M_δ	Re_{δ_2}	T_w/T_r
o 0101	19.3	214	0.199
● 0201	19 4	356	0.188
△ 0301	19 7	323	0.182

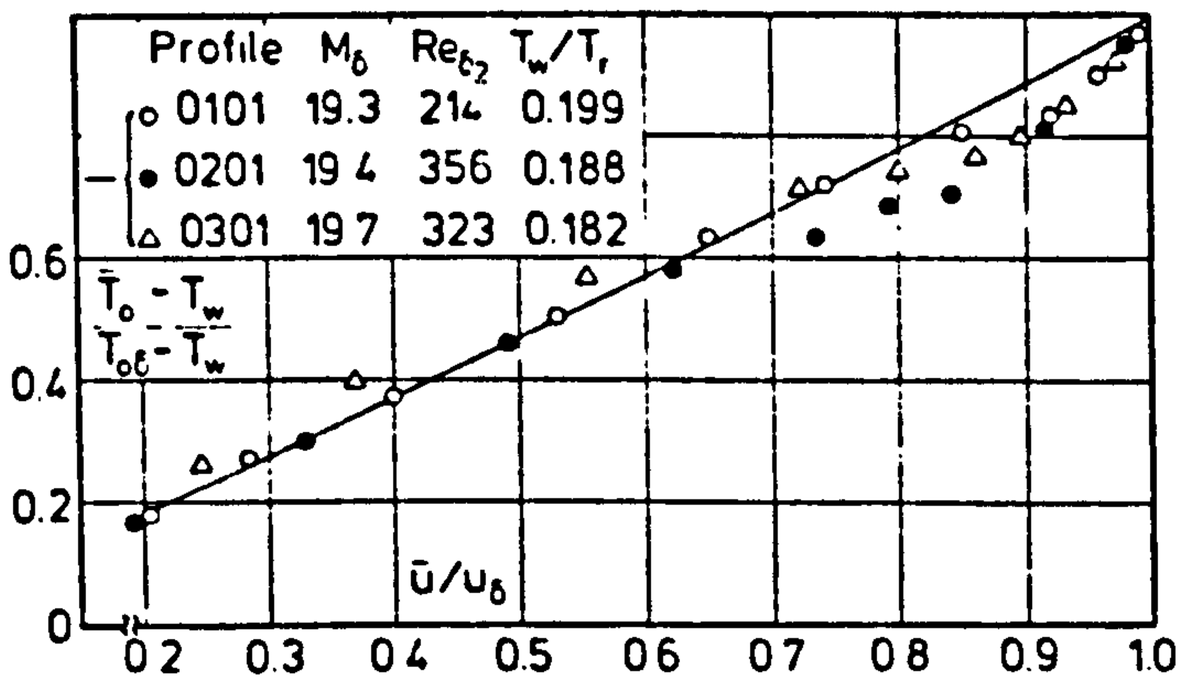

Profile	M_δ	Re_{δ_2}	T_w/T_r
o 1203	4.50	28058	0.232
● 1304	4 51	41822	0.259
△ 1501	4.37	29503	0.239
theoretical			

CAT 7304

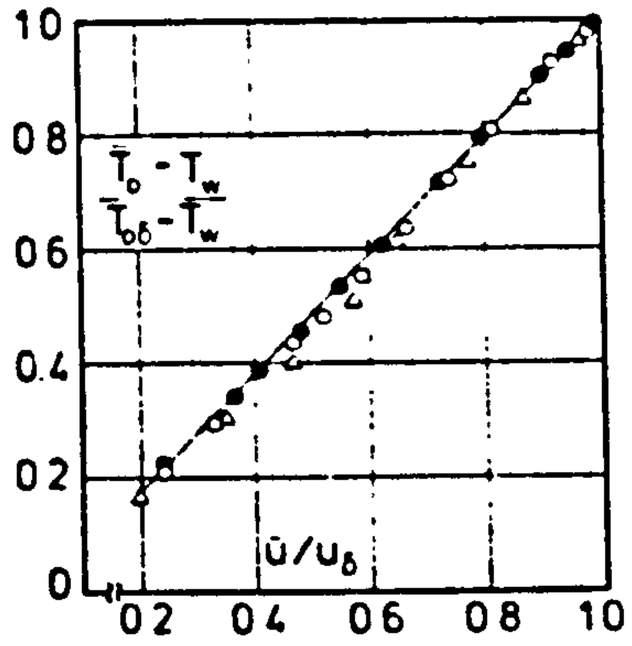

Fig. 1.2.3 Turbulent compressible velocity – temperature distributions.
Extracts from Fernholtz & Finley ref. 13

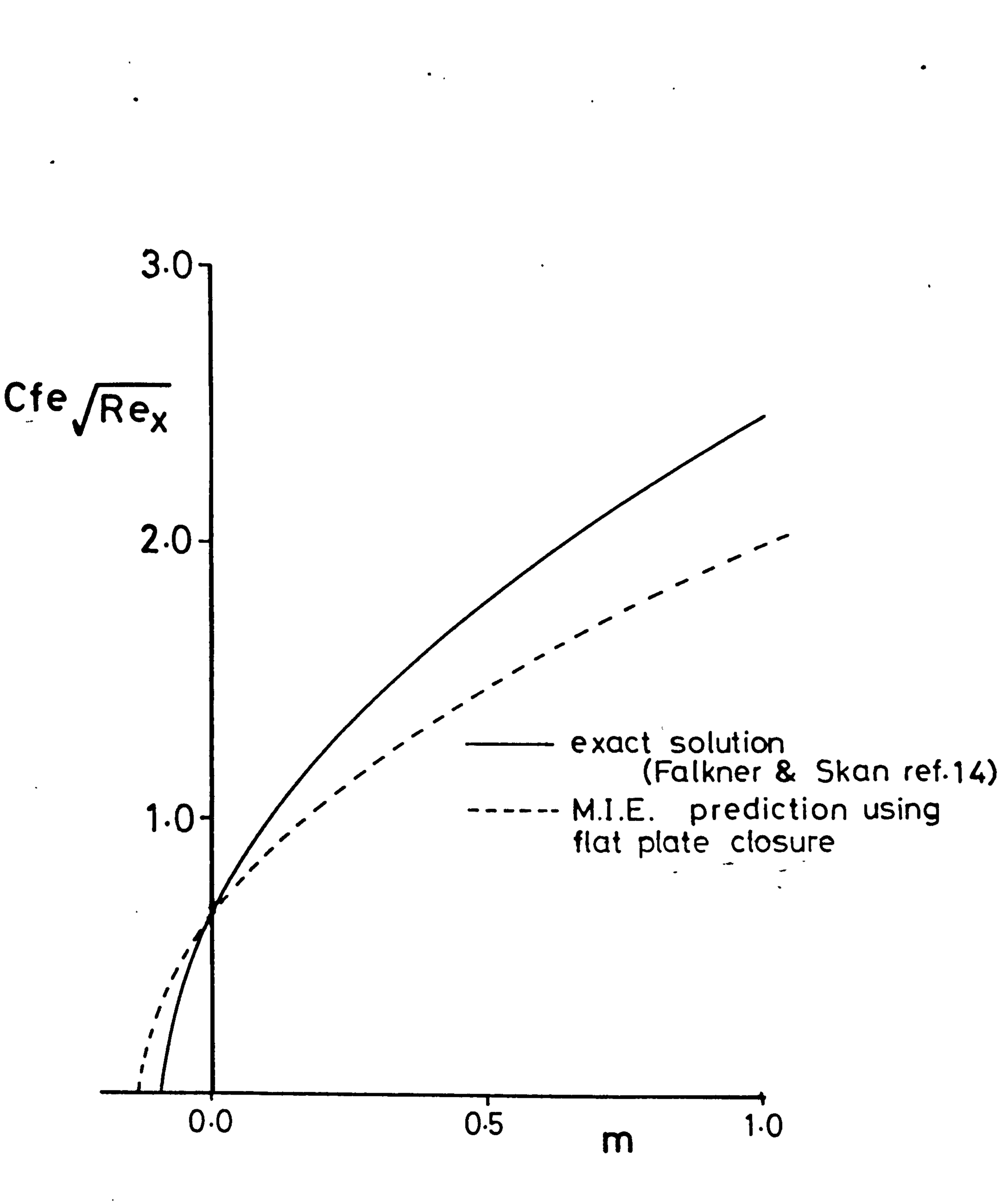

Fig 2.2.1 Skin friction in an incompressible laminar flow

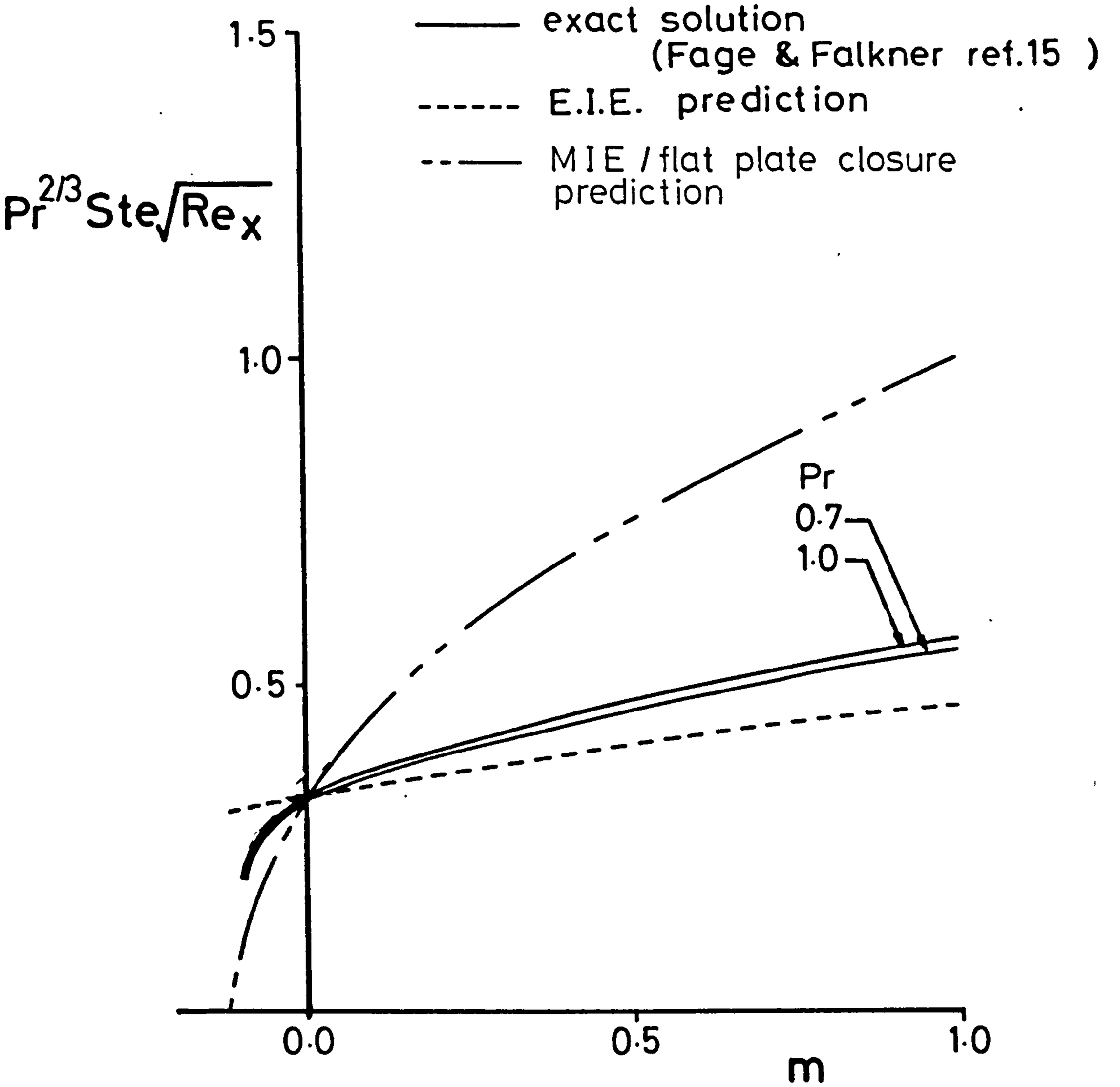

Fig 2.2.2 Heat transfer in an incompressible laminar flow (isothermal wall)

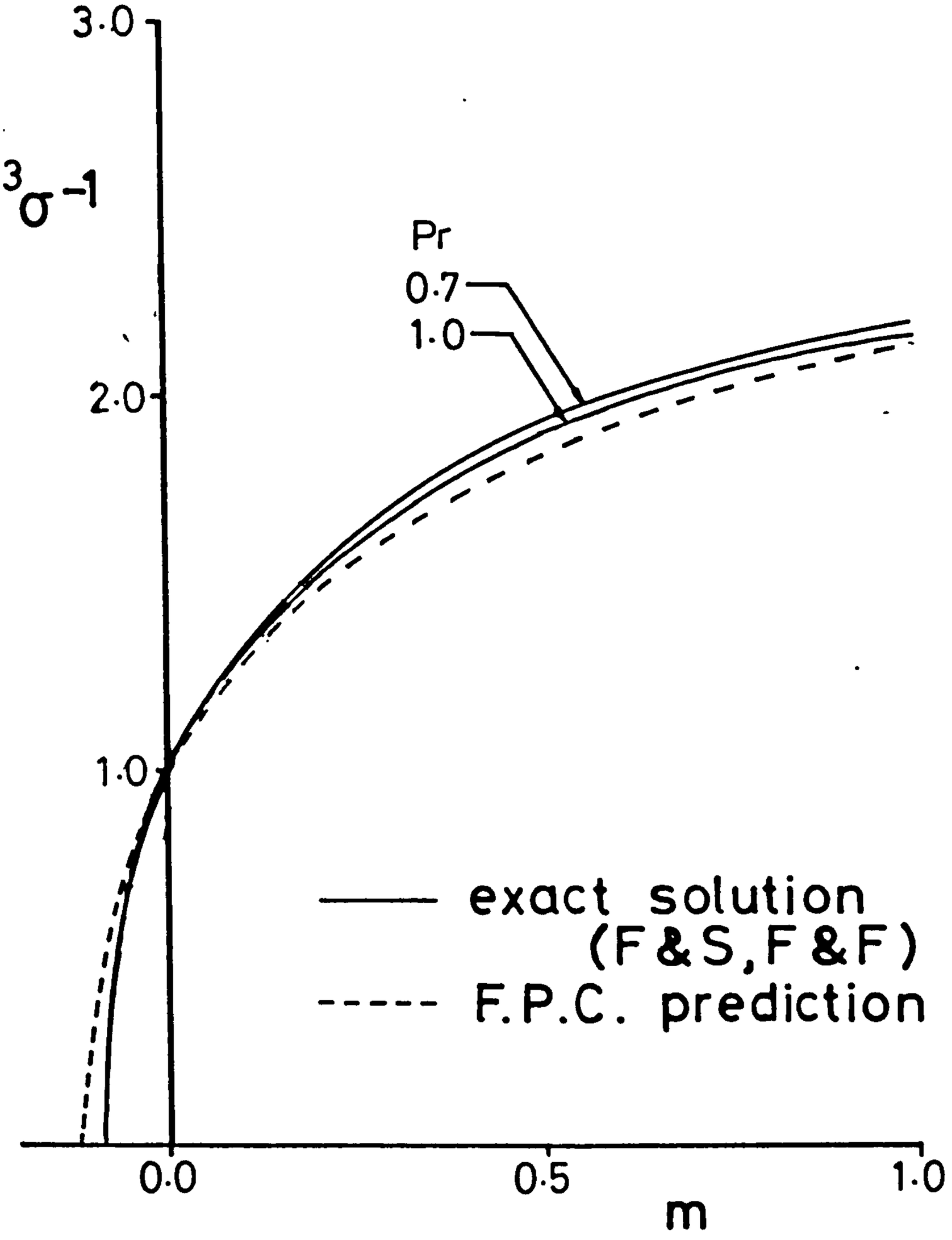

Fig 2.2.3 Reynolds analogy factor in an incompressible laminar flow (isothermal wall)

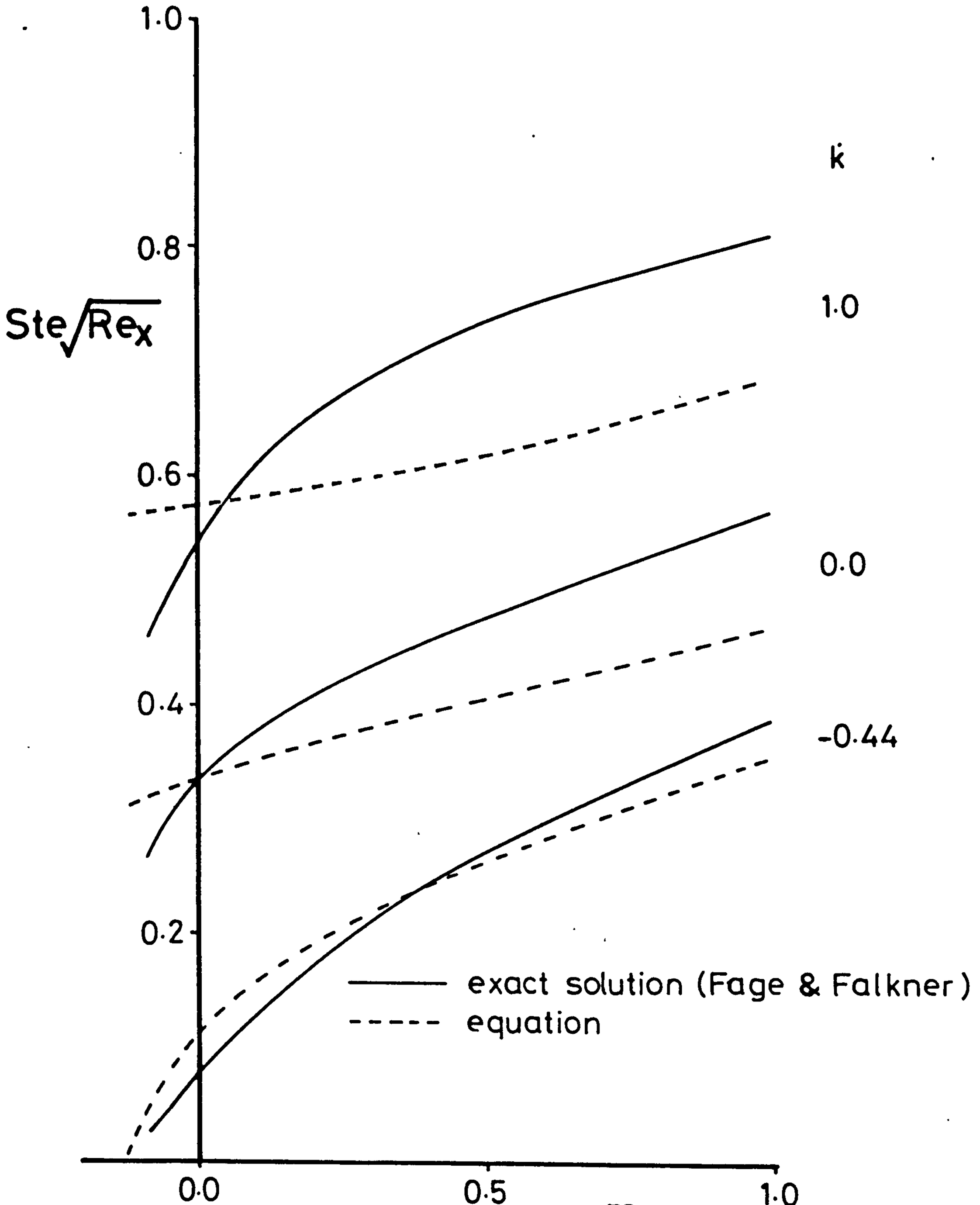

Fig 2.2.4 Heat transfer in an incompressible laminar flow. variable wall temp
Pr = 1

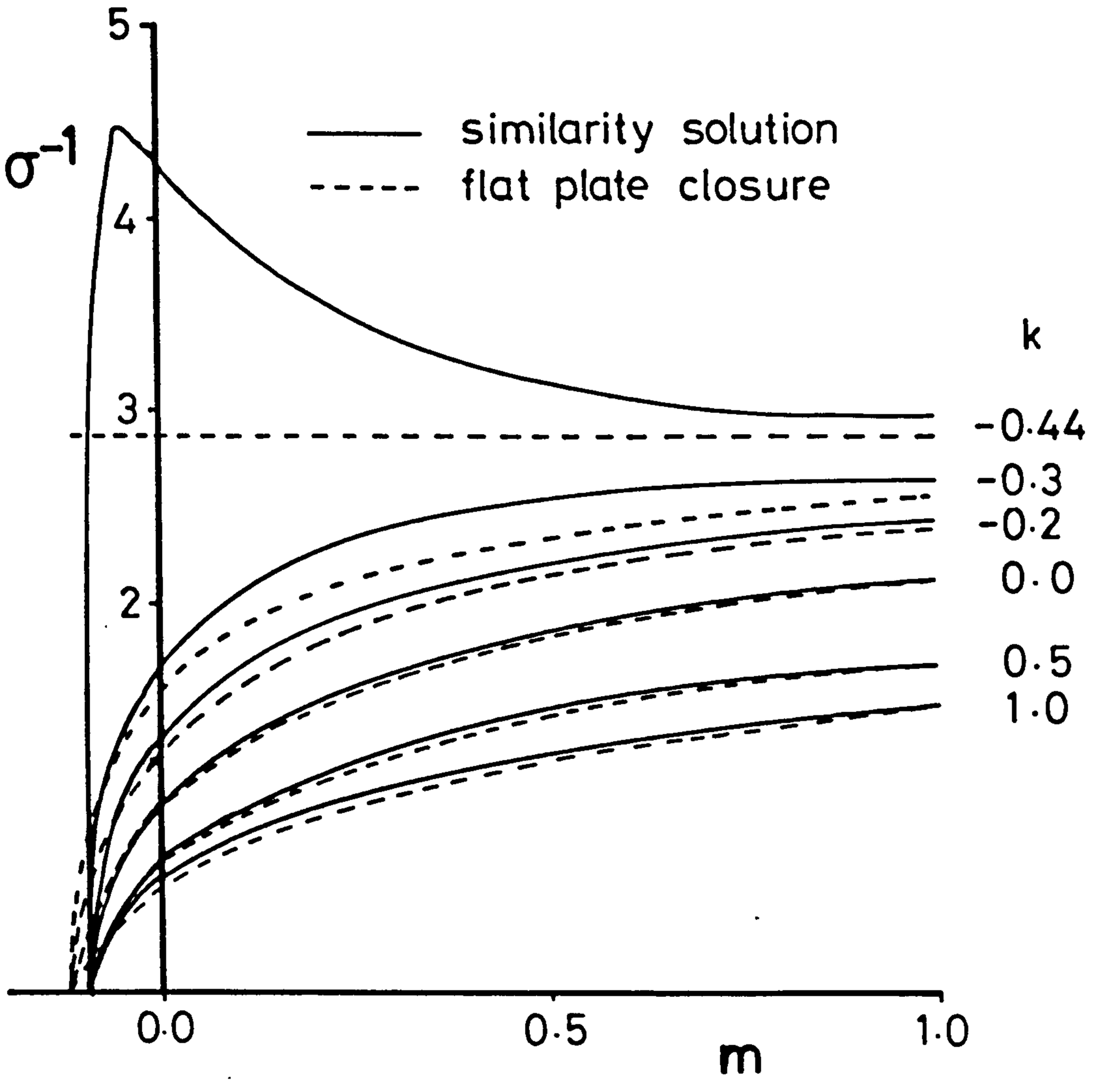

Fig 2.2.5 Reynolds analogy factor in an incompressible laminar pressure gradient flow with variable wall temperature.
(Pr = 1)

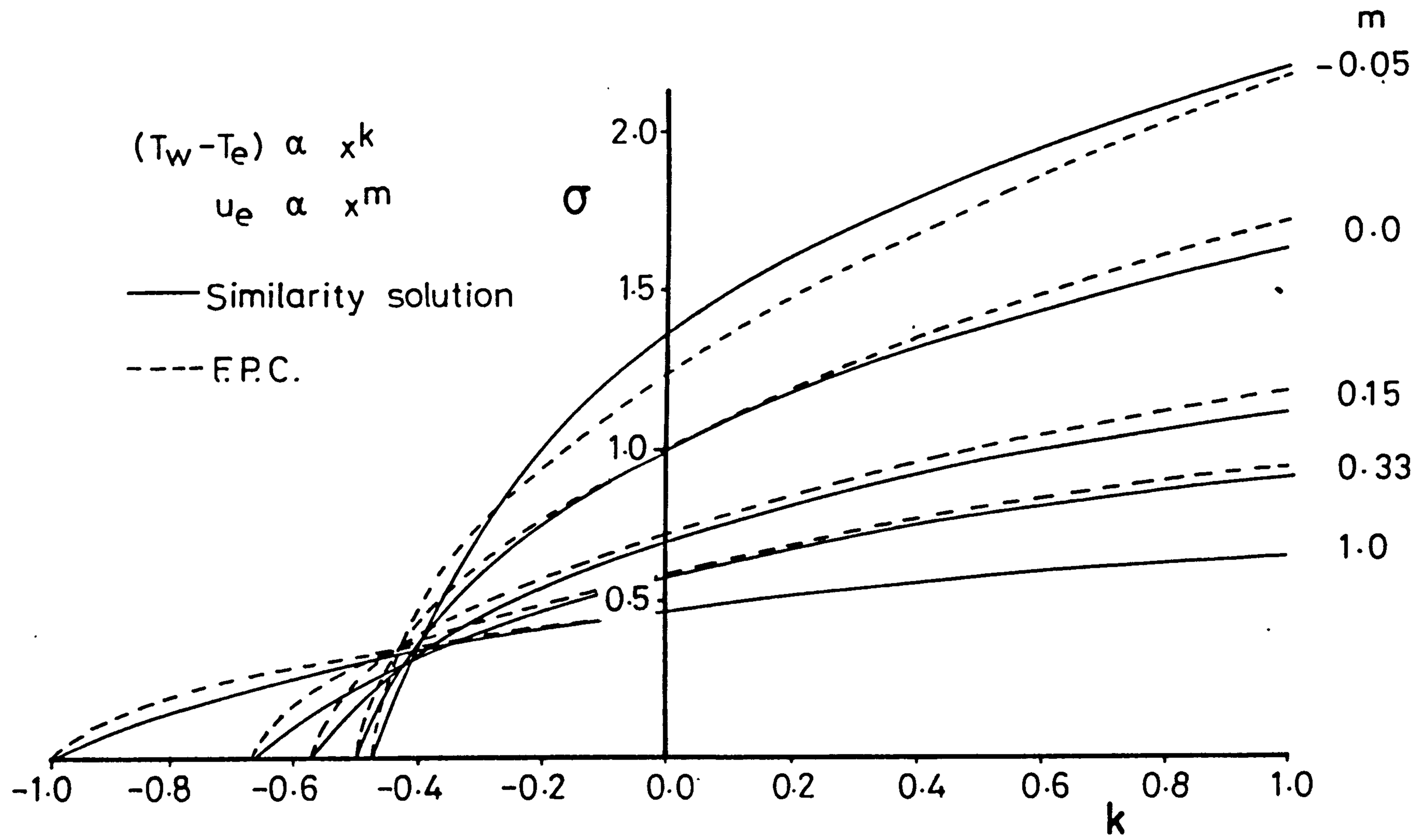

Fig 2.2.6 Reynolds analogy factor in an incompressible laminar pressure gradient flow with variable wall temperature

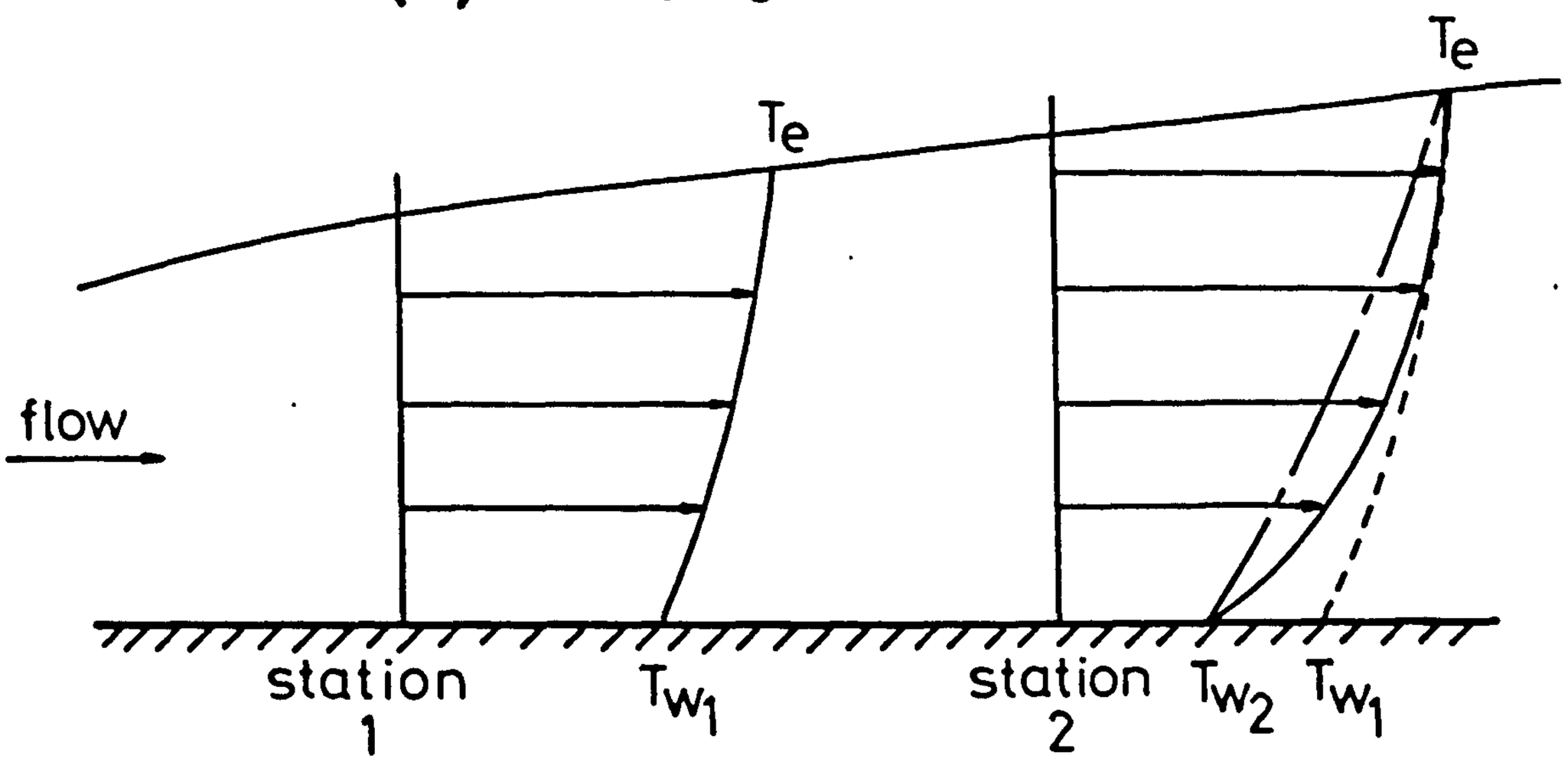

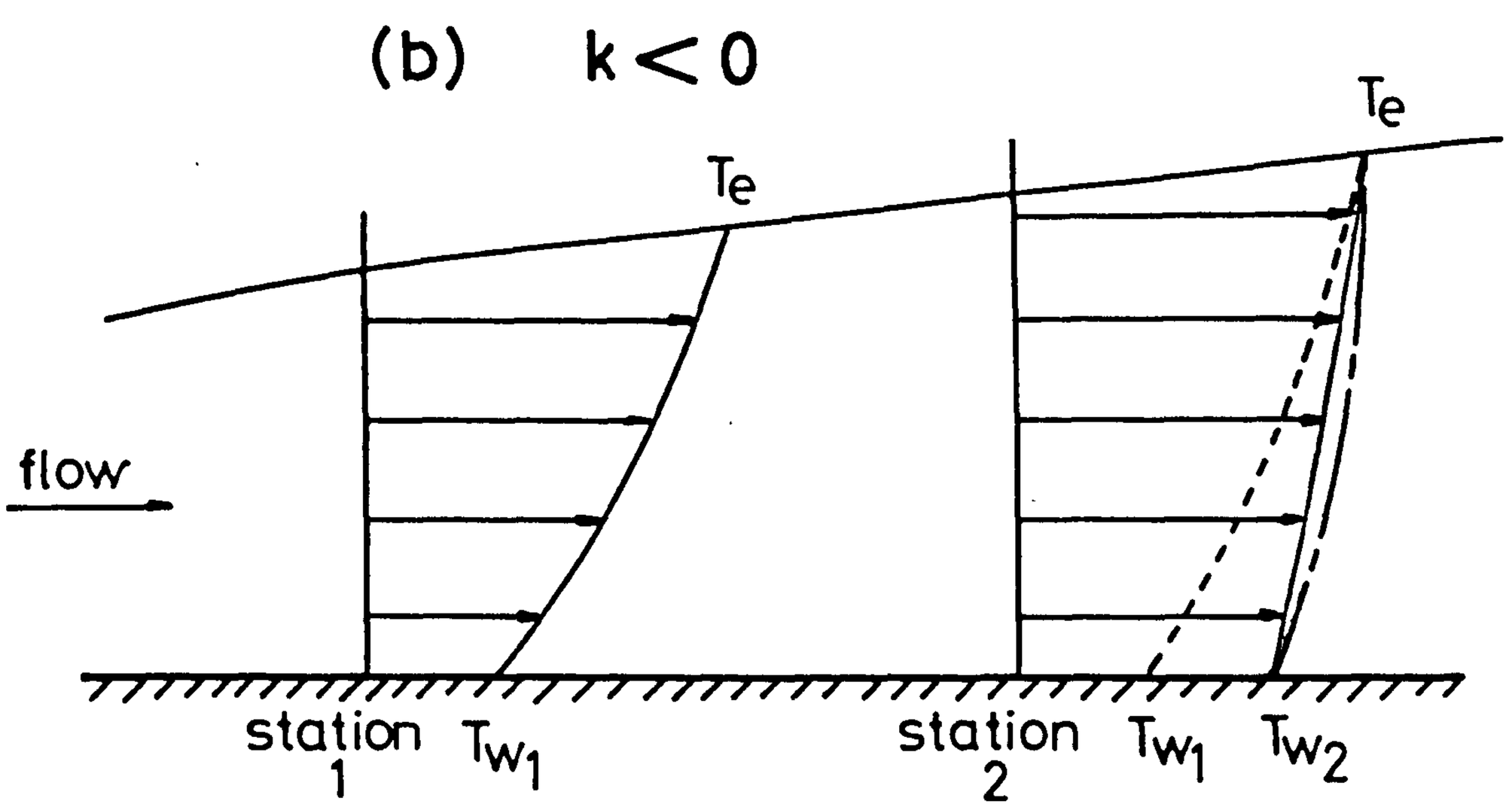

Fig 2.2.7 Boundary layer temperature profiles in variable wall temperature flows

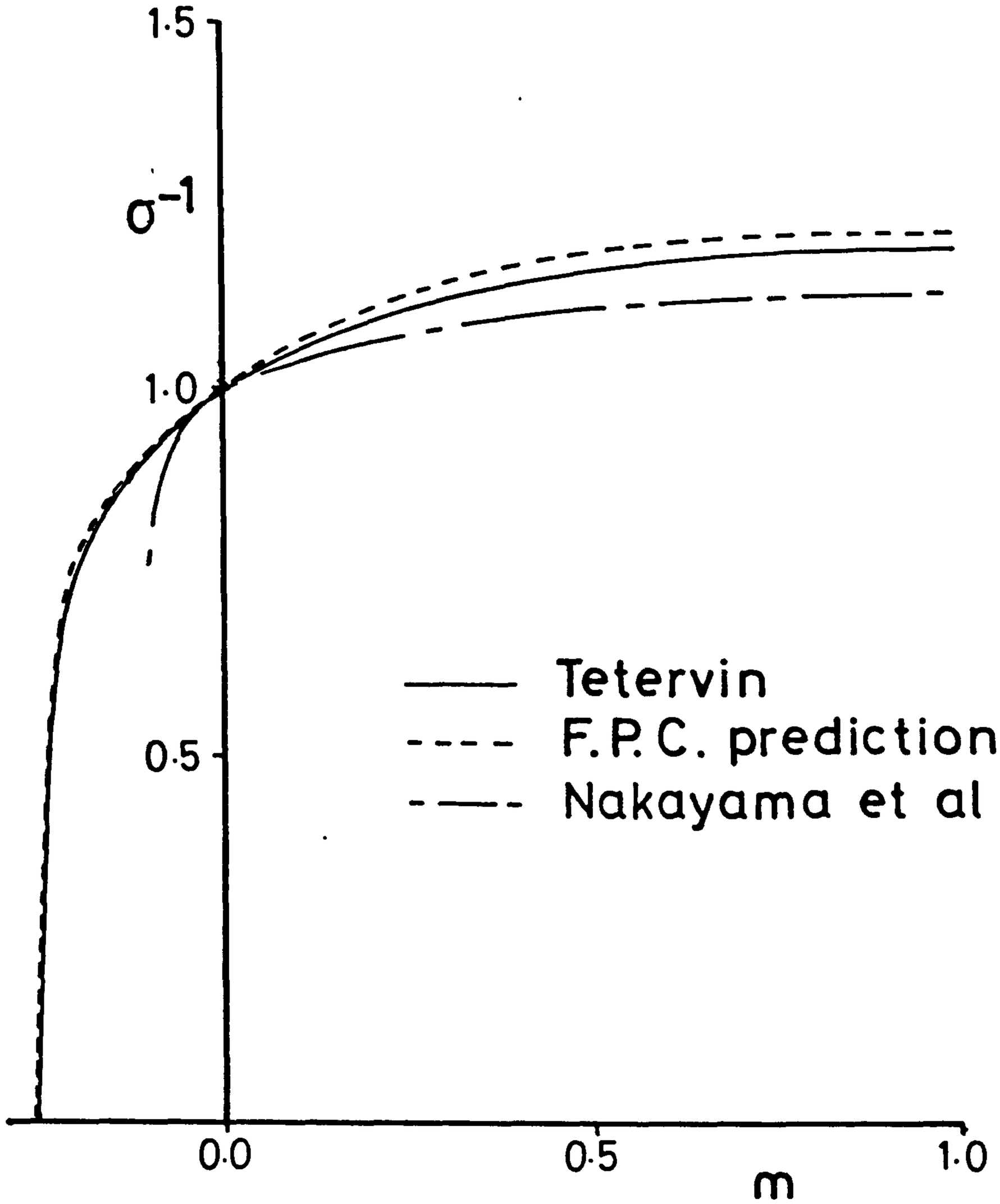

Fig 2.2.8 Reynolds analogy factor in an incompressible turbulent flow (isothermal wall)

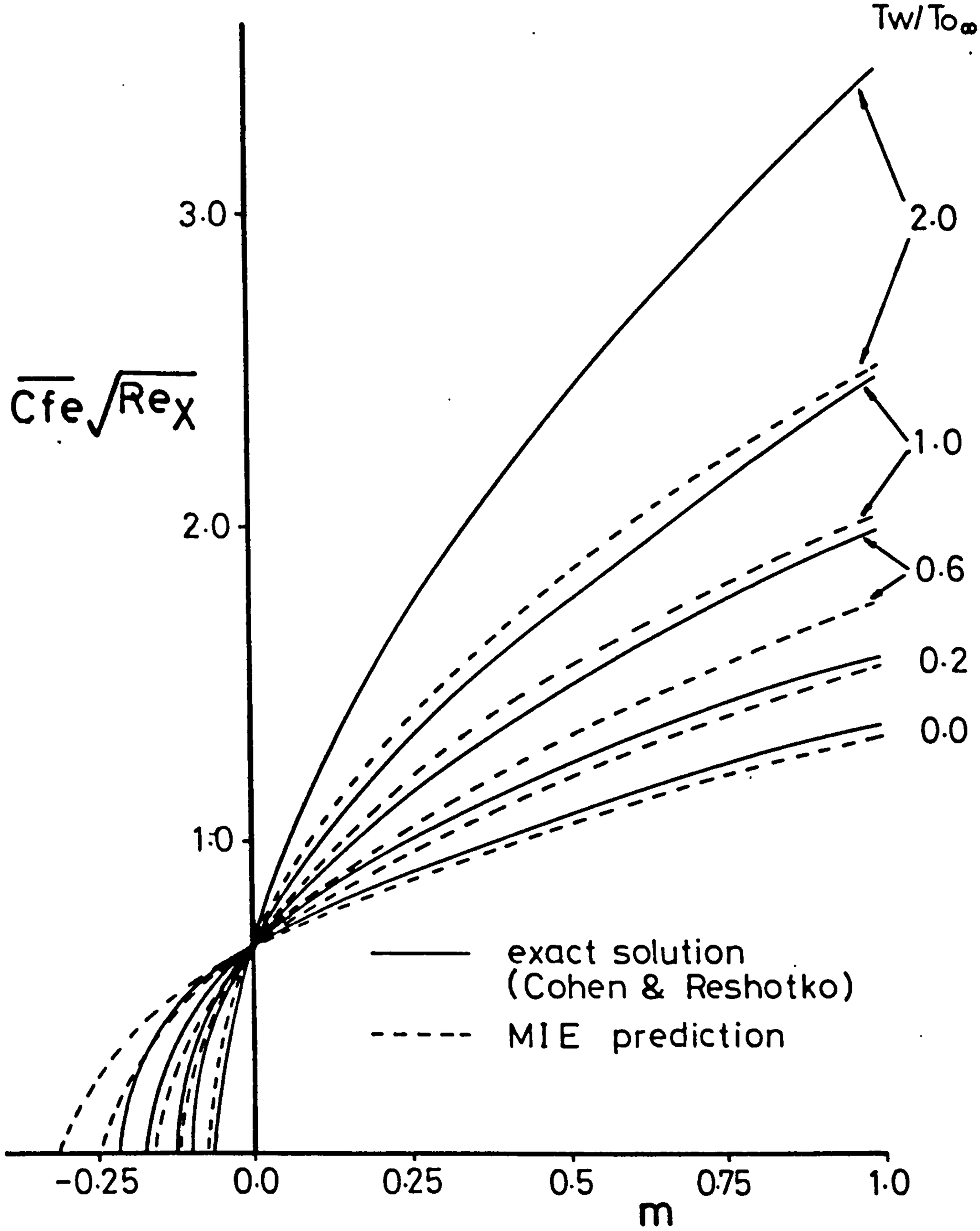

Fig. 2.2.9 Skin friction in a compressible laminar flow (isothermal wall)

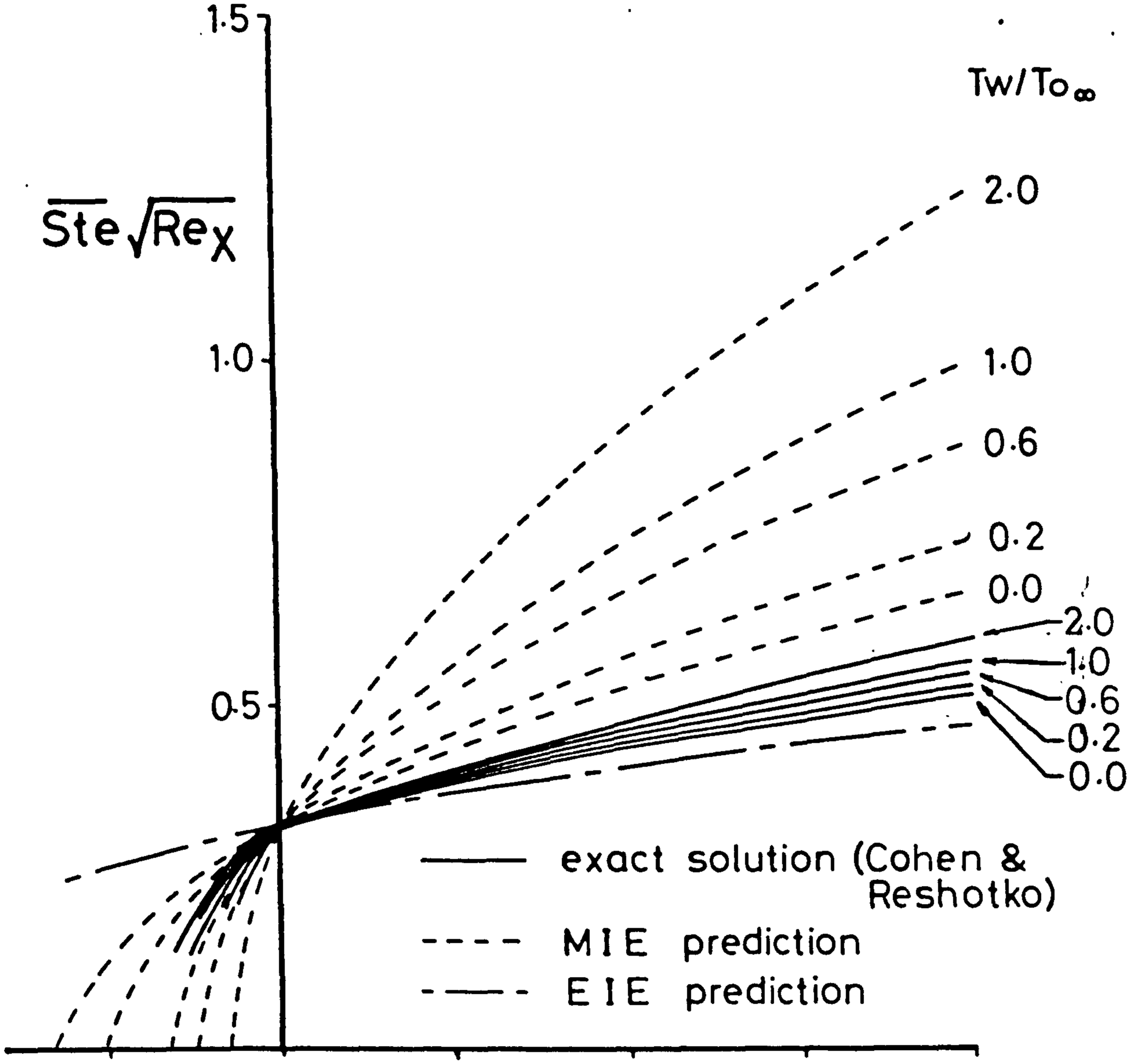

Fig 2.2.10 Heat transfer in a compressible laminar flow (isothermal wall)

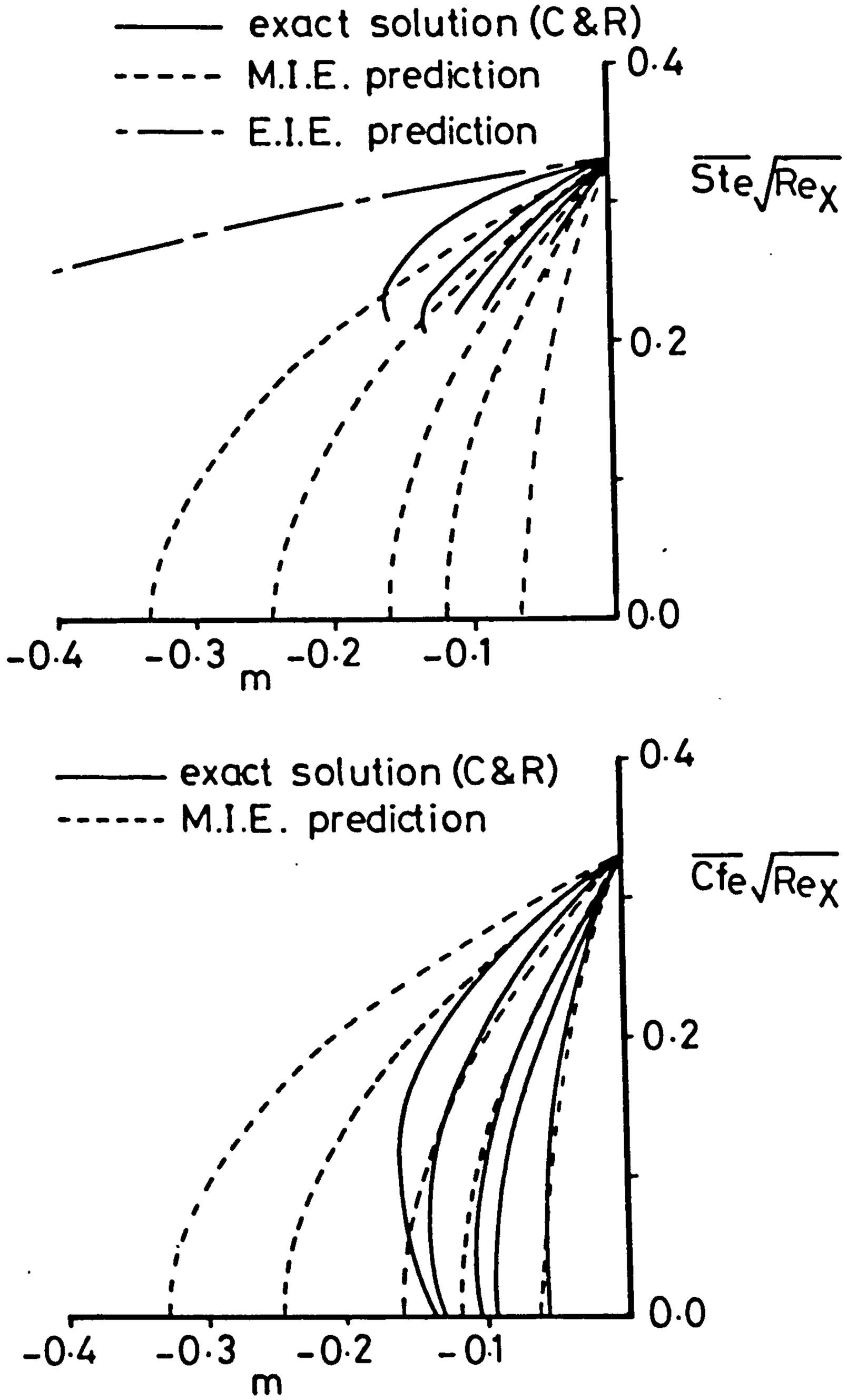

Fig 2.2.11 Adverse pressure gradient compressible laminar boundary layer (isothermal wall)

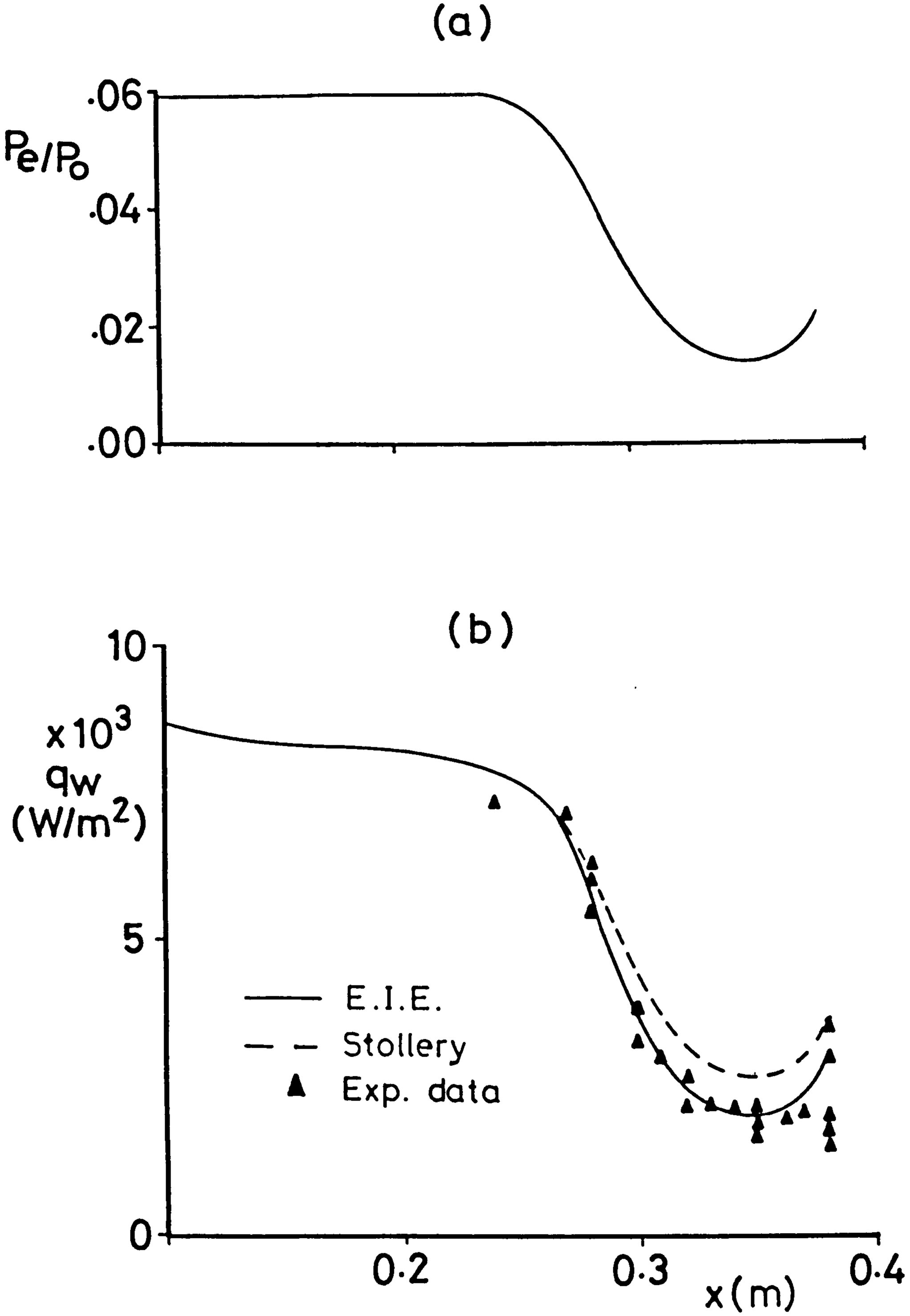

Fig 2.3.1 Turbulent boundary layer in a favourible pressure gradient heat transfer comparison with Thomann ref (20)

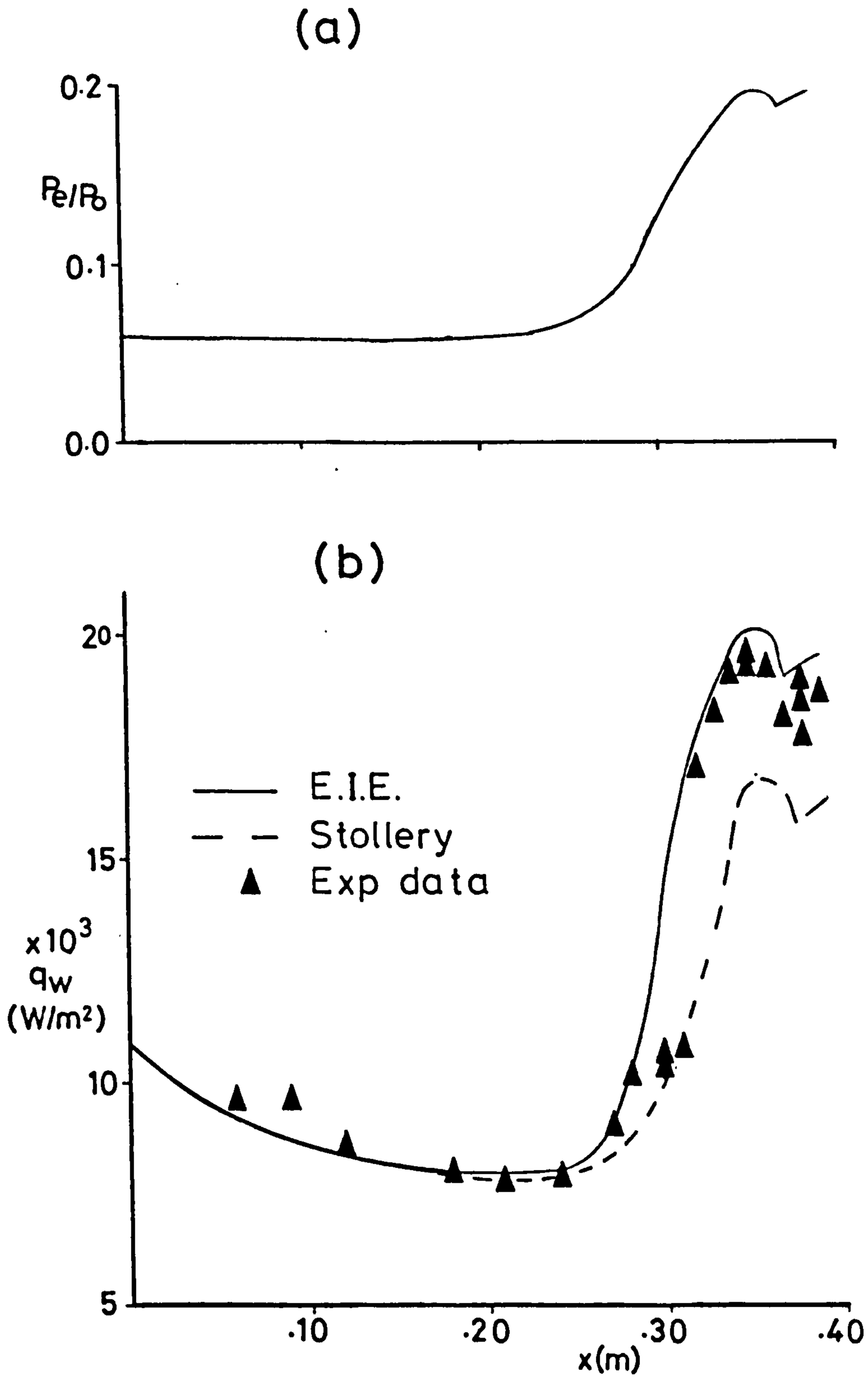

Fig 2.3.2 Turbulent boundary layer in an adverse pressure gradient heat transfer comparison with Thomann ref (20)

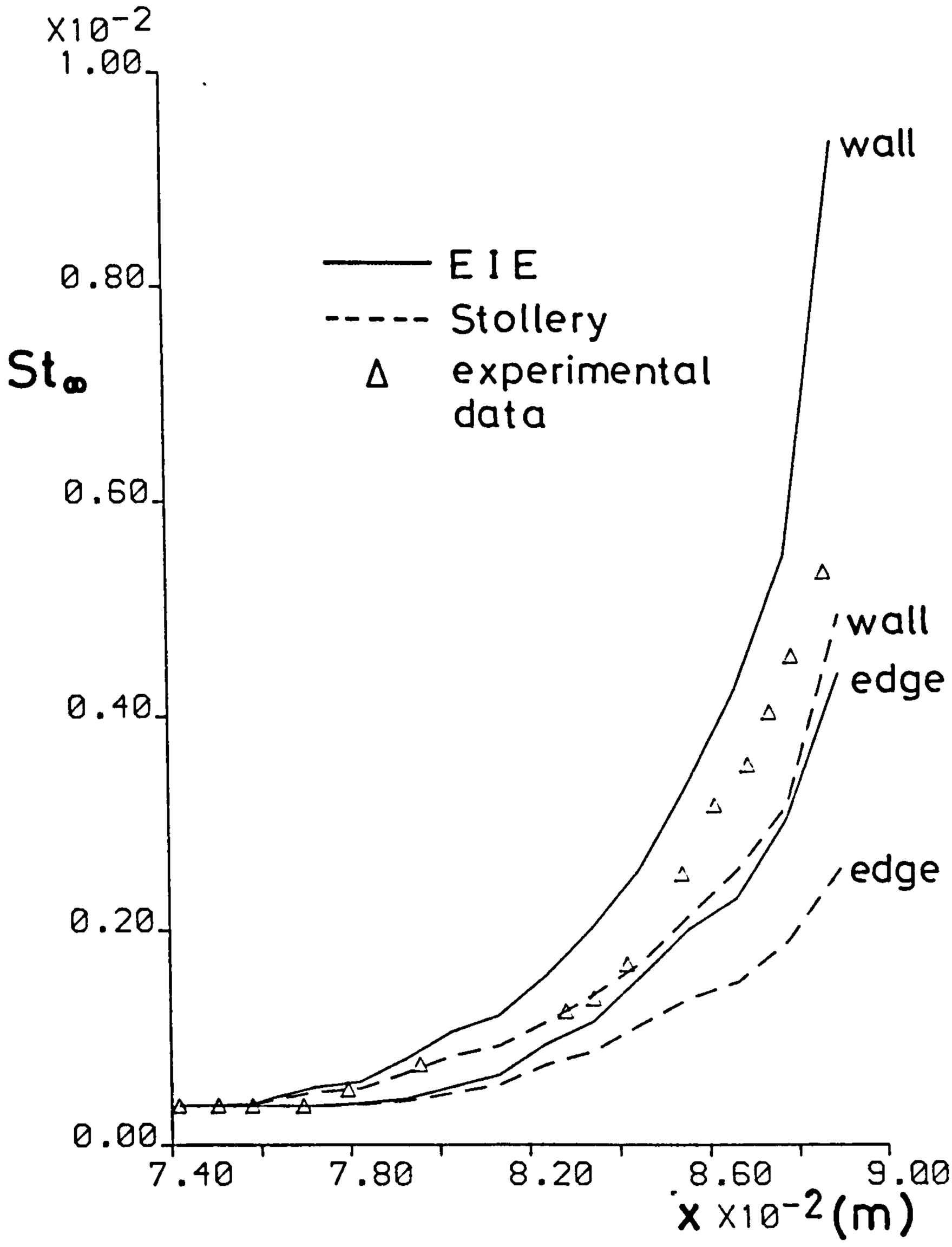

Fig 2.3.3 Turbulent boundary layer in an adverse pressure gradient heat transfer comparison with Hoydysh & Zakkay ref (21)

(a)

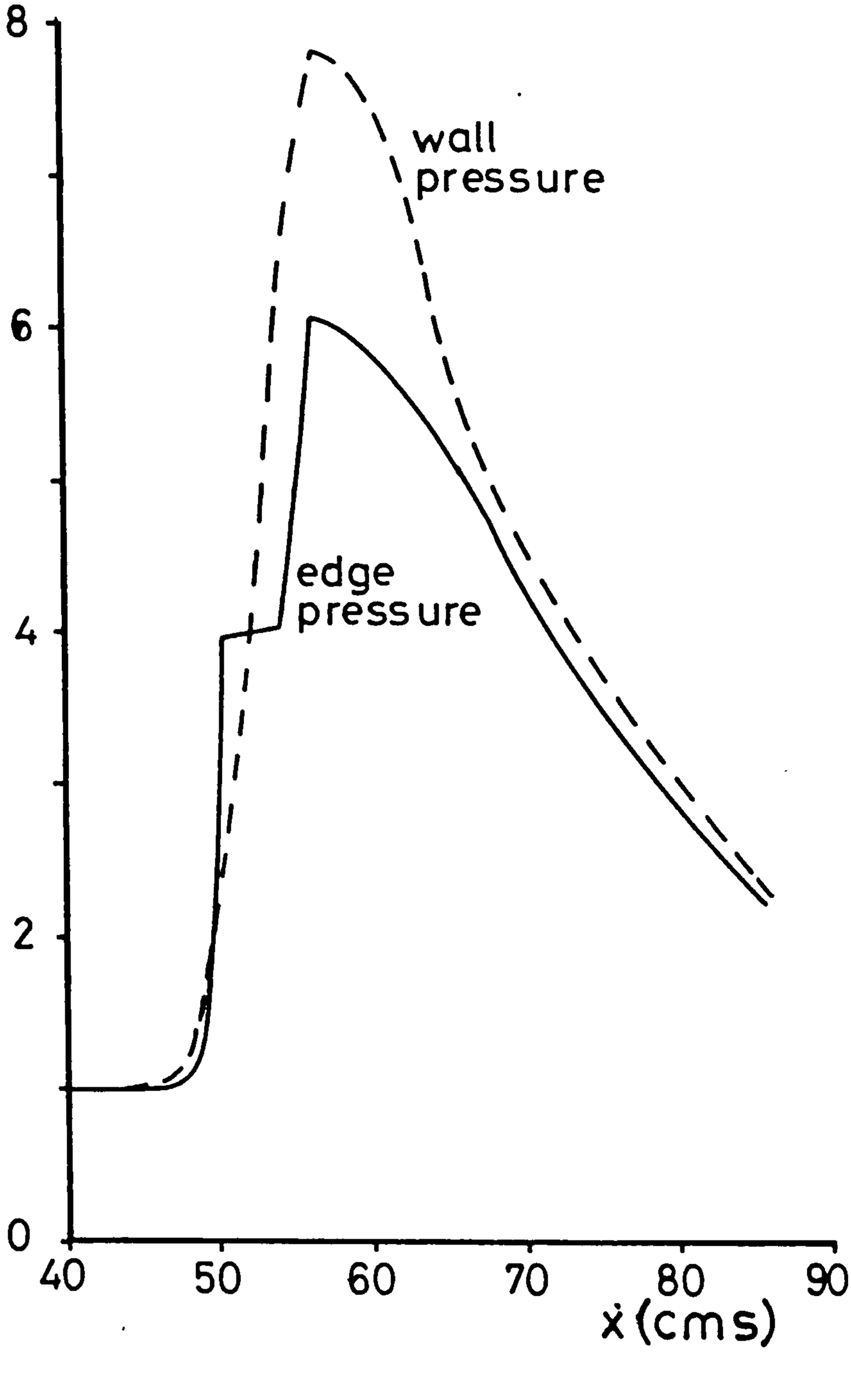

Fig 2.3.4 Horstmann pressure distribution 7.5° leading edge shock generator

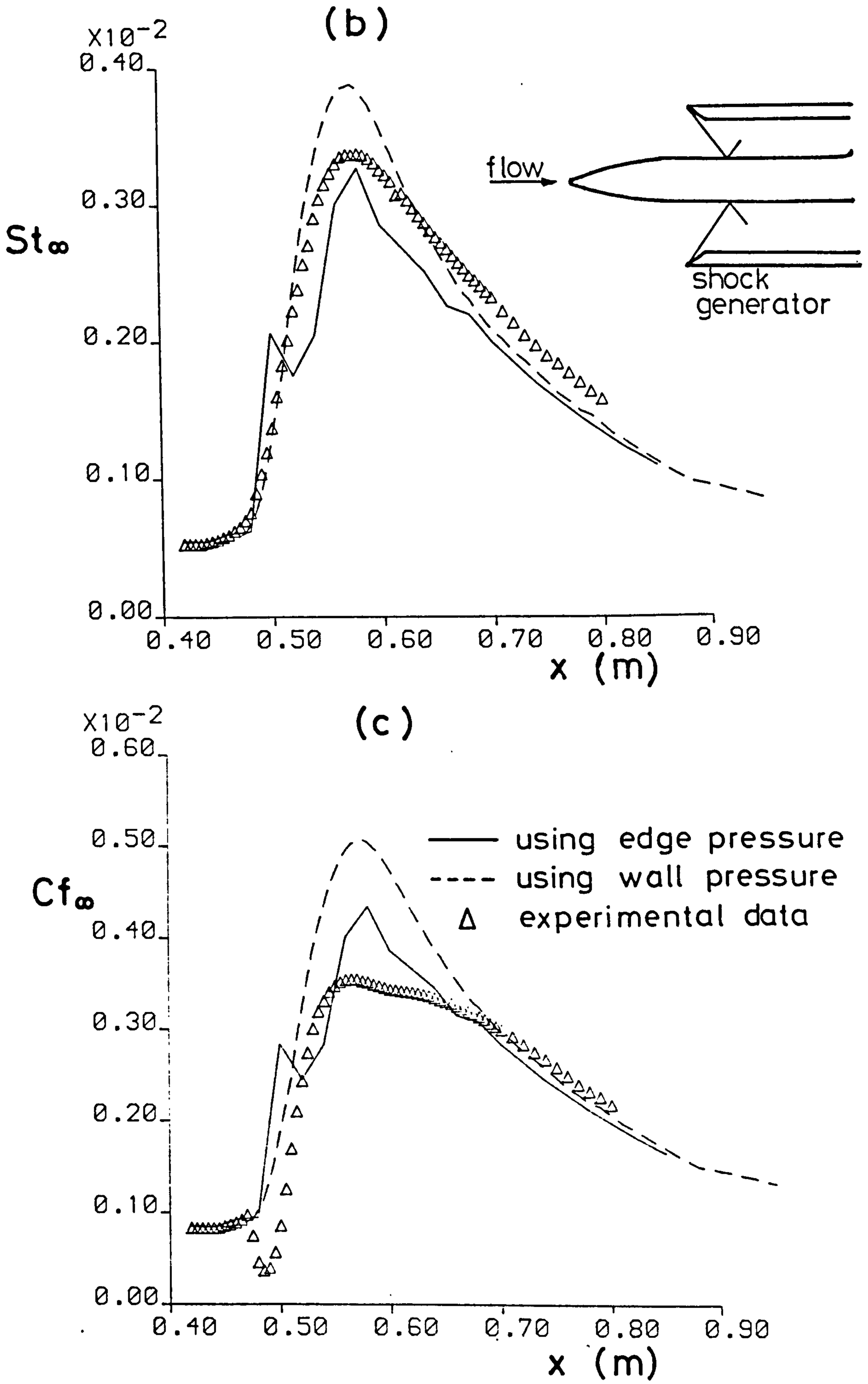

Fig 2.3.4 Horstmann heat transfer & skin friction
7.5° leading edge shock generator

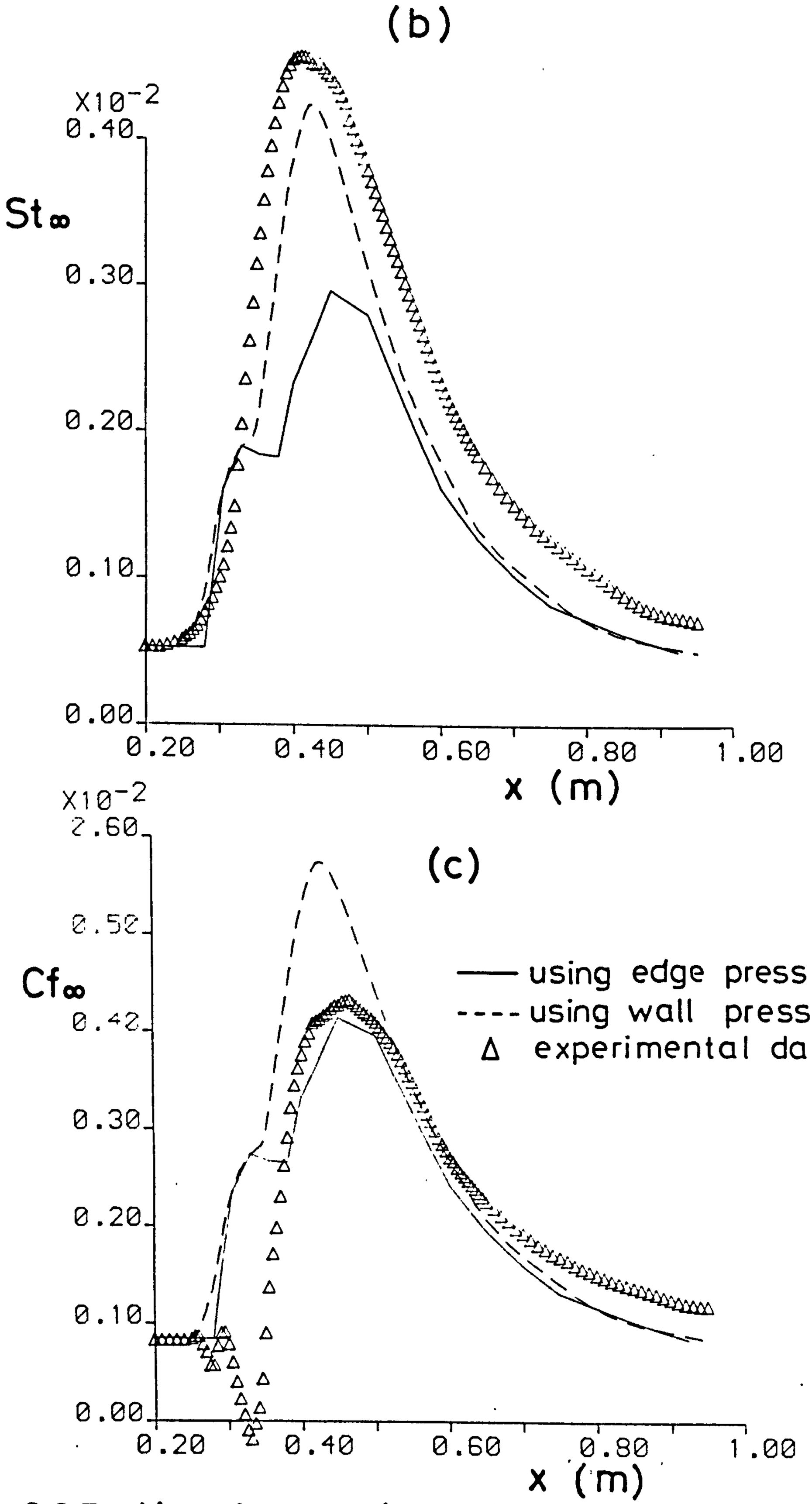

Fig 2.3.5 Horstmann heat transfer & skin friction 15° leading edge shock generator

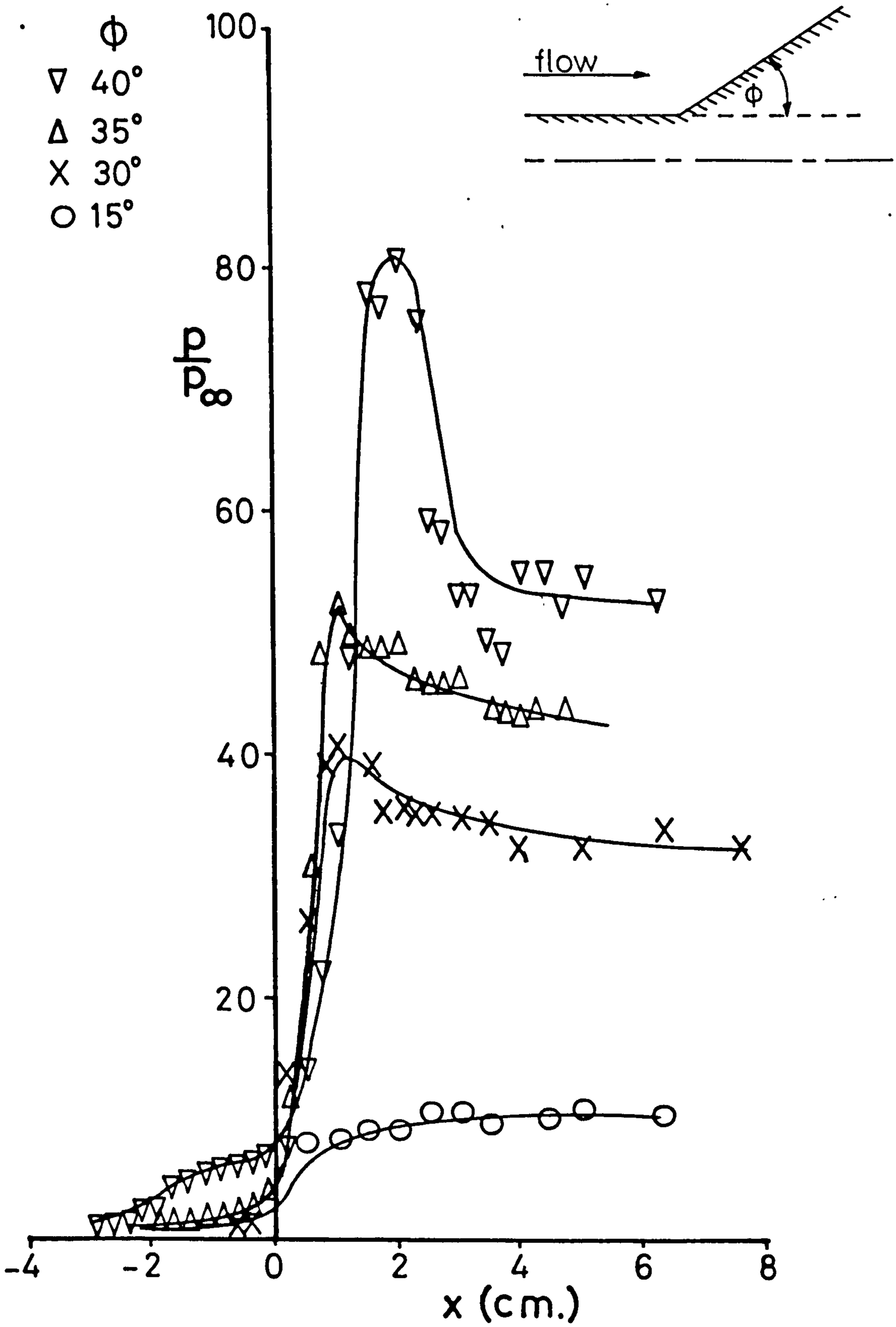

Fig 2.3.6 Pressure distribution over Coleman's cylinder-flare model, used in heat transfer predictions

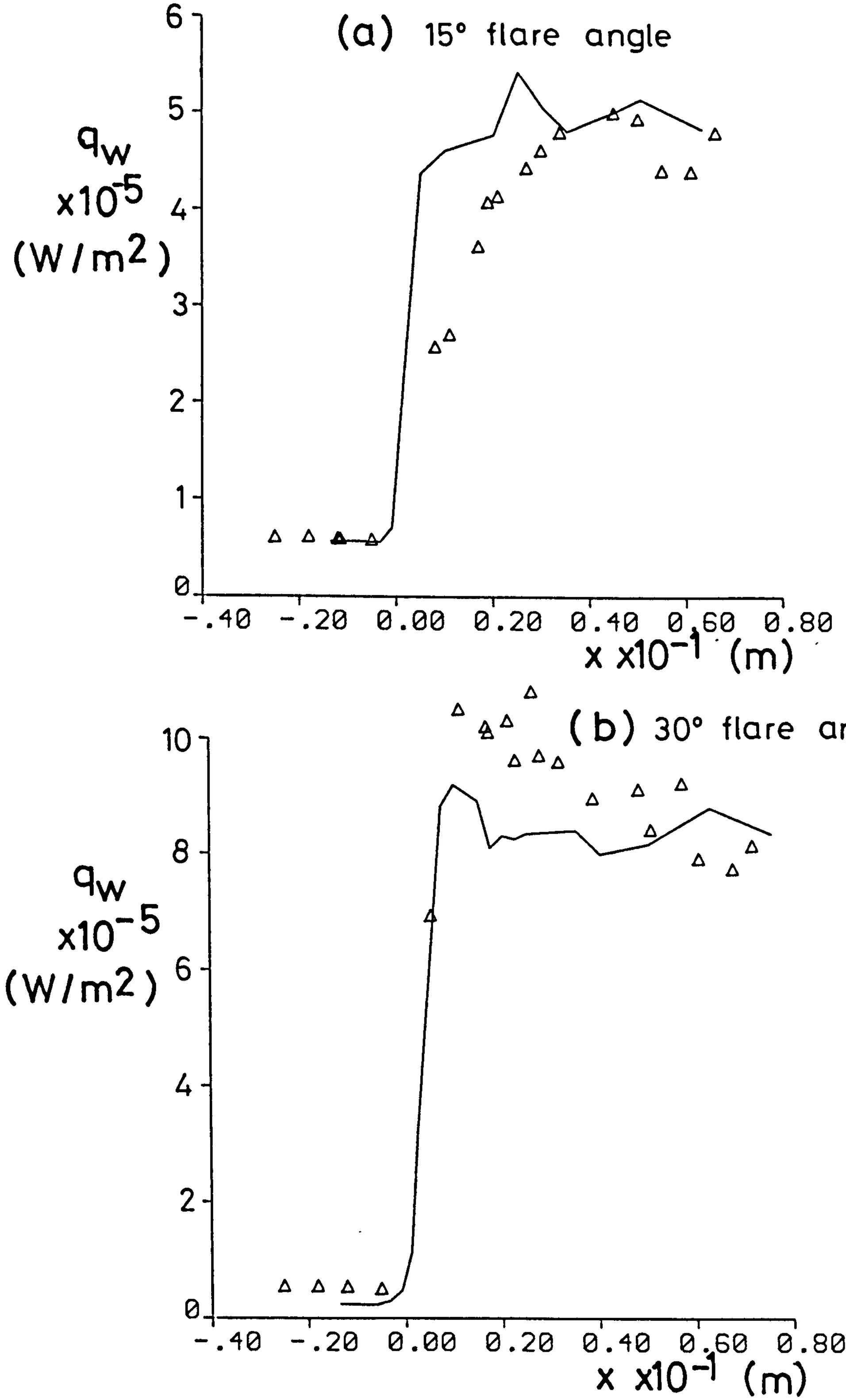

Fig 2.3.7 Heat transfer predictions on hollow cylinder-flare (Coleman)

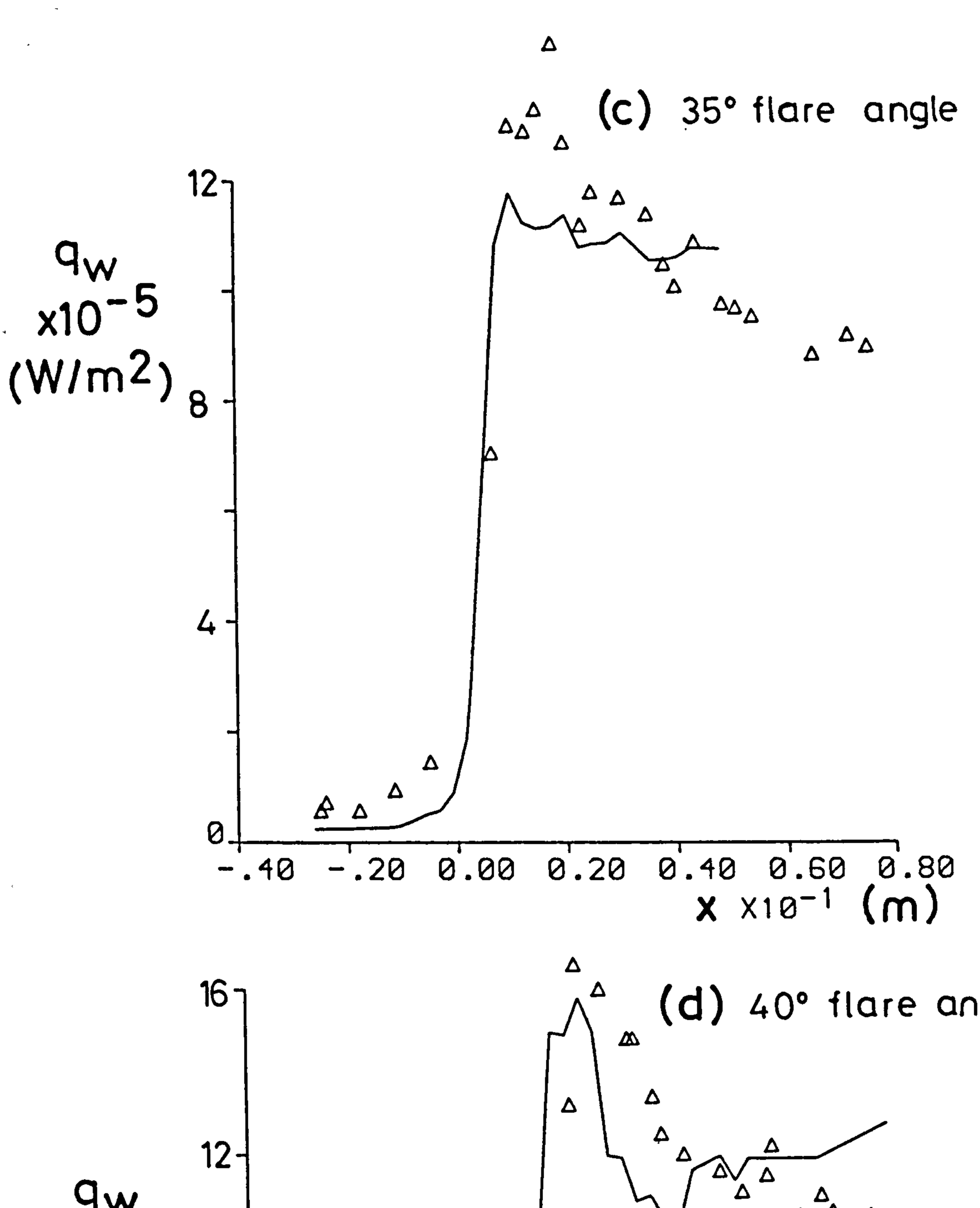

Fig 2.3.7 (contd.)

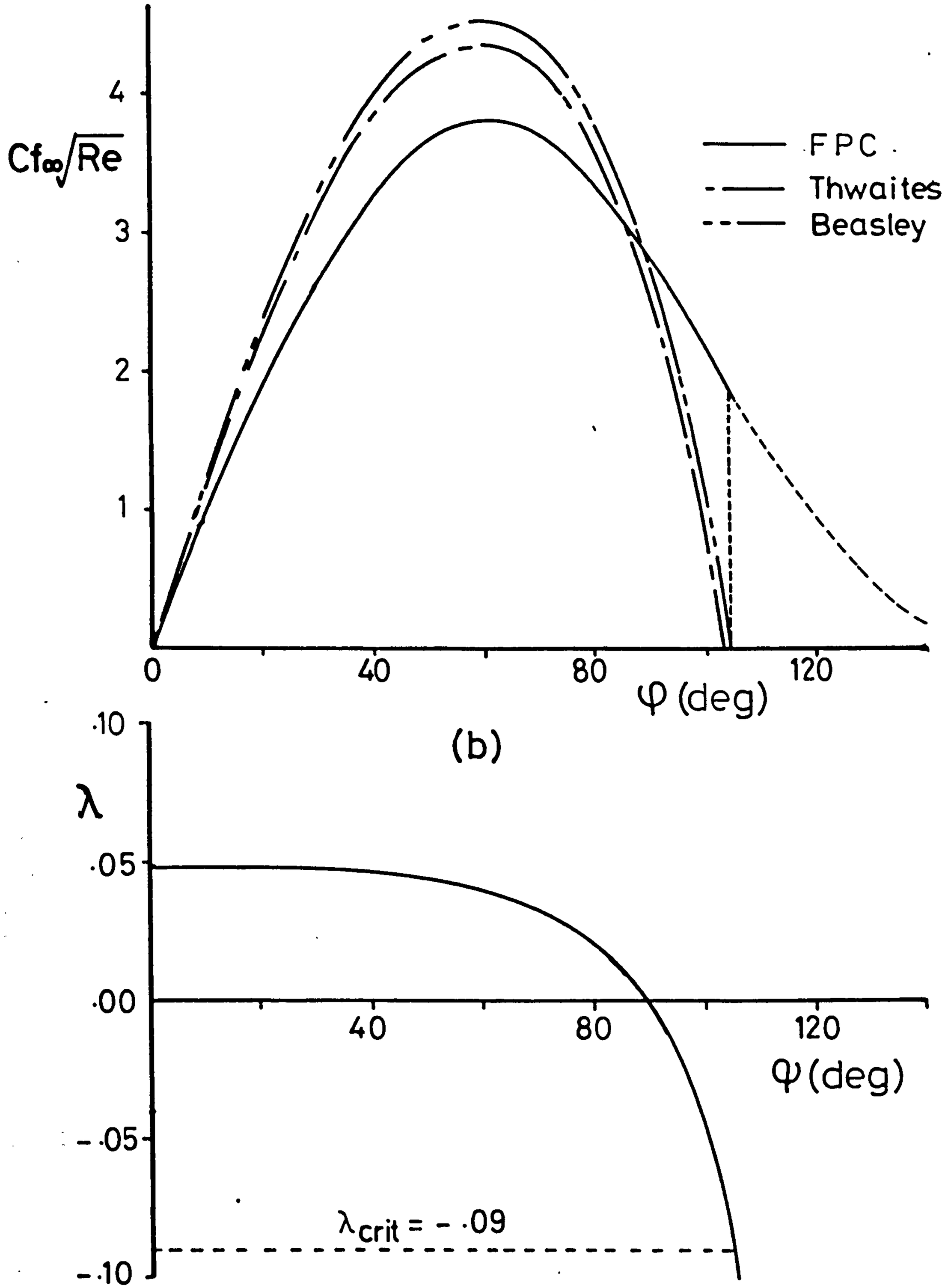

Fig 2.4.1 Laminar separation on an infinite cylinder, comparison between theories (skin friction)

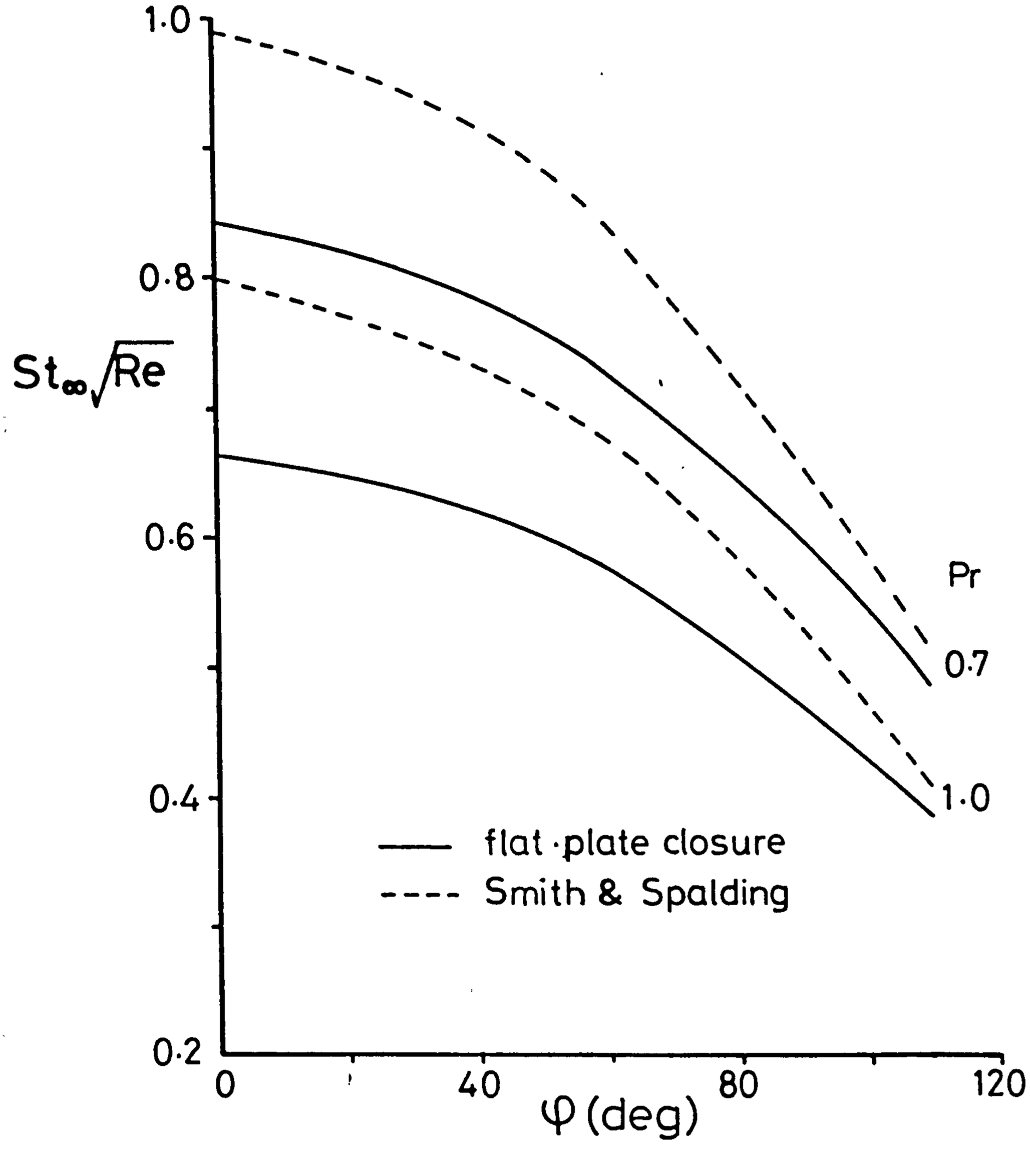

Fig 2.4.2 Laminar flow on an infinite cylinder, comparison between theories (heat transfer)

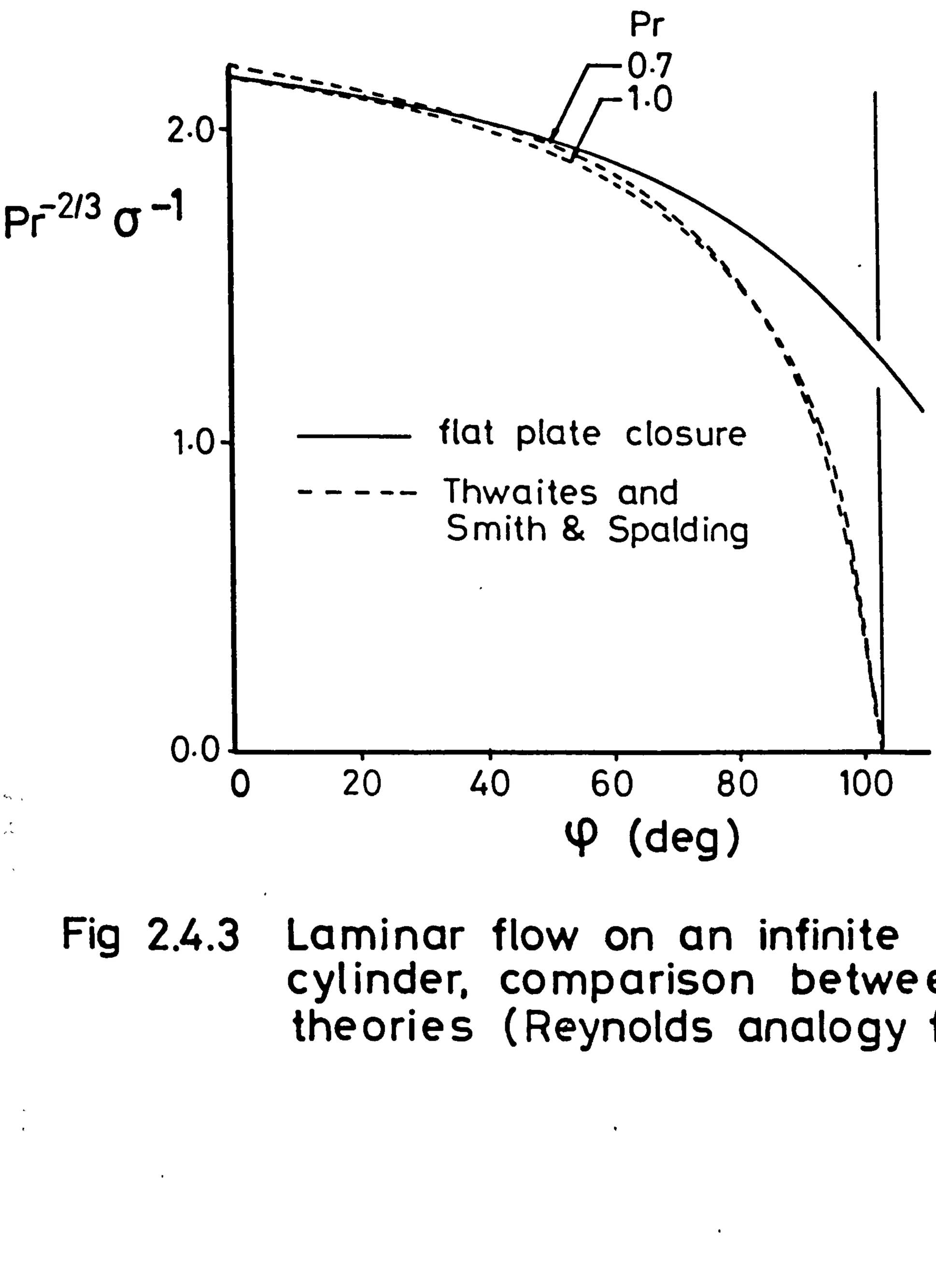

Fig 2.4.3 Laminar flow on an infinite cylinder, comparison between theories (Reynolds analogy factor)

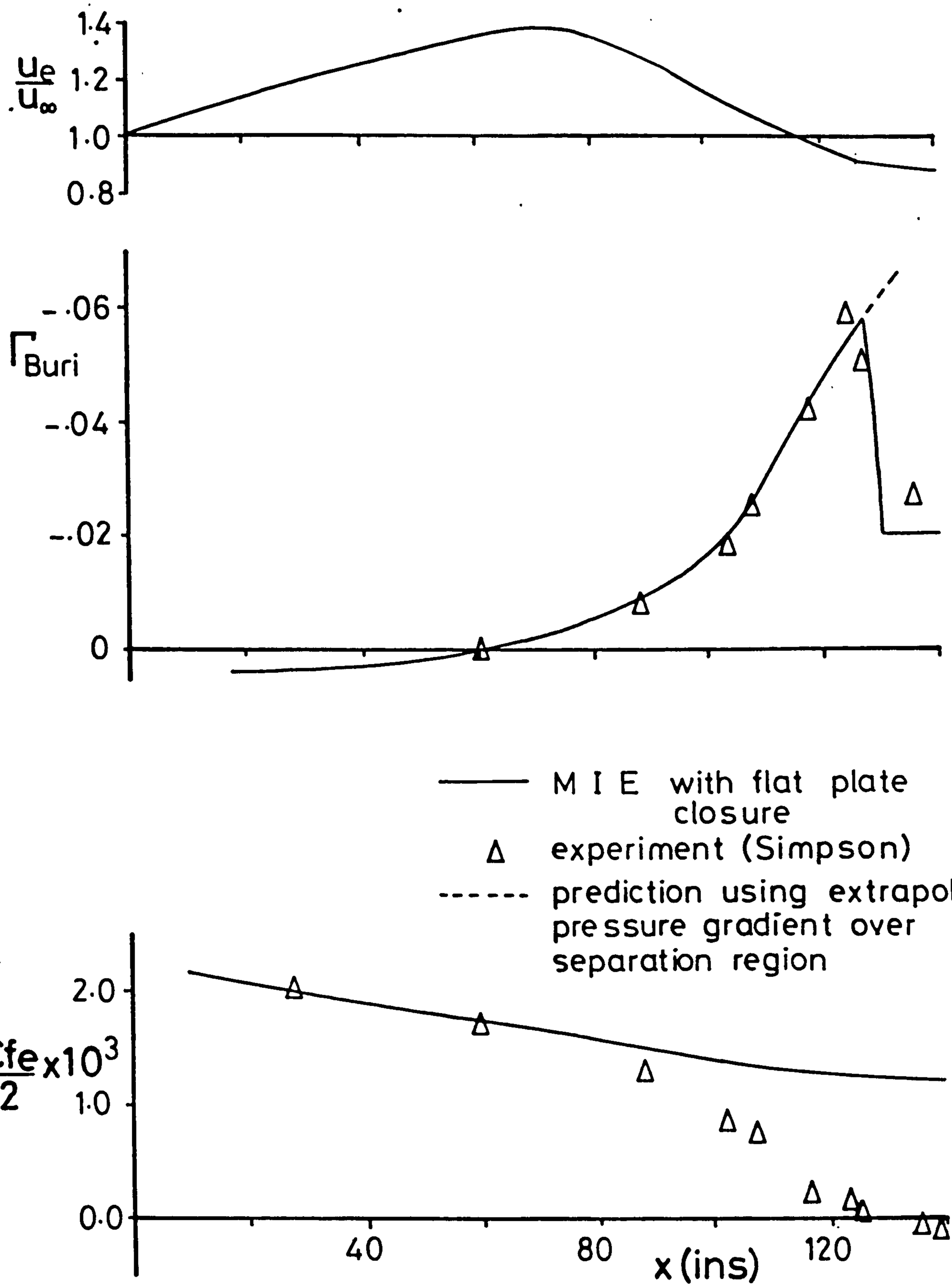

Fig 2.4.4 Turbulent separation flow, comparison between prediction using Buri's criteria and experiment

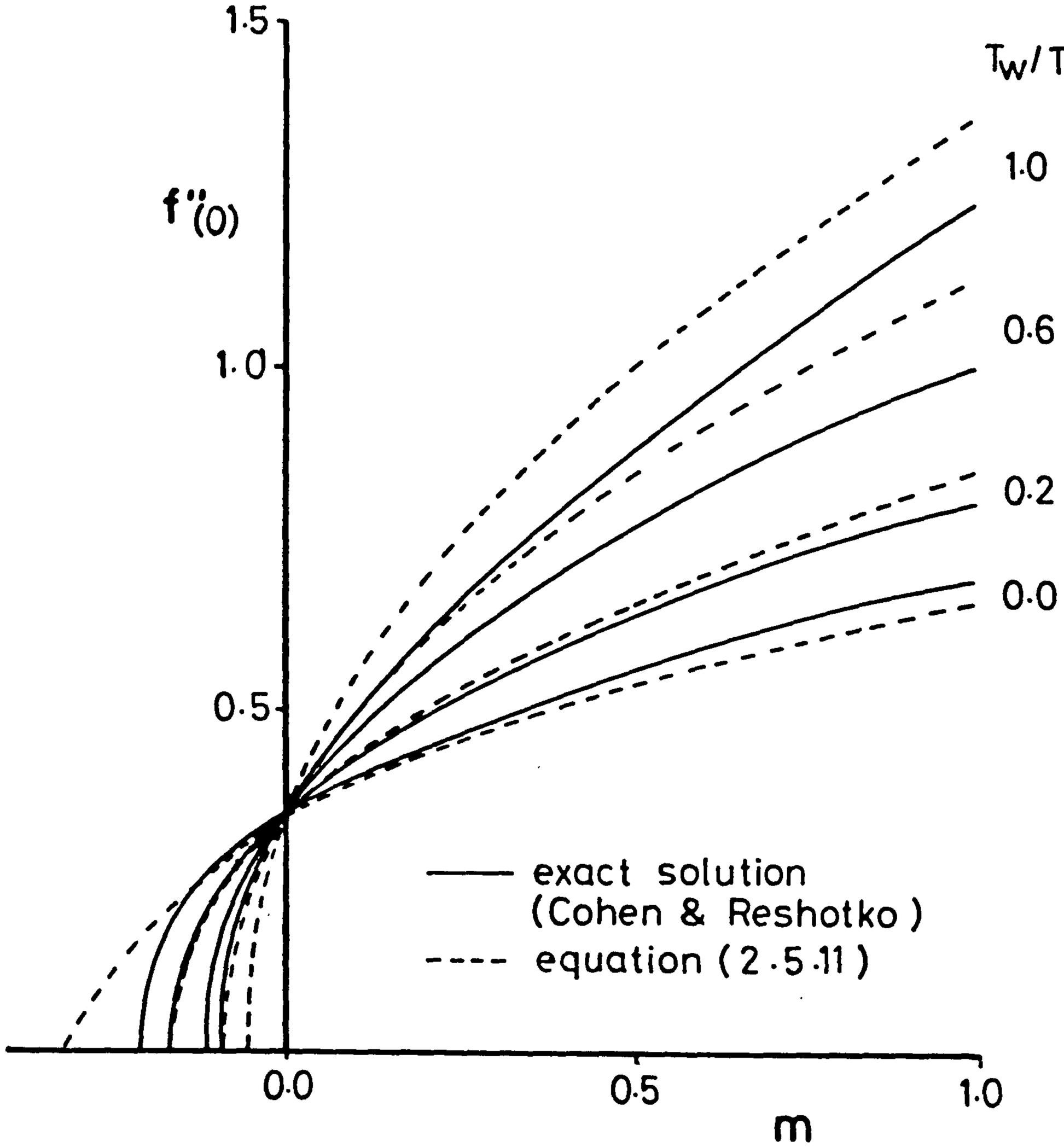

Fig. 2.5.1 Curve fit of Cohen & Reshotko similarity equation velocity gradient at the wall

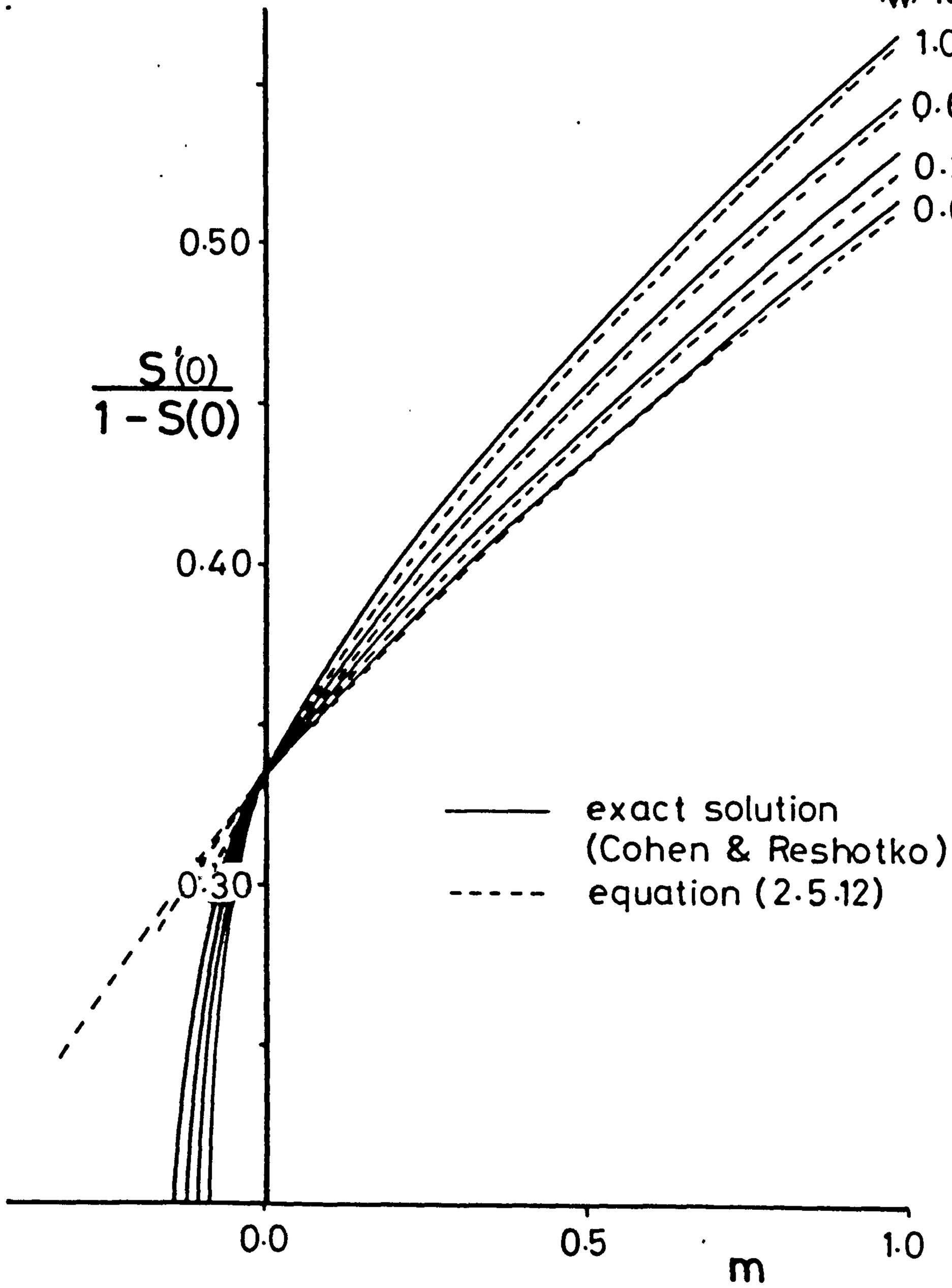

Fig 2.5.2 Curve fit of Cohen & Reshotko similarity equation temperature gradient at the wall

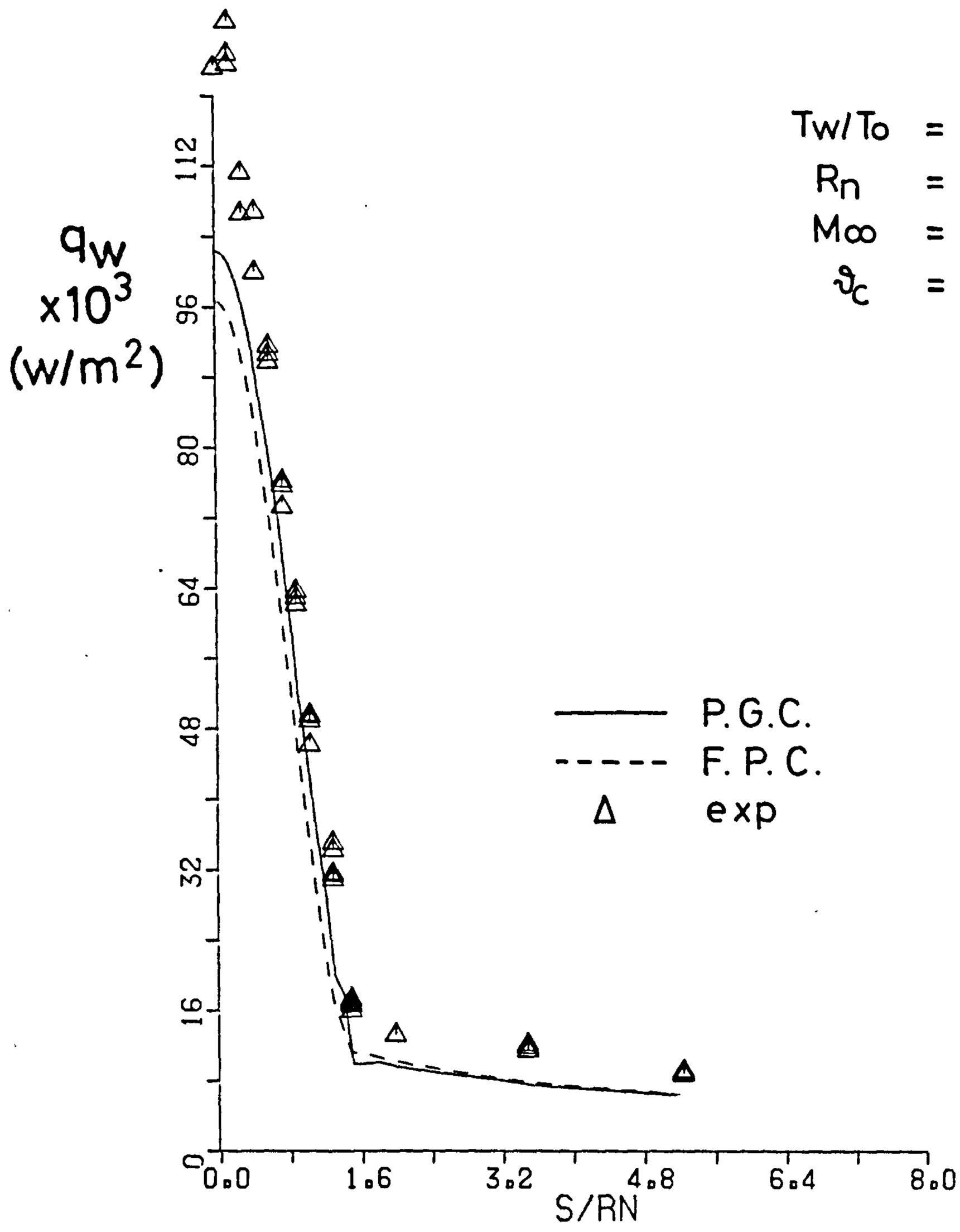

Fig. 2.5.3 Heat transfer rates to spherically blunted cones at zero incidence (Widhopf data ref 32)

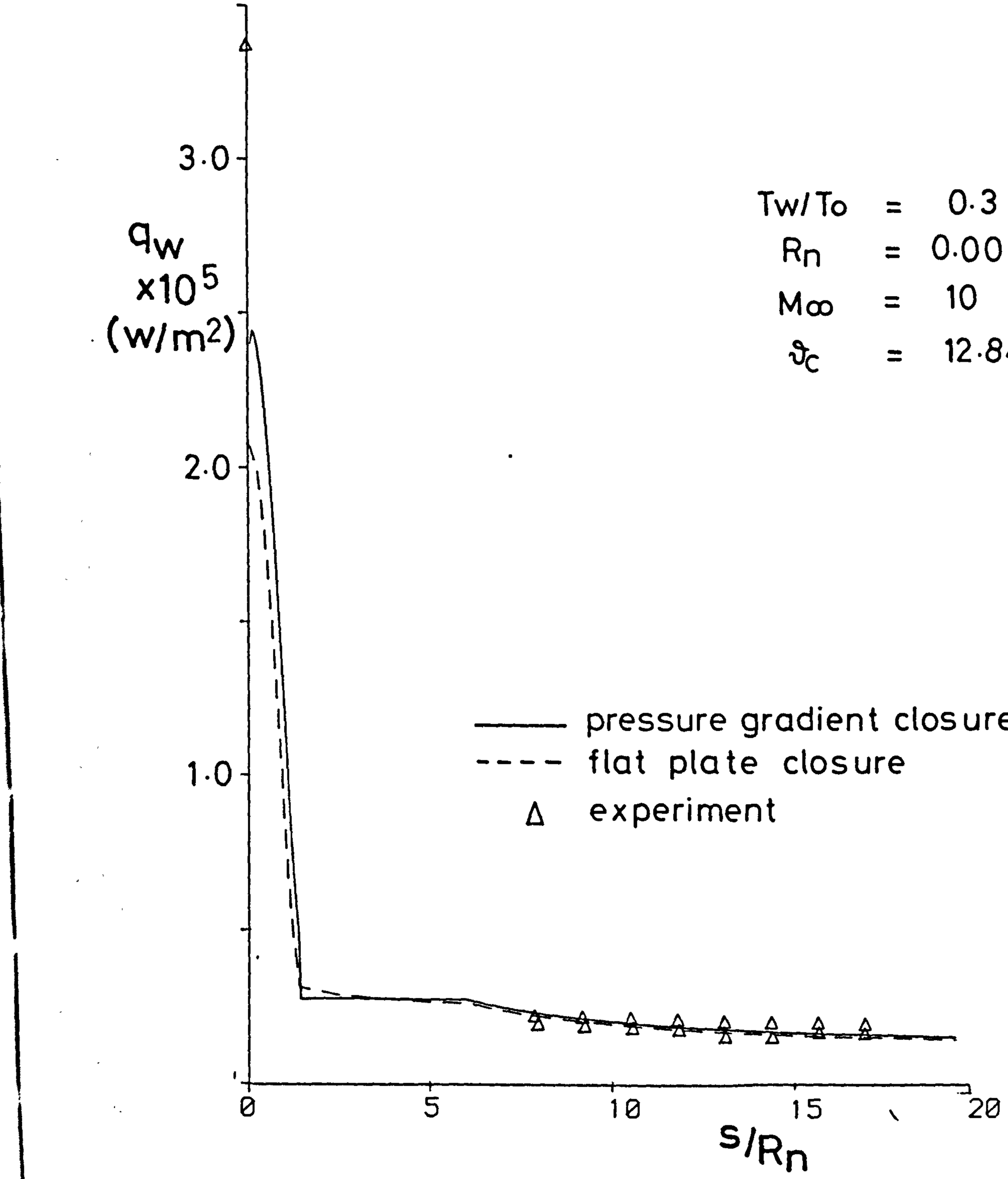

Fig. 2.5.4 Heat transfer rates to spherically blunted cones at zero incidence (Miller data ref. 33)

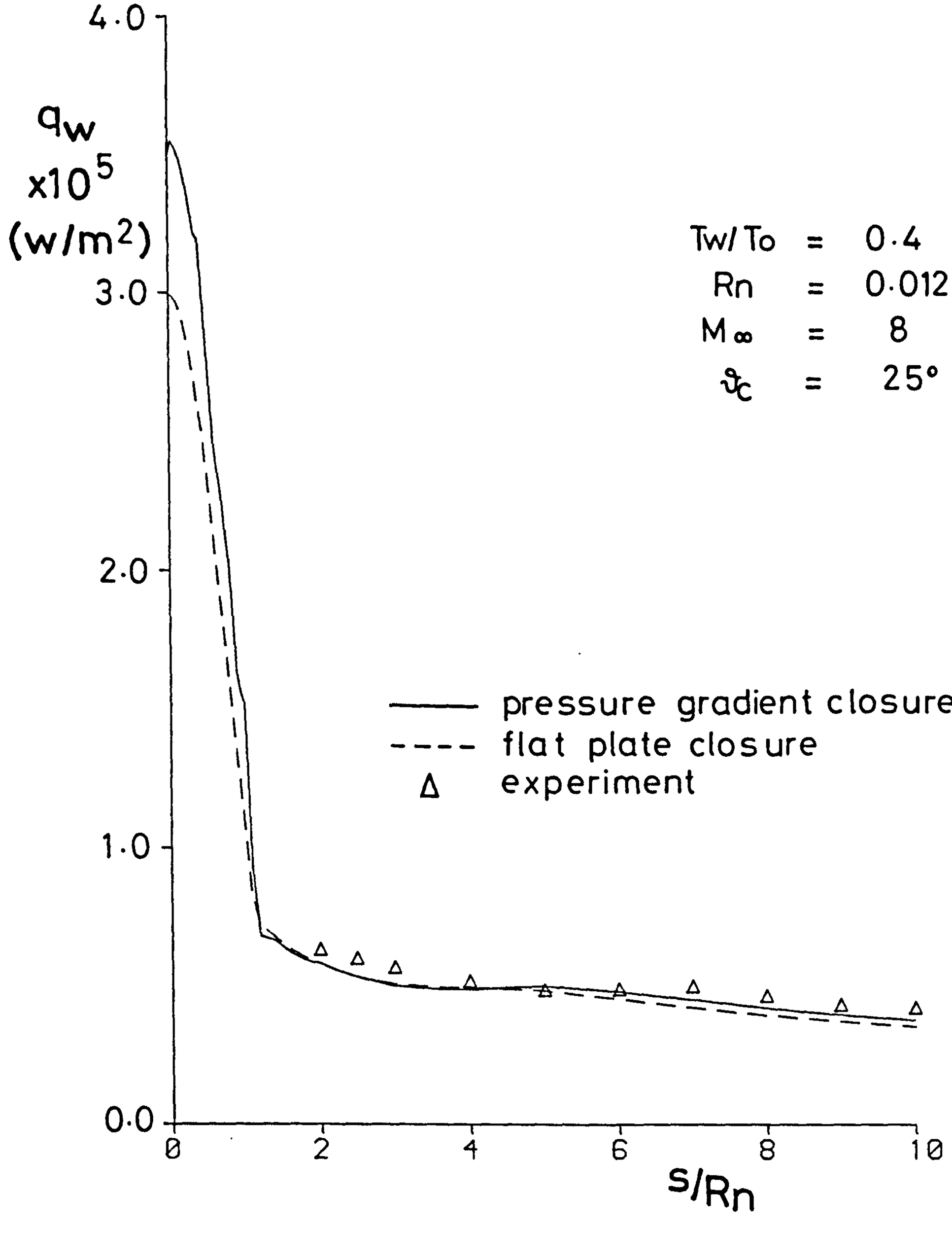

Fig. 2.5.5 Heat transfer rates to spherically blunted cones at zero incidence (Bushnell data ref. 34)

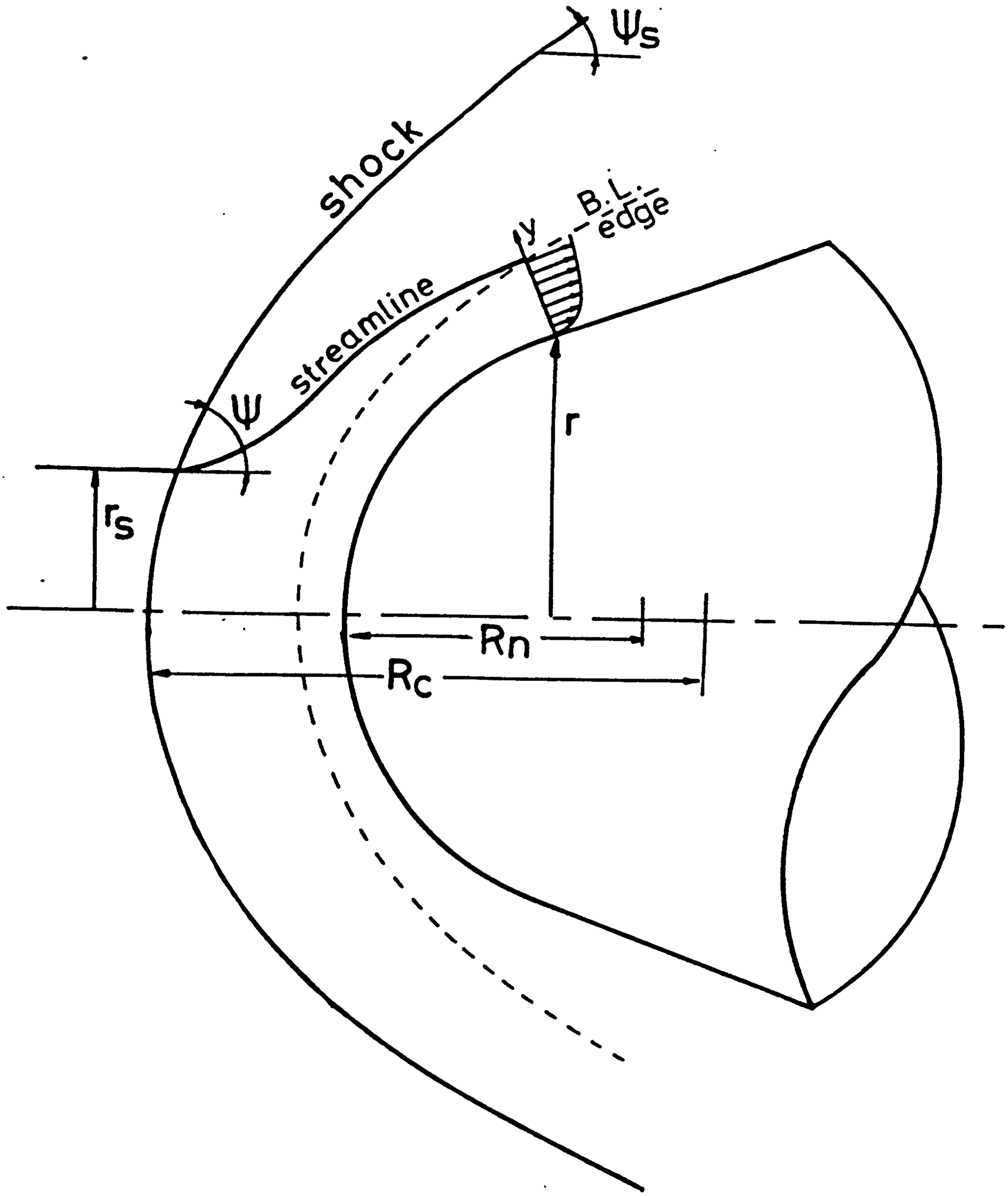

Fig. 2.5.6 Entropy swallowing on a blunt body flow

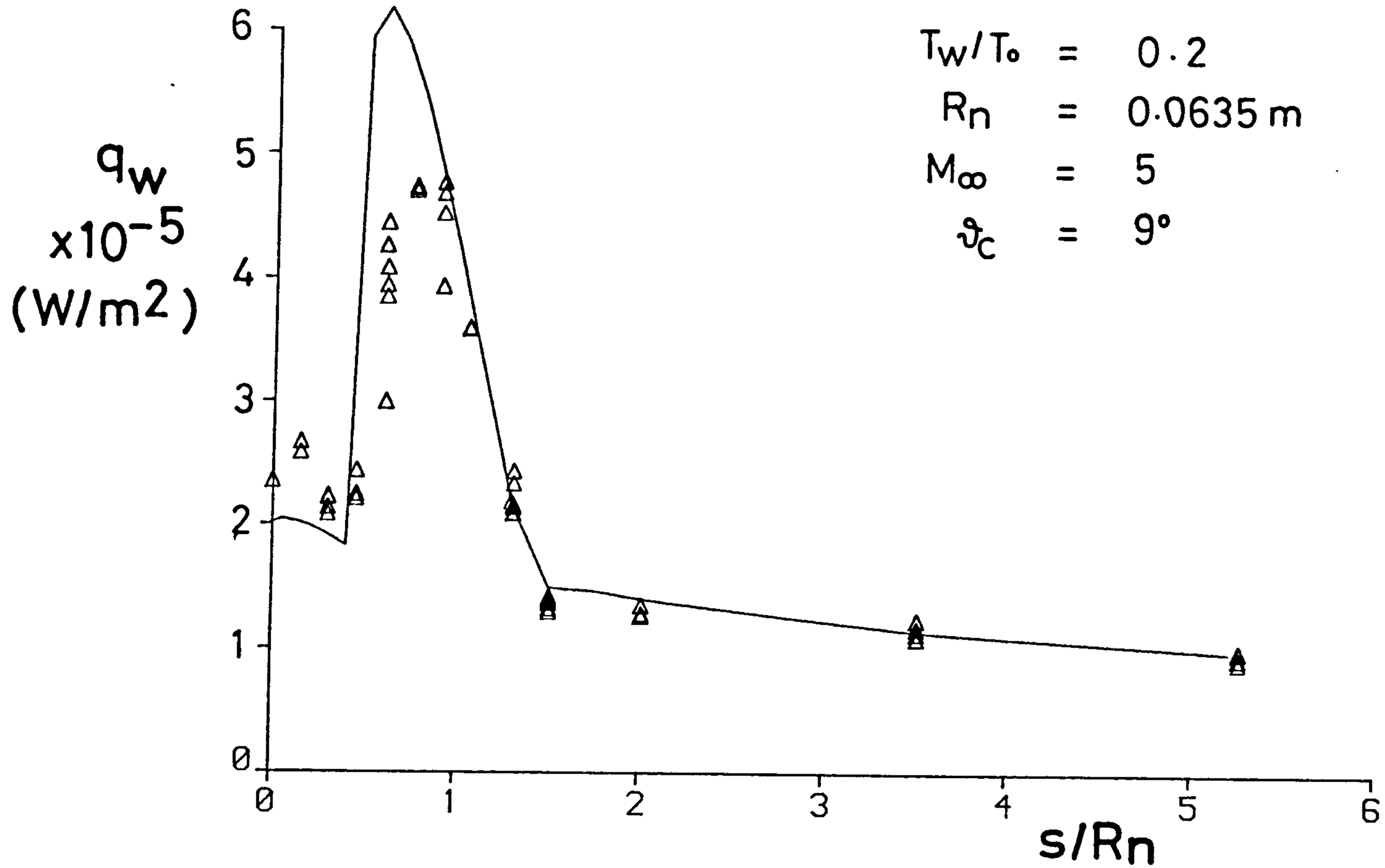

T_w/T_o = 0.2

R_n = 0.0635 m

M_∞ = 5

ϑ_c = 9°

Fig. 2.6.1 Transitional flow over a blunted cone

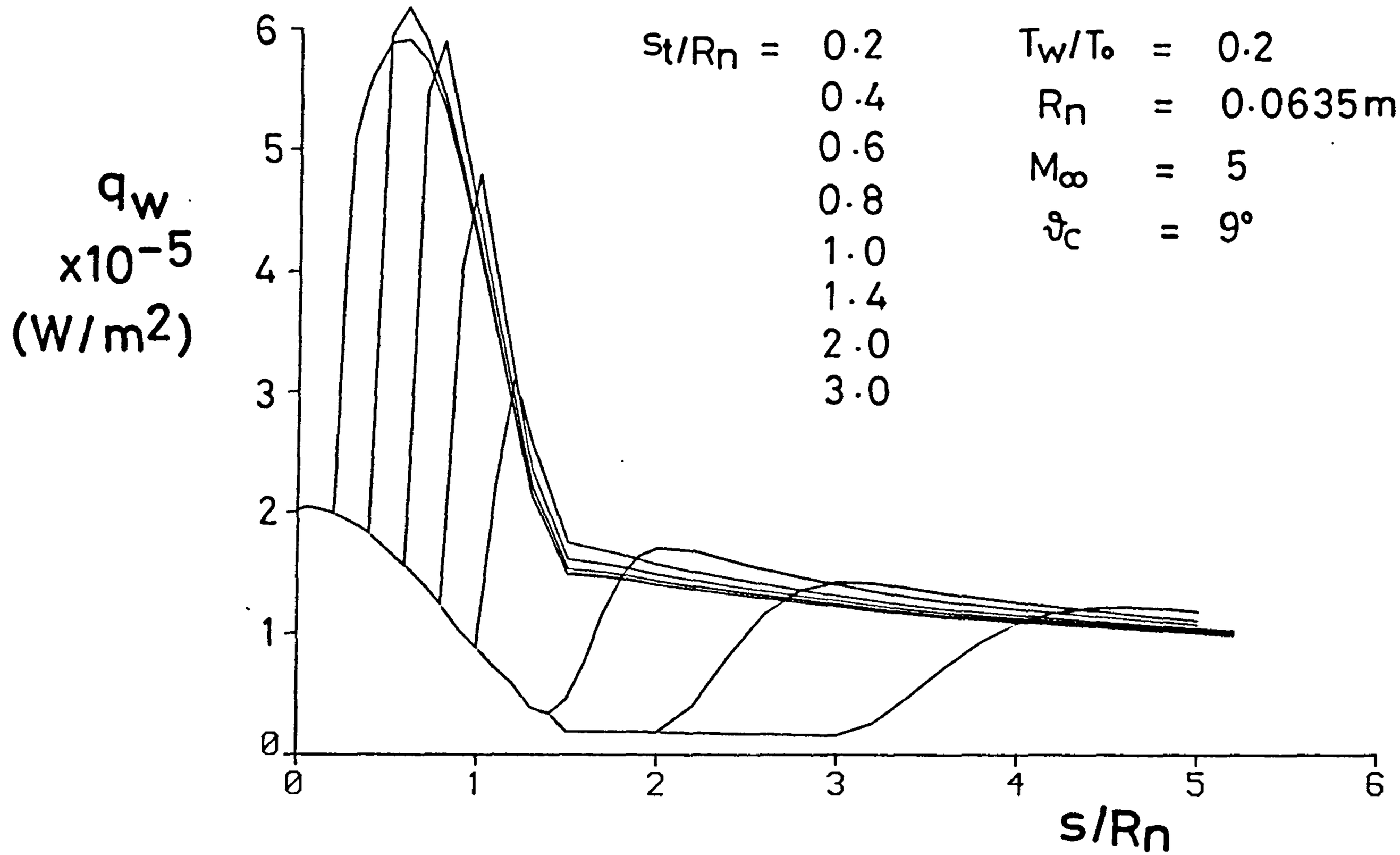

Fig. 2·6·2 Affect of variation of transition onset location on heat transfer over a blunted cone

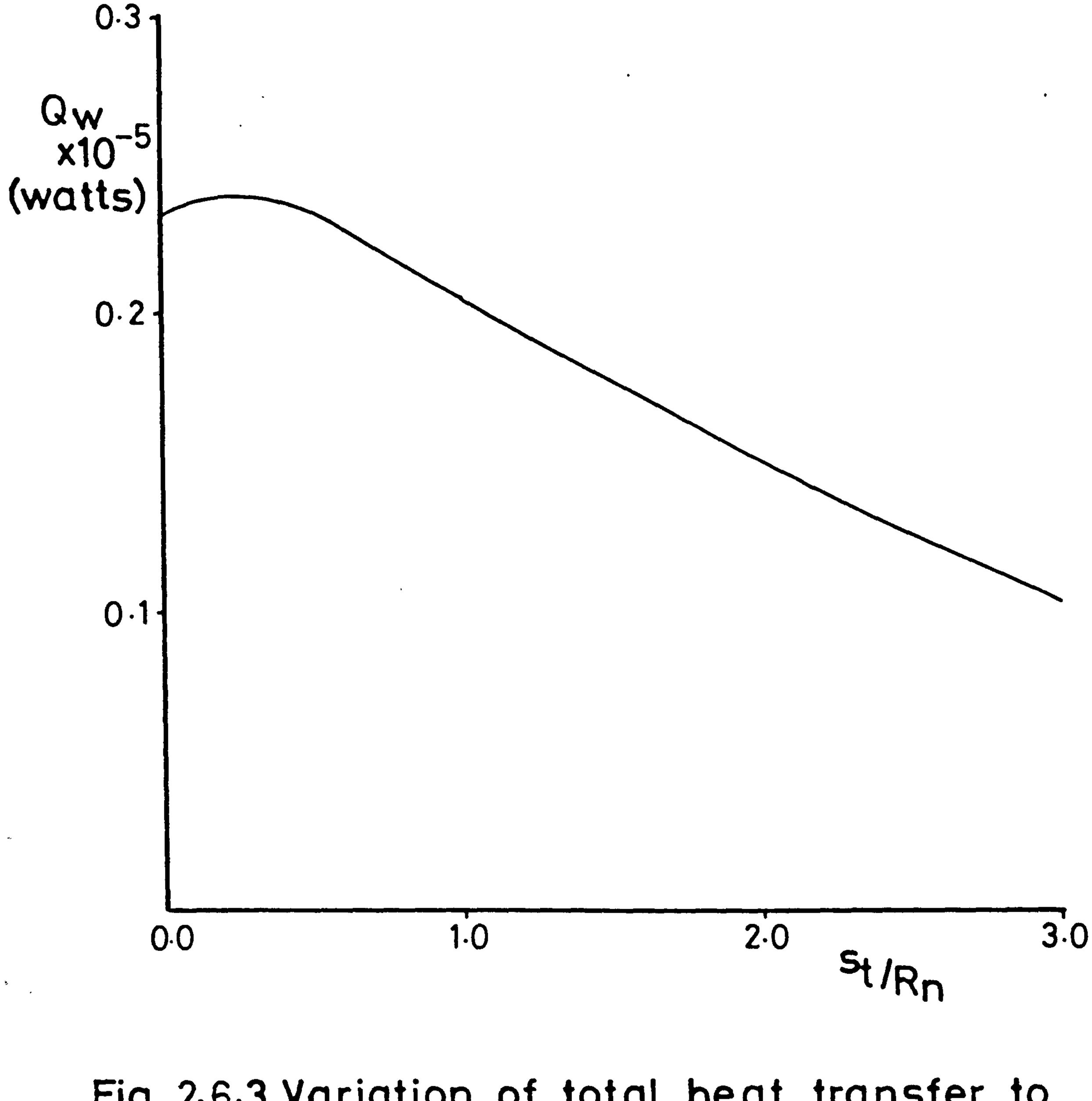

Fig. 2·6·3 Variation of total heat transfer to a blunt cone $s/R_n < 5$ with onset of transition location (integrated curves of fig(2.6.2))

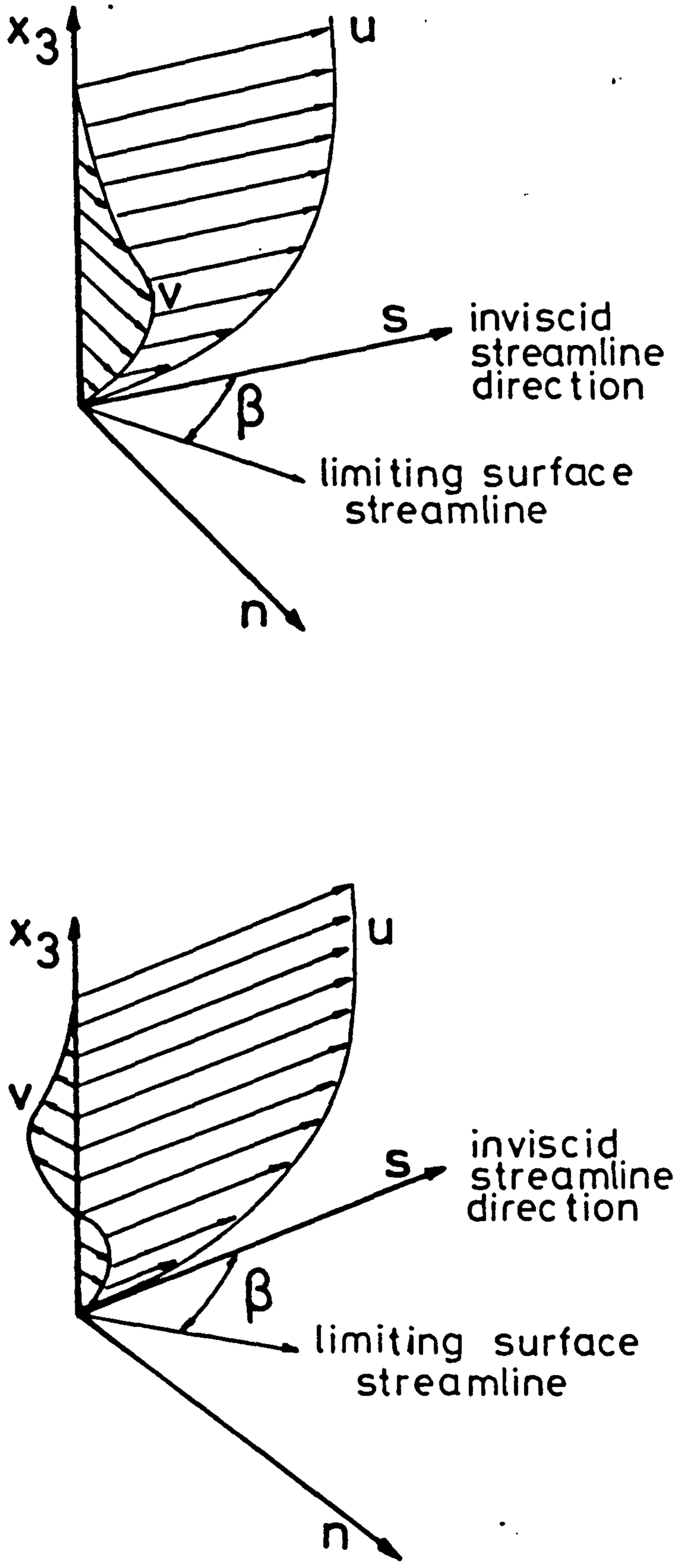

Fig.3.1.1 Shape of 3-dimensional boundary layer velocity profiles

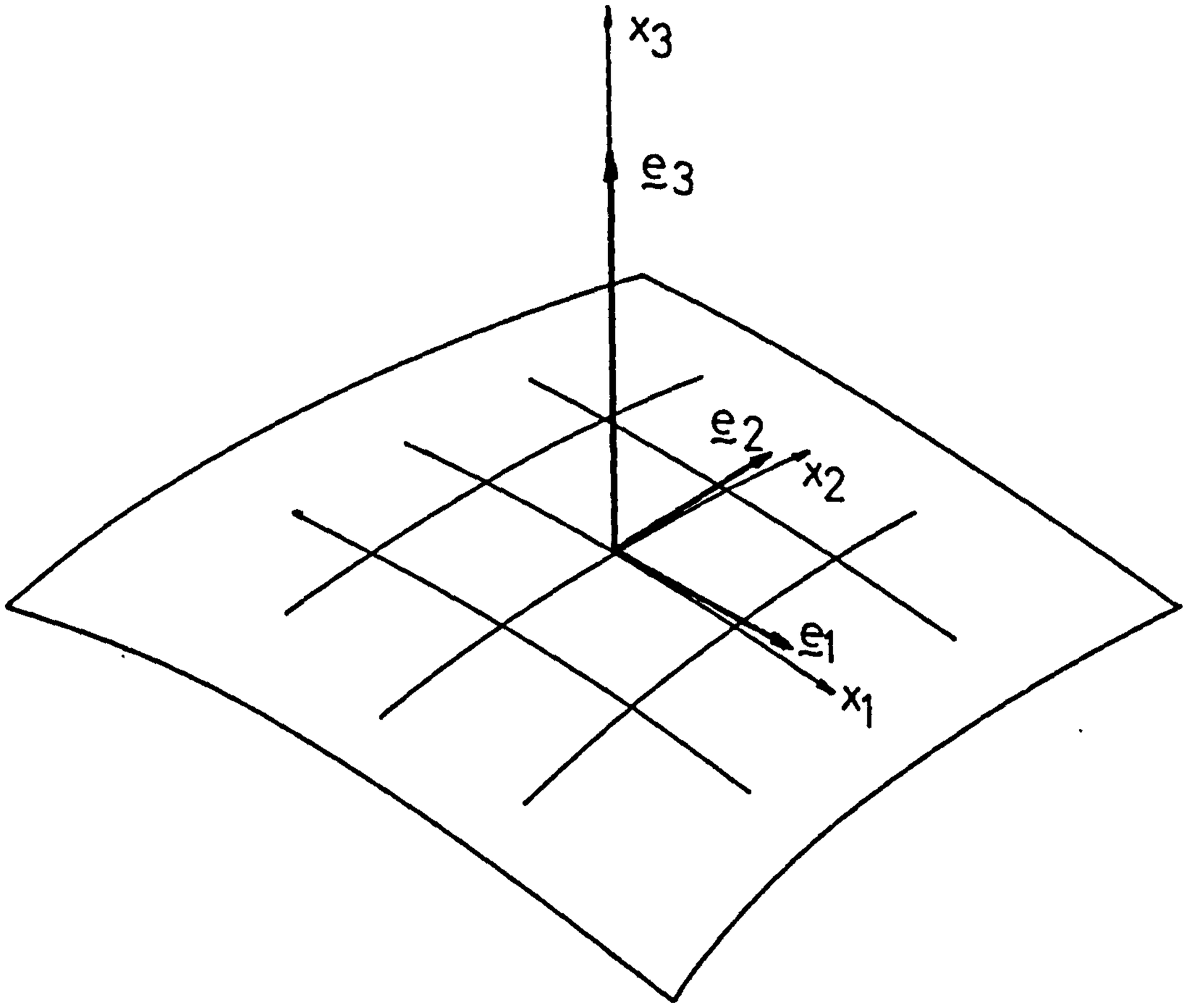

Fig. 3.2.1 Orthogonal curvilinear coordinate system

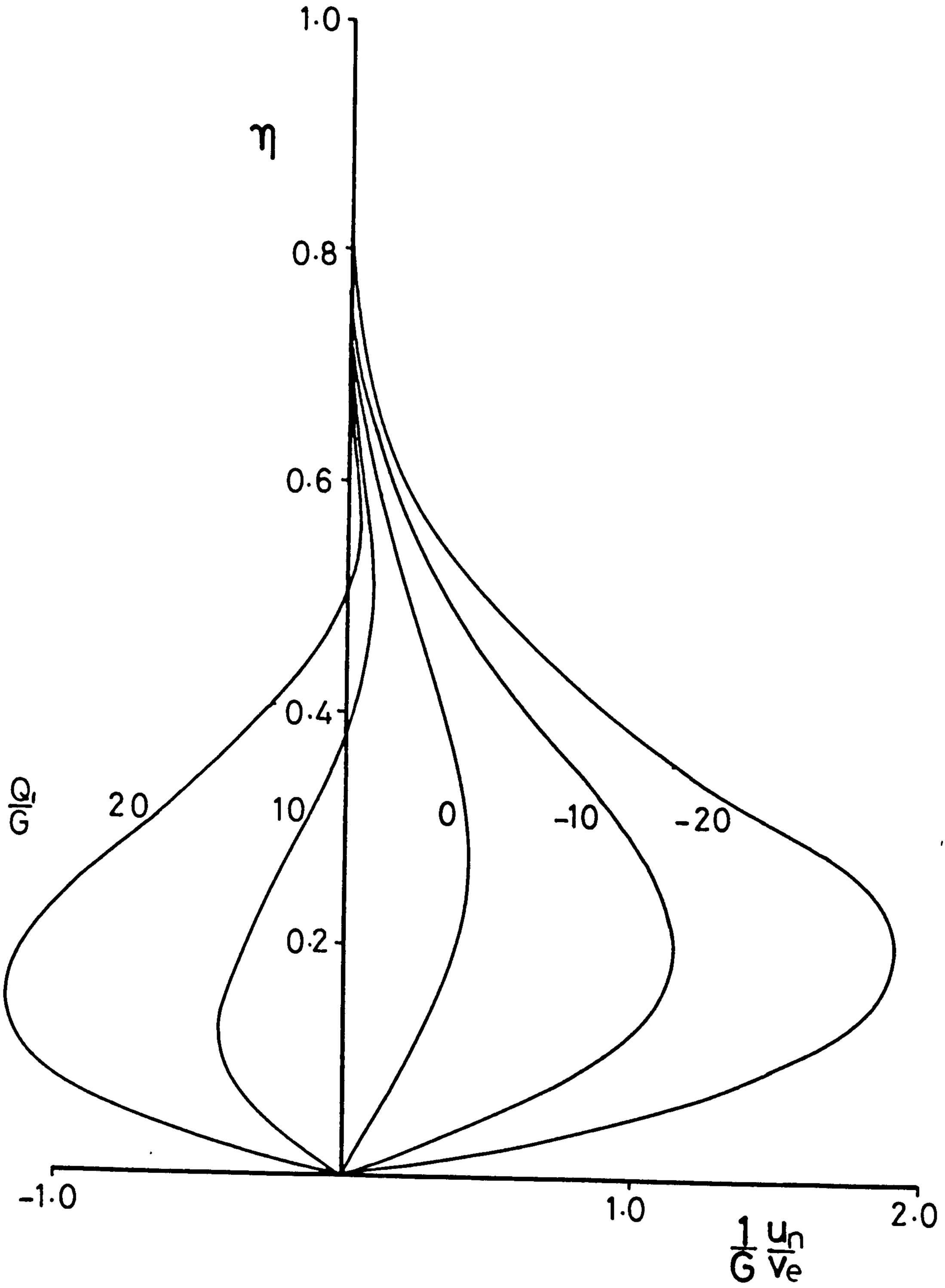

Fig.3.3.1 Kang crossflow profiles

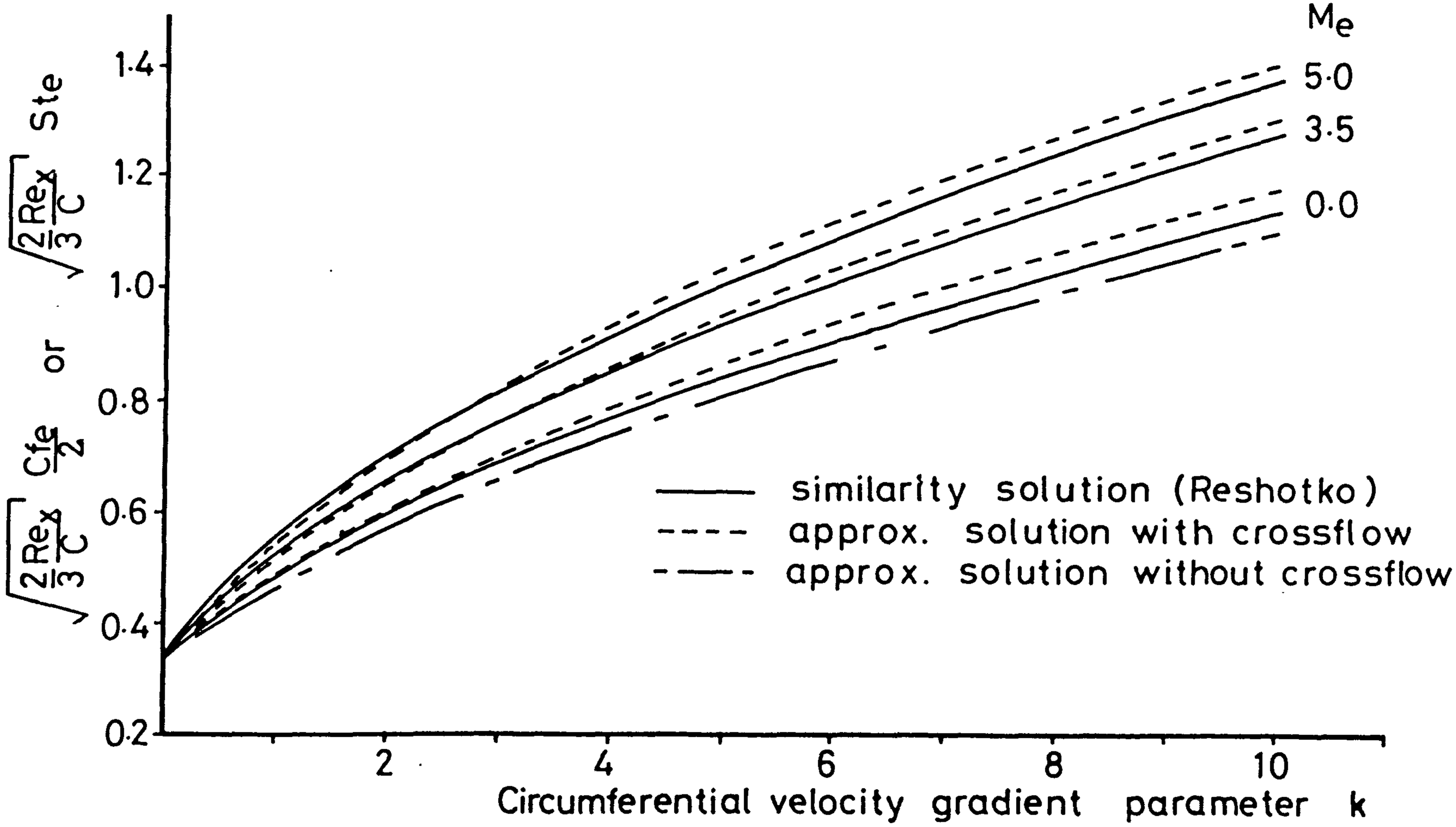

Fig. 3.4.1a Skin friction/heat transfer on attachment line of a sharp cone

$T_w / To_\infty = 0.0$

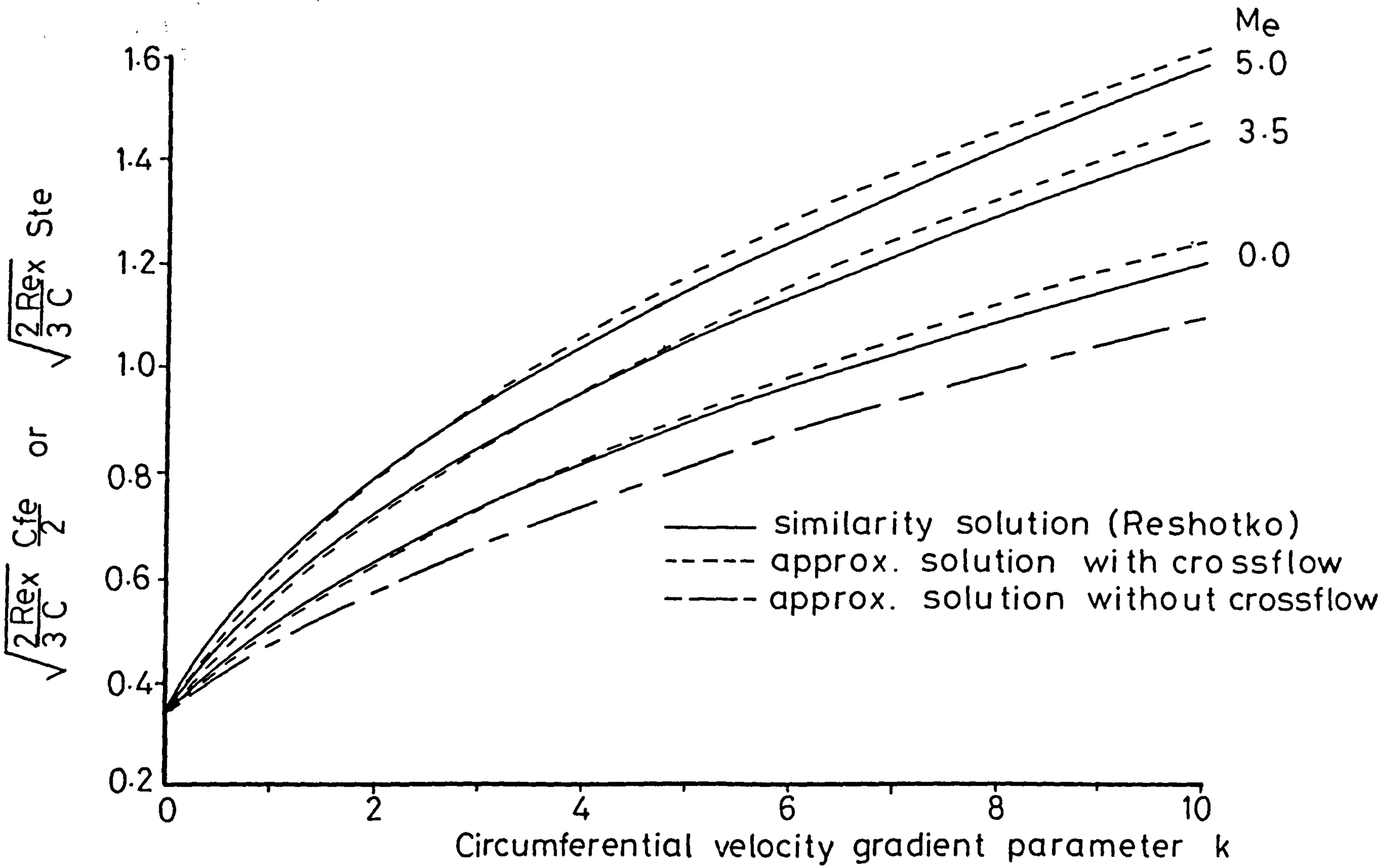

Fig. 3.4.1b $T_w/To_\infty = 0.5$

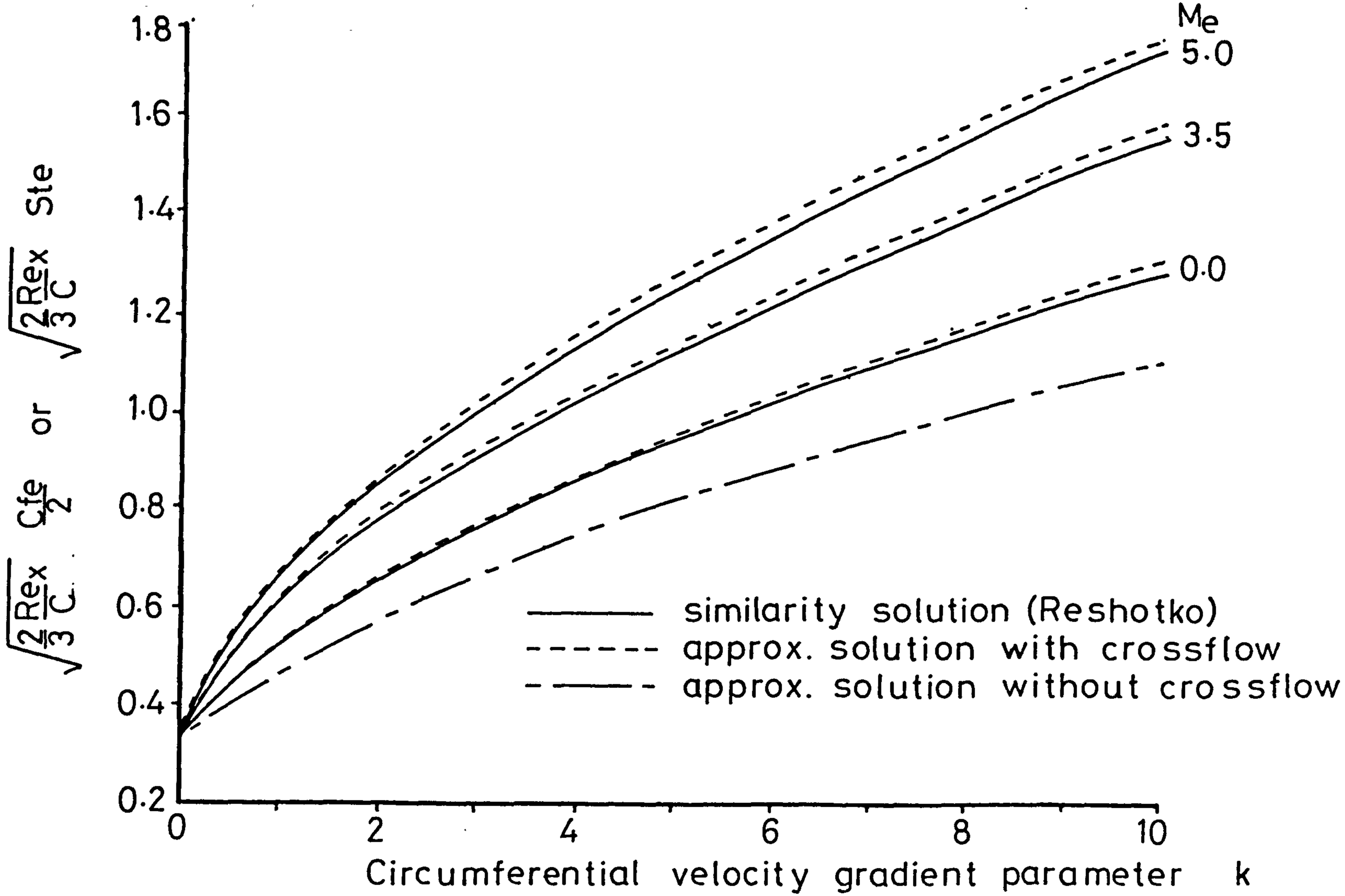

Fig. 3.4.1c $T_w / T_{o_\infty} = 1.0$

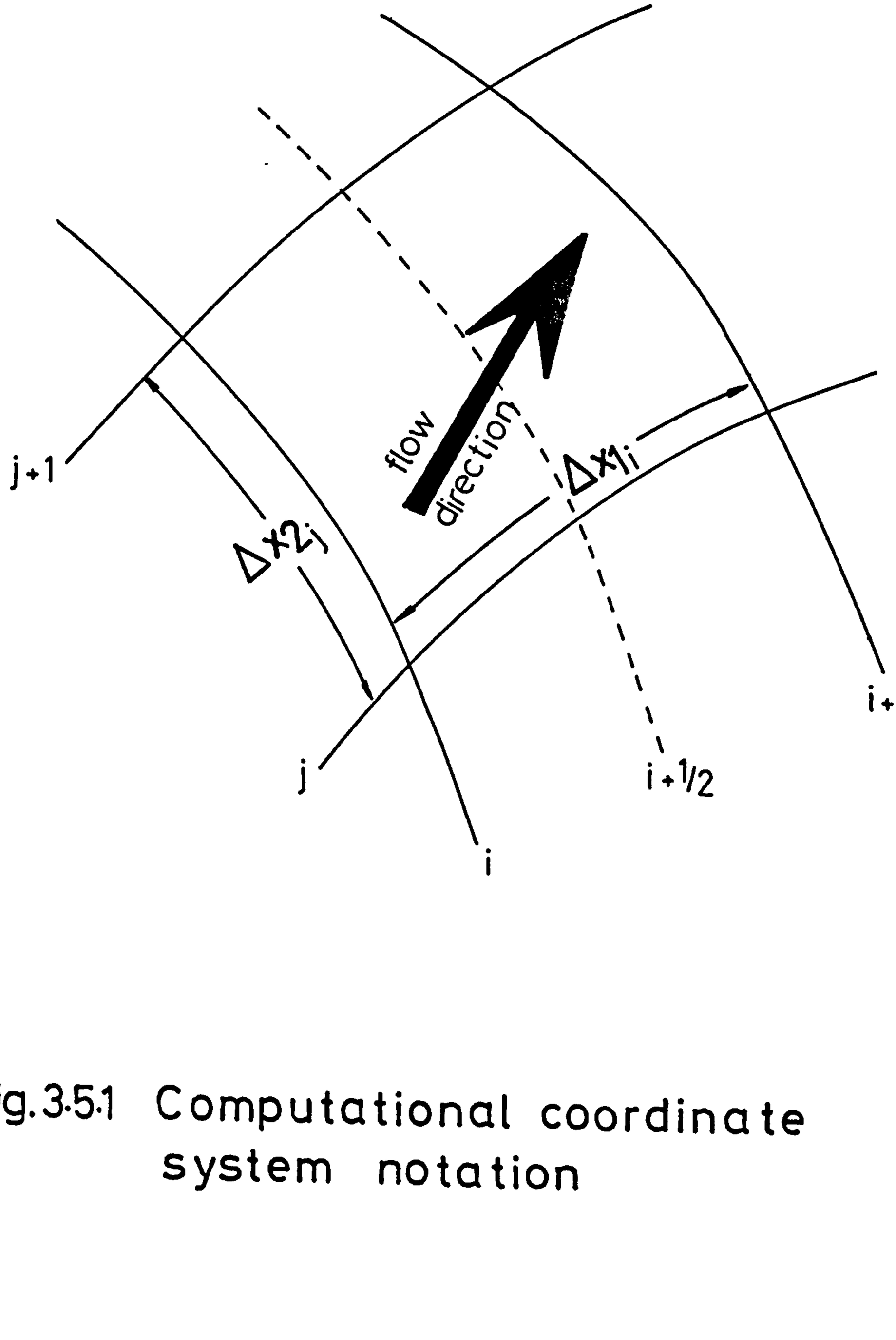

Fig.3.5.1 Computational coordinate system notation

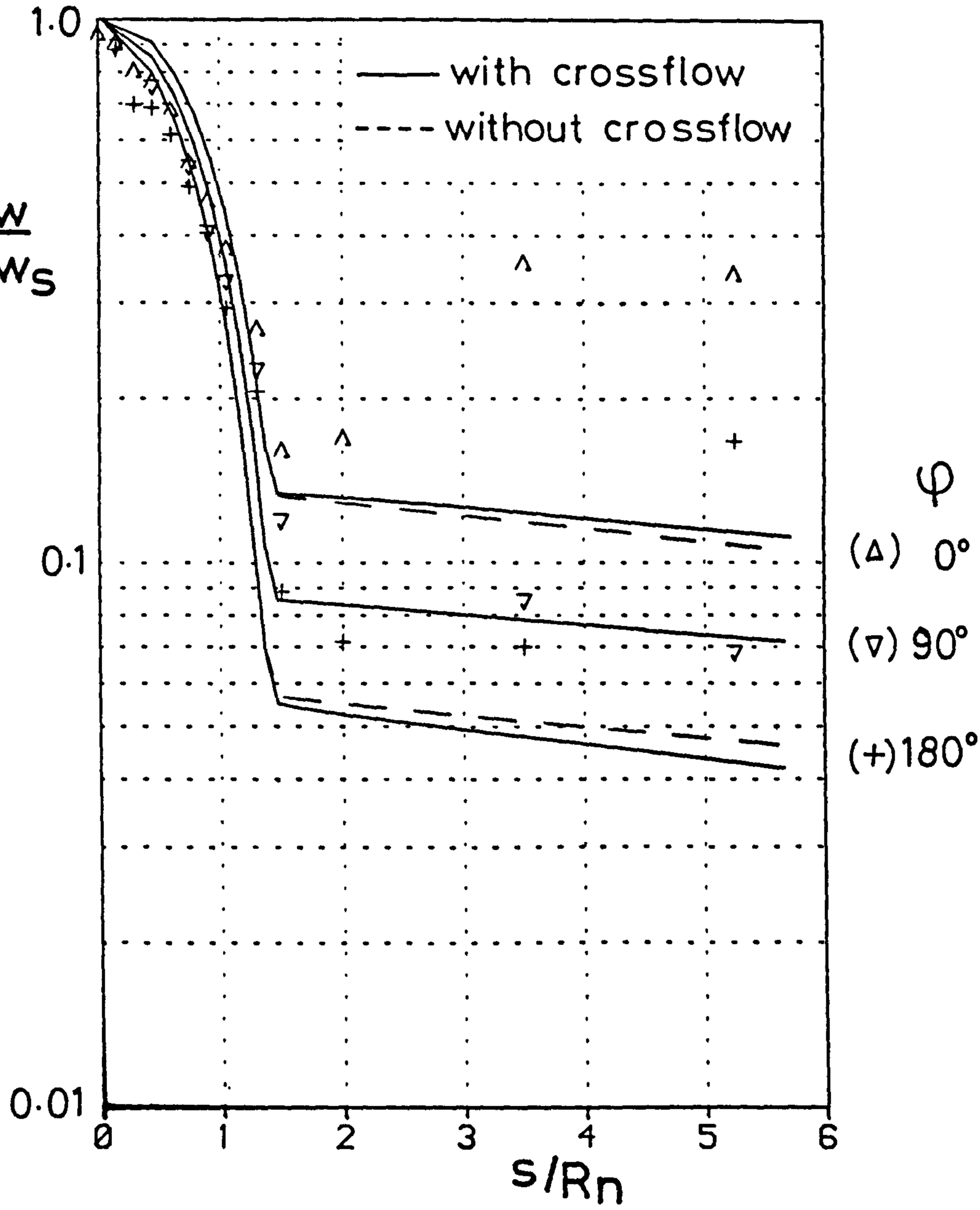

Fig.3.6.1a Blunted cone at incidence (Widhopf)

$\vartheta_c = 9°$ $M_\infty = 5$ $T_w/To_\infty = 0.28$

$\alpha = 5°$

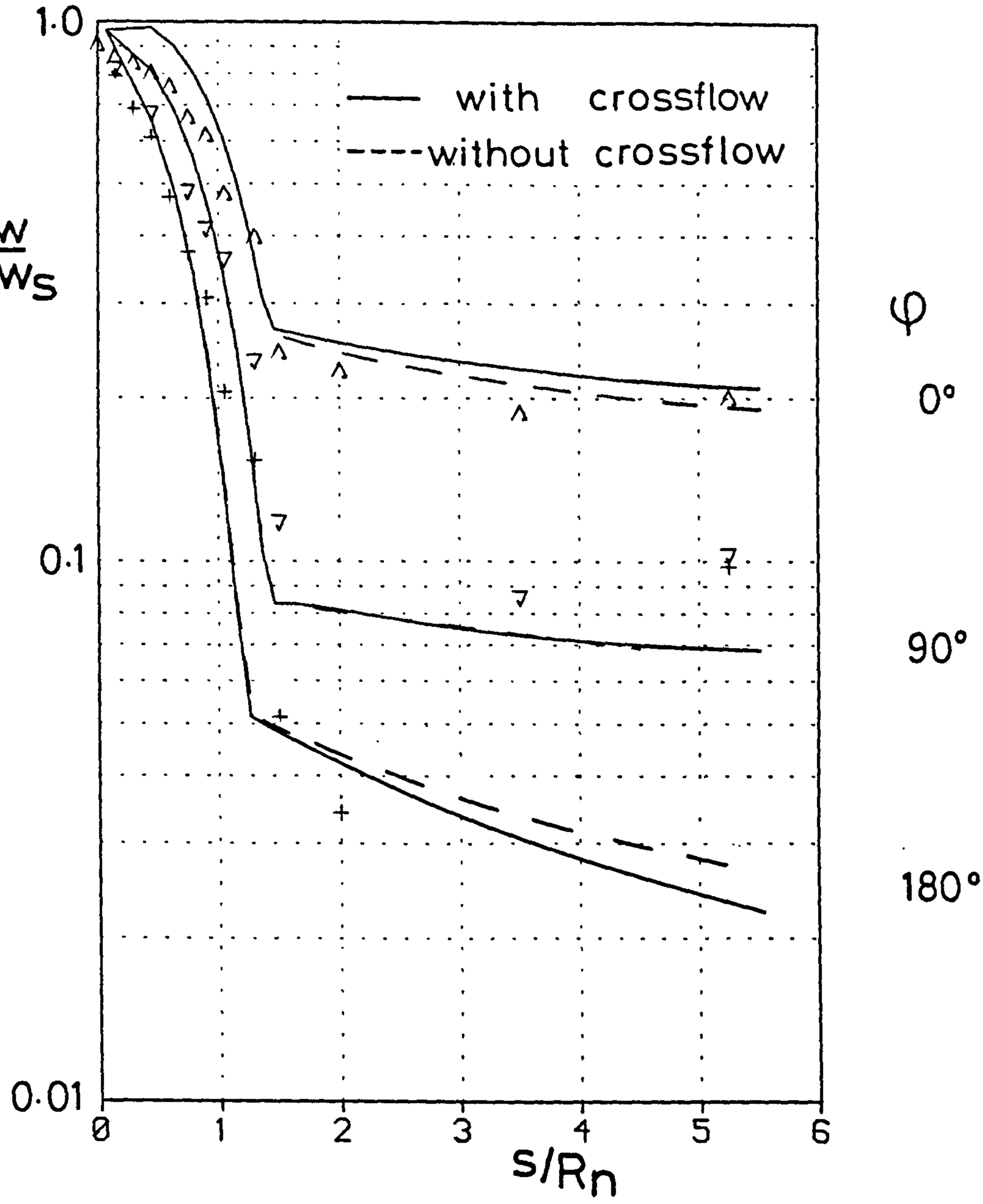

Fig.3.6.1b Blunted cone at incidence (Widhopf)

$\vartheta_c = 9°$ $M_\infty = 5$ $T_w/To_\infty = 0.28$

$\alpha = 15°$

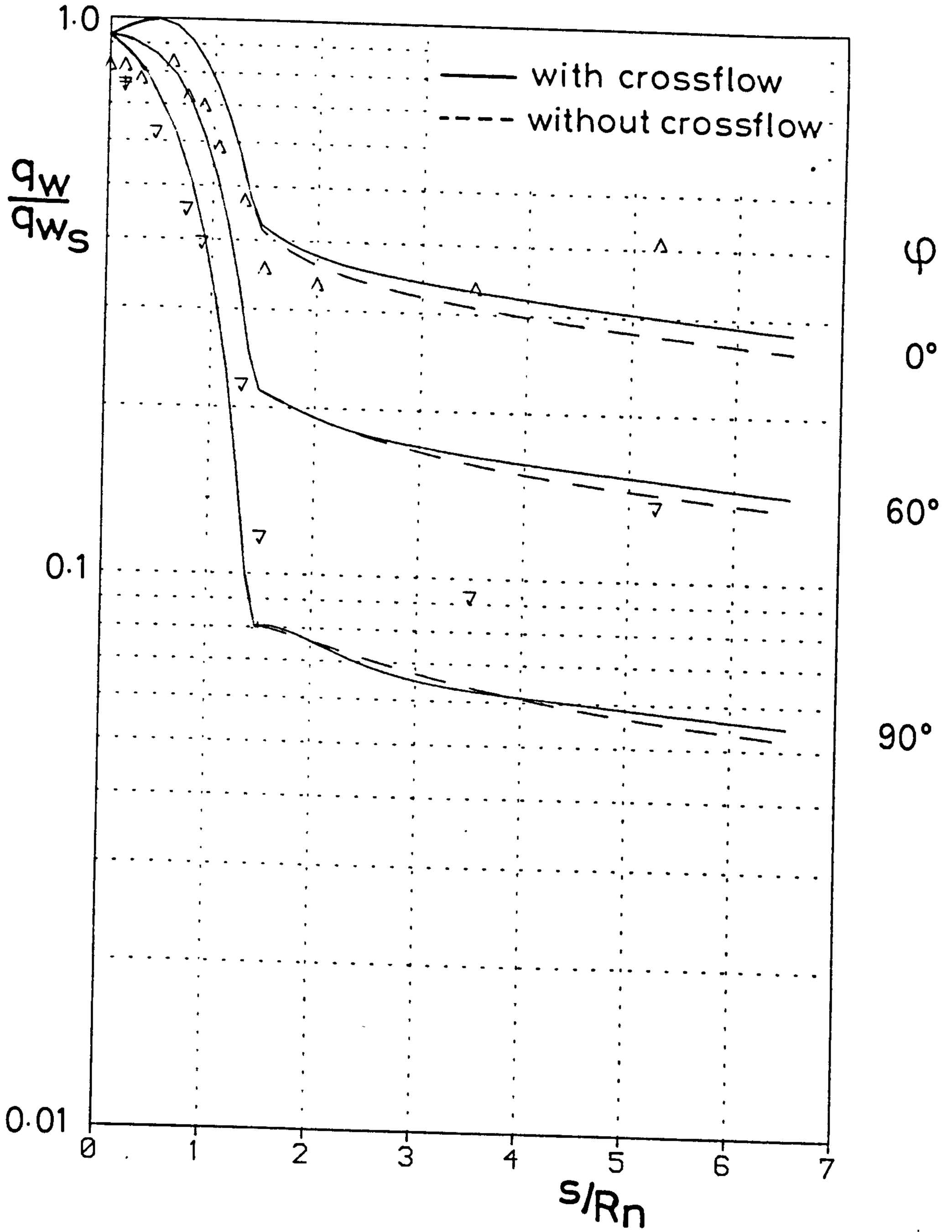

Fig. 3.6.1c Blunted cone at incidence (Widhopf)

$\vartheta_c = 9°$ $M_\infty = 5$ $T_w/T_{o_\infty} = 0.28$

$\alpha = 26°$

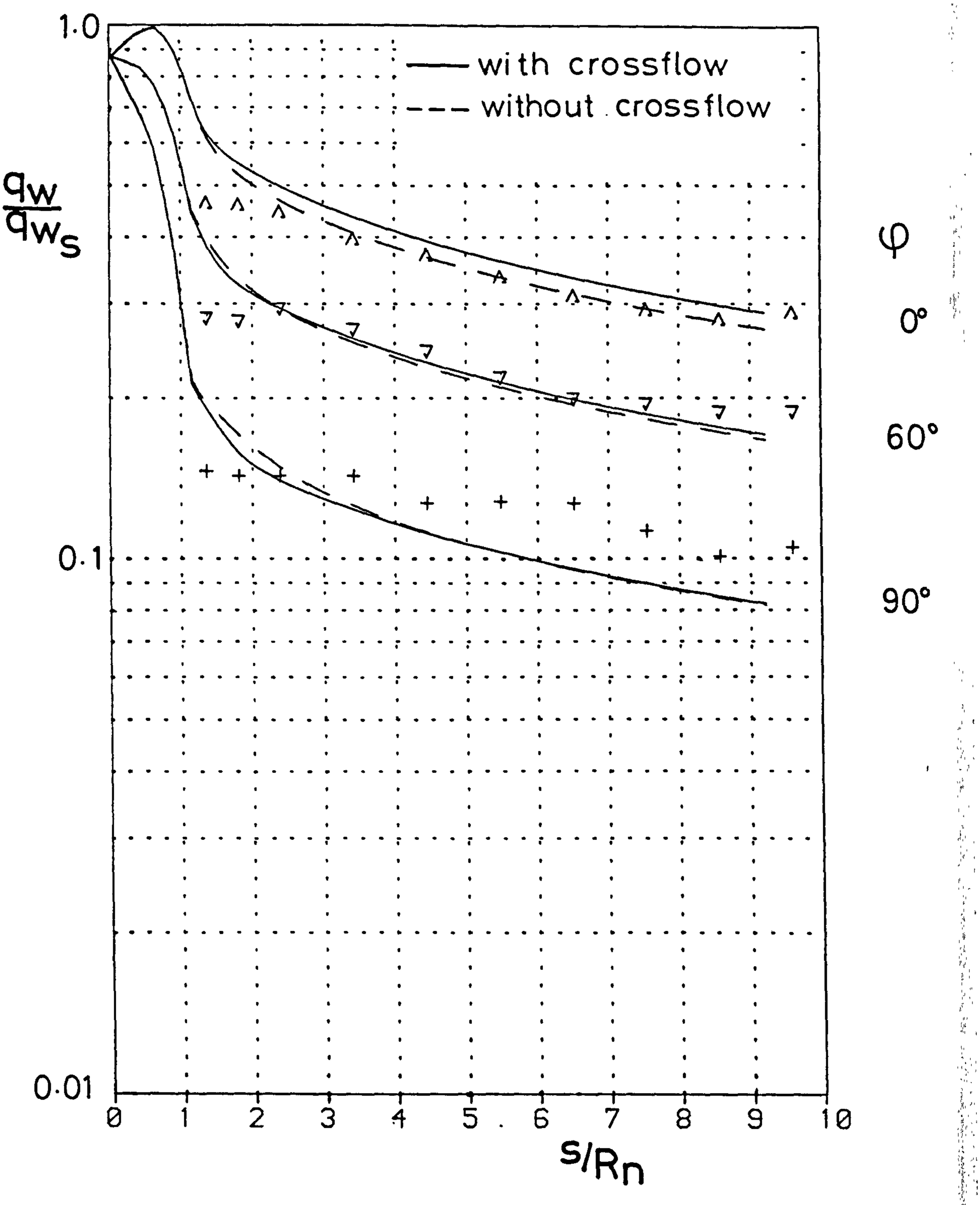

Fig. 3.6.2a Blunted cone at incidence (Bushnell)

$\vartheta_c = 25°$ $M_\infty = 8$ $T_w/To_\infty = 0.4$

$\alpha = 30°$

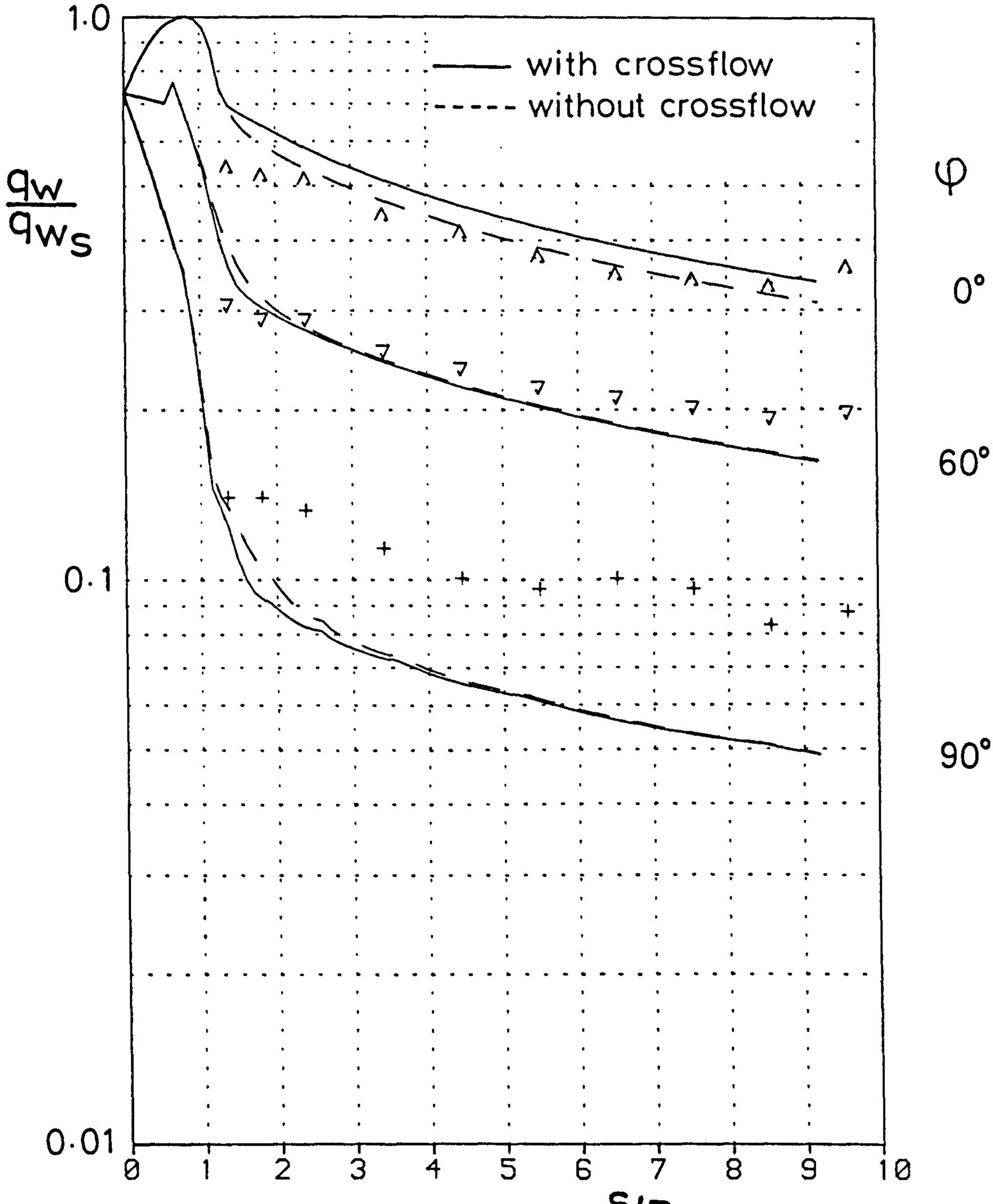

Fig.3.6.2b Blunted cone at incidence (Busnell)

$\vartheta_c = 25°$ $M_\infty = 8$ $T_w / To_\infty = 0.4$

$\alpha = 45°$

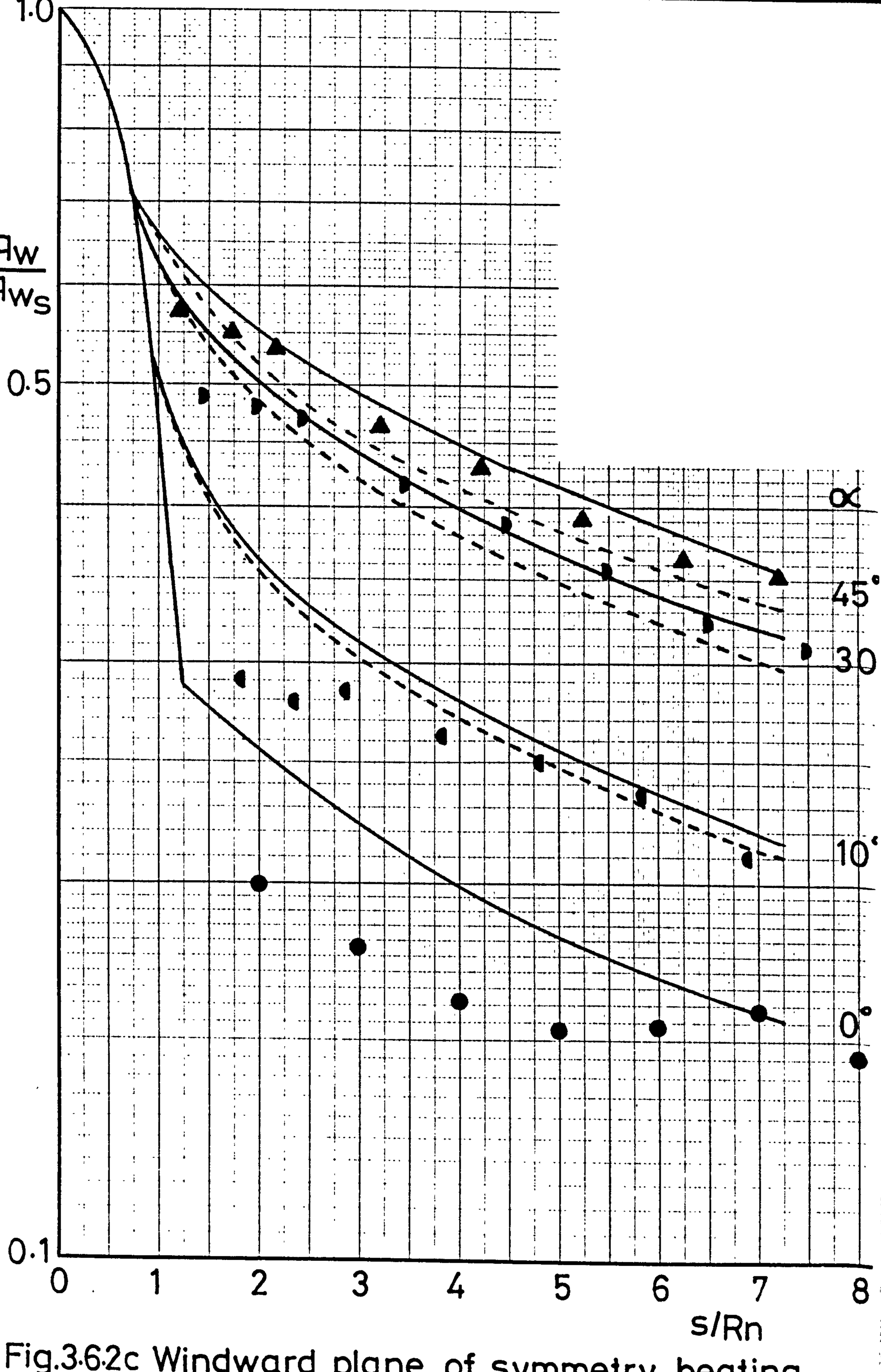

Fig.3.6.2c Windward plane of symmetry heating (Bushnell)

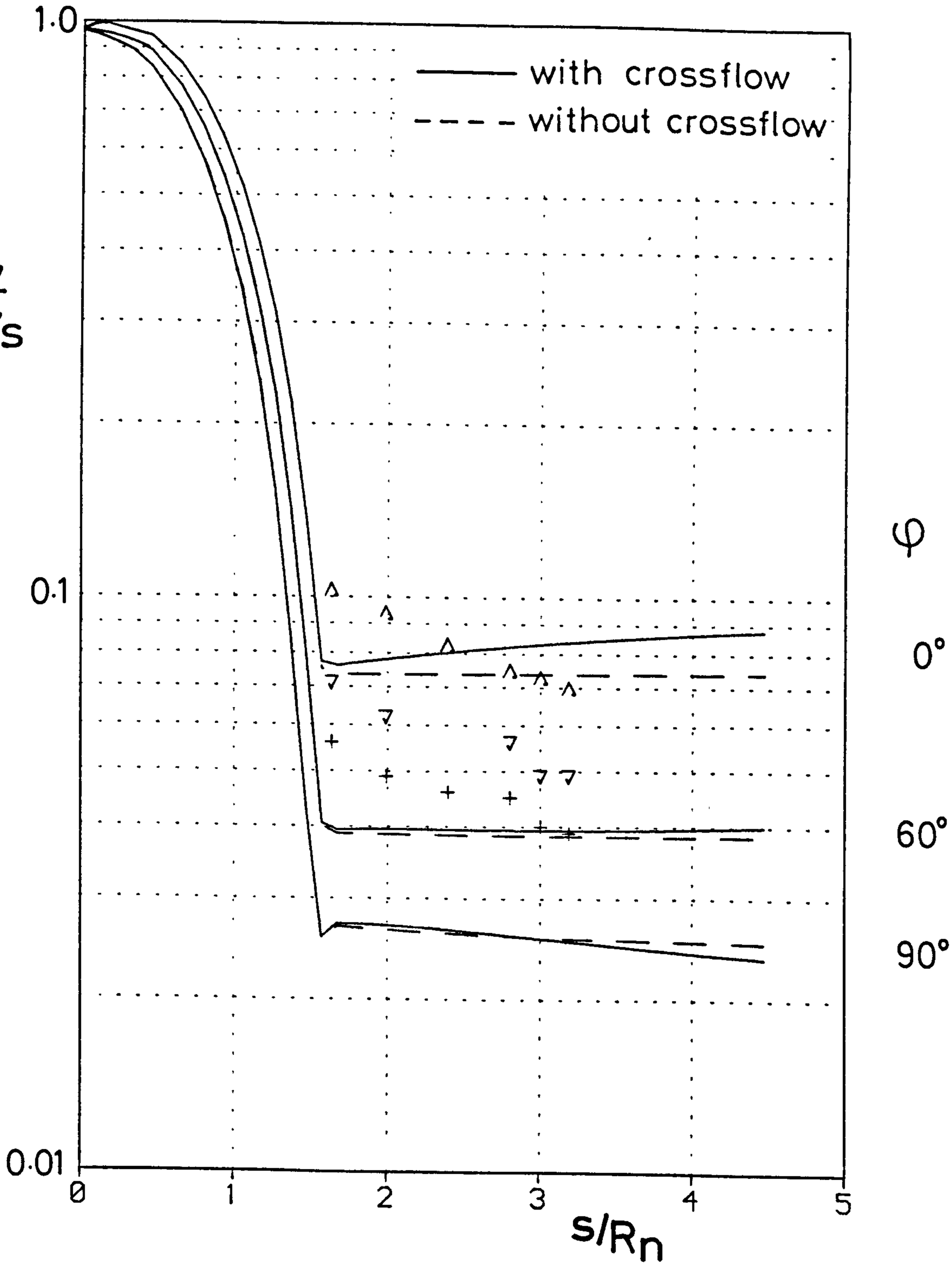

Fig.3.6.3 Blunted cone at incidence (Davies)

$\vartheta_c = 0°$ $M_\infty = 7$ $T_w/T_{o_\infty} = 0.4$

$\alpha = 10°$

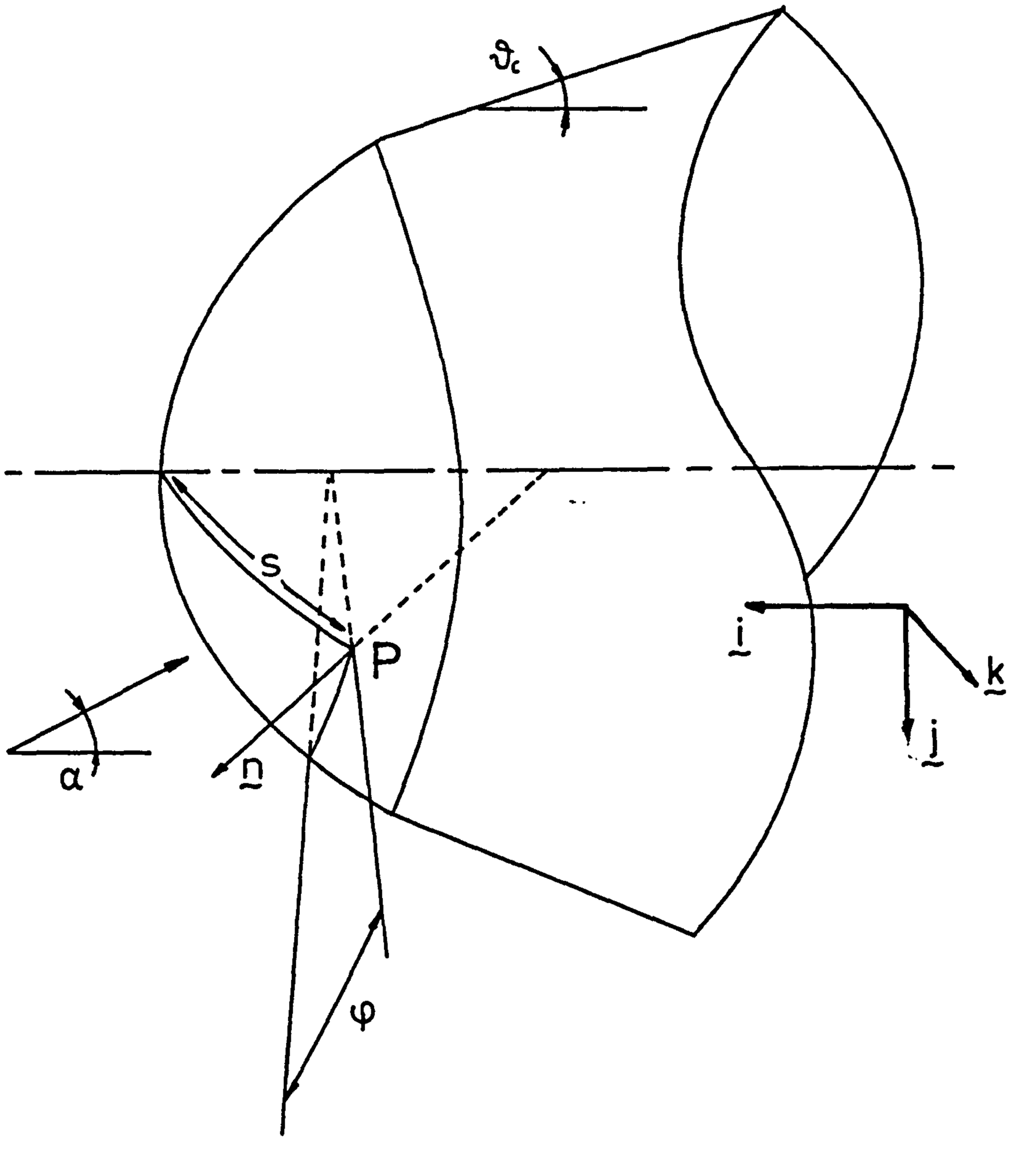

Fig 4.0.1 Hemispherically blunted cone at incidence

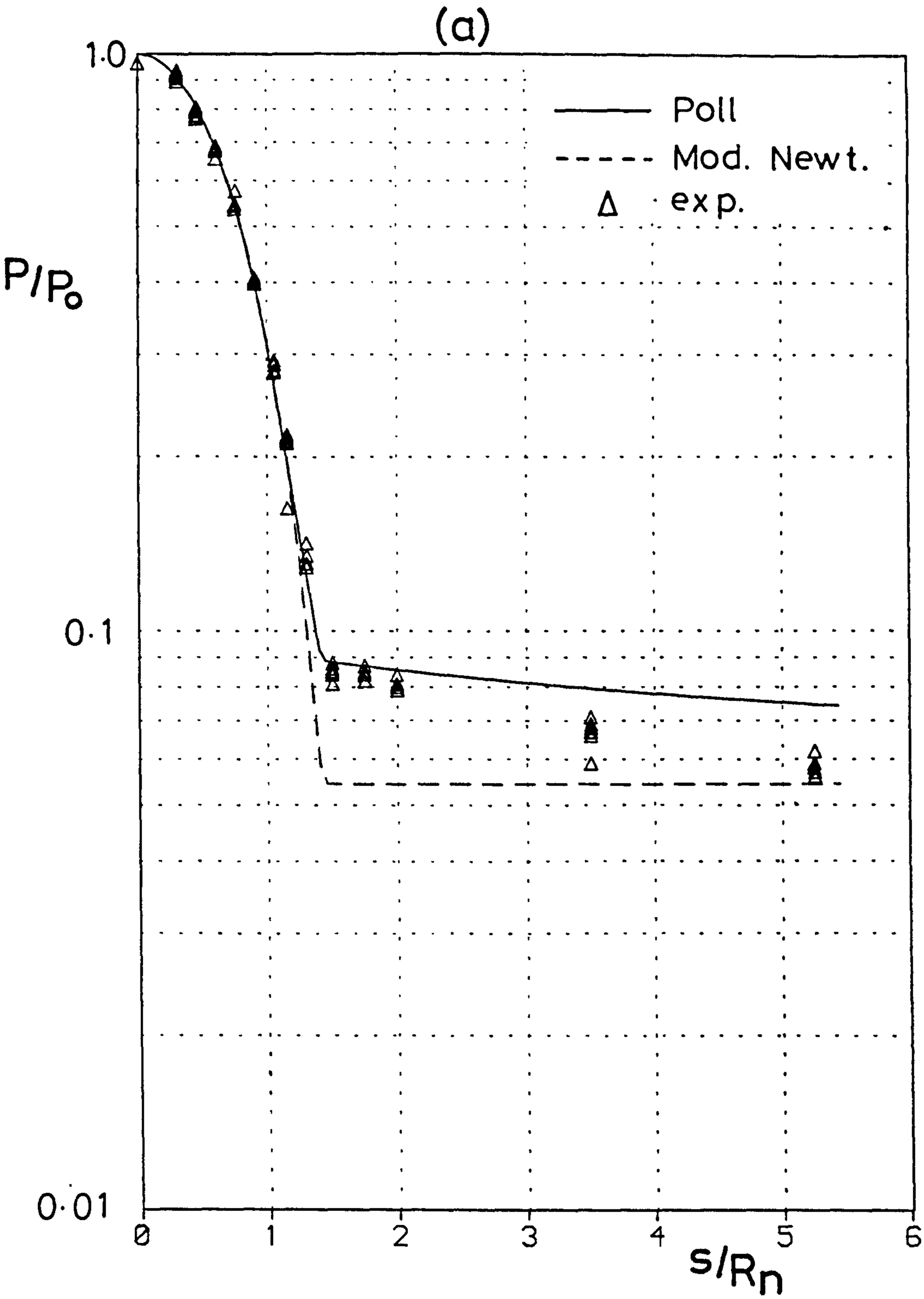

Fig 4.1.1 Pressure distribution predictions over sphere-cones Widhopf ref(32)

$M_\infty = 5 \quad \vartheta_c = 9° \quad \alpha = 0°$

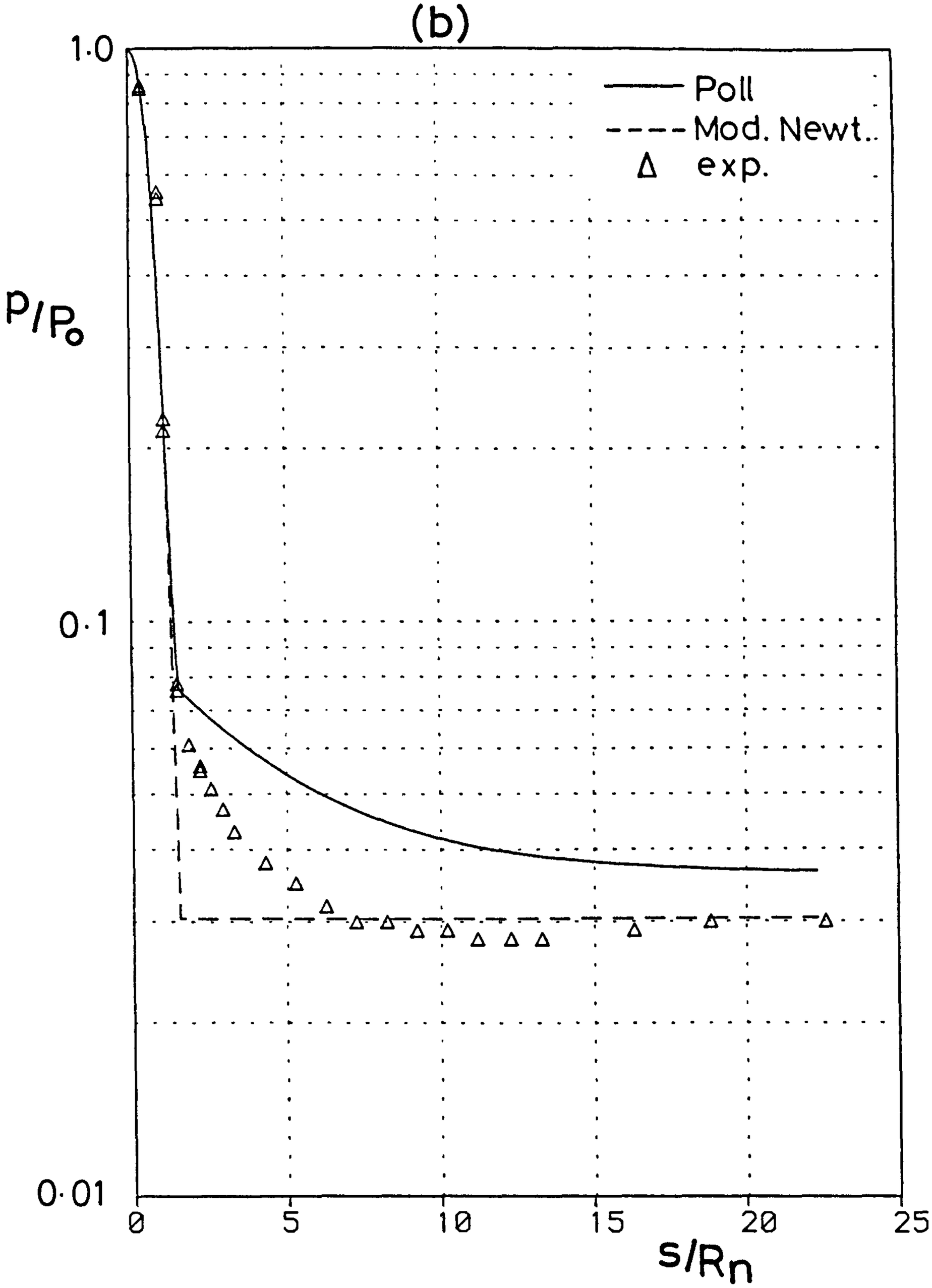

Fig 4.1.1 Pressure distribution prediction over sphere-cones King ref (63)

$M_\infty = 7 \qquad \vartheta_c = 7° \qquad \alpha = 0°$

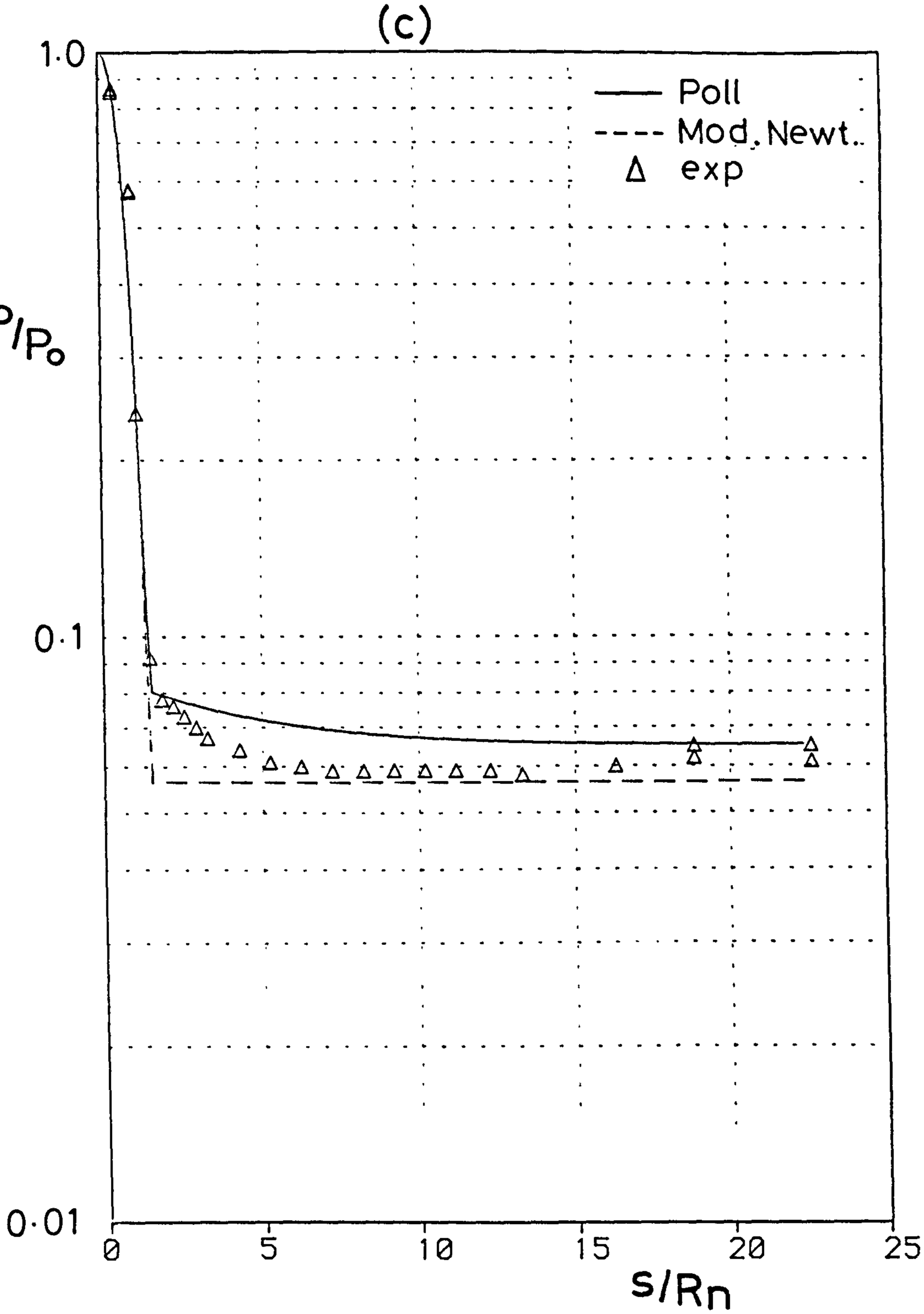

Fig 4.1.1 Pressure distribution predictions over sphere-cones King ref(63)

$M_\infty = 4.25 \quad \vartheta_c = 7° \quad \alpha = 0°$

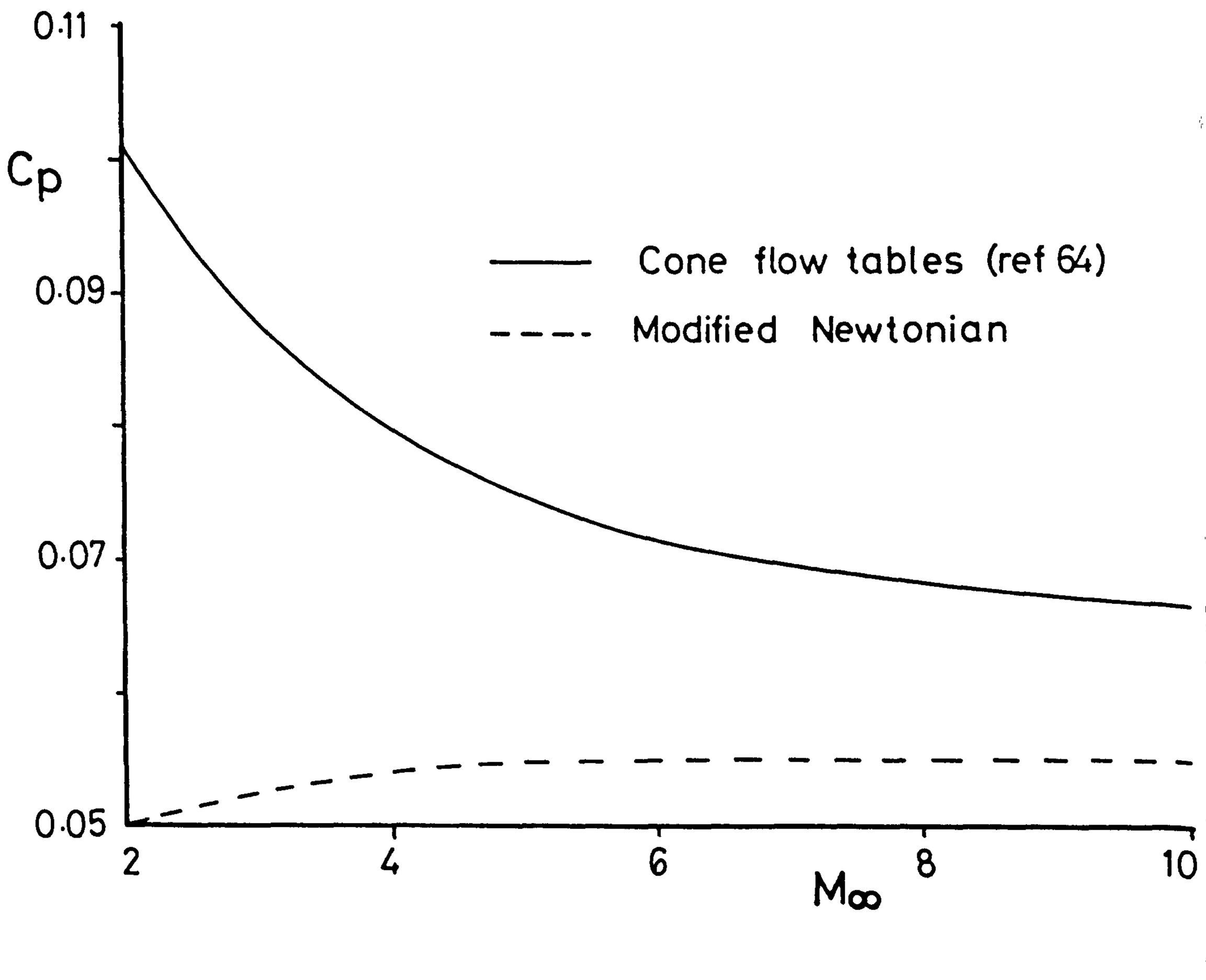

Fig 4.1.2 Modified Newtonian pressure prediction on 10° sharp cone at zero incidence

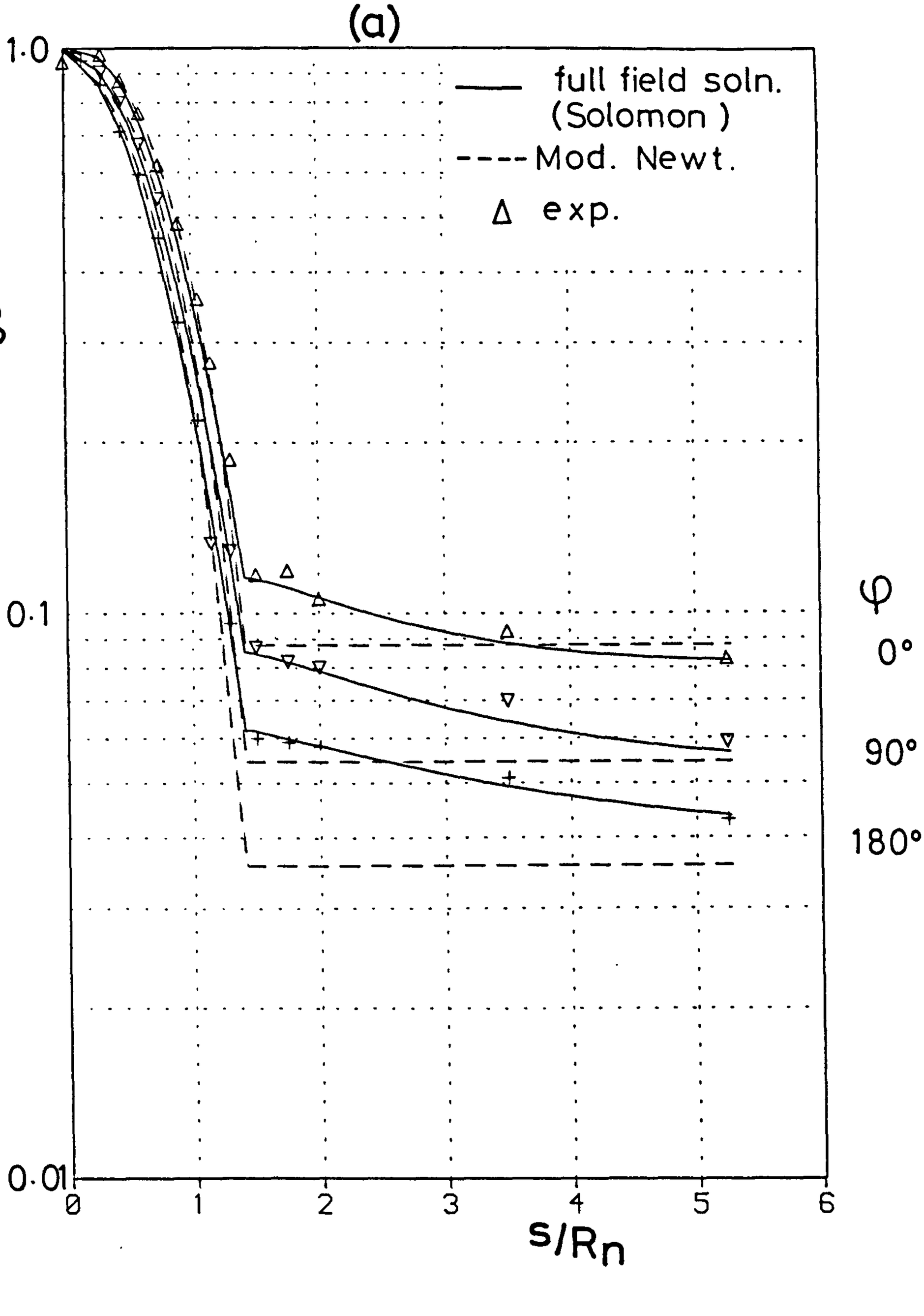

Fig 4.2.1 Pressure distribution prediction on a sphere - cone at incidence

$M_\infty = 5 \quad \vartheta_c = 9° \quad \alpha = 5°$

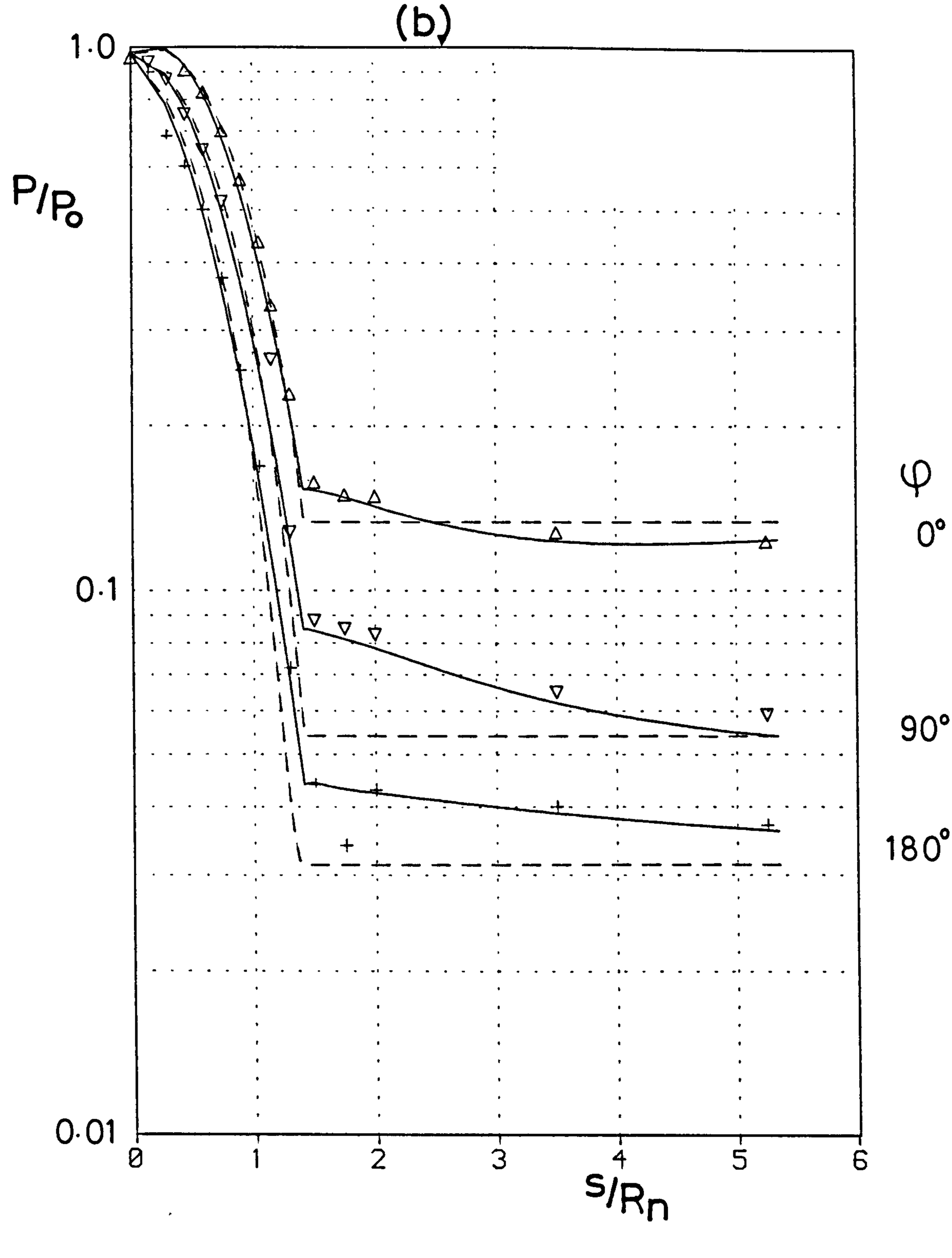

Fig. 4.2.1 (cont.) $\alpha = 10°$

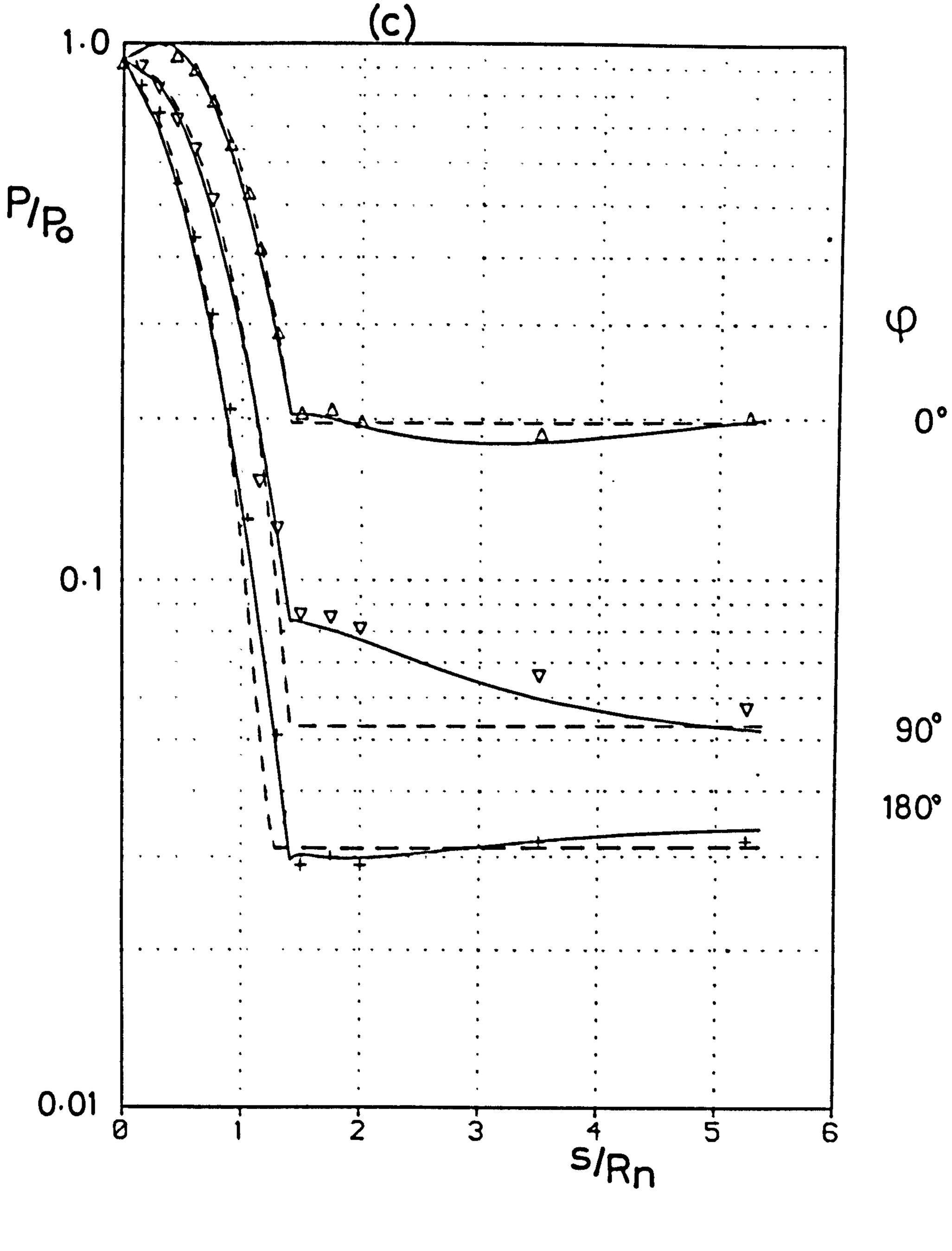

Fig. 4.2.1 (concl.) $\alpha = 15.4°$

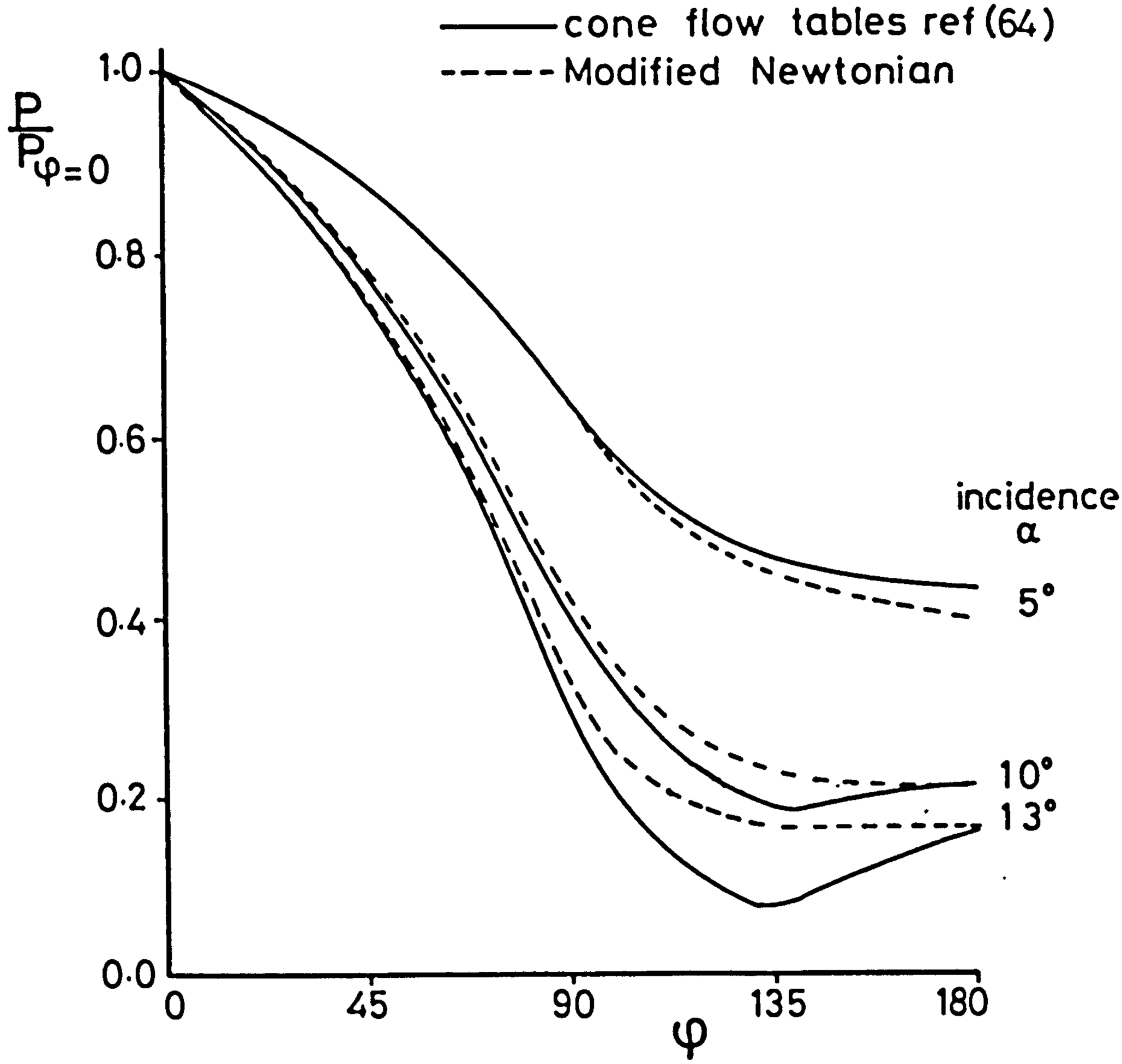

Fig.4.2.2 Circumferential pressure variation on a 10° sharp cone in a mach 5 free stream.

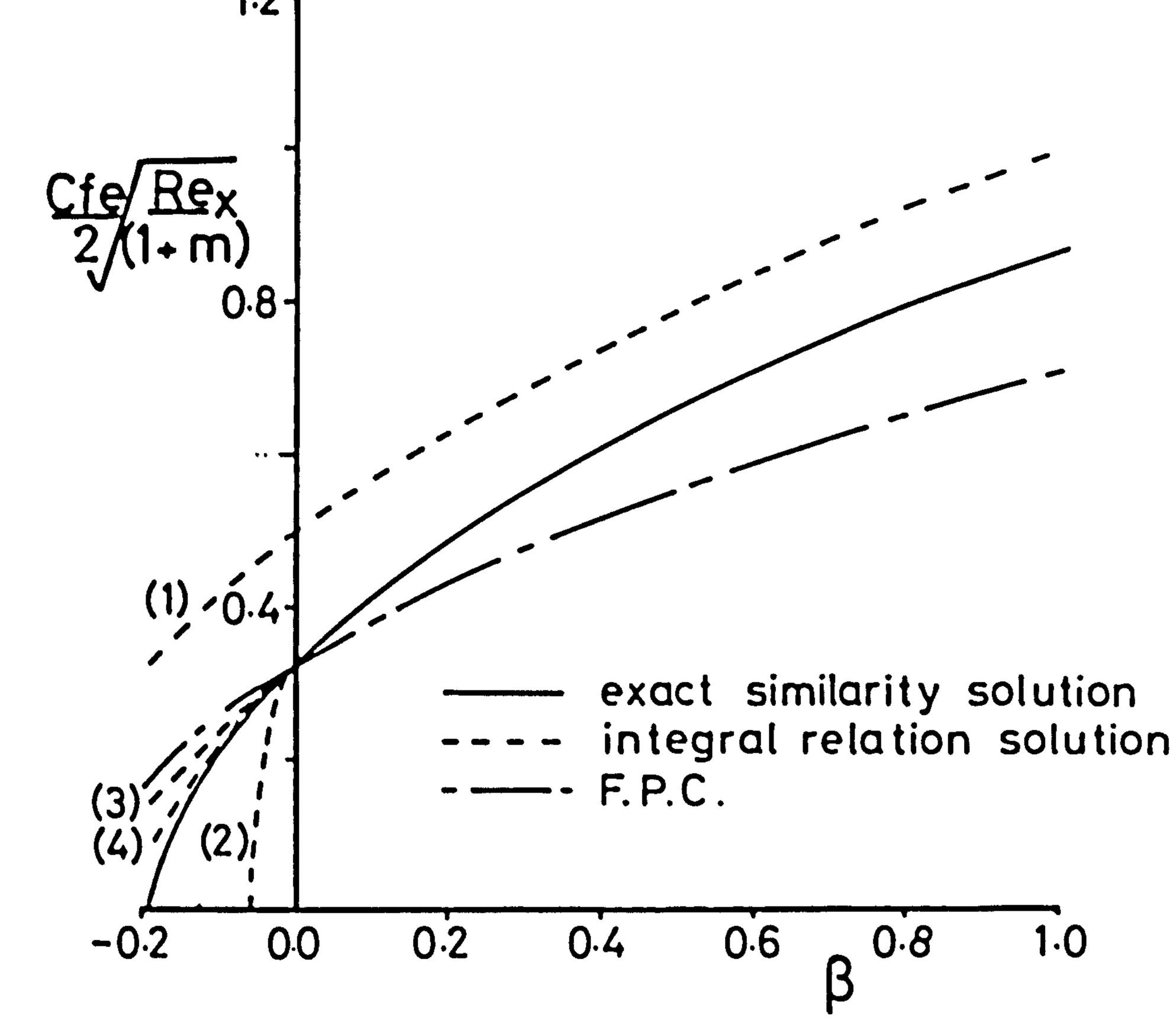

Fig. 5.1 Prediction of incompressible laminar similarity boundary layer by the method of integral relations

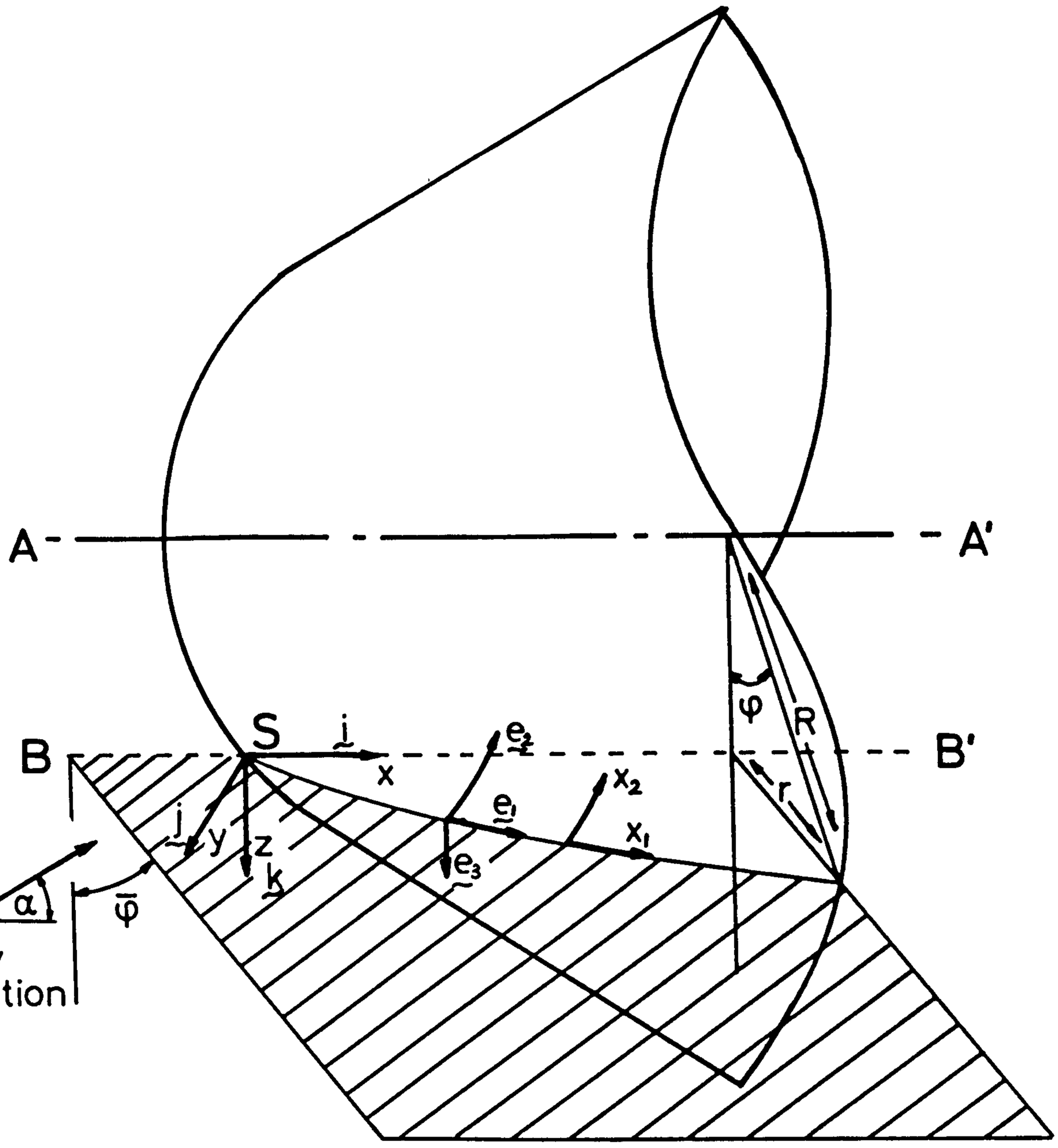

Fig D1 Generation of Blottner & Ellis coordinate system

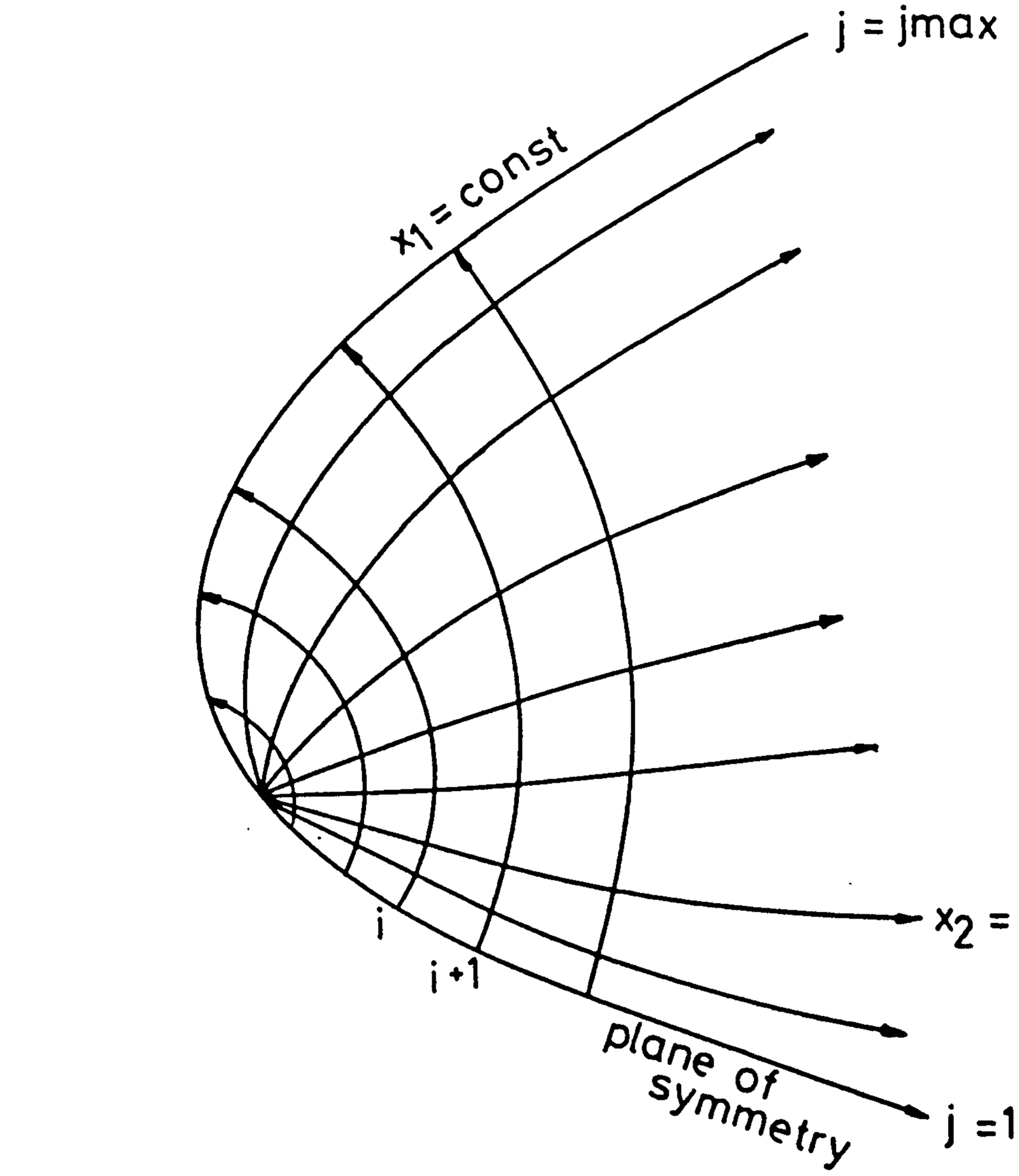

Fig. D2 Coordinate direction

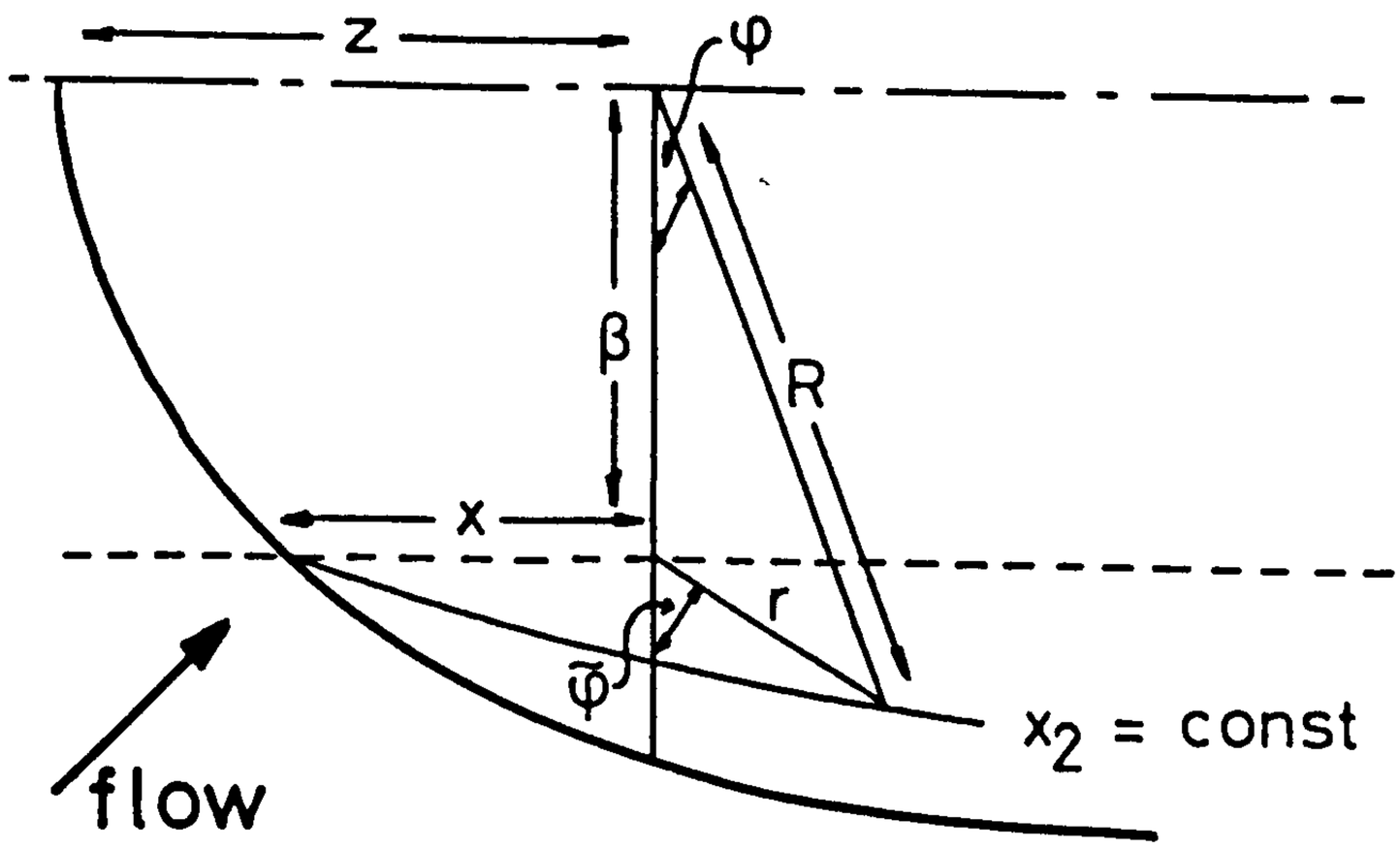

Fig. D3 Mesh notation